Cranfield UNIVERSITY

By Nicola J. Woolmore

The Failure of a Tungsten Carbide - Cobalt Cored Projectile Penetrating a Hard Target

Defence College of Management and Technology

Award: Doctorate of Philosophy

Cranfield UNIVERSITY

The Defence College of Management and Technology
Engineering Systems Department

PhD THESIS
2004 - 2005

Author: Nicola J. Woolmore

The Failure of a Tungsten Carbide - Cobalt Cored Projectile Penetrating a Hard Target

Supervisor: Dr Paul J. Hazell
Submission Date: January 2005

Abstract

Experimental results are presented from an investigation of the parameters of a ceramic-faced armour system that are required to induce damage in a tungsten carbide - cobalt (WC-Co) penetrator. A WC-Co material model has been successfully developed and implemented within the numerical hydrocode AUTODYN 2D. The understanding of penetration mechanisms was used to guide a parametric investigation, validating the WC-Co material failure model with experimental results.

A series of experiments has been conducted firing the Russian 14.5 mm BS41 WC-Co cored projectile into various thicknesses and types of alumina (Al_2O_3) and silicon carbide (SiC), backed by aluminium alloy or mild steel semi-infinite witness blocks. Results demonstrated that SiC B out-performed standard monolithic armours and a selection of other armour ceramics including PS 5000 SiC and Sintox-CL. After comminution, the SiC B consisted of particles of closely interlocked grains. These appeared to provide considerable resistance to deviatoric stresses. Results suggest that it is not only increased hardness but also the nature of the fracture of the ceramic ahead of the penetrator that improves the armour's ballistic performance at defeating WC-Co penetrators. If such superior ballistic response can be controlled and incorporated into practical armour systems, it will provide the basis for an advance in armour protective capability against WC-Co penetrators.

In addition, a numerical material model derived from experimental data was developed to provide a preliminary tool to study the WC-Co failure. It was demonstrated that the numerical estimation of WC-Co behaviour using a shock Equation Of State (EOS), a piecewise linear strength model and a principle stress failure model provides a good method to estimate spall behaviour under dynamic loading in AUTODYN 2D. Successful numerical simulation of the material model used demonstrated the future potential of the technique.

Key Words: Alumina (Al_2O_3), AUTODYN 2D, Depth of Penetration (DoP), Silicon Carbide (SiC), Tungsten Carbide – Cobalt (WC-Co).

Acknowledgements

I would like to express my sincerest thanks to my Director of Studies, Dr Paul Hazell whose constant guidance, enthusiasm, encouragement and not least patience has made this project both interesting and successful.

Much gratitude is deserved for my sponsors at the Defence Science Technology Laboratories (dstl) and the Engineering & Physical Science Research Council (EPSRC), Tom Stuart, Bryn James, Andy Baxter, Ross Jones, Ian Pickup and Richard Baird. Moreover I would wish to thank Colin Roberson, Morgan AM & T, Morgan Matroc Ltd, HC Stark and Cercom Inc. for their continued support and discussions making the experimental investigation possible.

I have received much support over the four years from other members of the Engineering Systems Department and Cranfield staff. Thanks to Ian Horsfall, Mike Iremonger, John Crocker, Jim Harber, Tim Rose and Jonathan Painter and to many others for their support throughout.

Lastly, I would like to thank all my family, good friends and colleagues: my mother and father Val and Ernie, my brother Adrian, my sister in law Gwen and my niece Holly, Crispin Doyle, Steve Champion, Charlie Ross, and Freudian's Lip for their constant selfless support and encouragement.

I would like to make a special thanks to the NOISE team (EPSRC) and the BBC for their inspiration and giving me the rare opportunity to share my work.

Table of Contents

LIST OF FIGURES **8**

LIST OF GRAPHS **14**

LIST OF TABLES **15**

LIST OF ABBREVIATIONS AND SYMBOLS **17**

CHAPTER 1 ..... **21**

INTRODUCTION **21**

1.1 CERAMIC ARMOUR: A NOVEL CONCEPT 22
1.2 IMPACT PHENOMENA: ASSESSMENT AIMS AND OBJECTIVES 24
1.3 PREFACE TO CHAPTERS 25

CHAPTER 2 ..... **28**

CERAMIC ARMOUR LITERATURE REVIEW **28**

2.1 FIREPOWER AND MOBILITY 29
2.2 CERAMICS FOR ARMOUR APPLICATIONS 29
2.2.1 Ceramic Microstructure *29*
2.2.2 Manufacturing Process, Cost and Availability *30*
2.2.3 Hardness *32*
2.2.4 Strength and Toughness *33*
2.2.5 Fracture Toughness *35*
2.2.6 Ceramic Porosity *36*
2.3 THE DEVELOPMENT OF CERAMIC ARMOUR LAYER DESIGN 37
2.3.1 Theoretical Advance in Ceramic Armour Layer Design *38*
2.3.2 Ceramic Bilayer Defeat Mechanisms *41*
2.3.3 Dynamic Stress Wave Propagation *44*
2.4 IMPROVING PERFORMANCE OF CERAMIC ARMOUR SYSTEMS 50
2.4.1 Confinement *50*
2.4.2 Adhesives *53*
2.5 14.5 MM BS41 RUSSIAN ARMOUR PIERCING PROJECTILE 55
2.5.1 WC-Co Armour Piercing Projectiles *56*
2.5.2 Russian BS41 14.5 mm Threat *57*
2.5.3 Manufacture of a Cemented Carbide (WC-Co) *59*
2.5.4 WC-Co AP Development *63*
2.6 CONCLUSIONS 66

CHAPTER 3 ..... **68**

EXPERIMENTAL METHODOLOGY **68**

3.1 EXPERIMENTAL BALLISTIC TESTS 69
3.1.1 V_{50} Technique *69*
3.1.2 Depth of Penetration Technique Methodology *70*
3.2 PERFORMANCE CRITERIA 71
3.2.1 Mass Efficiency and Differential Efficiency *72*
3.3 EXPERIMENTAL MATERIALS 73
3.3.1 Projectiles and Firearms *73*
3.3.2 BS41 Propellant *74*
3.3.3 Ceramic Material *76*
3.3.4 Hardness Measurement *78*
3.3.5 Grain Size Determination *78*
3.3.6 Witness Plate *79*
3.3.7 Interlayer Coupling: Tungsten Paste *80*
3.4 EXPERIMENTAL MEASUREMENTS 81

3.4.1 Velocity Measurement *81*
3.4.2 Yaw Angle *82*
3.4.3 Experimental Confinement *82*
3.4.3.1 Lateral Confinement Rig *82*
3.4.3.2 Bespoke Target Frame *86*
3.5 EXPERIMENTAL AIDS 87
3.5.1 High Speed Camera *87*
3.5.2 Flash X-radiography *89*
3.6 FRACTURE MORPHOLOGY ANALYSIS 91
3.6.1 Preparation Details *92*
3.7 EXPERIMENTAL METHODOLOGY SUMMARY 94

CHAPTER 4 95

EXPERIMENTAL ANALYSIS AND DISCUSSION 95

4.1 PART 1: EFFECTS OF CONSTRAINT ON TARGET AND PROJECTILE 96
4.1.1 Baseline Witness Block DoP Results *96*
4.1.1.1 WC-Co Fragmentation after Penetrating a Monolithic Armour *100*
4.1.2 1318b Aluminium Alloy Anisotropic Effects *101*
4.1.3 Comparison of Mild Steel and 1318b Aluminium Alloy Witness Block, both with a Sintox-CL Front Plate *103*
4.2 PART 2: EFFECTS OF ALTERING CONFINED CERAMIC ARMOUR CONFIGURATION 107
4.2.1 Change in Ceramic Strike Face *107*
4.2.2 Ceramic Front-Plate Ballistic Performance *108*
4.2.2.1 WC-Co Fragmentation after Penetrating a Ceramic Applique System *111*
4.2.3 Effects of Impact Velocity on Ballistic Performance *113*
4.2.4 Velocity Effects on Ceramic Fragmentation *114*
4.2.4.1 WC-Co Fragmentation after Impacing Ceramic at a Range of Impact Velocities *116*
4.2.5 Ceramic Comminution *117*
4.2.6 Effects of Ceramic Armour Appliqué System *119*
4.2.7 Discussion *122*

CHAPTER 5 129

MICROSCOPIC ANALYSIS AND DISCUSSION 129

5.1 SCANNING ELECTRON MICROSCOPY ANALYSIS FROM AN UNFIRED SAMPLE OF WC-CO CORE 130
5.2 ENERGY DISPERSIVE X-RADIOGRAPHY ANALYSIS FROM AN UNFIRED SAMPLE OF WC-CO CORE 132
5.3 FRACTURE ANALYSIS FROM A FIRED SECTION OF WC-CO 138
5.4 DISCUSSION 146
5.5 SUMMARY 149

CHAPTER 6 151

DEVELOPMENT OF A NUMERICAL MATERIAL MODEL TO PREDICT TUNGSTEN CARBIDE – COBALT FAILURE 151

6.1 NUMERICAL MODELLING FOR BALLISTIC APPLICATION 152
6.1.1 AUTODYN 2D *152*
6.2 MATERIAL MODEL DATA INPUT 154
6.2.1 Grady's Numerical Model *154*
6.2.2 Plate Impact Data *159*
6.2.3 Equation of State *165*
6.2.4 Shock EOS for Material K68 ..... *166*
6.2.5 Polynomial EOS *170*
6.2.6 Piecewise Linear Strength Model *172*
6.2.7 Failure Model *174*
6.3 SUMMARY 179

CHAPTER 7 181

NUMERICAL VALIDATION 181

7.1 AUTODYN 2D SIMULATION OF WC-CO 182
7.1.1 Numerical Validation Introduction 182
7.2 NUMERICAL PROCESSOR FOR MODELLING WC-CO FAILURE 182
7.3 SPHERE IMPACT TEST 184
7.4 BS41 COMPUTATIONAL STUDY 195
7.4.1 Modelling the DoP into a Witness Block 199
7.4.2 WC-Co Spall Failure Characteristics 200
7.4.3 Flash X-ray Configuration and Material Properties 204
7.5 DISCUSSION 210
7.6 SUMMARY 212

CHAPTER 8 214

CONCLUSIONS & RECOMMENDATIONS FOR FURTHER WORK 214

8.1 CONCLUSIONS 215
8.2 RECOMMENDATIONS FOR FURTHER WORK 220

CITED REFERENCES 224

APPENDICES

APPENDIX 1……... 236

APPENDIX 2…… 239

APPENDIX 3 ……..…….253

APPENDIX 4 ……..….266

APPENDIX 5 ……....270

List of Figures

Figure 1.1: Warrior Armoured Fighting Vehicle. 23

Figure 2.1: Florence Analytical Model 38

Figure 2.2: The Hetherington and Lemieux Obliquity Model 40

Figure 2.3: Characteristic armour failure modes (adapted from Zukas) 42

Figure 2.4: A Scanning Electron Micrograph taken from a sample of WC-Co (14.5 mm BS41) showing the presence of a pore at the spall surface with cracks propagating either side. 43

Figure 2.5: A graphical representation of a numerical simulation of a 14.5 mm BS41 projectile after impacting and penetrating a SiC front face and an aluminium alloy ductile witness plate 44

Figure 2.6: Diagram showing an example of the incident, reflected and transmitted stress wave between two materials after impact from a WC-Co penetrator. 47

Figure 2.7: Velocity (*V*): Events occurring on impact of projectile into a target from left to right (a) projectile (left) impacting target (b) position at instant of impact: (c) position after impact and during wave propagation stage 49

Figure 2.8: 14.5 mm AP-I Type BS41 jacketed projectile (length 51.2 mm) (left) and core (length 38.72 mm) (right)....57

Figure 2.9: SEM micrograph showing the grain structure of a WC-Co sample taken from the Russian BS41 14.5 mm projectile. 61

Figure 2.10: BS41 fractured WC-Co core. Captured by an 1318b aluminium alloy witness block after firing through a SiC B front face coupled to the 1318b aluminium alloy witness block. 64

Figure 3.1: DoP technique for assessing each ceramic's ballistic performance. 71

Figure 3.2: Houndsfield tensometer round tensile test sample dimensions, tolerance ± 0.10 mm 70.86 mm (*Lo*) 80

Figure 3.3: Modified Lateral Confinement Rig used for the experimental testing of the BS41; A = front steel block section and B = the back steel block section. 83

Figure 3.4: Schematic Diagram of the experimental set up. A = front steel block section and B = the back steel block section....84

Figure 3.5: Experimental set-up at Royal Military College of Science, Shrivenham...85

Figure 3.6: Bespoke target frame 86

Figure 3.7: 7.62 x 51 mm FFV during three stages of flight, left to right, surrounded by Sintox-CL Al_2O_3 ceramic debris.....88

Figure 3.8: 11.07 mm Sintox-CL Al_2O_3 plate impacted by the FFV 7.62 x 51 mm WC-Co cored projectile.....88

Figure 3.9: Displays 11.07 mm Sintox-CL Al_2O_3, FFV 7.62 mm WC-Co cored Projectile 200 µs after impact 89

Figure 3.10: Flash X-ray shadowgraph of the BS41 penetrating 25 mm Sintox-CL ceramic front plate. 90

Figure 4.1: From left to right: BS41, BS41 unfired core, core retrieved after firing into mild steel and core retrieved after firing into 1318b witness block.....100

Figure 4.2: Three rolling directions tested for the 1318b aluminium alloy sample, 1 = Longitudinal (roll), 2 = short transverse (minimum dimension) and 3 = long transverse direction. 101

Figure 4.3: 1318b, plane 1 (*Figure 4.2*), after impact from the BS41 102

Figure 4.4: WC-Co fragmentation pictures: (a) 58 kg/m^2 Sintox-CL (88%) (b) 58 kg/m^2 SiC B (29%) (c) 58 kg/m^2 SiC PS 5000 (34%) (% = Total Mass).....112

Figure 4.5: WC-Co core fragmentation for two different types of ceramics front plate and 1318b witness block (a) Sintox-CL (b) SiC B. From left to right 750 m/s, 850 m/s and 1100 m/s. 116

Figure 4.6: Fractographic images of the comminutia resulting from the ballistic impact tests (a) SiC PS 5000 failed in primarily transgranular cleavage mode (b) SiC B failed in primarily intergranular mode.....118

Figure 4.7: Schematic representation of the target configuration for the ballistic test. 119

Figure 4.8: Three 1318b aluminium alloy plates, thicknesses 30, 20 and 10 mm, deformed after impact. 121

Figure 4.9: X-rays of the residual penetration and the remnants of the WC-Co in the 1318b. (a) 10 mm, (b) 20 mm and (c) 30 mm, 1318b coupled to 18 mm Sintox-CL. 122

Figure 4.10: Aluminium alloy 1318b block after penetration (short transverse direction – *note* no splitting (*Section 4.1.2*)) from the BS41. Lip formation around the periphery of the impact crater can be observed with ductile hole growth. 124

Figure 4.11: Mild Steel witness block after penetration from the BS41. Typical crater formed around the periphery of the impact crater. 125

Figure 5.1: Scanning Electron Micrograph of the transverse cross section of the unfired WC-Co core. 1, 2 and 3 represent the locations of EDX analysis displayed in *Figure 5.8.* 130

Figure 5.2: Scanning Electron Micrograph of the longitudinal cross section of the unfired WC-Co core. 1, 2, 3, 4 and 5 represent the locations of EDX analysis. 131

Figure 5.3: Scanning electron micrograph of a void region in an unfired, polished, WC-Co core sample. 132

Figure 5.4: Schematic diagram of five possible fracture modes in WC-Co (WC grains surrounded by a Co matrix). 1: Ductile matrix failure, fracture through the Co matrix surrounding the WC grains *or* at cryogenic temperatures cleavage of the matrix, 2: Cleavage of WC grains (transgranular cleavage), 3: WC – WC grain boundary decohesion (intergranular cleavage), 4: WC side of the WC – Co interface decohesion and finally 5: Matrix side of WC – Co interface decohesion. 133

Figure 5.5: Scan map over the surface of the polished WC-Co sample. 134

Figure 5.6; Energy Dispersive X-ray; Identification of Co and W from a longitudinal unfired sample of WC-Co core. 135

Figure 5.7; Energy Dispersive X-ray map scan of void, point 1 (*Figure 5.3).* The target element is identified in the lower left corner of each scan. 136

Figure 5.8: Three Energy Dispersive X-rays of three points on the surface of the polished unfired WC-Co core sample shown in *Figure 5.1,* (a) (Point 1), W, C, traces of Fe and Pb (b) (Point 3), high C regions, with W, Pb and Fe (c) (Point 2), Pb. 137

Figure 5.9: BS41 WC-Co fractured core retrieved after firing into, from left to right, 18 mm Sintox-CL / mild steel semi-infinite WP, 18 mm Sintox-CL / aluminium alloy semi-infinite WP and 30 mm FA/ mild steel. 138

Figure 5.10: A SEM micrograph from a recovered WC-Co spall specimen after penetration into a SiC B front plate and a 1318b aluminium alloy witness block. 139

Figure 5.11: Scanning electron micrograph from a sample of WC-Co after penetration through a SiC B front plate and an aluminium witness block. Primary failure mode was transgranular cleavage of large WC grains. 140

Figure 5.12: A large grain of WC-Co failed by transgranular cleavage. Mixed transgranular and intergranular failure can be observed in the surrounding grains. 140

Figure 5.13: Scanning electron micrograph from a sample of WC-Co after penetration through a SiC B front plate and an aluminium witness block. Primary failure mode was intergranular cleavage of the small WC grains. 141

Figure 5.14: Fracture surface of WC-Co taken from a rear sample, revealing a large crack propagated across the diameter of the core 142

Figure 5.15: Micrograph from a sample of WC-Co after penetration through a SiC B front plate and an aluminium witness block, inclined to the plane of shock-wave (*Figure 5.14*). 142

Figure 5.16: Crack propagation arrests at a major void.....144

Figure 5.17: Large primary crack with a small secondary crack that propagated through major void regions. 144

Figure 5.18: Six fracture surfaces removed from different residual penetrators after penetrating SiC B. (A) WC-Co spall section (B – E) Different regions from spall section A - Typically a "River" cleavage failure pattern formed during prominent regions of transgranular cleavage and (F) Exposed Co matrix prominent down a primary crack. 145

Figure 5.19: Cleavage surface of fractured WC-Co coated in aluminium and other impurities after impact into a SiC B front plate and aluminium witness block..148

Figure 6.1: 14.5 mm WC-Co core impacting 25 mm B_4C front plate with a 25 mm aluminium alloy back plate, WC-Co tensile failure strain 0.5%. 156

Figure 6.2: 14.5 mm WC-Co core impacting 25 mm B_4C front plate with a 25 mm aluminium alloy back plate, WC-Co tensile failure strain 0.75%. 156

Figure 6.3: 14.5 mm WC-Co core impacting 25 mm B_4C front plate with a 25 mm aluminium alloy back plate, WC-Co tensile failure strain 1.00%. 157

Figure 6.4: Results from Roberson *et al.*: 7.62 mm FFV impacting 6.5 mm and 7.6 mm B_4C from left to right respectively. Increased fragmentation observed with increased thickness of ceramic front plate [125]. 158

Figure 6.5: Experiment 8403, Tardec Report [27], Grady and Moody [20] Velocity Interferometer System for Any Reflector (VISAR) (*not to scale*). 159

Figure 6.6: Schematic Stress Diagram.....164

Figure 6.7: AUTODYN 2D numerical set up for plate impact response.....176

Figure 6.8: Comparison of computed stress history with ceramic-window interface velocity profiles from Test 8403, plate impact experimental data 176

Figure 7.1: Sphere impact set-up, WC-Co Sphere impacting target 75 x 75 x 3.12 mm 184

Figure 7.2: WC-Co sphere and Lucite target mesh description implanted into the AUTODYN 2D numerical code 186

Figure 7.3: Numerical results for WC-Co sphere undergoing high velocity (2.44 km/s) normal impact on plate of PMMA [20,147], AUTODYN 2D SPH 122, 156 SPH (900), 0.224 mm nodes. (a) Tensile Failure Stress (TFS), 3.5 GPa and Crack Softening (G_f) 0 J/m^2: (b) TFS, 3.5 GPa and CS 102 J/m^2 (c) TFS, 3.0 GPa and CS 102 J/m^2: (d) TFS, 4.0 GPa and CS 102 J/m^2: (e) shadowgraph 27.7 µs down-stream from the impact point. 188

Figure 7.4: (a) WC-Co sphere shadowgraph 27.7 µs down-stream from the impact point, (b) Numerical results for WC-Co sphere undergoing high velocity (2.44 km/s) normal impact on plate of PMMA [20,147], AUTODYN 2D SPH 122, 156 SPH (900), 0.224 mm nodes. 189

Figure 7.5: (a) Radiograph for WC-Co sphere undergoing high velocity (2.44 km/s) normal impact on plate of PMMA. Shadowgraph 97.3 µs down-stream from the impact point (b) numerical result in AUTODYN 2D. 190

Figure 7.6: (a) Radiograph for WC-Co sphere undergoing high velocity (2.90 km/s) normal impact on plate of PMMA. Shadowgraph 26.5 µs down-stream from the impact point (b) numerical result in AUTODYN 2D. 191

Figure 7.7: (a) Radiograph for WC-Co sphere undergoing high velocity (2.9 km/s) normal impact on a plate of PMMA. Shadowgraph 85.6 µs down-stream from the impact point. (b) Numerical result in AUTODYN 2D. 192

Figure 7.8: (a) Radiograph for WC-Co sphere undergoing high velocity (3.43 km/s) normal impact on plate of PMMA. Shadowgraph 21.2 µs down-stream from the impact point (b) numerical results in AUTODYN 2D.....193

Figure 7.9: (a) Radiograph for WC-Co sphere undergoing high velocity (3.43 km/s) normal impact on plate of PMMA. Shadowgraph 71.4 µs down-stream from the impact point (b) numerical results in AUTODYN 2D.....194

Figure 7.10: 14.5 mm AP-I Type BS41 [9]. Upper Equation [Eq. 7-1] representing the polynomial for the core tip and the lower equation [Eq. 7-2] representing the polynomial for the jacket tip (Tecplot) 196

Figure 7.11: Mesh Description of the BS41 projectile implanted into AUTODYN computer numerical programme. Top Right Flash X-ray displaying the BS41 inner core during flight. 197

Figure 7.12: Comparison of material plots of the BS41 penetrating mild steel (Top = experimental picture (DoP = 74.69 mm); numerical top *with* (80.49 mm DoP) and bottom picture *without* (80.12 mm) its outer jacket, penetrating a confined 1006 mild steel witness block. 198

Figure 7.13: AUTODYN 2D material model Set-up: From left to right; BS41-Sintox-CL-Aluminium witness plate-air gap-aluminium witness block 201

Figure 7.14: 3D model of the WC-Co core captured in an aluminium alloy witness block after penetrating 18.29 mm Al_2O_3 Sintox-CL coupled to a 10 mm aluminium alloy followed by a 10 mm air gap. 202

Figure 7.15: From top to bottom a numerical simulation compared to an X-ray of the BS41 WC-Co core captured in a 1318b aluminium alloy witness block after penetrating 18.29 mm Al_2O_3 Sintox-CL coupled to a 10 mm 1318b plate followed by a 10 mm air gap. 202

Figure 7.16: Target and Projectile numerical grid 205

Figure 7.17: Experimental and numerical simulation, SiC B FP. Test Nos., from top to bottom, 4156, 4157, 4158 and 4169. 207

Figure 7.18: Experimental and numerical comparison. BS41 impacting 18 mm SiC B and 10 mm aluminium alloy back plate. Top: 150 µs, Middle & Bottom: 200 µs. 208

List of Graphs

Graph 2-1: Hardness versus fracture toughness. As grain size is decreased, both toughness and hardness are increased. 62

Graph 3-1: Displays the effect of NRN151H propellant charge weight (g) in a 20 mm cartridge case on the velocity of the BS41 fired from a 14.5 mm proof barrel 75

Graph 4-1: Instron 4206 tensile test, loading and unloading curve showing elastic recoverable strain and plastic deformation; 1318b aluminium alloy, short transverse direction of roll, 2 mm/min cross head speed, temperature 25 ^{0}C.....98

Graph 4-2: Instron 4206 tensile test, loading and unloading curve showing elastic recoverable strain and plastic deformation; Mild steel, orientation 2, 2 mm/min cross head speed, temperature 25 ^{0}C. Results presented in *Table 4-1.* 99

Graph 4-3: Areal density of 1318b penetrated in the three different roll orientations103

Graph 4-4: Ceramic areal density of three different thicknesses plotted against areal density of witness block penetrated. 105

Graph 4-5: Ceramic areal density of three different ceramics plotted against DoP, velocity of impact is kept constant 1016 m/s (± 10 m/s). Refer to *Table 4-2, pp. 100* for 1318b semi-infinite data (short transverse). 110

Graph 4-6: Comparing the areal density of mild steel penetrated versus the ceramic areal density of either Sintox-FA or Sintox-CL front plate. 111

Graph 4-7: Reduction in e_c of the ceramic armour system. Two different ceramic armour systems (SiC B and Sintox-CL) are plotted against impact velocity. 114

Graph 4-8; Sintox-CL ceramic target fragmentation retrieved after impact from the BS41.....115

Graph 4-9; SiC B ceramic target (18 mm) fragmentation retrieved after impact from the BS41.....115

Graph 4-10: The effect of different 1318b thicknesses coupled to two different ceramic (SiC B and Sintox-CL) front plates with a 10 mm air gap on e_c. Velocity of impact is kept constant, 1016 ± 10 m/s 120

Graph 6-1: Graph displaying WC-Co projectile tensile failure strain against, penetration of a B_4C ceramic front plate and an aluminium back plate. 157

Graph 6-2: Particle – shock, Hugoniot curve, and the derivation of the shock EOS from the shock velocity data, Grady, *Table 6-4* in the plastic regime. 168

Graph 6-3: Polynomial EOS, data from Grady, *Table 6-4* 171

Graph 6-4: Von Mises Stress versus Pressure (GPa).....174

List of Tables

Table 2-1: Examples of Current Ceramic Armour Types and Manufacturer Processing Routes 31

Table 2-2: A comparison of material properties used for calculating stress wave propagation 48

Table 2-3: Comparison of material properties of various ceramics and metals 60

Table 3-1: Material properties of the ceramics used in the investigation 77

Table 4-1: Instron 4206 tensile test data. (*Note*, spurious results in Italics were removed from the average. These could have been due to sample mixing) 97

Table 4-2: BS41 and B32 penetration results against mild steel and BS41 penetration results against 1318b witness blocks 100

Table 4-3: Results of BS41 fired into the three different planes of the 1318b aluminium alloy; 1 = Longitudinal (roll), 2 = short transverse and 3 = long transverse. (WB = witness block) 102

Table 4-4: Penetration results obtained by altering witness block and Sintox-CL front plate areal density 104

Table 4-5: Critical Thicknesses of Ceramic (*Graph 4-4*) 105

Table 4-6: DoP results for different ceramic front-plates and either 1318b or mild steel witness blocks 109

Table 4-7: Critical Thicknesses of Ceramic (*Graph 4-5*) 110

Table 4-8: DoP results for two ceramic front plates Sintox-CL and SiC B with 1318b witness block for impacts in the region of 750 to 1100 m/s. 113

Table 4-9: DoP results from firing the BS41 into different appliqué systems.....120

Table 6-1: Continuum Mechanics Equations [Eq. 6-1 – 6-3] 153

Table 6-2: Inputs to the AUTODYN model. WC-Co Constants from Grady 155

Table 6-3: Description of different Tungsten Carbide – Cobalt Materials Tested (Adapted from Tardec and Grady Report [20,27,148]. 160

Table 6-4: Test Data from Tardec report, original data from LASL Shock Hugoniot Data 163

Table 6-5: Linear EOS numerical data input for AUTODYN 2D. 166

Table 6-6: Shock and Thermodynamic Properties of Selected Materials.....170

Table 6-7: Shock Equation of State Constants for the WC-Co material model 170

Table 6-8: Polynomial Equation of State Constants for the WC-Co material model.172

Table 6-9: Data extracted from Grady 173

Table 6-10: WC-Co Constants from the Material Model 178

Table 7-1: WC-Co sphere impact experimental and numerical results 185

Table 7-2: Empirical and numerical baseline DoP and cratering 199

Table 7-3: Flash X-ray trial details used for numerical analysis 206

LIST OF ABBREVIATIONS AND SYMBOLS

A_m	-	Surface area material face
a_o	-	Inter-atomic spacing
A	-	Crack size
AFV	-	Armoured Fighting Vehicle
Al_2O_3	-	Alumina
AP	-	Armour Piercing
a_p	-	Projectile radius
AP-I	-	Armour Piercing Incendiary
APC	-	Armoured Personnel Carrier
APFSDS	-	Armour Piercing Fin Stabilised Discarding Sabot
ALE	-	Arbitrary Lagrange Euler
B_4C	-	Boron carbide
C	-	Carbon
C_R	-	Specific heat at constant volume
c_0	-	Bulk velocity
c_{oA}	-	Longitudinal wave velocity material A
c_{oB}	-	Longitudinal wave velocity material B
Co	-	Cobalt
d	-	Average distance between two points on a diamond
d_g	-	Average grain size
DoP	-	Depth of Penetration
dstl	-	Defence Science & Technology Laboratories
DU	-	Depleted Uranium
EDX	-	Energy Dispersive X-radiography
e	-	Specific entropy
E	-	The modulus of elasticity or Young's Modulus
ε_c	-	Breaking strain of the witness plate
e_c	-	Differential efficiency
e_H	-	Hugoniot pressure
E_m	-	Mass efficiency
EOS	-	Equation of State
F	-	Load
Fe	-	Iron
FRES	-	Future Rapid Effects System
G	-	Shear modulus
G_f	-	Fracture energy required to generate a unit area of crack
GFRP	-	Glass Fibre Reinforced Polymer
h_1	-	Front plate thickness
h_2	-	Back plate thickness
HEL	-	Hugoniot Elastic Limit
HEMP	-	Hydrodynamic Elastic Magneto and Plastic Computer Program
HHS	-	High Hardness Steel
HMG	-	Heavy Machine Gun
HPLC	-	High Performance Liquid Chromatography
Hv	-	Vickers hardness
LiF	-	Lithium Fluoride
K	-	Bulk modulus
K_c	-	Fracture toughness

KE	-	Kinetic Energy
KED	-	Kinetic Energy Density
LAV	-	Light Armoured Vehicle
L_{int}	-	Intercept length
LRP	-	Long Rod Penetrator
Mag	-	Magnification factor
MBT	-	Main Battle Tank
MoA	-	Minute of Angle
M_p	-	Projectile mass
MV	-	Muzzle Velocity
NBC	-	Nuclear Biological Chemical
Ni	-	Nickel
NRN	-	Nobels Rifle Neonite
P	-	Pressure
P_b	-	Lead
P_H	-	Hugoniot energy
PMMA	-	Poly (Methyl Methacrylate)
P_r	-	Residual penetration
P_{ref}	-	Penetration into a reference material
PUNDIT	-	Portable Ultrasonic Non-destructive Digital Indicating Tester
RHA	-	Rolled Homogeneous Armour
S	-	Constant for the Shock EOS
S_1	-	UTS of back plate
SA	-	Small Arms
SEM	-	Scanning Electron Microscopy
SiC	-	Silicon carbide
SPH	-	Smooth Particle Hydrodynamics
t_c	-	Tile thickness
TEM	-	Transmission Electron Microscopy
TiB_2	-	Titanium diboride
u	-	Penetration velocity
UK	-	United Kingdom
U_S	-	Shock velocity
u_p	-	Particle velocity
US	-	United States
UTS	-	Ultimate Tensile Strength
VISAR	-	Velocity Interferometer System for Any Reflector
$V_{L,T}$	-	Longitudinal and Shear wave velocity
V_p	-	Projectile velocity
v	-	Poisson's ratio
W	-	Tungsten
WC	-	Tungsten carbide
WC-Co	-	Tungsten carbide – cobalt
x	-	Penetration depth into reference material
Z_S	-	Sample elastic impedance
Z_W	-	Window elastic impedance
α	-	Coefficient of expansion
γ	-	Fracture surface energy
Δu_{pb}	-	Magnitude of the spall-back signal
σ	-	Stress

σ_x, σ_y & σ_z	-	Stress in the x,y and z planes respectively.
σ_f	-	Stress for fracture
σ_{SP}	-	Spall strength
ε	-	Strain
ε_n	-	Nominal strain
μ	-	Compression
ρ	-	Density
ρ_A	-	Density of material A
ρ_B	-	Density of material B
ρ_1	-	Density of the front plate
ρ_2	-	Density of the back plate
ρ_o	-	Initial density
ρ_{ref}	-	Density of reference material
ρ_c	-	Density of ceramic material
τ	-	Shear stress
Γ	-	Gruneisen Gamma

… Blank Page …

Chapter 1

The Failure of a Tungsten Carbide – Cobalt Cored Projectile Penetrating a Hard Target

Introduction

As soon as an armour system is put into service, movement in projectile technology will inevitably match its technology. The essential quest of the armour designer is, and always has been, to defeat the enemy's attacking abilities.

Chapter 1 introduces the origins and the current use of ceramic armour within the context of Tungsten Carbide – Cobalt (WC-Co) cored projectile defeat. The Russian BS41 14.5 mm Armour Piercing Incendiary (AP-I) projectile is introduced and the aims and objectives of this investigation are detailed. A preface to subsequent chapters is presented.

1.1 Ceramic Armour: A Novel Concept

By the late 1960s, the field of ceramic armour had emerged as a separate study discipline in itself. During the Vietnam War the United States (US) military were put into a situation and terrain that were well suited to helicopter operations; thus was the coming of age of the helicopter gunship. Many criticised the vulnerability of the helicopter on the battlefield. As a result the 60s saw the appearance of innovative ceramic armour systems to protect the helicopter and its crew [1,2]. Previously, almost all armours were exclusively of one type of metal or another. One of the major drawbacks was the weight penalty to be paid for improvements in performance to match the enemy's threat. The successfully designed boron carbide (B_4C) ceramic-based aircrew vests and later, in 1967, the development of the integrally-armoured ceramic helicopter seat as found in the Puma and Panther helicopters, offered adequate protection at an efficient minimum weight [1,3].

Ceramics became recognised for their outstanding properties of low density, efficient resistance to penetration, high hardness and yield stress under compressive loading, which makes them prime candidates for use in modern armour systems [3,4]. With their efficient achievement of projectile defeat, attention focused increasingly on the advancement of ceramic armour to defeat more challenging and complex problems of modern threats to land based vehicles [1,3].

Today the threat to Armoured Fighting Vehicles (AFV) is always increasing with the proliferation of shaped charge warheads, Armour Piercing Fin Stabilised Discarding Sabot (APFSDS) ammunition, Heavy Machine Gun (HMG) projectiles and Small Arms (SA) fire [5,6]. As these weapon systems become more prolific and possess more penetrability there is a need for the armour designer to keep pace with

developments to defeat these types of threats. One of these threats, the WC-Co cored ammunition that has been used by the former Soviet States, has become a problem in recent years; Gulf War I, Gulf War II and recently in Afghanistan [6,7,8]. The HMG variety (BS41) uses a WC-Co core that has the ability to penetrate over 584 kg/m^2 of mild steel and over 297 kg/m^2 of armour aluminium alloy [9]. The BS41 therefore poses a significant risk to thin-skinned vehicles or lightweight AFV such as the BRDM-2 Armoured Reconnaissance Vehicle, the BTR-94 Armoured Personnel Carrier (APC) and parts of the Warrior (*Figure 1.1*) [10,11].

Figure 1.1: Warrior Armoured Fighting Vehicle [12].

Light tanks and armoured cars play a vital role in providing the Main Battle Tanks (MBT) with detailed information on the strength, position and future direction of enemy forces during combat manoeuvre. The Warrior (*Figure 1.1*) is a Nuclear Biological Chemical (NBC) proof Light Armoured Vehicle (LAV), armed with a 30

mm Rarden cannon and coaxial 7.62 x 51 mm Hughes Chain Gun. The Warrior took part in Operation Desert Storm in early 1991. Since then it has been deployed in a number of operations across the world. The 14.5 mm BS41 acts as a threat against the Warrior and other LAV's armour [10,12]. An understanding of the WC-Co cored ammunition threat provides important information for meeting current, legacy and future protective requirements such as for the Future Rapid Effects System (FRES) project. These future projects are to enhance the deployability of United Kingdom (UK) Land Forces by delivering a family of medium weight, network capable armoured vehicles [13]. Therefore, highlighting the importance of the requirement for a highly mass effective armour system, for modern AFV design.

1.2 Impact Phenomena: Assessment Aims and Objectives

The UK Defence Science Technology Laboratories (dstl) initiated this program of research to give an expanded knowledge of WC-Co projectile core failure. Throughout the period, attention has concentrated on the development of ceramic technology to up-armour land vehicles to meet current threats. Some research efforts in this area have achieved more popularity than others. However, none of these efforts strive to exploit the failure of such WC-Co cored Armour Piercing (AP) projectiles. With little knowledge on the impact phenomena of the 14.5 mm BS41 WC-Co core projectile, and with the interest in industry as it poses a threat to LAVs, this thesis will concentrate on the failure of the Russian BS41 14.5 mm AP-I.

The primary aim of the work is to explore the implementation of different layered armour designs to defeat the BS41 projectile. No single mechanism dominates the dynamic failure of the armour system or the projectile during penetration. This investigation sets out to determine the factors that influence damage phenomena in WC-Co AP penetrators. This is to be achieved by applying well-characterised published measurement techniques to analyse the ballistic efficiency of different ceramic target systems. Methods such as the residual Depth of Penetration (DoP) test [14,15,16,17,18], Plate Impact [19,20], Flash Radiography [21,22,23] and High Speed Camera [24,25] have been referred to. Experimental results are later compared with a

numerical WC-Co material model developed in AUTODYN 2D to predict the behaviour of WC-Co fragmentation during impact.

An indication of performance is a necessary component of the development and comparison of any armour system. It provides a conceptual and practical tool to enable the judgement of the impact of changes made to a system. In many cases it will also suggest a design solution for a particular problem. It is instructive to look at the range of ceramics and projectiles that are currently available commercially. Sadly, although such interrogation would prove invaluable, it would be inherently complex, time consuming and expensive and beyond the scope of this thesis.

Therefore, the main effort will be the study of the Russian BS41 WC-Co cored projectile with respect to impact into a limited number of commercially available ceramics and target system designs.

1.3 Preface to Chapters

Subsequent chapters provide a detailed account of the research carried out and a summary of objectives of foreseeable future analysis.

Chapter 2 provides an overview of target and projectile, ceramic and WC-Co material properties. It covers an introduction to the stress effects in solids caused by dynamic loading of projectiles on layered armour. It is not the aim to be exhaustive, as this is a very complex problem. A rich literature exists on these subjects and will be cited as needed.

Chapter 3 describes the experimental methodology and compares a number of different experimental techniques and performance criteria commonly applied to ballistic testing [14-25]. A detailed account of the experimental techniques employed in *Chapter 4* and *Chapter 5* is presented.

The factors that influence damage phenomena in WC-Co core AP projectiles are not fully understood. Moreover, the design of armour is determined by both the type of

threat and the required material properties to offer resistance. Therefore, *Chapter 4* reports a summary of experimental analysis on failure of the BS41 WC-Co core sought by performing impact experiments. The target and projectile failure mechanisms affected by the constraints introduced by the armour confinement and system layers are detailed. The Scanning Electron Microscope (SEM) and Energy Dispersive X-Radiography (EDX) provide a detailed account of the morphology and chemical composition, respectively, of the fracture surfaces of failed ceramic armour. *Chapter 5* reports the summary of the WC-Co fracture morphology and chemical composition examined.

Practical experimentation was supported by AUTODYN 2D computational modelling which aimed to simulate the fracture of WC-Co observed during impact and provides a further insight into WC-Co failure. Previous numerical work has not been capable of predicting the complex fragmentation behaviour [20]. A novel WC-Co numerical model derived from experimental data was developed to provide a preliminary tool to study WC-Co failure [14,20,26,27]. This numerical approach is detailed in *Chapter 6*.

This understanding of penetration mechanisms was used to guide a parametric investigation, validating the WC-Co material failure model with experimental results. The computational model is tested against WC-Co sphere impact experimental results performed by Grady [20]. To supplement the work, an initial series of numerical simulations has been constructed and compared to experimental data from the impact behaviour of the BS41. A discussion of the parametric investigation is presented in *Chapter 7*. The work presented contributes to the further understanding of the material properties of the Russian WC-Co and demonstrated the ability to model the fragmentation behaviour of WC-Co.

The complex behaviour of WC-Co impact phenomena is shown. Large variations in the nature of the resultant fragmentation of the BS41 WC-Co core, depending upon the ceramic test target used, was exhibited. It is demonstrated *via* a computational material model in AUTODYN 2D that numerical data could significantly aid analysis of WC-Co failure in the future. With further analysis and input to the material libraries a meaningful preliminary assessment predicting WC-Co failure may be used for evaluation of target systems under a variety of circumstances. A conclusion based

on the results of the work is presented in *Chapter 8*. Possibilities for future development and recommendations are presented and examined.

Chapter 2

Ceramic Armour Literature Review

The approach in investigating the impact of the BS41 on different ceramic armour systems takes a number of paths. Understanding the interactions of WC-Co cored projectiles and targets will assist in obtaining an optimised solution to defeat the BS41. This will provide information, which may be used to develop a numerical WC-Co material model in the non-linear dynamic code AUTODYN 2D.

Firstly, the fundamental techniques employed by ceramic armour systems to defeat AP projectiles are explained and an overview of the effects upon the projectile is provided. The failure modes and internal stresses of the target and projectile interaction are described. Physical property data on selected materials that could be considered for the role of WC-Co projectile defeat are introduced.

Subsequently, the projectile, the 14.5 mm BS41 must be considered. A basic description of the BS41 projectile and WC-Co material properties are discussed and a short historical review is presented.

2.1 Firepower and Mobility

"Goliath had what must have been regarded as the most effective armour of the day, yet the penalty he paid in terms of lack of mobility and failure to bring his weapons to bear against David lead to his downfall…."[1]

The first true tanks were clad in Vickers armour steel up to 10 mm in thickness, the best compromise between firepower, protection and mobility of the day. However, this thickness of armour could not stop German AP rounds, and the thickness was eventually increased to 12 mm in the Mark IV tank [10]. As the weapon systems possessed more penetrability, there was a limit to how much a monolithic solution could be up-armoured at the expense of firepower and mobility.

The need for better materials to replace the armour for the vehicles was evident. The most significant armour advancements to date have involved the development of advanced ceramics. During the last three decades effort has been devoted to the study of utilising their exceptional material properties for use in modern armour systems. This has resulted in vast research into new emerging ceramic materials, fuelling the survivability requirements for future passive lightweight armoured systems. *Section 2.2* of this review will concentrate on the ceramic material properties for protection against SA Kinetic Energy (KE) threats. *Section 2.3* will review the development of ceramic multi-layered armour systems. This will focus on their mechanisms of defeat and dynamic stress wave propagation.

2.2 Ceramics for Armour Applications

2.2.1 Ceramic Microstructure

The word ceramic comes from the Greek "*keramos"* which means 'burnt stuff' [28]. Ceramics are non-metallic inorganic solids with inter-atomic bonds that usually have both ionic and covalent characteristics. Ceramics used in many applications today are polycrystalline and polyphase materials with grain sizes that typically vary from 0.1 to 10 μm. They contain a complex crystal structure. Ceramics used for armour

applications tend to be polycrystalline. The phase and orientation of the grains and the microstructure of the grain boundaries influence the properties of these materials [29].

Ceramics are sometimes split into two defined groups, traditional ceramics and new ceramics. Traditional ceramics include those primarily of the silicate industries and refractories [33]. The new ceramics include specialised electro-optic ceramics, magnetic ceramics, those for the nuclear industry and pure oxide ceramics. Research into certain ceramics has received considerable attention in the armour industry, and this will be the focus of this review. The main findings of work so far accomplished are given below. This is by no means an exhaustive review. The analysis of ceramics used in ballistic applications is a vast subject and the reader is referred to a number of reports for an overview of the subject [30,31,32,33,34].

2.2.2 Manufacturing Process, Cost and Availability

If the properties of ceramic materials are compared with those of metals, it is found generally that they lack ductility and they have lower tensile strength and thermal conductivity. On the other hand they can withstand considerably higher temperatures, resist corrosion, low density and have high hardness and yield stress under compressive loading. Due to their superiority in the last three properties, ceramics have been recognised for their use in armour design.

The key to an ultimate ceramic for armour applications has been brought about by advances in the manufacture processing. Numerous armour ceramics exist with different processing routes, but generally the ceramics can be put into two groups: the lower cost sintered (*e.g.,* Morgan Matroc's alumina (Al_2O_3)) and the higher cost hot pressed ceramics (*e.g.,* Cercom's B_4C). A full description of the different processing techniques may be found elsewhere [30,31,32,33,34, 35]. However, in brief, fabrication of ceramic materials follows a number of stages. The powder of the base ceramic is formed into the desired shape. This is then densified by a sintering step. Alumina for example, is cold pressed, followed by pressureless sintering. Pressureless sintering can have limitations on size and shape of the ceramic. For most applications Al_2O_3 is mixed with a sintering aid in order to allow more rapid and lower temperature

sintering. The sintering aid forms a soft, low melting point phase between the grain boundaries therefore affecting the mechanical properties of the ceramic. Alumina 85% contains approximately 15% sintering aid, whereas Al_2O_3 99.5% contains in the region of 0.5% sintering aid. By decreasing the sintering aid both the hardness and compressive strength can increase [36]. Some of the most widely available and cost effective raw ceramics are Al_2O_3 and silicon carbide (SiC).

Traditionally Al_2O_3 has been used in the design of appliqué systems that are used on modern AFVs [3,4,10,11,12]. However, the problem is that cost has been shown to be a major limiting factor in the design and use of armour at the expense of performance. The lower cost sintered materials, like the Morgan Matroc Al_2O_3 can be used when cost *is* a limiting factor, weight is *not* a limiting factor and the threat allows [18,37,38,39]. However, at higher-level threat levels the performance of Al_2O_3 is generally insufficient.

Whilst most of the attention was concentrated on the development of Al_2O_3, there had been a steady development into the use of other ceramics like B_4C, titanium diboride (TiB_2) and hot pressed SiC [3,4]. Several kinds of ceramics have been ranked against AP projectile threat. An overview of some of the ceramics used in armour applications today and the manufacturing processes are presented in *Table 2-1*.

Table 2-1: Examples of Current Ceramic Armour Types and Manufacturer Processing Routes

Ceramic Processing Type	Manufacturer / Type
Sintered	Morgan Matroc / Al_2O_3 [165] Ceradyne / Sintered SiC
Reaction Bonded	M-Cubed (Simula) / SiC [4] MC^2 (Australia) / SiC [4]
Metal Matrix Composite	Lanxide / Dimox-HT [4] Lanxide / Dimox AS109 [4]
Hot Pressed	Cercom / SiC B, Tungsten Carbide (WC), [164] Ceradyne / B_4C

Ceramics like B_4C and TiB_2 when compared to Al_2O_3, can be more efficient at defeating SA projectiles at much lower areal densities. However, they have proven more expensive due to the lack of available raw materials and expensive manufacturing routes. We must now consider some of the material properties important in the defeat of WC-Co cored projectiles.

2.2.3 Hardness

The properties required within ceramic armour depend on the type of threat to be countered. Both hardness and the strength of the ceramic are important material properties for the disruption of a projectile so that the armour can reduce the projectile's penetrative ability. Ceramics are good at both eroding and fragmenting the oncoming AP threat, spatially spreading the impact energy onto a backing layer. When a large elastic-plastic wave propagates into a projectile inducing fracture (*Section 2.3.3, pp. 44*), it is much easier to arrest than a projectile penetrating as a rigid body. Problems arise when the WC-Co cored ammunition's hardness is approximately the same or greater than that of most commercial Al_2O_3, thus offering little resistance to penetration [40].

An effective solution for defeating the WC-Co projectile would require the use of a hard ceramic front plate, like SiC, B_4C or TiB_2. It would also require some form of backing material to capture both the projectile core and the ceramic debris, like Rolled Homogeneous Armour (RHA) or aluminium alloy. Hardness for a ceramic can be as high as 2300 Hv, (Vickers Hardness) for SiC (described later in *Section 3.3.4*), whereas for RHA steel it can be as little as 270 Hv or for aluminium alloy, 130 Hv [125]. Therefore, high hardness ceramic materials make better projectile disrupters than metals. It has been found that as the hardness of the ceramic tile offered to a 7.62 mm WC-Co core projectile increased, it resulted in an increase in armour performance [125].

Ceramics with higher hardness have increased atomic bond strength and hence higher melting points. Ceramics containing carbides and nitrides require higher sintering temperatures to overcome the bond energies [29,30,32]. Even with suitable sintering

aids this can still be a time consuming and expensive process. Titanium diboride and SiC are such examples, both of which are expensive to process and not as easily available as Al_2O_3. The use of such materials as WC, B_4C and TiB_2 has been recognised as unjustifiably expensive, and not always cost effective [51,41,42,43]. The other major disadvantage is the manufacturing difficulties involved in shaping and forming such ceramics. Considering the different criteria, SiC appears to be the most interesting ceramic considering its ballistic efficiency and cost ratio [4,27,125].

2.2.4 Strength and Toughness

The strength and toughness of the ceramic are also very important material properties at ensuring a good level of resistance to ballistic penetration. For a ceramic, the theoretical strength, σ, that can be achieved can be defined by the following equation:

$$\sigma = \{E\gamma/a_o\}^{1/2} \qquad \text{[Eq. 2-1]}$$

where, E is defined as the modulus of elasticity or the Young's modulus, γ is the fracture surface energy, the energy required to create a fracture surface and a_o is the inter-atomic spacing. Broken down, the elastic modulus measures the resistance of the material to elastic deformation when a load is applied. Ceramics with strong covalent bonding have higher values of E whilst those with weaker ionic bonding have lower values of E.

A stress pulling at right angles to the face is defined as the tensile stress; a stress loading in the opposite direction is defined as compression. A stress acting at an angle to the face may be defined in terms of shear stress, τ. The material responds to stress by a resulting deformation in terms of strain, ε. The strain is calculated by dividing the material's measured extension by the original length [44,45]. The elastic moduli are defined through Hooke's law. Simply, through experimental observation, when strains are small, the nominal strain, ε_n is very nearly proportional to the stress that is they are linear-elastic:

$$\sigma = E\varepsilon_n \qquad \text{[Eq. 2-2]}$$

In the same way, the shear stress is proportional to the shear strain. However, the behaviour of a projectile and ceramic target interaction is different at high rates of loading than at relatively low loading rates. At high rates, the rate of deformation the projectile encounters is much greater than is observed when compared to conventional quasi-static material tests. For materials subjected to relatively high strain rates, the yield strength can change, and for most materials increase markedly. The reason for the increased yield strength is due to complex microstructural behaviour that is dependent on the nature of the material (*e.g.,* in metals dislocation movement).

Ceramics have relatively high dynamic compressive strengths when compared to other materials like steel and aluminium. Ceramics at low rates of compressive loading appear to be strain-rate insensitive. However, at high rates of compressive loading, some ceramics have appeared to exhibit rapid strain rate strengthening. During plate impact experiments a uniaxial strain shock is formed that can deform the material at a very high rate. Under these impact-loading conditions it is possible to measure, from the shock profile, the point at which the ceramic material ceases to behave elastically, and begins to behave in-elastically. This point, at the peak stress for the elastic regime, is referred to as the Hugoniot Elastic Limit (HEL). The HELs for ceramics are relatively high when compared to metals, for example SiC B can be as high as 12 GPa whereas metals exhibit a HEL in the range of 0.5 – 2.0 GPa [46].

Unlike metals the compressive strength of brittle materials has been shown to change under the influence of high pressure, affecting their ballistic efficiency. There has been some evidence that suggests that ceramic materials "pressure-harden" under shock loading retaining high shear strengths at very large confining pressures. Although, Al_2O_3 has been reported to have a "catastrophic" loss of shear strength when shocked above the HEL [47]. This is in agreement with data presented by Rosenberg *et al.* [47]. The strength of intact material is a very important property that must be considered for the armour system. However it is also the combination of intact material and the strength of the fractured material and the time it takes from moving from one state to another that affects the resistance to penetration.

2.2.5 Fracture Toughness

The factors limiting the strength of ceramics, as for all materials, are fracture and plastic deformation. A limitation of using a ceramic as part of an armour system is its brittle nature, requiring only a small fraction of the impact energy to fracture [48]. This compromises its multi-hit capabilities [49].

Because ceramics are brittle the typical failure mechanism is fracture rather than plastic deformation. Fracture in brittle materials occurs at usually unpredictable levels of stress, by the sudden propagation of a crack initiated at grain boundaries, pores or micro-cracks. The first explanation offered for the discrepancy between the theoretical strength and the low observed strength in ceramic materials was provided by Griffith [188]. He developed the theory that the low observed strength was due to the presence of many fine elliptical cracks. These can form during the multiple stages of the manufacturing processes of ceramics. At the tip of each of these fine cracks there is a strong concentration of stress. A profusion of empirically-based fracture theories have evolved over the decades relating to crack growth in brittle solids and Griffith's theory. These are complex and are based on the laws of mechanics and thermodynamics. Literature can be found elsewhere detailing the fracture and crack theories and phenomena [188,187,189].

The equation that defines the fracture strength of the material in terms of the crack size (A) and fracture toughness or critical stress intensity factor, (K_c) of the material is:

$$K_c = \sigma_f \sqrt{\pi A} \qquad \text{[Eq. 2-3]}$$

where, σ_f is the stress applied for fracture [29,44]. The simplest inherent flaw found in ceramics is the pore. It must be noted that the fracture strength is dependent on the largest flaw defect size. For flaws of a given shape, it is the largest flaw that produces the greatest stress concentration.

During the penetration process the ceramic fractures ahead of the projectile. This is called comminution. For a ceramic the fracture toughness can be found to be as low as 3 MPa $m^{3/2}$ (SiC), however for metals the fracture toughness value ranges from

aluminium alloys around 23 MPa $m^{3/2}$ to high strength steels at 154 MPa $m^{3/2}$ [29,44]. This makes metals desirable materials for the compliant backing in an armour system, absorbing the KE of the projectile and capturing the ceramic and penetrator debris. However, despite their poor tensile properties, ceramics have favourably low areal densities compared to metals making them more attractive for armour applications.

2.2.6 Ceramic Porosity

Temperature and porosity affect the elastic modulus of a ceramic. As the temperature of a ceramic is increased, the interatomic spacing increases due to thermal expansion, thus a reduction in the *E* is observed. Furthermore, *E* decreases with increased porosity, but the rate of decrease becomes less as the volume fraction of pores increases [34,50]. The porosity or void content, which is nearly always present as a result of the incomplete densification of the material during the firing process, is an important factor with ceramics. It is advantageous for the mechanical properties of the ceramic to remove as much of the residual porosity as possible by improved manufacture processing. The use of more uniform finer powders or alternative routes with more complex sintering operations involving hot pressing or reaction bonding are examples.

Ceramics generally do not come close to their theoretical strength [*Equation 2-1, pp. 33*] as the voids and inhomogeneities provide sources for crack propagation. During the sintering process a powder compact is heated at a temperature below its melting point, powder particles fuse together, voids between the particles decrease and eventually a dense solid can be obtained. Improved manufacturing processes have made it possible today to sinter polycrystalline bodies which have almost no porosity [34]. However, the improved performance that is offered by the high density ceramic might not always offset the accompanying increase in areal density of the armour system as a whole.

The most successful routes at reducing porosity have utilised hot pressing, involving an inert atmosphere around a heated die. By hot pressing, the shape forming and sintering are done simultaneously resulting in the parts containing less sintering aid

with a lower porosity [3,31,32]. Hot pressing is excellent for gaining a homogeneous material, maintaining complete control over the ceramic material grain size, shape and size distribution. Hot pressing can be used to make SiC, B_4C and TiB_2.

There are a number of additional results from ceramic armour research, which aid understanding of the remainder of this work. We now consider the armour system layer design.

2.3 The development of Ceramic Armour Layer Design

The impact behaviour of different layered ceramic armour systems is well publicised [125,127,128,130, 51 , 52 , 53 , 54 , 55 , 56]. The Tardec report provides the most comprehensive presentation summarising some of the most significant results to date [27].

To trace the history of ceramic armour, we begin in 1918 with the discovery of one of the most important ceramic armour developments; the first observations of the principle of composite armour, consisting of two layers, a hard, enamel facing (typically a layer consisting of a ceramic material), on a metal ductile backing (possibly aluminium or steel) [57 , 58 , 59 , 60]. The result was armour with a significantly enhanced ballistic protection compared to that of the monolithic armour. The performance of the ceramic armour system was found to be heavily dependent upon its configuration.

A significant contribution to the understanding of ballistic failure came from the success of Florence (*Section 2.3.1*) and Wilkins (*Section 2.3.2*) in the early 1960s, developing theories on the penetration of such composite armours [61,62,63,64,65,66]. With the development of ceramic armour for the attack helicopter during the Vietnam War and the pronounced interest in the development of ceramic armour, they realised the importance of a multi-layer system for defeat of the projectile. The ceramic appliqué system provided an efficient solution to defeat the oncoming threat with increased weight efficiency, both of critical importance when assessing its viability.

2.3.1 Theoretical Advance in Ceramic Armour Layer Design

Florence established a theoretical model that predicted trends in behaviour of two-component composite armour impacted by a rigid projectile at sub-hydrodynamic velocities [61,62]. Expressions were developed for the optimum thickness ratio of the ceramic front plate and the backing plate. The KE of the round was equated to the energy absorbed in the backing plate after impact and the work done in stretching the plate for "just" defeating the projectile (*Figure 2.1*). This leads to the prediction of the ballistic limit velocity, V_{50}, the velocity that gives a 50% probability of penetration, given in the Florence equation.

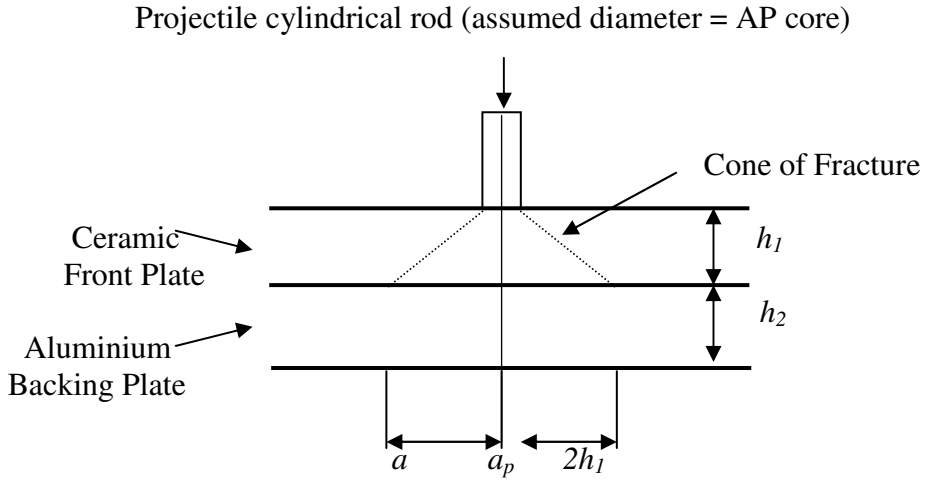

Figure 2.1: Florence Analytical Model adapted from [62]

In its most basic form the Florence theoretical equation predicts the ballistic limit velocity of the armour with respect to armour layer and projectile details (*Equation 2-4*). It assumes that the backing plate will fail via the maximum strain failure criterion, *i.e.,* when the radial strain equals the critical breaking strain of the backing material, thus:

$$V_p = \sqrt{\frac{\varepsilon_c S_1}{0.91 f(a) M_p}} \qquad \text{[Eq. 2-4]}$$

where, V_p is the projectile velocity, M_p represents the projectile mass and ε_c is the breaking strain of the backing plate, S_1 is the Ultimate Tensile Strength (UTS) multiplied by h_2 and $f(a)$ may be calculated by the relationship:

$$f(a) = M_p / \left(M_p + (h_1\rho_1 + h_2\rho_2)\pi a^2\right)\pi a^2 \qquad \text{[Eq. 2-5]}$$

where, a may be calculated by $a_p + 2h_1$ (conoid base radius), a_p is the projectile radius, ρ_1 and ρ_2 are the densities of the front and backing plate respectively and h_1 and h_2 are the front and back plate thicknesses respectively.

The formula suggests that the ballistic limit velocity will be increased if the backing material is ductile and has a high tensile strength. It only provides an approximate and rapid prediction of ceramic composite armour performance to the armour designer. Several assumptions were made by Florence to keep the problem analytically tractable with regard to *Figure 2.1*. The diameter of the circular area of the backing over which the momentum is distributed is taken as the base diameter of the fracture conoid in the ceramic facing plate. The fracture conoid radius is assumed equal to the projectile radius, a_ρ, plus double the ceramic thickness, h_1, ($a_\rho + 2h_1$). This is an empirical observation and results in a cone angle of 63^o (126^o included angle).

The most often quoted paper that describes the theoretical theory is that of Florence published in 1967 [61]. Others, most notably Hetherington [60,64,67] and Prior [68] performed calculations using the Florence theoretical model and compared it to experimental data. Both found that the results correlated well with their experimental data, though Hetherington concluded that a model based on the concept of cratering offers a more realistic description of the event [60,64]. Hetherington *et al.* investigated two component armour systems to defeat 7.62 mm AP rounds. The optimal ratio of h_1/h_2 resulting in the maximum value of V_{50} for the 7.62 mm AP round was 2.4. However, the Florence model has been shown to underestimate the ballistic limit velocity, V_{50} and the fracture conoid base radius assumed by Florence seems to be only held in cases where the target is either un-backed or has a high thickness ratio [42]. This was slightly under the theoretical value obtained by Hetherington, compared to Lowery's results [53].

Extensive investigations into the ceramic / metal armour system ratio have shown that the h_1/h_2 ratio is strongly dependent on the velocity and the obliquity at impact [69]. Impacts into high obliquity ceramic tile arrays have shown that penetrator yaw is increased. Iremonger carried out experiments with the 5.56 mm projectile, altering the

obliquity of impact [70]. On comparison with AUTODYN the results were encouraging. The discrepancies could have been due to lack of precision in measurements and the variables within the projectile, and inhomogeneities of the targets. Comparisons can be made with numerical simulations, altering both obliquity and target configuration, requiring three-dimensional analysis. Analysis of the target hole profiles could also be made as part of the analysis.

Alteration of the obliquity and velocity of impact will cause the projectile to penetrate or ricochet. When the angle of obliquity is below 15^0 the mechanism of penetration is similar to that of normal impact. When the angle is over 60^0 the projectile begins to ricochet. Yaw occurs especially when a hard projectile impacts a ductile material. The target then experiences high shear forces and petals slightly. Resistive forces can then cause the projectile to turn back to normal impact. During the oblique impact, bending stresses within the projectile may cause premature failure by flexure. The improvement in armour performance at high obliquity angles is well acknowledged and many practical investigations have been performed. The author refers the reader to a number of studies [71,72,73,74].

Hetherington and Lemieux also attempted to look at the effects of obliquity assuming that the alteration in armour angle would deform the projectile tip into an ellipse giving a quasi-elliptical fracture conoid base. Their model extended that of Florence, finding a very good correlation between results when the cone angle was reduced from 63.5^o to 30^o (*Figure 2.2*).

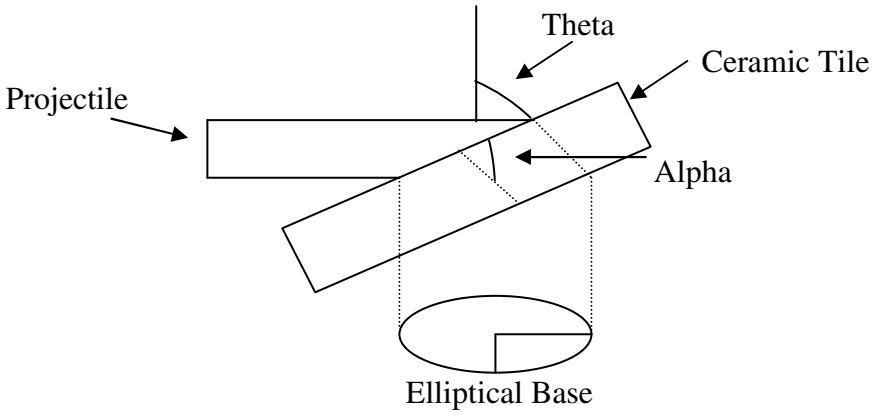

Figure 2.2: The Hetherington and Lemieux Obliquity model

The synergistic effects of combining a hard brittle ceramic front target with the properties of a ductile metallic witness plate are well known [52,53,54,55,56,58,59,60,75]. This section has introduced a brief theoretical overview of the concept of the ceramic / composite configuration by Florence. The next stage is to quantify the threat in mechanical terms as a terminal ballistic problem. The choice of the materials for a ceramic armour system depends not only on the intrinsic behaviour of each material, but also on the considered application and threat. These will now be discussed.

2.3.2 Ceramic Bilayer Defeat Mechanisms

The design of a ceramic target system is based on its ability to fracture the penetrator and the ability of the compliant backing layer to capture the ceramic and penetrator debris [4,76,77].

Wilkins *et al.* provided the first armour research program analysing the penetration failure mechanisms and physical processes that occur during the impact of SA into ceramic faced armour. By using high-speed cameras, flash x-radiography and numerical simulation, Wilkins and his colleagues identified the important physical processes during penetration and the important material parameters that operate during the impact [65,66].

During the initial stages of penetration, the projectile shattering duration is the most critical phase if the ceramic armour is to be efficient. During sub-hydrodynamic impact of projectiles the fracture mechanism occurs early in the process [76]. The high amplitude stress wave generated as a result of the relatively large acoustic impedance of the ceramic front plate and its much higher elastic compressive limit compared to hard steel, can lead to spallation of the projectile core. This shall be discussed in more detail in *Section 2.3.3*. During this period energy conversion of the KE of the projectile into deformation and delamination of the compliant backing occurs [76,77]. As we move into the hydrodynamic regime [76], as applied to Long Rod Penetrators (LRP), the process becomes more complex and for a longer duration [78,79].

Previous work describing the hydrodynamic behaviour of impact interprets some of the complex processes where the hydrodynamic behaviour dominates the behaviour of the colliding solids [14,80,81,82,83,84,85,86,87,88]. While the penetrator and target interaction processes follow similar routes, hydrodynamic threats require different emphasis on the armour design. The velocity of the BS41 lies in the sub-hydrodynamic regime, where traditionally the mechanical properties of the target and penetrator dominate. Hardness, strength, toughness are all-important in both the threat and the target properties. Thus, the focus of this investigation was on the strength effects of material impact during sub-hydrodynamic impact.

The Florence theory was based on how the projectile impacts in the sub-hydrodynamic regime into the hard-faced ceramic, forming a cone of fracture material. Traditionally, it has been proposed that materials have six characteristic failure modes. These are brittle fracture, ductile hole-growth (ductile penetration), radial fracture, plugging (reduced energy absorbed by the target), shearing mechanism (little deformation and no lateral compression), fragmentation and petaling (*Figure 2.3*) [76].

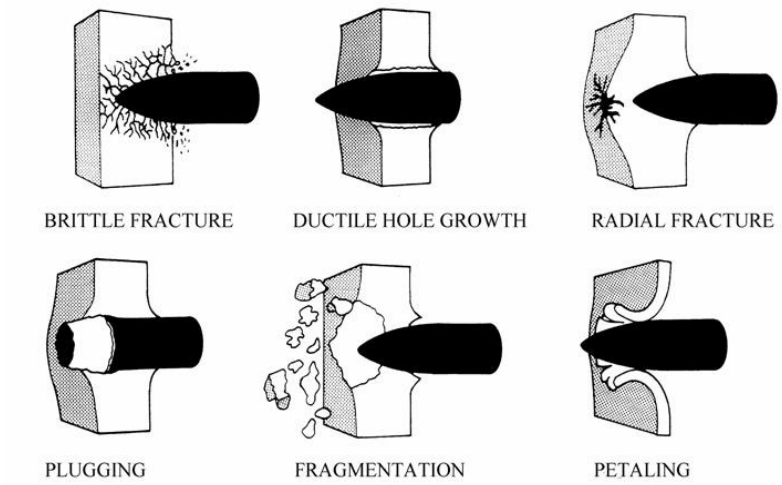

Figure 2.3: Characteristic armour failure modes (adapted from Zukas) [76]

During the penetration process one of the most important failure mechanisms in the ceramic is comminution due to its low fracture toughness (*Section 2.2.5*). The fracture cone initiates at the interface between the projectile and the target. The geometry of the cone will depend on the contact area between the projectile and target and the thickness of the ceramic tile. During the impact a localised compressive state of stress

exists at the projectile tip, whilst around the periphery of the contact area the material is placed under tension, forming ring cracks, referred to as Hertzian cracks. This gives rise to the formation of conical fractures due to a complex state of stress in the ceramic. The fracture cone as described by Florence [61,62] spreads the load of the projectile onto a relatively wide backing layer. The most common materials utilised for this support are aluminium alloys or steel, such as RHA. This enables the KE of impact to be dissipated by the plastic deformation of a ductile backing material.

The final stage involves transfer of momentum mechanisms as the ceramic and backing combine to reduce the penetrator velocity and catch the material. During this process, cracks propagate in the ceramic leading to the further formation of smaller fragments. Griffith (*Section 2.2.5, pp. 35*) developed the theory that the ceramic's low fracture toughness was due to the presence of many small cracks concentrating stress at their tips. *Figure 2.4* displays a pore with propagating cracks either side found on the spall surface of a sample taken from WC-Co under the SEM.

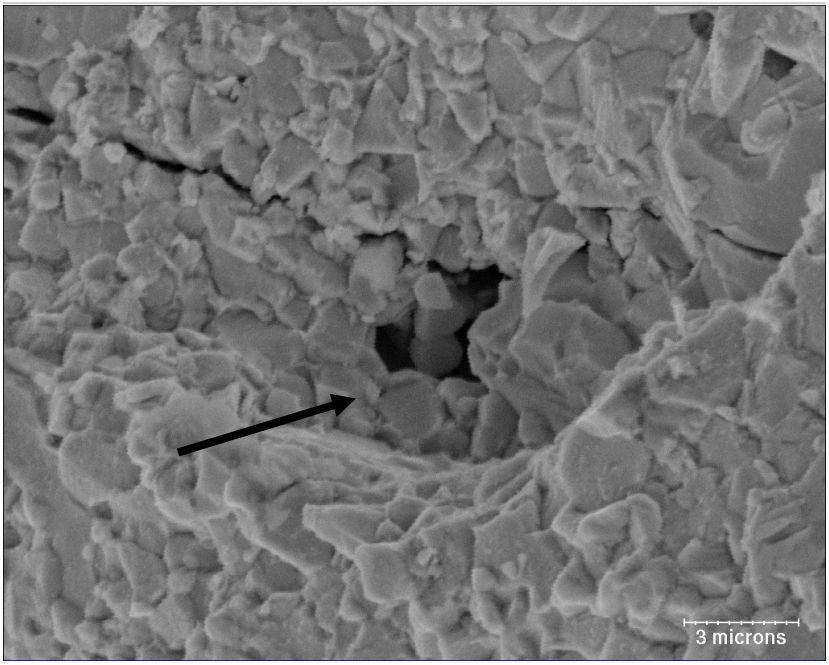

Figure 2.4: A Scanning Electron Micrograph taken from a sample of WC-Co (14.5 mm BS41) showing the presence of a pore at the spall surface with cracks propagating either side.

As the penetrator continues to penetrate the ceramic target system, if the KE is sufficiently high, the ductile backing will begin to fail due to the propagation of small cracks emanating from the rear surface of the plate due to bending.

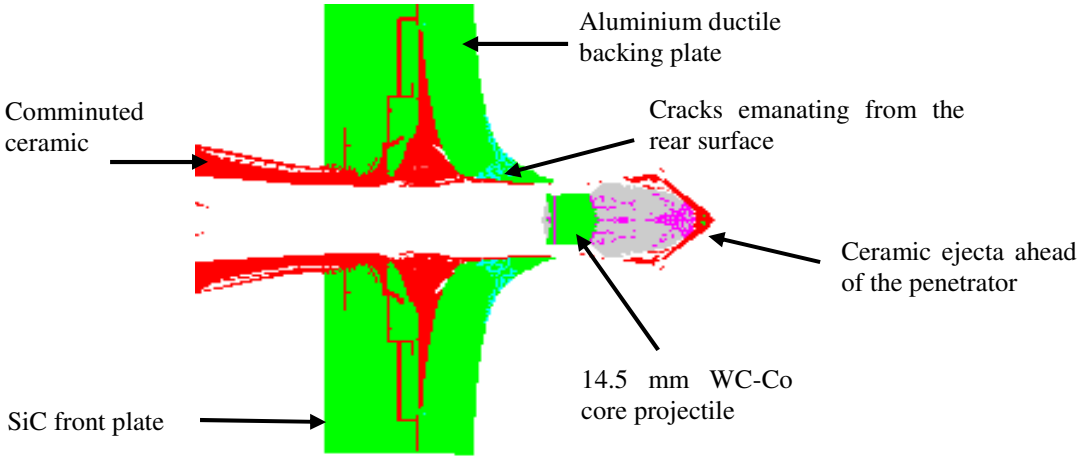

Figure 2.5: A graphical representation of a numerical simulation of a 14.5 mm BS41 projectile after impacting and penetrating a SiC front face and an aluminium alloy ductile witness plate

The projectile perforates the target pushing the cone of ceramic in front of it (*Figure 2.5*). Cracks formed are clearly visible emanating from the rear of the aluminium ductile backing.

The AP core (*e.g.,* WC-Co) continues to penetrate and undergoes mass erosion. Flexing of the ceramic may occur, causing cracks that spread radially from the impact point. The back layer not only ensures a structural role but also absorbs the energy of impact through plastic deformation.

2.3.3 Dynamic Stress Wave Propagation

Response of solid materials to impact loading is a complex process. Solids react to loading in three different ways. In low intensity stress conditions both the target and projectile geometry and material properties are important. When conditions result in stresses below the yield point, the solids may behave elastically. As the intensity of the load is increased heating occurs, large permanent deformations are formed and the material is driven into the plastic regime. With further increases in loading intensity the pressures generated can exceed the strength of the colliding solids, which then behave hydrodynamically [76]. Localised effects occur and the constitution of the

material in the vicinity of load application rather than the total geometry is important. The elastic, inelastic (plastic) and shock wave propagation all play a key role.

When a projectile impacts a target, part of the energy of the impact is transmitted to particles close to the site of the impact as Kinetic Energy. Within the material a force is applied resulting in particles transferring through a succession of impacts all, or part of their momentum to adjacent atoms. The rate at which this occurs is dependent upon the materials particles spacing and the interatomic forces, atomic attraction and repulsion that exist between them. The movement of the particles results in a compressive wave front. As the compressive wave reaches a rigid boundary, the stress wave is reflected back along its path as a compressive wave. If there is no rigid boundary the particle momentum continues until it is decelerated by tension. As the material is under tension, this wave is known as a tensile wave front, therefore as the compressive wave encounters a free surface, it is reflected back as a tensile wave. During this process the particles are moving in the opposite direction to the wave front. These processes continue until all of the energy in the system is expended.

The speed of stress wave propagation depends on the sonic velocities of each material. The greater the difference in sonic properties between the armour and projectile, the greater the ability of the armour system to induce projectile fracture [76,77]. For example, comparing steel (c_o = 4,878 m/s) and B_4C (c_o = 14,634 m/s), the high sonic velocity of the ceramic correlates to the high modulus of elasticity. This is due to the strong covalent molecular bonding, characteristic of the ceramic (*Section 2.2.1, pp. 29*) [44].

Two important material parameters to take into consideration during the stress wave propagation are the wave propagation velocity, c_0 and the magnitude of the impact stress. The velocity of the wave c_0 for a uniaxial stress state in a bounded media is given by:

$$c_0 = \sqrt{E/\rho} \qquad \text{[Eq. 2-6]}$$

where E is the Young's modulus and ρ is the density of the material. For an elastic wave travelling in a semi-infinite medium the wave speed is slightly higher and is a function of Poisson's ratio, v, E and ρ:

$$c_0 = \sqrt{E(1-v) \Big/ \rho(1+v)(1-2v)} \qquad \text{[Eq. 2-7]}$$

The average velocity of a given particle, u_p, dependent on stress, σ, is given by:

$$u_p = \sigma \Big/ \sqrt{E \Big/ \rho} \qquad \text{[Eq. 2-8]}$$

The velocity of an inelastic wave can be determined by substituting the E in *Equation 2-8* with S, the slope of the stress strain curve, beyond the elastic limit. Because E is greater than S, the elastic wave travels faster than the inelastic wave, separating the two wave fronts in the material with time.

A shock wave is a very strong pressure wave in any elastic medium that can be produced by very high impact speeds that can create large changes in pressure. The compression wave is formed when the speed of a projectile (thus, magnitude of stress increase) relative to the target medium exceeds that at which the medium can transmit sound. The material behind the wave is compressed so its apparent stiffness increases and causes an increase in the wave speed. The inelastic wave catches up with the elastic wave and a shock wave is produced. Unlike inelastic waves, shock waves steepen with amplitude as higher amplitude stresses are transmitted faster. There is a body of work describing the analysis of shock waves in detail [89,90,91].

At boundaries the waves are reflected differently when encountering a change in material status, acoustic impedance ($\sqrt{E\rho}$). The amplitudes of the transmitted and reflected waves can be calculated using the densities and the wave velocities, thus acoustic impedance, of the two media [76,77]. At an interface between dissimilar materials we can consider the incident compressive stress wave of intensity σ_I, through material A, reflected stress wave of intensity σ_R, and the transmitted stress wave of intensity σ_T, into material B. For example, *Figure 2.6* depicts a WC-Co penetrator

impacting an Al_2O_3 (material A) front-plate and an aluminium alloy witness plate (material B).

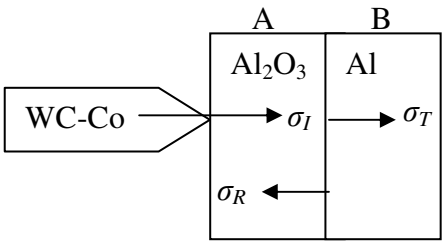

Figure 2.6: Diagram showing an example of the incident, reflected and transmitted stress wave between two materials after impact from a WC-Co penetrator.

The interaction of a wave is much simpler when the incidence is normal. For this example we shall assume the projectile impacts at zero obliquity. The stresses can be measured as a percentage reflected, and transmitted from the original incident stress wave carried through the different interfaces. The equations representing the reflected and the transmitted stresses in the two materials are [76]:

$$\frac{\sigma_T}{\sigma_I} = \frac{2\rho_B c_{oB}}{\rho_B c_{oB} + \rho_A c_{oA}} \qquad \text{[Eq. 2-9]}$$

$$\frac{\sigma_R}{\sigma_I} = \frac{\rho_B c_{oB} - \rho_A c_{oA}}{\rho_B c_{oB} + \rho_A c_{oA}} \qquad \text{[Eq. 2-10]}$$

where, ρ_A and ρ_B are the densities of materials A and B respectively and c_{oA} and c_{oB} are the longitudinal wave velocities of materials A and B respectively. It is clear from *Equations 2-9* and *2-10* that the acoustic impedance of each material determines the amplitude of the transmitted and reflected pulses. When material B has a higher acoustic impedance than material A, a compressive wave (positive stress) is reflected at the interface. When material B has a lower acoustic impedance than material A, a tensile stress is reflected (negative stress) at the interface. In the case of an incident wave reflected at the Al_2O_3 and aluminium interface as described in *Figure 2.6* we would expect a tensile wave reflected. This is because Al_2O_3 has a higher acoustic impedance than aluminium. Ceramic armour materials, because of their low tensile strength are very susceptible to these edge effects. Therefore, any tensile wave

reflected is likely to initiate crack propagation and cause fracture. During fragmentation of the ceramic, the resistive load that is offered by the ceramic is reduced [92,93]. Pickup *et al.* defined a triple layered armour system including a high impedance front layer to initiate damage in the projectile, low impedance glass absorber layer and a polymer backing to catch debris. The areal density of the armour system to defeat a 7.62 mm AP projectile was found to be reduced by over 50% when compared to traditional low impedance front layer faces [183]. *Table 2-2* compares the acoustic impedances of a number of materials.

Table 2-2: A comparison of material properties used for calculating stress wave propagation

	E (GPa)	ρ (kg/m^3)	$\sqrt{E\rho}$ (kgs/m^{2}s)	c_0 (m/s)
Tungsten Carbide (WC-Co)	652	14532	97.34 x 10^6	6698
Tungsten (W)	411	19220	88.88 x 10^6	4624
Silicon Carbide (SiC)	420	3140	36.32 x 10^6	11565
Sintox-CL (Al_2O_3)	367	3890	37.78 x 10^6	9713
Sintox-FA (Al_2O_3)	320	3694	34.38 x 10^6	9307
Boron Carbide (B_4C)	480	2520	34.64 x 10^6	13856
Mild Steel	200	7800	39.50 x 10^6	5064
Aluminium Alloy	79	2900	15.14 x 10^6	5219
Brass	103	7200	27.23 x 10^6	3782

The response of a material to stress and shock waves requires the consideration of its material properties. These are experimentally determined and are usually presented in the form of a linear relationship between the particle velocity, u_p and the shock velocity, U_s. Plate impact experiments enable various material properties to be measured characterising the material's response to dynamic loading. During plate impact experiments a one-dimensional strain shock is formed that can deform the material at a very high rate. A Laser Velocity Interferometer System for Any Reflector (VISAR) is used to measure the compressive and release wave behaviour by monitoring the longitudinal motion at the target sample / window interface. These relationships are incorporated into the conservation of energy, momentum and mass

and are used in the computer numerical models. The five shock parameters can be separated into ten pairs, provided by twenty different equations described in comprehensive detail by Meyer [204].

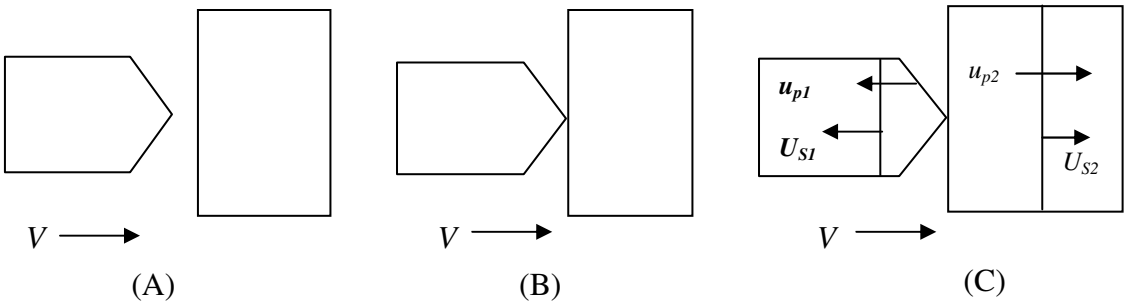

Figure 2.7: Velocity (*V*): Events occurring on impact of projectile into a target from left to right (a) projectile (left) impacting target (b) position at instant of impact: (c) position after impact and during wave propagation stage [204]

Shattering of the projectile can occur by shock waves formed during impact. On impact two compressive shock waves are formed, one with velocity U_{S2} travelling into the target and second with velocity U_{S1} travelling into the projectile. *Figure 2.7,* displays the compressive wave formed in the projectile, which will reach the core's outer free surface. At this point a shock wave at the free surface reflects as a tensile wave (*i.e.* changes sign) and propagates inward, back against the direction of the original compressive wave [3]. High-tension forces develop at the wave front, in turn pulls the projectile apart causing shattering [3].

The Equation of State (EOS) takes care of the volumetric part (volume change) of a material during impact. The EOS expresses the pressure (volumetric stress) as a function of density and specific internal energy (temperature) within the material. By using the equation from the conservation of momentum we can determine the pressure formed in the target and projectile (momentum = mass x velocity).

For the target:

$$P_2 = \rho_{O2} U_{S2} u_{P2} \qquad \text{[Eq. 2-11]}$$

For the projectile:

$$P_1 = \rho_{O1} U_{S1} u_{P1} \qquad \text{[Eq. 2-12]}$$

The EOS for the two materials:

$$U_{S1} = c_1 + S_1 u_{P1} \quad \text{[Eq. 2-13]}$$

$$U_{S2} = c_2 + S_2 u_{P2} \quad \text{[Eq. 2-14]}$$

The EOS is used to determine the pressure, density and internal energy changes that occur within a material during numerical simulations.

2.4 Improving Performance of Ceramic Armour Systems

By the early 1990's research progressed, adapting the existing knowledge to optimise the target-layer design. Various important aspects of the interaction between the projectile and the ceramic target impact have been extensively addressed. Such techniques of improving performance include methods such as confinement, spaced target systems, use of adhesives and altering support and target materials. These will now be discussed.

2.4.1 Confinement

Efficient design of an armour system requires an understanding of the behaviour of materials and structures subjected to intense impulsive loading. The failure mechanisms during penetration of the projectile may be affected by the rigidity and inertia of the armour module introduced by the confinement and the design of the backing layer [94]. It is well known that confined ceramics perform extremely well under ballistic impact. A limitation of using a ceramic as part of an armour system is its brittle nature, requiring only a small fraction of the impact energy to fracture (*Section 2.2.5, pp. 35*). If ceramic materials, with such low fracture toughness are not suitably contained then their multi-hit capabilities may be significantly compromised. During impact tensile stress waves reflected from the tile interface propagate into the ceramic causing crack propagation and fracture (*Section 2.3.3, pp. 44*). During fragmentation of the ceramic, the resistive load that is offered by the ceramic is

released and ceramic fragments that absorbed the projectiles KE are ejected. By altering the constraints of a ceramic the ballistic properties may be changed and the characteristic failure time of the ceramic may be prolonged [95]. Increasing the ceramic failure time could provide enough resistance to disrupt and destabilise a WC-Co core.

In a paper presented by Sherman and Ben-Shushan at the Israel Institute of Technology, they reported on a study of the effects of confinement on failure mechanisms of Al_2O_3 [96]. They wanted to look at the role of lateral mechanical constraint in inhibiting some failure modes. They found the failure in the confined tiles dropped significantly, radial tensile cracks did appear as a result of the local bending induced by local deformation at the opposite surface, crushing and shear dominated cone cracks formed. The lateral compression reduced the damage dramatically improving performance. One reported mechanism is a hydrodynamic cushion that pressurises the ceramic after it has comminuted. The highly pressurised region inhibits the flow of damaged material in front of the penetrator [95].

Hauver *et al.* first demonstrated the effects of altering the ceramic geometry and confinement [97]. They examined the ceramic systems that delayed the generation of damage in the ceramic tile and thus, improved armour efficiency. The experiments employed compressive confinement of the ceramic tile and techniques to delay the tensile wave and bending damage to the ceramic. They increased the shattering and erosion phase of the penetrator defeat process, as a result completely eroding the penetrator. This process is termed dwell. It was found that with sufficient rear-face support to prevent flexure of the ceramic and compressive confinement, this penetrator defeat was observed.

A serious limitation of model scale experimentation is how confinement can represent design reality (*e.g.,* that found on AFVs). Confinement rigs are designed to attempt to avoid the effects of elastic reflections from the lateral extents of the target assembly affecting penetrator performance. Therefore, the rig mimics the effects of a laterally infinite target. Ceramic tiles retain much of their original armour properties as long as suitable confinement exists and intergranular coupling remains. A paper presented by Littlefield *et al,* reported on a study of the effects of confinement of radially finite

steel targets [98]. It was concluded that DoP increased when the ratio of target diameter to projectile diameter fell below 20, emphasising the importance of target confinement [98]. The results from the simulations demonstrated that as the Penetrator (diameter) to Length (target diameter) ratio (P/L) begins to increase, the extent of plastic flow in the target reaches the radial boundary. The results therefore provided an estimate of the target diameter needed to reduce radial edge effects. In order to avoid lateral edge effects, Rosenberg concluded that the target diameter should be 15 to 25 times that of the penetrator, depending on impact velocity and target strength [99].

Results from ceramic armour research aid understanding of the effects of confinement on ballistic performance, stressing the importance of experimental design. It has been observed that to counter ballistic threats of moderate to severe intensity the ceramic elements must be confined within metallic plates to achieve full potential of ceramic resistance to penetration [100]. Westerling *et al.* demonstrated that the improvement in ballistic performance related to how the tiles are implanted into the LAV system. James emphasised the importance of impedance mismatch between layers, strongly influencing the crater hole, fragment number and size [39]. With an increase in the shock wave induced there was greater degree of fragmentation of the participating materials and distinctly larger hole diameters. This is an important consideration for the design of a target system to fragment the WC-Co core.

More recently Lundberg reported the finding that the influence of confinement thickness on penetration was small at high (1400 m/s to 2600 m/s) impact velocities [101]. It was concluded that, in the transition region, where there was asymmetrical penetration as well as extended lateral flow, the penetration was dependent on confinement and impact velocity. This could be due to the larger diameter confinement maintaining maximum penetration resistance, offering the fragmented ceramic suitable confinement providing further protection. Note that these results were in the hydrodynamic velocity regime and could be different to those during sub-hydrodynamic impact.

The confinement helps to prevent radial and axial expansion thereby maximising the target-projectile interactions. Work carried out in the US Army Research Laboratories

has emphasised the importance of confinement on the ballistic efficiency of the ceramic tile, and that dwell-type defeat of penetrator can be achieved on ceramic front surfaces first observed by Hauver [102]. It must not be forgotten that cover plate confinement also has some degree of effect. Anderson *et al.* provided evidence that on alteration of the extent of confinement, the ceramic tile performance was improved [103].

The interface between the ceramic tile and backing plate can help prevent the propagation of long distance cracks, thus delaying the onset of failure at distance from the penetrator impact site, and increasing the inertial confinement of the ceramic material [103]. Overall, the ceramic type and mechanical properties, impedance mismatch, projectile velocity and backing plate stiffness, have been shown to influence the target-penetrator impact, therefore emphasising the importance of maintaining a controlled system for both numerical and experimental analyses.

2.4.2 Adhesives

The first multi-piece hard plate vest inserts were produced from B_4C in 1965. Joints were found to represent a potential weak spot. The objective is to minimise joints to all ceramic armour components, from vests, armoured vehicle mounted panels to armoured seat buckets. In 1966 a monolithic B_4C vest insert with improved performance was produced with the elimination of joints between adjacent tiles [1,2,3,4].

Since the 1960's many practical investigations into development of adhesives to eliminate joints for ceramic armour targets have been performed. Adhesives are increasingly used in armour applications since they create a better stress distribution upon ballistic impact between armour plates than other joining techniques (*e.g.,* welding and mechanical fasteners) [104,105]. The research into the effect of adhesive properties on the target systems is well publicised, yet little detailed investigations analysing the effectiveness of the different adhesives available has been carried forward [106,107,108,109,110].

Using adhesives represents a significant advantage as the adhesive bonding can contribute to improvement in the strength to weight ratio of the armour construction, has good fatigue resistance and allows the fabrication of complicated structures. Primarily the adhesive is of low density, low impedance and low shear strength. Several observations can be drawn from the work of Tod and Wylie on four common adhesives used in ballistic trials:

- Ciba-Geigy Araldite 2005: Two part epoxy resin, high shear (25 MPa) and peel strength (flexibility), negligible shrinkage on curing, heat resistant to 80 ^{0}C, resistant to water and a wide range of chemicals [104,117].
- Ciba-Geigy Redux 326, high temperature modified bismaleimade film adhesive having a service temperature in excess of 200 ^{0}C, prone to cohesion failure [104].
- Hysol XEA 9361, a high elongation two part room temperature cure adhesive having excellent low temperature properties with a combination of high shear and peel strength (16 MPa), high flexibility and water resistance [104].
- Hysol EA 9395, a two part room temperature cure adhesive having high mechanical strength and high temperature performance, up to 175 ^{0}C [104,117].

The unfavourable impedance mismatch effects at material boundaries and induced tensile failure across the boundaries have been well documented [104,106,107,108]. A disadvantage of using adhesives arises from air being trapped during the adhesive drying stages in armour construction. A further disadvantage is that they require considerable time to process and set uniformly. Other disadvantages include poor long-term resistance to moisture and the low maximum service temperature. This can cause plasticisation of the adhesive, corrosion of the substrate and displacement of the adhesive from the substrate [104]. High temperature resins in aerospace applications and for high impact velocities may have to survive at 600 ^{0}C or more [104,111,112]. There is also a requirement for adhesive bonds on light alloys and aluminium joints which possess high peel strength whilst retaining relatively high shear strength [113]. Reduction in the wear resistance, stability of the armoured vehicle construction, the ability to resist climate changes and the use of practical adhesives for battle damage tolerance, are important problems [114, 115]. These disadvantages need to be

considered in the decision to whether such adhesive solutions are viable or whether possible combinations of mixtures could be useful.

There are a number of additional results from ceramic armour research, which aid understanding of adhesive application [109,113,116]. However, Aldridge provides a comprehensive presentation summarising the tests analysing adhesive performance on composite armour [117]. This work was in fact preceded by an extensive investigation into the effects of epoxy on the ballistic performance of lightweight ceramic-faced armour [118]. Ceramic layers were found to prematurely fail when no adhesive was applied to mating surfaces (front and back plate interface). As the Araldite adhesive layer thickness was increased at the interface, bending may have occurred of the ceramic front plate and ballistic performance was found to improve. Ballistic performance was found to reduce when a lower acoustic impedance Sikaflex adhesive was applied to the armour compared to that of Araldite with a higher acoustic impedance [118].

2.5 14.5 mm BS41 Russian Armour Piercing Projectile

In order to discuss the approach of this work, a basic overview of ceramic armour has been presented. The fundamental techniques employed by ceramic armour systems to defeat AP projectiles have been discussed. Next we must consider the type of threat which determines the design of armour system. First the projectile (WC-Co core) must be considered, *Section 2.5.1* and *Section 2.5.2*. After, a basic description of WC-Co is provided (*Section 2.5.3*). Material properties and armour system design on selected materials that could be considered for the role of WC-Co projectile defeat are discussed in *Section 2.2*. Finally a short historical review is presented (*Section 2.5.4*).

The principle used by projectiles to defeat armoured vehicles is by providing sufficient KE to achieve penetration. Until the Second World War, AP shells were simple full-calibre rounds, made from hard steel. High density, high velocity and reduced drag were the principles explored for the attack of armour. The response was to make the armour harder and thicker to defeat the rounds. Problems arose when the projectile threats were re-designed heavier and faster. This saw the failure of such projectiles

when the large solid steel projectiles could not withstand the stress of high velocity impact against armour, and would defeat themselves rather than the armour they were attacking [28]. It was not until the 1930's that the readily available alternatives such as WC-Co and later in the 1980's Depleted Uranium (DU) came into use to defeat the monolithic armoured vehicles. These materials were shown to overcome the effects observed with larger steel core rounds.

2.5.1 WC-Co Armour Piercing Projectiles

Armour piercing projectiles are special anti-tank shells with unique features. The performance of a given projectile depends largely on the amount of KE it possesses at the moment of impact. The response of the target to projectile threat is governed largely by the Kinetic Energy Density (KED). When the KED is low (sub-hydrodynamic) the target materials respond as solids and the interaction can be described in terms of strength properties. This situation applies for impact velocity V approximately up to 1 km/s. As the KED is increased into the region of hydrodynamic attack following a transition velocity, (V > 1 km/s) stresses that develop are large in comparison to the strength of the target and projectile, therefore they behave as fluids [157,158]. To understand the required defeat mechanisms and armour designs the calibre, velocity and energy of the threat projectiles must all be considered.

Historically, ceramic composite armours were designed to defeat AP projectile KE threat from sub-hydrodynamic attack. Some of the oldest types of AP rounds are the common AP projectiles appearing before the Second World War [119]. Generally AP projectiles consist of either a moderate density core, (7.85 g/cm^2) like the steel cored B32 14.5 mm projectile (1941 - 1942) or, in some select rounds, a harder, denser core was employed like the BS41 14.5 mm (1940) or the FFV 7.62 x 51 mm (1980) WC–Co cored rounds (13.5 to 15.0 g/cm^2) (see *Appendix 1, Figure A1.2 & 3*). The high-density WC-Co sub-calibre core raises the KE on the unit cross sectional area in the core. This enables it to out-perform the lower density steel core, providing more effective penetration in hard ceramic-faced targets [8,121,122]. The 14.5 mm BS41 projectile represents a significant increase in threat level. Penetration tests into mild steel have revealed a 45% drop in ballistic performance of the smaller cored projectile,

7.62 mm WC-Co cored FFV and a 10% drop in performance of the 14.5 mm steel core B32 projectile, compared to the BS41 (*Section 4.1*).

Today, hypervelocity AP projectiles have been developed to defeat modern heavy tanks in battle. With the previous successful employment of high-density hard core threats, more powerful rounds were developed. Examples may be found like the Terminator (KEW) APFSDS-T Tungsten heavy alloy penetrator containing 90% Tungsten by weight and mixed with other alloying elements (*e.g.,* Co, Nickel (Ni), Iron (Fe)) or the LRP containing DU [120]. WC-Co and tungsten alloys may fall short in one aspect of performance (*e.g.,* DoP) compared to their principle competitor, DU, however they do not have the same health, safety and environment barriers to their development.

2.5.2 Russian BS41 14.5 mm Threat

In 1939 the 14.5 mm cartridge originated as the main cartridge for Russian anti-tank rifles. The BS41, designed in the early 1940's, proved itself as one of the most powerful and effective HMG cartridges in service (*Figure 2.8*).

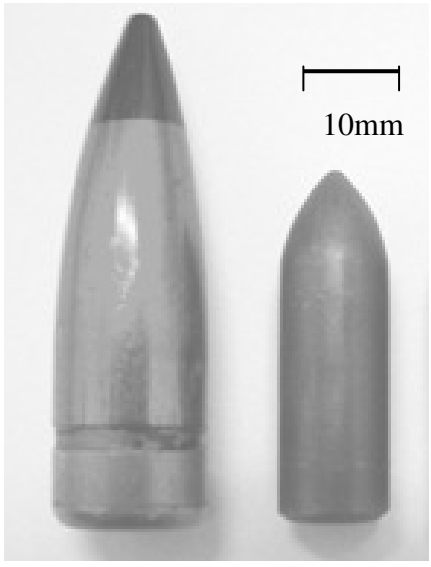

Figure 2.8: 14.5 mm AP-I Type BS41 jacketed projectile (length 51.2 mm) (left) and core (length 38.72 mm) (right). Projectile mass: 64.2 g, muzzle velocity 1016 m/s. (Further information may be found in *Appendix 1 –Figure A1.1* and *Table A1-1*)

During the war new designs of anti-tank machine guns were developed, the Degtyarev–designed PTRD and the Simonov-designed PTRS. In 1944 the Soviet Union introduced the Vladimirov KPV HMG firing the 14.5 mm x 114 cartridge and the PTRD and PTRS became obsolescent. The KPV HMG is the weapon in widespread service today in both ground and anti-aircraft roles. It serves as the main turret armament of the BRDM-2 amphibious scout car, and the BTR-60PB, BTR-70 and BTR-80 APC [121,122,123].

Five service projectile types are known to exist, all of Russian origin. Table *A1-2, Appendix 1* lists the various types and codes for the 14.5 mm ammunition [121,122]. Typically WC-Co used for AP projectiles consists of W-88%-C-5.58% grains, a Co-5.7% matrix, Ta-1.9% and less than 0.3% Nb and Ti trace elements by weight, and has a Rockwell Hardness of 93 [9,20]. Today brass-washed steel, coated initially with gilding metal and later with zinc, is the standard bullet envelope material [121,122]. An incendiary content is held within the envelope nose. The hard core is encased with a softer outer jacket to enhance aerodynamics. Typically the projectile has a length to diameter ratio (L/D) ratio of 5:1 with moderate muzzle velocities of 1016 m/s ± 10 m/s (*Section 3.3.1*). With such a low L/D ratio a high residual projectile mass may provide effective lethality against LAV. In comparison, the LRP where the L/D ratio may exceed 20, is designed to defeat MBTs [5,119]. It has been cited that for low L/D applications, tungsten alloys have equalled or even outperformed DU [124].

Tungsten Carbide cores used for AP projectiles have been used in the field for nearly a century, yet the research into the failure of WC-Co is still relatively new and the mechanisms are not fully understood. Other WC cored rounds include [12,125]:

- 12.7 x 108 mm AP Projectile Egyptian Manufacture AP-I-T B62 (Red Trace to 1200 m, 62 g, Muzzle Velocity (MV) 825 m/s).
- 7.62 x 51 mm FFV ammunition (Bofors – Carl Gustav) (*Appendix 1, Figure A1.3*).
- 3VBM-42, 125 mm APFSDS Round, Upgraded 3BM-17 projectile with WC-Co plug [126].

The effort of this work is concentrated on the failure of the Russian 14.5 mm BS41 projectile. The experimental and numerical research can provide insight to the impact

behaviour of the BS41 projectile. This work should provide insight, and act as a catalyst for further research into other such rounds.

2.5.3 Manufacture of a Cemented Carbide (WC-Co)

The principles behind the protection required by an armoured vehicle to defeat the BS41 WC-Co cored projectile may be compared to that required at defeating other rounds. There is a body of work on ceramics and the penetration mechanics of light armour [127,128,129,130]. Within this work there are a number of useful studies, which may be at least partially relevant to WC-Co projectile defeat. However it is first necessary to summarise the threat material to which the armour system is to respond.

To trace the history of WC, we must begin in 1781 after Scheele's discovery of tungsten, but it was not until 1923 that the first patents on WC-Co were issued to a German company "Osram Studiengesellschaft". In 1926 the first marketable WC was produced under the name of "Widia" [136]. If a material could be produced displaying the high hardness and yield stress under compressive loading of ceramic materials (*Section 2.2*), whilst also possessing the high tensile strength of metals, it would clearly be a superior material for the design in armour and projectiles. Cermets are ceramics, which have a metal phase (metallic binder), improving tensile strength by deflecting and absorbing energy from advancing cracks [131, 132]. It was identified that by introducing ductility into a ceramic it can increase its toughness.

Tungsten Carbide - Cobalt consists of hard WC particles bonded together in a 6 to 10% tough cobalt (Co) matrix; hence the term *cemented carbides* or *cermets*. WC-Co belongs to a class of hard, wear resistant, refractory materials. Processing of WC-Co follows a complex and expensive route, traditionally liquid phase sintering [133].

Initially the raw WC is made [134]. A common route used by industry is to form WC powder by a solid state reaction. A mixture of ultra fine powdered tungsten metal and carbon are raised to a very high temperature by an arc of electricity. During this phase the mixture is held in a carbon crucible. The two elements form a large mass of WC.

$$W_{(S)} + C_{(S)} \rightarrow WC_{(S)}$$

The process requires a number of heating and milling stages. A chemical calculation shows that the product of the gas/solid reaction of WO_3 and CO will be WC [135]:

$$WO_{3(S)} + 5CO_{(g)} \rightarrow WC_{(S)} + 4CO_{2(g)}$$

This mass of WC is then crushed and milled to form a fine powder. The powder can then be screened down to uniform particle sizes.

The next stage in the production of WC-Co is the mixing of very hard WC powder grains in a binder matrix of tough Co metal to form a uniform combination by liquid phase sintering. A full description of liquid phase sintering may be found elsewhere [30,31,35]. High temperatures are required to melt the Co. Depending on the solubility of the phases, inter-diffusion occurs at the contact points of the powder particles. The high solubility of WC and metallic Co during the process result in an excellent densification during liquid phase sintering. Once cooled the compact is one of high melting point WC particles surrounded by a Co matrix [135]. As a result of this, the cemented carbide obtained, WC-Co, combines high toughness, strength and hardness. *Table 2-3* below compares a number of mechanical material properties of WC-Co to various ceramics and metals [44].

Table 2-3: Comparison of material properties of various ceramics and metals [44]

Material	**Density (Mg/m^3)**	**Toughness, (kj/m^2)**	**Fracture Toughness ($MN/m^{3/2}$)**	**Hardness Hv**	**Yield Strength (MN/m^2)**
WC-Co	14.0-17.0	0.30-0.50	14-16	1289	6000
SiC	2.5-3.2	0.05	3	1900	10000
Al_2O_3	3.9	0.02	3-5	1500	5000
Mild Steel	7.8	100	140	195	220
Aluminium Alloys	2.6-2.9	8-30	23-45	145	100-627

The grain structure of WC-Co can vary depending on the manufacturing process. *Figure 2.9* displays the grain boundaries of a WC-Co sample under high-resolution SEM [137].

Figure 2.9: SEM micrograph showing the grain structure of a WC-Co sample taken from the Russian BS41 14.5 mm projectile [137].

Over the past century research has focused on improving the manufacturing process. An example has been published by Ramkumar *et al*. [138]. They investigated the production of cemented WC using microwave irradiation. The route proved cost effective, reduced time and energy and resulted in activation of grains and formation of a compound with enhanced mechanical properties [138]. Although there is limited specific work on the failure of WC-Co cored projectiles to date, there is a more general body of work on the manufacture of WC-Co used in the tool industry [136]. Since the material was originally developed for use in cutting materials, withstanding the high compressive stress and wear imposed during the cutting process is important. Cermets provide the majority of turning tools and milling cutting tools, apart from wear resistant structural parts.

For the different manufacturing processes, the WC-Co coated particles can vary in grain size between 1 µm and 5 µm [140]. A WC-Co sample taken from the BS41 has shown this can increase to over 20 µm (*Figure 2.9*) [137]. Etched transverse and longitudinal samples of WC-Co were placed under the optical microscope to analyse

their grain structure. The unusual occurrence of significantly larger grains of 20 microns were scattered on the surface. This could have been due to different size particles of WC before the processing into the Co matrix.

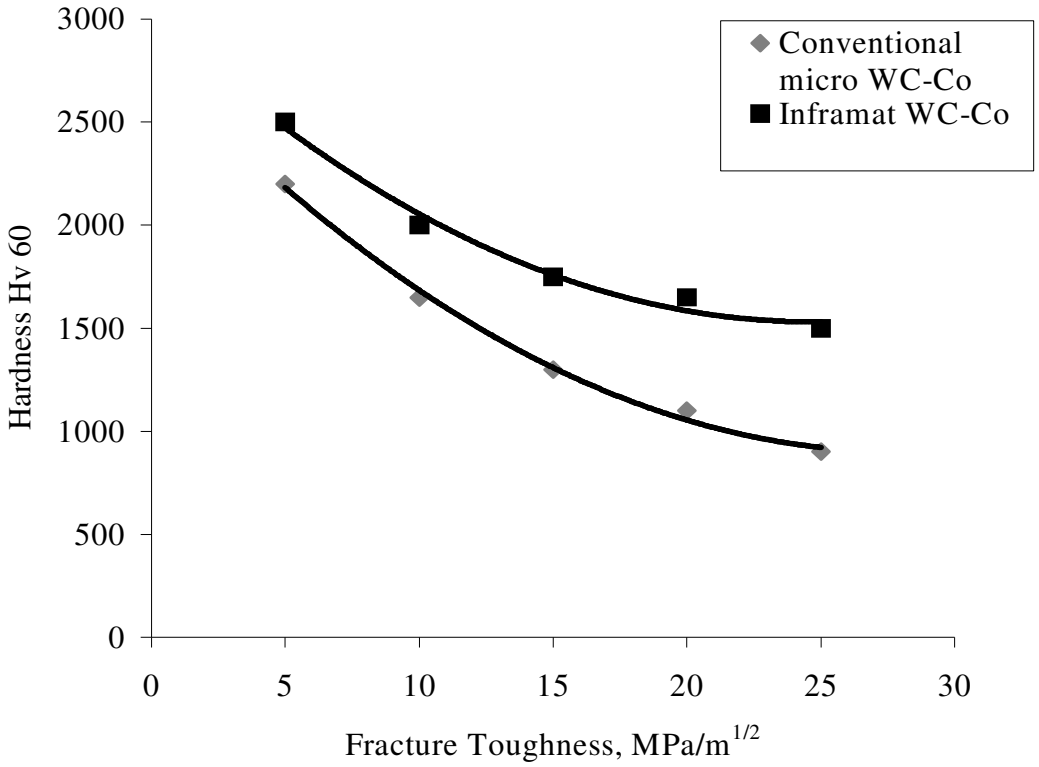

Graph 2-1: Hardness versus fracture toughness. As grain size is decreased, both toughness and hardness are increased. Results adapted from ref. [136].

Graph 2.1 compares the hardness of two WC-Co materials. Inframat (manufactured by Inframat) with a grain size of 0.2 µm to 0.4 µm, whilst maintaining a reasonable fracture toughness has a superior hardness compared to conventional larger grain WC-Co [136].

The manufacturing process is important because with variations in grain size, porosity and void fraction within a sample, the relevant characteristics of WC; brittle behaviour, strength and hardness, may all be affected. The amount of Co significantly affects the properties of the WC-Co [138,139,140]. It has been shown that as the Co content is increased, the strength, hardness and wear resistance of WC-Co decrease, while the toughness increases [139,140]. This is because of the higher toughness of the Co.

This work reviews WC-Co for KE penetrator applications. The ability to vary the density, toughness and strength produced by varying the proportions of particulate phase and binder make WC-Co suitable for a range of penetrator applications. During sub-hydrodynamic attack it is important that the projectile has maximum resistance to mass loss. Increasing WC-Co toughness assists this, although mechanisms of projectile attrition under these circumstances are not fully understood.

2.5.4 WC-Co AP Development

Conventional engineering properties of a penetrator material, such as strength, ductility and toughness are important parameters in designing a projectile. With such attractive material properties, it is surprising that more work on the failure of WC-Co has not been carried out. Despite the scarcity of directly applicable work it is possible to identify a number of areas in which useful information may exist, this chapter devotes a few paragraphs.

Prior to the use of harder core projectiles, armour was subject to attacks from an array of weapons. This led to the adoption of ceramic armour, first commercially introduced in the 1960's [1,3,4]. The mechanisms of failure that may occur are diverse including deflection (altering obliquity) and crack initiation and coalescence. These ceramic multi-layer targets aimed to reduce the perforation of the target system by combining three main stages of projectile defeat: shattering, erosion and catching the projectile within the witness plate dissipating the core KE (*Figure 2.10*). An overview of the penetration mechanisms can be found in *Section 2.3*.

Figure 2.10: BS41 fractured WC-Co core. Captured by an 1318b aluminium alloy witness block after firing through a SiC B front face coupled to the 1318b aluminium alloy witness block.

The prime aim of the design of armour to defeat high-density cores is to increase the initial shattering time and increase the comminution and erosion processes. Research has shown that altering the confinement on the ceramic armour system may increase armour efficiency, particularly if the comminuted ceramic material is further constrained [141,142,143,144] (*Section 2.4.1, pp. 50*).

A number of studies have been performed on the impact of different types of WC projectile. Sphere impact tests have extensively been studied. In a reviewed paper presented at the Royal Armament and Research Development program, Williams reported a study of the impact effects of two types of small WC projectiles [145]. Conical headed projectiles penetrated RHA by plastic deformation and flow whereas spherical headed projectiles caused failure by a shear mechanism. It was concluded that the softer the target material the smaller the plug sheared. He also found that the

conical headed projectile lodged in the plate and fractured transversely. This could have been due to the strength of the reflected tensile shock wave after impact [145]. Similar failure was observed during the impact of the BS41 into Sintox-CL Al_2O_3 targets [9]. The ballistic performance of a material is sensitive to projectile shape or orientation. One definition described by Laible relates the shape of a projectile to the mass and average area viewed in all directions of the projectile [77].

Andersson *et al.* analysed the effects of WC-Co spheres impacting ceramic-faced targets. Analysing the spheres impacting at lower velocities enabled their study of the crack propagation, stress levels for crack initiation and their crack patterns [146]. At 30 m/s they verified cracking and possibly non-linear deformation. The cracking and deformations were complex, implying the need for a non-linear analysis, which was possible to perform from their perturbation method. Interestingly this would be important in the numerical modelling in simulating the propagation of the cracks accurately.

In considering the penetration mechanisms of the WC-Co cored projectile, parallels can be drawn with a number of well-documented ballistic methodologies. The most promising lines of investigation are those carried out by Grady *et al.* [20,147,148]. Work performed by Hertal & Grady looked into the effects of WC-Co spheres impacting poly methyl methacrylate (PMMA). Using flash x-rays they recorded the break-up of the WC-Co at different time intervals. They then compared their experimental data to that of the numerical results in Shock Physics three-dimensional code, CTH [20]. They found that the simple analytical models were not capable of predicting the complex fragmentation behaviour witnessed in their experimental investigation [20]. Of particular interest, Grady reports on results from dynamic compression and dynamic tension (spall) tests [20]. These may be used to define empirical constants for numerical modelling.

A numerical model would help aid ballistic prediction and validation of experimental efforts. The ability to simulate accurately the failure of the inhomogeneous ceramic target comminution has proven difficult for decades. In order to do this a powerful model would be required where void information and crack propagation could directly simulate each particular specimen. This would prove extremely difficult.

Additionally, the fragmentation and crack propagation phenomena need to be fully understood.

Numerical techniques can advance our experimental and theoretical understanding of impact. Rapid advances in computer research aid the advance in computer simulations. AUTODYN is a non-linear dynamic code from Century Dynamics [195]. It is a powerful numerical tool that may predict the sequence of events that occur during the penetrator and target interaction. It allows the user to interrogate a number of material dependent parameters during the penetration and the subsequent perforation. However there is still limited published data on the dynamic material properties of the projectile and target materials and, without extensive dynamic testing, a number of approximations have to be made. Therefore some form of calibration with experimental data is necessary. Nevertheless, these models can still provide useful insight into the penetration phenomena observed in experiments [149].

2.6 Conclusions

When a new armour system is brought into service it will inevitably be superseded by developments in projectile technology. Therefore, armour and projectile technologies have always driven each other. The applications of ceramics are growing rapidly as the need for lighter and more efficient armoured vehicles increase.

Multi-layer systems are more efficient because projectile defeat is not entirely dependent on a single layer. The synergistic effects of combining a hard brittle ceramic front target, with the properties of a ductile metallic backing plate are presented (*Section 2.3*). Important parameters include the material's mechanical and physical properties (*Section 2.2*), dynamic stress wave propagation (*Section 2.3.3*) and the impact stress level. Designed carefully, the multi-layered ceramic systems can perform highly efficiently over a spectrum of threats (*Section 2.5*). Achieving each of these qualities is extremely difficult in practice and this has kept research in this field fuelled for the last four decades.

The link between specific ceramic properties and ballistic performance remains tenuous. *Section 2.2* has outlined some of the important properties and trends for material properties *vs.* improved performance. The effect of hardness, strength and toughness are to control both resistive force and induce projectile fracture and erosion. Ceramics generally do not come close to their theoretical strength as the pores, grain size and micro-cracks provide a source for crack propagation effecting their ballistic performance. It is important, regardless of ceramic type that the ceramic is confined to prevent radial and axial expansion in order to maximise target projectile interactions.

The background and reasons for work on this project have been outlined. It is evident that for the project to be a success, development should proceed both on the experimental front, to analyse the 14.5 mm WC-Co core failure during dynamic impact and on the computational front, to develop a WC-Co material model simulating the WC-Co failure characteristics observed.

Chapter 3

Experimental Methodology

The experimental analysis investigates the efficiency of a ceramic armour configuration to defeat the BS41 threat. Considerations underlying the experimental investigation and the rationale behind the approach are presented. Experimental methodologies are compared and alternate performance criteria are discussed. Conclusions are drawn from the advantages and disadvantages of the various procedures. Material selection, target set-up and a basic description of the experimental techniques employed are presented.

3.1 Experimental Ballistic Tests

In order to judge the relative merits of each measurement methodology, it is important that the tests are designed and interpreted properly in order to assess accurately the ballistic performance of ceramics [150]. Particular attention was paid to the ability of each method to cope with difficulties presented by armour layer design then cost. The rationale governing each final choice of technique is summarised.

With today's threat to modern AFVs, an armour system must be tested so as to express, in quantitative terms, a meaningful measure of its protective capability. A range of traditional and non-standard tests have been used to characterise and to study impact phenomena. Two common ballistic measurement methods employed to analyse penetrator performance against different armour systems are the *V_{50} technique* [77,151] and the *Depth of Penetration (DoP) technique* [150]. There is a body of literature detailing the different approaches by which the impact behaviour of projectiles into armour systems is understood and evaluated [20,24,36,125,128,129,130,135,152].

3.1.1 V_{50} Technique

A problem encountered in the study of impact phenomena is the determination of a velocity below which a projectile will fail to perforate a particular barrier. This is of prime importance in the design of a protective armour system, for example in evaluation of military vehicle armour. A well-established probabilistic approach relies on data consisting of the projectile's striking velocity and some form of statement of either defeat or non-defeat of the armour, depending on the ballistic limit criteria and definition. This is often expressed as V_{50} ballistic testing, where V_{50} is the estimated striking velocity at which there is a 50% chance of a complete penetration. [77,151]. It is straightforward to determine experimentally and has provided the basis for evaluating the ballistic performance of a potential target [153]. One method of determining the V_{50} is by averaging three of the lowest complete penetration velocities with three of the highest velocity partial penetrations within a maximum range of 40 m/s. This is the American Military Specification System (Mil spec.). Other standards differ like the UK's RARDE 802, performance criteria for evaluating Glass Fibre

Reinforced Plastic (GFRP) spall liners. This accepts the two slowest complete penetrations and the two fastest partial penetrations within a 30 m/s spread.

The V_{50} technique is widely used and accepted in the commercial world as a standard for armour development. A disadvantage is that it can require a large supply of both ammunition and targets. This can prove both time-consuming experimentally and expensive (target and ammunition). During this investigation limited ammunition and targets were available. Moreover, the focus for this investigation was on the failure of the WC-Co core penetrating different ceramic armour systems, therefore other ballistic tests were considered.

3.1.2 Depth of Penetration Technique Methodology

The DoP technique is a well-established and effective method of obtaining ballistic penetration data for comparison of different target systems. Because of this, the technique and its implementation have been detailed and discussed frequently in the literature [14,15,16,17,18,88,163,150,154]. The technique is an effective method of providing experimental data on residual penetration for validation of numerical constitutive modelling. Therefore the DoP technique was employed.

The DoP technique as first introduced by Yaziv *et al.* [155,156] and described by Rozenberg and Yeshurum [93], was used for this study to measure the ballistic performance of each target configuration. It provides the most literal interpretation of the results from a ballistic trial. The method consists of the measurement of penetration capability of a projectile into a baseline target. DoP assessments are made into the back-block material at nominally the same velocity at which the material under investigation will be tested. The penetration capability can then be compared to penetration into alternative ceramic target systems.

For each ceramic tile of specific thickness (t_c), a single projectile was fired at the target and the residual penetration (P_r) into the witness block was measured as described in *Figure 3.1*.

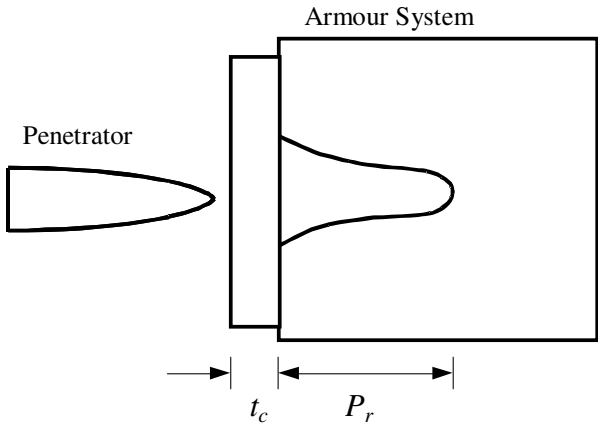

Figure 3.1: DoP technique for assessing each ceramic's ballistic performance.

It is important that DoP tests are properly designed and interpreted in order to assess correctly the ballistic performance of each target system. At least three experiments were done for each tile thickness where materials were available. The DoP was then interpreted using a performance criterion described in *Section 3.2*. By plotting a graph of ballistic efficiency versus experimental parameter (*e.g.,* velocity) for each experimental condition, the most effective target system is identified.

3.2 Performance Criteria

Experience has shown that no single armour system provides maximum protection to all on-coming threats, each material has certain attributes and certain limitations. The DoP test alone cannot provide a good source of comparison between different ballistic trials. A form of performance criterion must be employed. The maximum protective performance of ceramic armour materials may be achieved by applying published performance techniques to analyse the ballistic efficiency of different ceramic target systems. Different investigators have studied a number of methods during the last three decades. Several test techniques have been employed in these studies, such as the *Mass Efficiency* [15,156] and the *Differential Efficiency Factor* [9,88,155]; both are well-characterised performance criteria.

3.2.1 Mass Efficiency and Differential Efficiency

Armour performance tests for a particular ceramic target system are sometimes summarised in a single performance value for each impact velocity. The Mass Efficiency (E_m) equation compares the DoP of each of the targets systems to DoP into a reference material of reference areal density (*Equation 3-1*) (*e.g.,* RHA or other reference material of choice like aluminium alloy). Rolled Homogeneous Armour, a low alloy steel is used today is the benchmark by which armour and armament performance is judged. During World War Two it was used widely for AFVs at a maximum hardness consistent with structural integrity. It is good at defeating ballistic threats and easy to manufacture. Armour thickness is often quoted as the equivalent thickness of RHA, and a projectile is usually described as having the ability to penetrate a certain thickness of RHA [157, 158].

The Mass Efficiency is useful as it defines the protection of an armoured vehicle within a particular weight limit. It is determined from the penetration depth into a semi-infinite reference material, P_{ref}, the residual penetration into the target system back block P_r, the thickness of ceramic material t_c, and ρ_{ref} and ρ_c, the areal densities of the reference material and ceramic respectively. The definition of the E_m is given by:

$$E_m = \frac{P_{ref}\rho_{ref}}{t_c\rho_c + P_r\rho_{ref}} \qquad \text{[Eq. 3-1]}$$

The E_m is important as it provides a good representation of the ballistic efficiency of different target systems to reference monolithic armour.

Also used to calculate the ballistic efficiency of a ceramic system is the Differential Efficiency factor (e_c). The Differential Efficiency states the factor by which mass per unit area has to be multiplied to achieve the same degree of protection if the ceramic were to be replaced by the reference material (*e.g.,* RHA). This measure is reported by James *et al.* and provides correction algorithms, normalisation methods and calculations for the determination of the value, for comparing results to open literature [18]. The Differential Efficiency factor is defined by:

$$e_c = \frac{(P_{ref} - P_r)\rho_{ref}}{(t_c \rho_c)} \qquad \text{[Eq. 3-2]}$$

Both of these performance criteria can be used as a method of comparison between different target systems. The e_c was chosen to compare ballistic performance between experimental results, as a good measure of a comparison of mass saving of armour systems to a reference witness block.

3.3 Experimental Materials

3.3.1 Projectiles and Firearms

The principle projectile tested in this investigation was the Russian 14.5 mm BS41 AP-I projectile described in *Section 2.5,* obtained from the Defence Science and Technology Laboratories (dstl). It has a WC-Co core consisting of W-88%-C-5.58%, matrix Co-5.45%-Fe-0.34% and the Vickers hardness is 1289 Hv (2 kgf load) [9,137]. This was evident from the Inductively Coupled Plasma, Atomic Emission Spectroscopy analysis performed by Sheffield Testing Laboratories.

The BS41 was launched from a fixed proof barrel taken from a KPV Russian HMG. The 14.5 mm barrel had been re-chambered to accept a 20 x 128 mm cartridge case so greater propellant mass can be used to attain high impact velocities. The Bofors 7.62 x 51 mm FFV AP, WC-Co core projectile was also used in the investigation. The core material consists of, W-82.6%-C-5.2% in a matrix of Co-10.5%-Fe-0.41%, hardness 1200 Hv (2 kgf load), density of 14800 kg/m^3 mounted in a low carbon steel jacket with gilding metal, on an aluminium cup [125], the projectile weight being 8.2 g [128]. It was launched from a fixed 7.62 mm proof barrel. The FFV core has a 5.05% greater weight of Co compared to that of the BS41. It has been shown that as the Co content is increased, the strength, hardness and wear resistance of the WC-Co decrease, while the toughness increases (*Section 2.5.3, pp.59*). This must be taken into consideration when comparing the experimental and numerical results.

The test barrels were mounted a distance of 10 metres from the target. Correct alignment between the barrel and the target was essential and measurements were made with an optical protractor to ensure the target was perpendicular to the gun barrel. A bore sight was also used to aid the alignment of the target. Before each trial calibration firings were performed using the 14.5 mm B32 or the 7.62 x 51 mm ball round to confirm correct alignment.

3.3.2 BS41 Propellant

Initial ballistic tests performed recorded unexpectedly high velocity measurements, typically 1100 m/s to 1200 m/s. High Performance Liquid Chromatography (HPLC) was used to determine the Russian BS41 propellant type. This was performed as to confirm that it did not contain a source of high-energy propellant, which could explain the unusually high velocities. Typically, double base propellants with high nitroglycerine content can achieve high velocity performance [159]. HPLC is suited to the determination of potentially unstable nitro-compounds such as that found in propellants [160]. The measurements were taken under ambient conditions.

The BS41 contained a single base propellant containing 90% or more nitrocellulose. It contained diphenylamine, dibutyl and diamyl phthalate. The remainder was made up of plasticiser, stabiliser and residual solvent from the manufacturing process. There was no nitroglycerine present which is indicative of double and triple base propellants. There were minor constituents (*e.g.,* inorganic anti-flash additives like potassium sulphate and cryolite) that could not be analysed by liquid chromatography. All the soluble energetic ingredients, *e.g.,* nitroglycerine, and the organic additives like the stabiliser and plasticiser could be detected. Single base propellants are typically utilised in Russian SA rounds, mortars and howitzers [161,162]. It was concluded that the flash caused interference with the velocity electronic measurements. Appropriate measurements were taken, as described in *Section 3.4.1* for all remainder firings.

Experiments were performed, comparing the effects of velocity on target and projectile impact using NRN151H (Nobels Rifle Neonite) propellant. A 14.5 mm

barrel was especially chambered to accept 20 mm cases to enable larger masses of propellant to be used. Charge mass was varied to give the desired velocities of 750, 850, 1016 and 1100 m/s.

Graph 3.1 below shows the effects of varying the mass of NRN151H on the velocity of the BS41. Cotton wool made up any shortfall in propellant volume inside the cartridge.

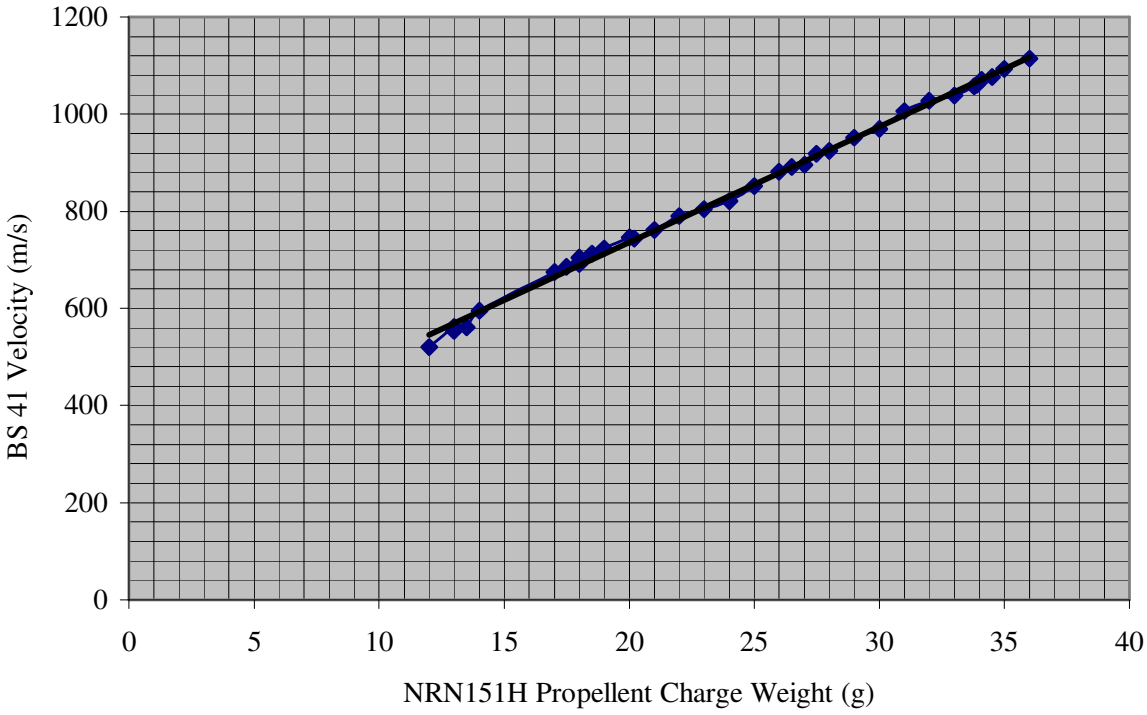

Graph 3-1: Displays the effect of NRN151H propellant charge weight (g) in a 20 mm cartridge case on the velocity of the BS41 fired from a 14.5 mm proof barrel. Results taken from Fort Halstead.

All firings were performed under ambient conditions of temperature and pressure and at zero obliquity. The rounds were weighed and measured to make sure there were no large variations in projectile size and mass within the same batch and the projectile and barrel temperature kept constant. These variations can influence velocity and flight aerodynamics, thus penetration. Each weapon was rest mounted and fired electrically by means of a solenoid attached to the trigger mechanism.

3.3.3 Ceramic Material

Model-scale tests were carried out to check the influence of different ceramics on ballistic performance. All the ceramic tiles were 100 x 100 x *n* mm (*n* ranging from 9 mm to 30 mm) to prevent variables, such as altered lateral stress wave reflections from affecting penetration. In order to avoid radial edge effects, Rosenberg concluded that the target diameter should be 15 to 25 times that of the penetrator, depending on impact velocity and target strength [99,163]. Only limited thicknesses and diameters were available for the more expensive ceramics. The cost of manufacture of certain desirable ceramics and sizes was beyond the budget of this project. This made it difficult to alter particular ceramic target material properties and size accordingly to compare effects on impact. *Table 3-1* provides some material properties of these ceramics.

In summary the ceramic targets used in the trial were as follows:

Two grades of Al_2O_3 supplied by Morgan Matroc: Sintox-FA (95% purity) containing a low viscosity glassy phase and Sintox-CL (98.6% purity) a die pressed and sintered, harder ceramic but with a lower fracture toughness.

Two grades of SiC were compared: AM & T PS 5000 SiC, die pressed and sintered with a boron / carbon sintering aid system supplied by Morgan AM & T and SiC B manufactured by pressure assisted densification and supplied by Cercom USA.

Table 3-1: Material properties of the ceramics used in the investigation

Material Property	***SiC B***	***PS 5000 SiC***	***Sintox-CL Alumina***	***Sintox-FA Alumina***
Bulk Density (kg/m^3)	3180	3140	3890[2]	3694[2]
Hardness Hv (2 kgf)	1969[1]	2644[1]	1705[1]	1357[1]
Average Grain Size (μm)	3-5	-	3.2	6.1 (4)[3]
Young's Modulus (*E*) (GPa)	430	420	367	320
Flexural Strength MPa	560	-	410	-
Compressive Strength (MPa)	4900	-	2000	3310[2]
Bulk Modulus (K) (GPa)	-	-	-	195
Weibull Modulus (*m*)	11	-	-	-
Shear Modulus (*G*) (GPa)	195	-	150	124
Elastic Modulus	460	428[4]	382[2]	308[2]
Poisson's Ratio (υ)	0.16	0.14[4]	0.234[2]	0.237[2]
Fracture Toughness (Chevron notch) (MPa-m$^{1/2}$)	4.4	-	3.5	4.6
Thermal Expansion (RT-1000^{0}C) 10^{-6}/^{0}C	4.5	-	8.0	-
Velocity Trans. (m/s)	7650	-	6207	7266
Velocity Long. (m/s)	12250	11990[4]	10535	9890[2]

[1] Vickers Hardness Results measured using an Indentec HWDM7 Digital Micro Hardness Machine at 2.0 kgf; Cercom's quoted value for the SiC B is 2400 [164], which is somewhat higher than measured in this programme. Both Sintox-CL and FA were slightly higher than quoted from the manufacturer [9].

[2] Sintox-CL Morgan Matroc Ltd. manufacturer's data sheet [165]

[3] Grain Size [166]

[4] PS 5000 material properties [167]

3.3.4 Hardness Measurement

The hardness of WC-Co, the different ceramic materials and the witness blocks can be measured using a number of techniques. Published measurement techniques include the Vickers, Knoop and Brinell hardness tests. There is a body of literature detailing the different approaches from which hardness of ceramics and the materials behaviour can be measured [168,169,170,171,172,173,174,175]. The indentation of ceramic materials, including WC-Co, shows the resistance of the material to plastic deformation. The Vickers indenter test was chosen, as it is an effective and widely used method. The Vickers hardness number is measured by forcing a small diamond indenter having pyramidal geometry into the surface of the specimen. The resulting impression is observed under a microscope and measured. This measurement is then converted into the Vickers Hardness number (Hv). It is calculated by:

$$H_v = 1.854 \, F/d^2 \qquad \text{[Eq. 3-3]}$$

where, F is the load applied to the indenter and d is the average distance between the opposite corners of the diamond indentation.

The specimens used were un-etched but mounted and polished to ensure a well-defined indentation that could be accurately measured. It may be seen in *Table 3-1* that the hardness of each of the ceramics, with the exception of the Sintox-FA Al_2O_3, was significantly higher than that of the Russian WC-Co at 1363 Hv.

3.3.5 Grain Size Determination

For each ceramic, the average grain size was measured from SEM micrographs. A 10 mm cubic sample was cut, hot-mounted in conducting Bakelite and polished. Grain boundaries were sufficiently clear after polishing and therefore it was not necessary to etch. The grain size can be determined by a polished cross-section of the material to be analysed. Effective grain sizes (d_g) can be determined using the expression:

$$d_g = \frac{1.56 L_{\text{int}}}{Mag} \qquad \text{[Eq. 3-4]}$$

where, L_{int} is the intercept length and *Mag* is the magnification factor used in the SEM (1.56 is an effective correction factor derived by Mendelson [176]). *Table 3-1* presents the average grain sizes from each of the micrographs.

3.3.6 Witness Plate

The witness plate material is important, as it is known to affect the efficiency of an armour system (generally related to the rigidity of the support it provides, see *Section 2.4.1, pp. 50*). When a ductile material such as steel or aluminium is loaded under tension, the behaviour of the material can be summarised by a stress-strain curve. The engineering tension test is widely used to provide information on the strength of materials and as an acceptance test for the specification of materials. The yield strength and the UTS of the two metallic samples were measured. Two armour plates; mild steel and 1318b aluminium alloy were considered to be similar to those in use in commercial LAVs in terms of mechanical properties. The 1318b blocks were aligned with the short transverse direction of the roll in line with the axis of the penetration. Comparisons were made in the long transverse and longitudinal direction.

Tensile tests were performed using an Instron 4206 tensile testing machine connected to a computer which, using Instron software recorded the tensile strength data. *Figure 3.2* displays the Houndsfield tensometer tensile test piece. The length of the cylindrical test piece on which elongation was measured was 70.86 mm (*Lo*), before application of the force. The final gauge length after rupture of the test piece is *Lu*. The elongation is expressed as the percentage increase in length over the original gauge length at the end of the test. Four samples were measured from each block. Tests were performed under controlled conditions; at a cross head speed of 2.00 mm/min, sample rate 10 pts/sec, temperature 25 ^{o}C, relative humidity 50% and the grip separation was 60 mm.

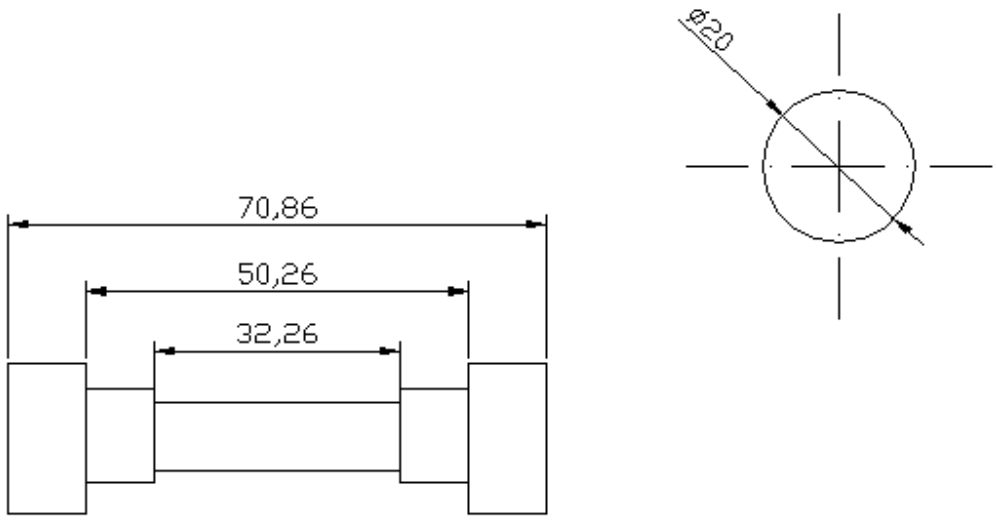

Cross-sectional area 64.60 mm^2

Figure 3.2: Houndsfield tensometer round tensile test sample dimensions, tolerance ± 0.10 mm 70.86 mm (*Lo*)

For each ballistic experiment the witness block samples were made up of 100 x 100 x 100 mm blocks. The critical surfaces were polished and lapped flat to assist bonding to the front ceramic plate.

3.3.7 Interlayer Coupling: Tungsten Paste

The synergistic effects of combining hard brittle targets with the properties of a ductile metallic backing plate are well known (*Section 2.3.2, pp. 41*). However, the joints between the target layers represent a potential weak spot. Therefore, tungsten 25-micron powder mixed with lithium molybdenum grease (from B & Q), 0.5 mm thick was applied between the mating surfaces of the ceramic front plate and the witness blocks. This was used to achieve a good bonding surface between the ceramic tile and the witness block interface and to conform to any small irregularities and avoid large air inclusions. For future work it is recommended to use some form of adhesive with a low acoustic impedance (examples found in *Section 2.4.2, pp. 53*). However, within this investigation the work is comparative and bearing in mind the practical difficulties

of using adhesives (processing time and non-uniformity), it was felt unnecessary to introduce an adhesive into the armour system.

3.4 Experimental Measurements

3.4.1 Velocity Measurement

The impact velocity was recorded using a pair of photoelectric detectors spaced four metres apart and positioned two metres from the target. The mean impact velocity for the 7.62 x 51 mm FFV was 962 m/s ± 13 m/s. Initial experiments showed a mean impact for the BS41 in the region of 1100 m/s ± 30 m/s. This was in disagreement with the impact velocity of the BS41 trials performed by dstl. In order to judge the accuracy of these results three rounds were test fired on an outdoor range allowing free flight. A Doppler radar system was used to calculate the muzzle and free flight velocity. The muzzle velocities recorded were 1016, 1016 and 1015 m/s. The mean impact velocity for the BS41, generated with factory-loaded propellant, was 1016 m/s with experimental error of ± 10 m/s. The initial spurious results were disregarded and the mean velocity was taken as 1016 m/s ± 10 m/s.

All subsequent trials used break foils to measure the projectile velocity. The Doppler radar system and foils have the advantage of being unaffected by the projectile's incendiary and muzzle flash unlike the range photoelectric detectors.

During flash X-radiography experiments carried out at QinetiQ, Fort Halstead, two 150 keV X-ray heads, 500 mm apart and one metre from the target face, were used to measure the impact velocity.

3.4.2 Yaw Angle

Measurement of yaw angle *versus* penetration depth would have been desirable. This would have necessitated the firing of a substantial number of projectiles. Since the supply of ammunition was limited, yaw angle measurements were not undertaken in this investigation.

3.4.3 Experimental Confinement

Practical experimentation is often compromised by physical limitations of the equipment used. An experimental test jig was developed in order to carry out controlled ballistic experiments using each of the designed target systems.

3.4.3.1 Lateral Confinement Rig

It is well documented that the failure mechanisms during penetration of the projectile can be affected by the rigidity and inertia of the armour module introduced by the confinement and design of the backing layer. As presented in *Chapter 2*, confined ceramics have been found to perform extremely well under ballistic impact. Therefore, in order to perform experimental analysis of the 14.5 mm impacting various target systems a confinement rig was used. *Figure 3.3* shows the lateral confinement rig developed for the model scale tests, based on a design presented in Sherman *et al.* [177,96]. Detailed drawings can be found in *Appendix 3*. In order to judge the relative merits of Sherman's confinement rig, particular attention was paid to the ability of the experimental rig to cope with difficulties presented by preliminary trial experiments carried out using the 7.62 x 51 mm FFV AP round. After which, ease of use was considered before redesigning a rig to cater for the larger 14.5 mm BS41.

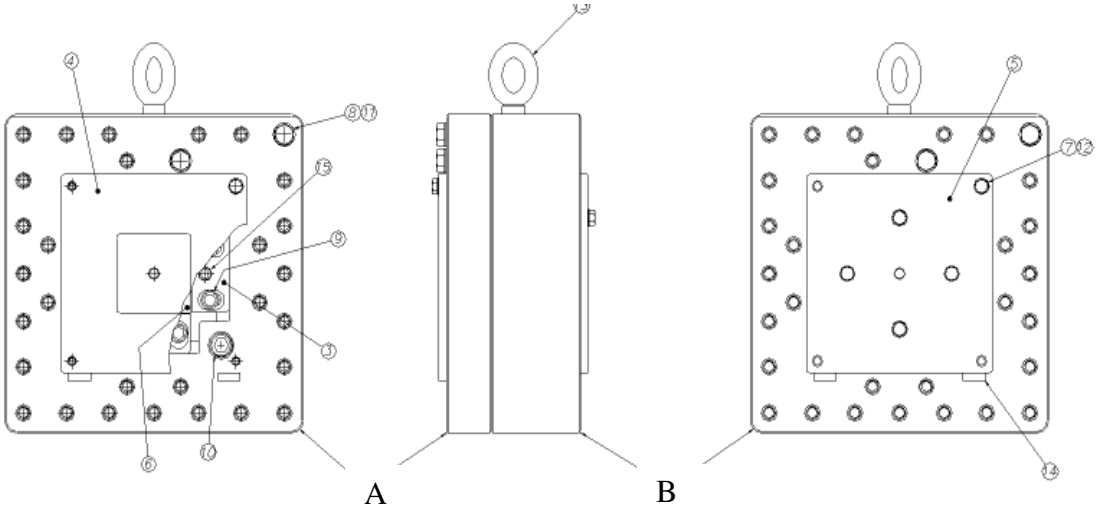

Figure 3.3: Modified Lateral Confinement Rig used for the experimental testing of the BS41; A = front steel block section and B = the back steel block section.

The rig was designed to enable ballistic tests to be performed firing the 14.5 mm BS41 into a number of semi-infinite target systems. The confinement rig was made up of two steel block sections, front block A and a lower block B as presented in *Figure 3.3*. Four wedges were positioned centrally to provide lateral containment to the ceramic front plate.

The original rig design was made up of eight mild steel pieces held together with dowling pins. The rig was redesigned using two pieces of mild steel EN24 making up block A and B respectively. This stiffer support with better dimensional stability to prevent the creeping of the blocks was achieved. This increased the overall strength of the structure. Multiple high tensile M16 and M20 bolts held the two blocks together. A good fit between each of the blocks was achieved by careful machining and polishing. A high hardness front plate was positioned on the front surface of block A to protect the rig from damage. A further back plate was positioned at the rear of block B to provide support to the rear of the target witness block. A modular design was used so that parts of the jig could be replaced when they became damaged or worn. *Figure 3.4* below summarises the experimental set up.

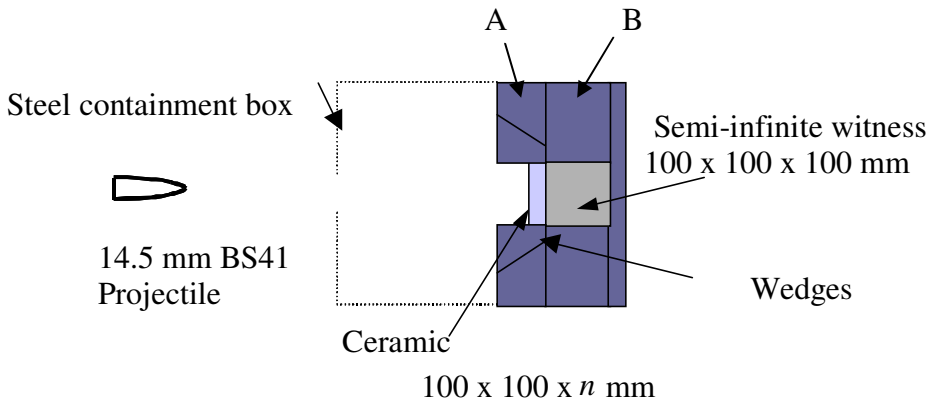

Figure 3.4: Schematic Diagram of the experimental set up. A = front steel block section and B = the back steel block section

The wedges that supported the ceramic front plate in position were designed with a 15° angle as employed by the Israeli team [96]. This provided a large clamping load on the tile with moderate stresses on each of the wedge bolts. A calibrated torque wrench was applied to each of the wedge bolts during each experiment to keep the ceramic confinement consistent. The new confinement rig had extraction bolts in the wedges to assist in their removal in case of difficulties, as presented in initial trials, with comminuted ceramic caught up in the threads. The ceramic was positioned in the centre and front section of the rig with the witness block positioned centrally to the rear.

Initially, the inner wedges bolted to the lower block, responsible for the lateral containment of the ceramic target were made from mild steel. These were extensively damaged during initial firings. Therefore, four vertical high-hardness mechanical wedges were later utilised. These had enough freedom to permit movement, apply a lateral load to the ceramic as well as shielding the inner surface of the wedge from damage.

During impact tensile stress reflected at boundaries propagate into the ceramic causing comminution (*Section 2.3.3. pp. 44*). The resistive load that is offered by the ceramic is released and ceramic fragments that have absorbed the projectiles KE are ejected. After initial 14.5 mm trials it was decided after significant damage was caused to each of the wedges by the ejected ceramic, that brass shims would be incorporated. These were positioned between the ceramic outer surfaces and each wedge respectively. Soft

brass shims supplied by Metal Goods Ltd. were used, size 100 x *n* x 0.9 mm (*n* representing each ceramic tile thickness).

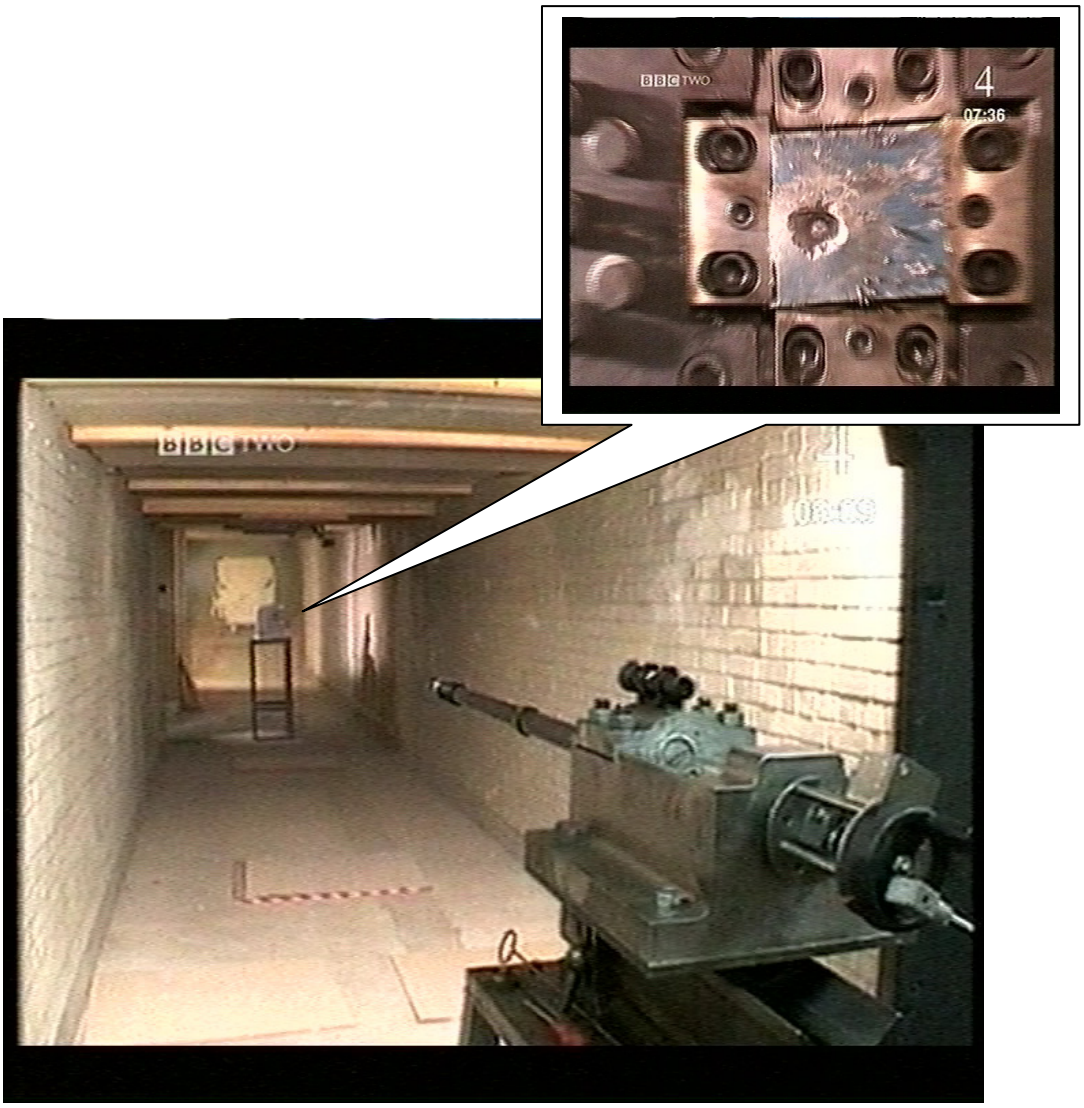

Figure 3.5: Experimental set-up at Royal Military College of Science, Shrivenham [178].

Firings were conducted at the SA range Shrivenham (*Figure 3.5*), and at Fort Halstead. The rig was positioned on a test fixture axially aligned with the direction of shot 10 metres down range. A recessed angled-steel frame was used to secure the rig in position ready for the firing. The targets were mounted in the central position of the rig. The ceramic target systems were firmly clamped in by wedges with bolts tightened to 65 Nm torque. All tests were carried out at normal impact angle, *i.e.,* zero obliquity. An inclinometer was used to check accuracy for target assemblies to within ± 10 MoA (Minute of Angle) and the final obliquity of the target was recorded.

The impact of a ceramic target by a 14.5 mm projectile results in ejection of both comminuted ceramic and WC-Co fragments which are required for analysis, away from the target. A steel containment box with a central hole to allow the projectile to pass through was positioned over the face of the jig to collect all the ceramic and projectile debris. The projectile core captured was magnetically separated and weighed. The ceramic and penetrator fragments were sieved through eight progressively finer wire sieves using British Standard 410 Endecotts Laboratory Test Sieves with the following dimensions: 10.00, 5.00, 3.35, 2.36, 1.18, 0.6, 0.425 and 0.30 mm. Separating the fragments in each sieve according to size, and weighing the fragment mass provided the degree of fragmentation. This permitted the WC-Co and ceramic fragment mass distribution and fracture morphology to be analysed.

3.4.3.2 Bespoke Target Frame

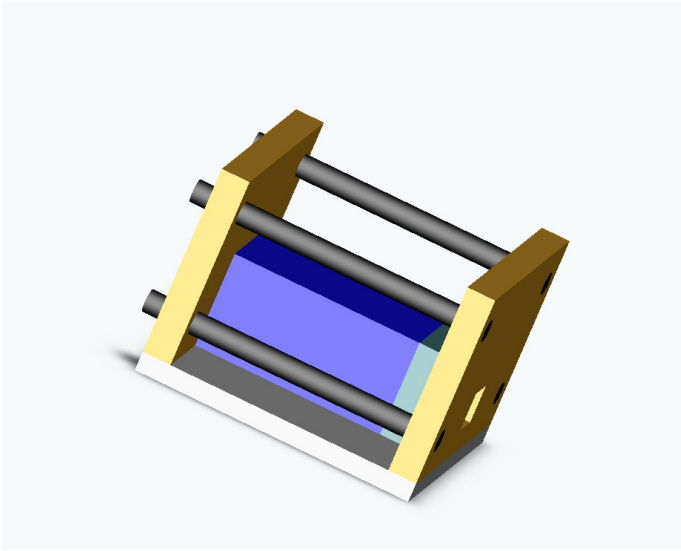

Figure 3.6: Bespoke target frame. Full details may be found in *Appendix 3*.

Having designed a rig that could provide lateral and potentially full confinement a second bespoke target frame was developed with partial confinement in order to carry out X-ray studies for numerical analysis (*Figure 3.6*). A schematic diagram may be found in *Appendix 3*. The rig was based on a simple target frame commonly used in ballistic trials. Emphasis was placed on the ability to perform X-radiography on any part of the armour target system. This was important due to the limitation in material thickness penetrated by the flash X-rays (*Section 3.5.2*). The lateral confinement rig was too thick for the 150 keV and 300 keV flash X-ray heads to X-ray each target.

3.5 Experimental Aids

3.5.1 High Speed Camera

The impact speed of the BS41 lies in the range of 1016 m/s ±10 m/s (*Section 3.3.1*). To obtain information on the penetration process is challenging. Acquiring accurate information is necessary if numerical modelling of such events is to represent reality. A number of experimental aids exist to provide visual information on the penetration process. High-speed cameras can be used to obtain data on transparent materials but most ceramics and metals of armour interest are opaque to light. Even if transparent materials are of interest, optical photography alone may not provide all the information required for numerical modelling and analysis. As most transparent objects are impacted the localised zone can become opaque due to failure processes obliterating the view of the impactor.

Initial trials were carried out using the Cordin Image conversion high-speed camera using four separate cameras to capture images within image intervals of down to 40 nanoseconds to obtain information on the fragmentation of the 7.62 mm FFV WC-Co core round. Alteration of the target set-up was necessary to contain the ceramic cloud. Variations included metallic spall plates and tape. The results allowed visualisation of the WC-Co core in flight after impact through a simple target system. The target was mounted on the test fixture supported by brackets so that the optical axis of the camera was orthogonal to the plane of the test target. Timing on the film allowed the film speeds to be accurately determined. Illumination of the target was provided by a stand-alone light source.

After positioning the test target in the desired area of the field of view of the camera and adjusting the target angle as required, the camera was focused using the automatic focusing system. The firing was synchronised with the running of the cameras such that when the projectile arrived at the target the camera was triggered to take photos at predetermined times. After making exposures as desired, the images were transferred to a PC and were stored in a Tagged Image File Format, a compressed image format.

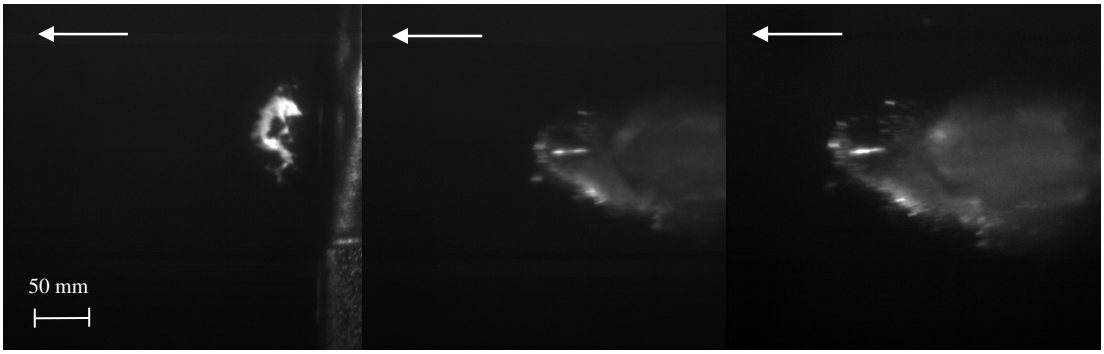

Figure 3.7: 7.62 x 51 mm FFV during three stages of flight, left to right, surrounded by Sintox-CL Al_2O_3 ceramic debris. Arrows represent the flight direction.

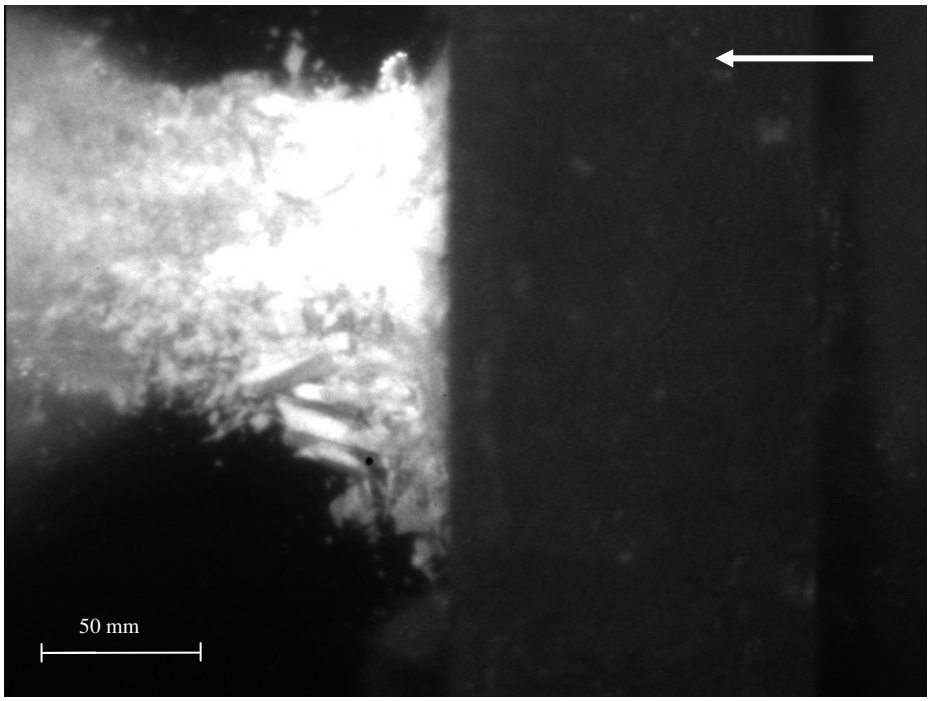

Figure 3.8: 11.07 mm Sintox-CL Al_2O_3 plate impacted by the FFV 7.62 x 51 mm WC-Co cored projectile. Arrows represent the flight direction.

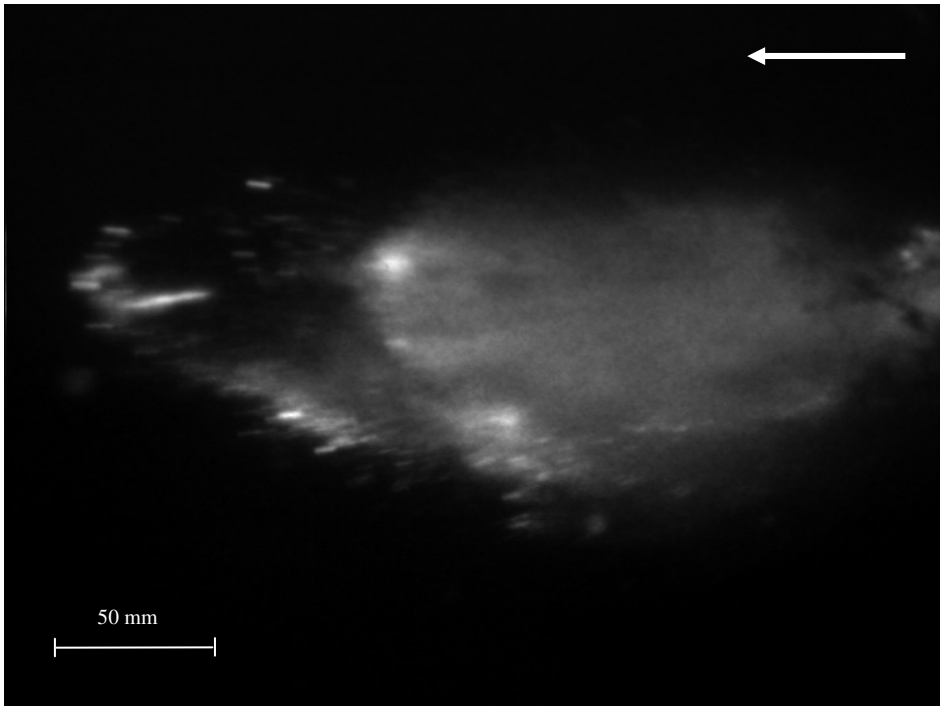

Figure 3.9: Displays 11.07 mm Sintox-CL Al_2O_3, FFV 7.62 mm WC-Co cored Projectile 200 µs after impact. Arrows represent the flight direction.

It may be seen in *Figures 3.7* to *Figure 3.9* that the high-speed camera technique presents a good visual aid of transport of material through flight. A further advantage to the technique was the quantity of firings that may be performed in a given time span. The disadvantage was problems arose with ceramic and target debris obscuring the view of the FFV core (*Figure 3.8* and *Figure 3.9*). After careful considerations to the results it is only the physical limitations of the production of the photographs by high-speed camera that leads us to consider using flash X-ray. Conversely, the flash X-ray technique may expose the image so as to see in detail crack propagation in the WC-Co during and after penetration through ceramic. The flash X-ray system was chosen to determine crack formation and fragmentation of the BS41 WC-Co.

3.5.2 Flash X-radiography

An alternative to high-speed camera is to use flash X-radiography in a similar manner to above. X-radiography can be used to obtain visual analysis of core fragmentation without being obscured by target debris. A major disadvantage to the technique is the

cost and the limitation of firings in a given period. Another limitation is the thickness of ceramic that may be penetrated by the X-rays, depending on the X-ray heads utilised. This necessitates small targets, because generally the X-rays may not penetrate more than 50 mm of ceramic. Taking into consideration the limitations of the technique an experimental configuration for investigating the fragmentation properties of the BS41 was set up.

The trial analysed the fragmentation of the BS41 when impacted upon SiC B and Sintox-CL ceramic targets followed by an air gap and backed with an aluminium alloy witness block. To avoid problems associated with the limits of penetration of the X-rays through the 100 mm of dense ceramic (*Figure 3.10*), the target system was constructed with an air gap. This allowed for X-rays to be performed on the WC-Co core directly after emerging from the ceramic front plate. Whilst the author advocates the above controlled approach to determine WC-Co fragmentation during the initial stages of the penetration through the ceramic, it was not possible in this case due to the limitations of resources.

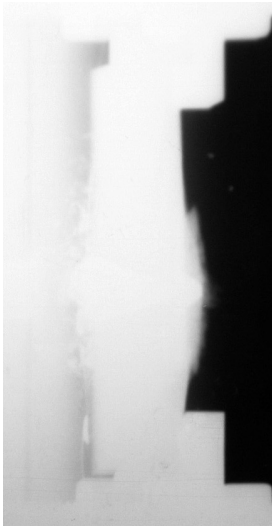

Figure 3.10: Flash X-ray shadowgraph of the BS41 penetrating 25 mm Sintox-CL ceramic front plate. It was not possible to view the WC-Co core during the penetration due to limitations of the X-ray heads.

The flash X-ray trials were conducted at QinetiQ, Fort Halstead facility X44. All targets were supported on a flat table by a bespoke target frame (*Section 3.4.3.2).* X-ray shadowgraphs were obtained using 150 keV and 300 keV flash X-ray heads. The heads were placed 1000 mm from the line of target debris and provided orthogonal shadowgraphs of the fragment debris. Approximate delay times were calculated from

the predicted impact velocity and a foil on the surface of the target independently triggered the X-ray tubes. The X-ray film cassette was stationed about 60 mm from the centreline of debris trajectory. Calculation of the residual velocity of the WC-Co core after penetration of the ceramic front plate was determined from radiographs of each test.

3.6 Fracture Morphology Analysis

"Microstructure is the link between the science and technology of materials"[181]

At the heart of understanding the factors that influence penetrator performance, and the tests and properties that measure these factors, are microstructural investigations. These can systematically guide development of future armour and analysis of the penetration phenomena. Quantitative metallographic investigations have proven particularly useful in the investigation of harder tungsten alloys in projectile design [179,180]. It was not until 1887 when Sorby first revealed grain morphology by chemically etching polished samples. Since then, technology has moved on and measurement of the chemical distribution and crystal phase and crystal orientation have been made possible [181]. The first Scanning Electron Microscope (SEM) became commercially available in 1965. It provides a good tool for analysing microstructures providing magnification in the range of 2 to 100000 times and a greater depth of field compared to the conventional optical microscope [107].

In this present study the Jeol JSM-T330A SEM incorporating Energy Dispersive X-ray (EDX) analysis was used to investigate the WC-Co failure after impact into ceramic targets. The SEM can provide detailed images of the fracture surfaces of the failed WC-Co whilst the EDX may be used to gain details on the composition of the sample. In this technique the energy of X-rays generated from the sample surface is measured and related to its elemental content. The limitations of such a technique is that it is unable to provide a detailed analysis of the carbon content. An alternate technique would be the Rutherford backscattering technique (RBS) which may resolve adequately the carbon peaks [107].

Ceramic samples typically have high electrical resistance and, in the absence of a conductive coating can quickly acquire charge. This charge in turn can cause an electrical potential that is large enough to cause a dielectric breakdown in some regions of the sample and variations in the surface potential. This can result in astigmatism, image instabilities, disproportionate brightness and erroneous x-ray signals, obscuring the images and making it difficult to perform analysis [181]. It is desirable to use a conductive coating that has a low atomic number or that can be effective as a very thin layer. Carbon has a very low atomic number and can be deposited as a continuous amorphous film.

When the beam of the electron microscope is directed on to a sample material, different scattering events give rise to a variety of signals. In most conventional metallographic images, contrast is produced by differences in orientation. For example, topological contrast can be formed by etching a sample with an etchant that attacks grains of different orientation at different rates. Grain boundaries can also be distinguished by applying an etchant.

Since the SEM and EDX have been shown to be valuable tools in examining mictrostructural samples, this equipment examined fractured WC-Co surfaces after dynamic impact.

3.6.1 Preparation Details

The WC-Co core was cut using spark eroding, enabling samples of acceptable sizes to be produced. The spark eroder cuts slowly under low temperatures, which helps minimise any damage to the material. The longitudinal wave velocity of the sample was measured using the Portable Ultrasonic Non-Destructive Digital Indicating Tester (PUNDIT) Longitudinal Wave Velocity machine. The device has a generator with an amplitude of 500 V. It generates and receives ultrasonic waves. A receiving probe is positioned at the opposite end of the specimen. The PUNDIT measures the time of transmission of the ultrasound waves from the transmitting head to the receiving head. Knowing the length of the specimen the longitudinal wave velocity can be calculated (distance between transducers / time). Both transducers are held against the surface of

the sample using a coupling agent, vaseline, to ensure a good pulse transmittance. The apparatus was calibrated using a known sample before a minimum of five readings was taken for each sample.

The sample specimens were mounted and polished ready for the microstructural and elemental analysis. Special attention was given to the WC-Co surface preparation prior to coating. If the surface layers are not free from debris the coating becomes more of an obstacle to obtaining a good image. Therefore polishing and removal techniques in the centrifuge were performed before sample analysis. Details are given below:

- The core specimen was mounted in conducting Bakelite in a Buehler Metaserv mounting press for approximately 10 mins.
- The specimen was then polished to 1.00 µm using Met. Prep. Metallographic Material of varying grits. Silicon carbide grinding paper was used for wet grinding.
- The polishing schedule was as follows:
    - 6 min. grit p60
    - SiC grit p180 (as long as deemed necessary)
    - SiC grit p320 (as long as deemed necessary)
    - SiC grit p600 (as long as deemed necessary)
    - SiC grit p1200 (as long as deemed necessary)
    - 2 min. on 6 µm grit
    - 1 min. on 1 µm grit
    - 1 min. using master-polish suspension
- The final material preparation involved etching. The WC-Co was etched in a mixture of 2 g of Sodium Hydroxide, 100 ml of H_2O and 15 g of Potassium Ferrite Cyanide solution. The sample was placed in the etching solution for a short period of time until the grain structure became prominent. The core was then removed and washed ready for the microstructural analysis.

3.7 Experimental Methodology Summary

To implement all contemporary methods of ballistic measurement methods within this body of work would present a significant challenge; therefore specific techniques were selected representing various degrees of complexity. The DoP test was chosen as representing the simplest and most effective method of evaluating ballistic performance with limited materials. The traditional Differential Efficiency Factor was used to calculate and compare the ballistic performance from the experimental results.

The main effort was on the study of the 14.5 mm WC-Co core BS41 projectile provided by dstl into a limited number of ceramics and target systems. The 7.62 mm WC-Co core FFV projectile was used for initial firings to re-design the confinement rig to cater for the BS41. Each experiment was either unconfined using a bespoke target frame to support the target system or confined using the modular test jig. Two grades of Al_2O_3 (Sintox-FA and Sintox-CL) and two grades of SiC (SiC B and SiC PS 5000) were used in the trials backed by either 1318b aluminium alloy or mild steel witness blocks.

Other experimental methods were also employed to assist in the final analysis. These included Flash X-ray and microstructural analysis using the SEM and EDX. After each experiment blocks were X-rayed which allowed the residual penetration to be accurately measured. Furthermore the level of fragmentation of the core and the penetrator crater was assessed from each X-ray. A summary of experimental results is presented in *Chapter 4* and *5*.

Chapter 4

Experimental Analysis and Discussion

Experimental results are presented from a model scale investigation of the parameters of a ceramic-faced armour system that are required to induce damage in a Tungsten Carbide – Cobalt (WC-Co) penetrator. *Section 4.1* introduces the effects of witness block constraint on WC-Co projectile defeat. *Section 4.2* presents the effects of altering ceramic armour appliqué systems on ballistic performance. Conclusions are drawn on the nature of failure of the projectile core, Depth of Penetration (DoP) and the ballistic damage mechanisms in ceramic tiles subjected to sub-hydrodynamic impact of the Russian 14.5 mm BS41. Recommendations for an efficient armour system at defeating the BS41 are presented.

4.1 Part 1: Effects of Constraint on Target and Projectile

The performance of the ceramic armour is known to be heavily dependent upon the configuration of the system (*Section 2.3*). The effect of the ceramic boundary constraints introduced by the armour confinement and the witness block on the target and projectile failure, are examined.

Using the experimental arrangement and method described in *Chapter 3* a series of single shot ballistic firings was conducted to evaluate the performance of the BS41 impacting different witness block materials. Armour systems consisting of 1318b aluminium alloy and mild steel witness block are reported. The performance was assessed using the DoP test described (*Section 3.1.2, pp. 70*).

4.1.1 Baseline Witness Block DoP Results

The DoP test is used to calculate a ballistic efficiency for a material. The value calculated depends upon the parameters of the material used as a reference. Rolled Homogeneous Armour, a low alloy steel is used today as the benchmark by which armour and armament performance is judged. Only limited RHA thicknesses were available for trials. Instead, two semi-infinite witness blocks of different yield strengths and hardnesses, used in commercial armour systems, were compared to evaluate the DoP and the WC-Co core failure. The assessment was conducted using both mild steel and 1318b alloy, 100 x 100 x 100 mm witness blocks as described (*Section 3.3.6, pp. 79*). It is suggested that future experiments are performed using a generic UK RHA or High Hardness Steel (HHS) back block to allow consistent use to be made of the DoP results to industry.

The yield strength and the hardness for the two witness blocks were determined using the Instron 4206 tensile testing machine and the Vickers hardness test respectively (*Section 3.3.6 & 3.3.4, pp. 78*). *Table 4-1* summarises the percent elongation, yield strength and UTS for the two witness blocks in the three orientations.

Table 4-1: Instron 4206 tensile test data. (*Note*, spurious results in Italics were removed from the average. These could have been due to sample mixing)

Material	Orientation	Elongation to Failure (%)	Yield Stress (MPa)	Ultimate Tensile Stress (MPa)
1318b Aluminium alloy	Longitudinal	14.63	433	481
		12.00	433	480
		15.65	448	521
		15.10	453	523
	Average	**14.35**	**442**	**501**
	Short transverse	5.89	401	473
		3.16	400	475
		15.00	*448*	*481*
		3.72	478	-
	Average	**4.26**	**426**	**474**
	Long transverse	10.01	453	513
		14.01	449	481
		4.00	*433*	-
		12.99	449	513
	Average	**12.34**	**450**	**502**
Mild Steel	1	35.80	260	441
		36.48	288	445
	Average	**36.14**	**274**	**443**
	2	35.96	268	441
		34.78	260	442
	Average	**35.37**	**264**	**441**
	3	39.55	260	437
		38.81	252	441
	Average	**39.18**	**256**	**439**

1318b aluminium alloy had an average measured yield strength of 426 MPa in the short transverse direction and a Vickers hardness of 159 Hv, whilst the mild steel was found to have a lower yield strength of 264 MPa and a higher hardness of 195 Hv.

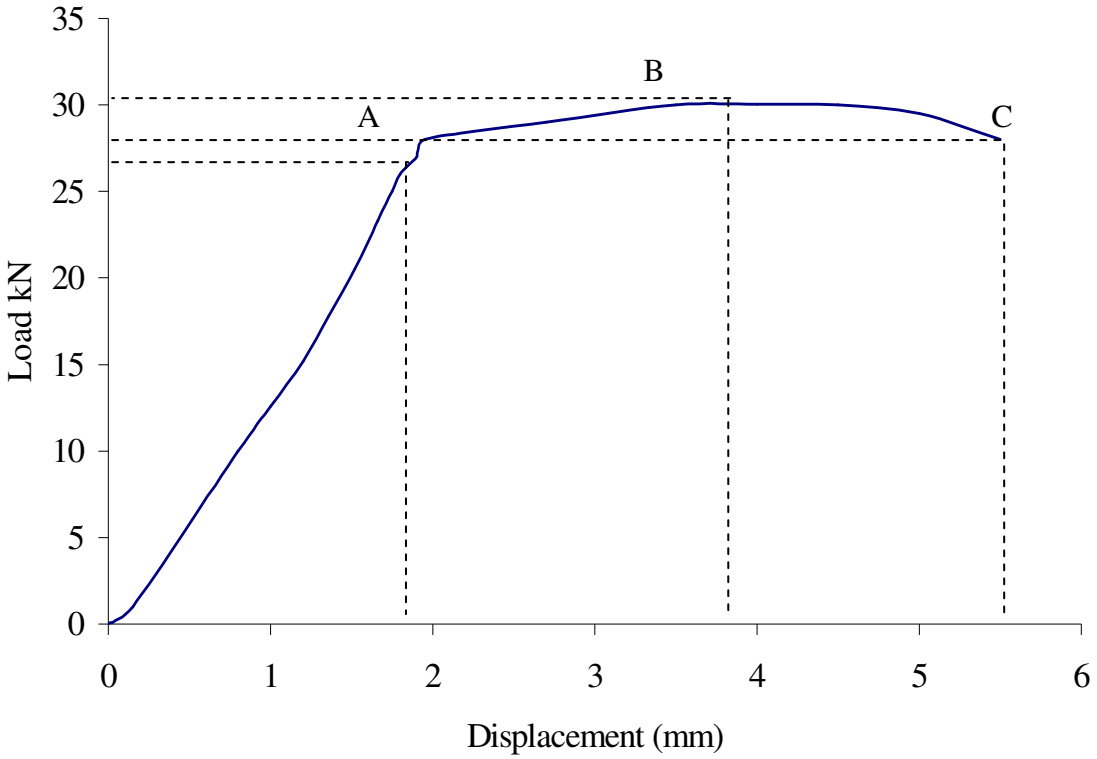

Graph 4-1: Instron 4206 tensile test, loading and unloading curve showing elastic recoverable strain and plastic deformation; 1318b aluminium alloy, short transverse direction of roll, 2 mm/min cross head speed, temperature 25 ^{0}C. Results presented in *Table 4-1*.

Graph 4-1 and *Graph 4-2* show two examples of the measured tensile tests for 1318b and mild steel, respectively. The initial part of each curve represents the elastic region. In the elastic region, stress is linearly proportional to strain (*Section 2.2.4, pp. 33*). When the load exceeds the yield strength of the material (*i.e.,* point A, *Graph 4-1*), the specimen undergoes plastic deformation. The stress to produce continued plastic deformation increases with increasing plastic strain *i.e.* strain hardening. The load continues to rise until a point is reached where the decrease in specimen cross-sectional area is greater than the increase in deformation load arising from strain hardening. Thus, the maximum engineering stress is reached which is known as the UTS (*i.e.,* point B, *Graph 4-1*). As the cross sectional area of the tensile specimen decreases far more rapidly than the deformation load is increased by strain hardening,

the load required to deform the specimen falls off until fracture occurs (*i.e.,* point C, *Graph 4-1*). Although 1318b has a higher yield strength, the mild steel has a similar UTS (*Table 4-1*). 1318b had an average measured UTS of 474 MPa in the short transverse direction and a density of 2965 kg/m^3, whilst the mild steel was found to have an UTS of 441 MPa and a higher density of 7786 kg/m^3.

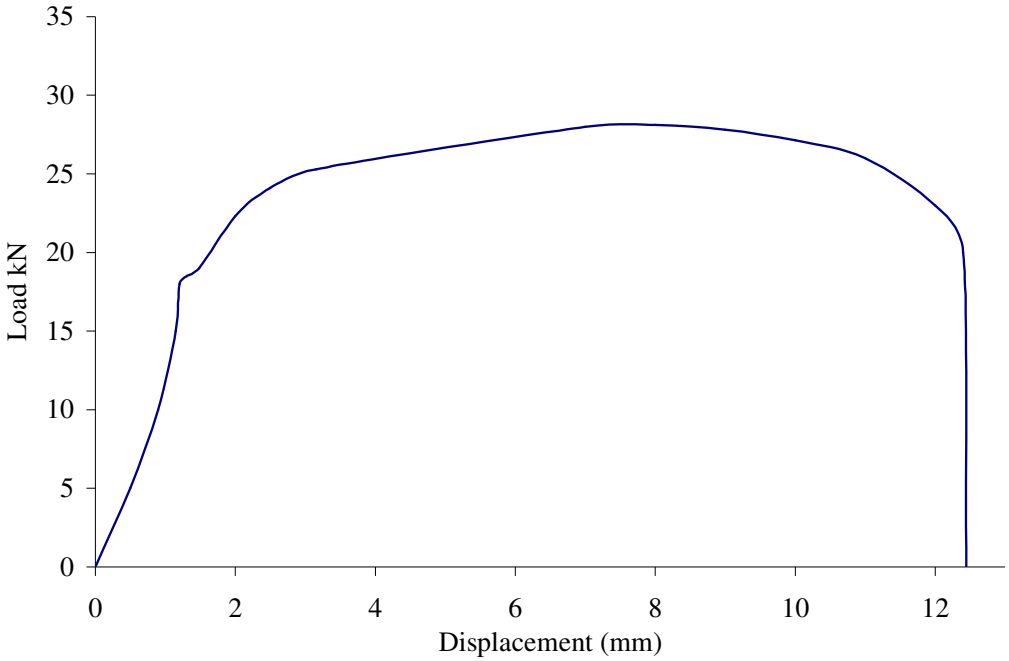

Graph 4-2: Instron 4206 tensile test, loading and unloading curve showing elastic recoverable strain and plastic deformation; Mild steel, orientation 2, 2 mm/min cross head speed, temperature 25 ^{0}C. Results presented in *Table 4-1.*

To allow for the computation of Differential Efficiency e_c, an initial series of shots was conducted to determine the average baseline DoP value in the two types of witness blocks, *without* a ceramic front plate. This provided data for the e_c to be calculated to evaluate the effectiveness of the different ceramic targets in *Section 4.2*. Results are presented in *Table 4-2*.

Initial firings into 1318b witness blocks were carried out unconfined. Later a confinement frame, which was capable of generating high biaxial compressive stress, provided confinement for the ceramic armour system (*Section 3.4.3, pp. 82*). Each plate was subjected to impact by the BS41 projectile travelling at sub-hydrodynamic velocities of approximately 1016 m/s ± 10 m/s.

Table 4-2: BS41 and B32 penetration results against mild steel and BS41 penetration results against 1318b witness blocks

Witness Block	Projectile	Residual DoP (mm)	DoP Areal Density (kg/m^2)	Impact Velocity (m/s)
Mild Steel Confined	BS41	74.69	584.82	1016.00
	B32	67.52	528.68	1002.04
Aluminium Alloy Confined (short transverse)	BS41	103.46 104.63 106.21	279.34 282.50 286.77	1021.78 1016.00 1014.60
Aluminium Alloy Unconfined (short transverse)	BS41	114.46	309.06	1013.27

Table 4-2 shows the DoP and areal density obtained after firing the BS41 into 1318b and mild steel. Results from the softer cored 14.5 mm B32 projectile into mild steel are presented for comparison. The WC-Co cored BS41 projectile was found to outperform the steel cored B32 14.5 mm projectile. Upon confinement the monolithic 1318b witness block was found to perform better than the mild steel at defeating the BS41.

4.1.1.1 WC-Co Fragmentation after Penetrating a Monolithic Armour

Figure 4.1: From left to right: BS41, BS41 unfired core, core retrieved after firing into mild steel and core retrieved after firing into 1318b witness block.

Figure 4.1 compares the WC-Co core after penetrating 286.07 kg/m^2 of 1318b and 584.82 kg/m^2 of mild steel witness block. Standard metallic blocks impart little damage in WC-Co Core projectiles. The projectile core tends to pass in an un-deformed manner; slight surface erosion was noted. Precision non-contact three-dimensional surface profiling was performed. Results revealed that slight surface erosion had occurred despite the relatively higher hardness of the WC-Co core compared to each of the witness materials (*Appendix 4*).

4.1.2 1318b Aluminium Alloy Anisotropic Effects

During the initial witness block tensile analysis different elongation to failure was noted during the tensile tests in different orientations of 1318b witness block (*Table 4-1, pp. 97*). A series of single shot ballistic firings was conducted to investigate the influence of altering the orientation of the roll direction of the 1318b to the line of fire in order to evaluate the effect on BS41 performance. Rolled aluminium alloy has an anisotropic structure unlike mild steel, which is isotropic. The three different planes of the 1318b tested are described in *Figure 4.2*. The impact on 1318b failure was noted.

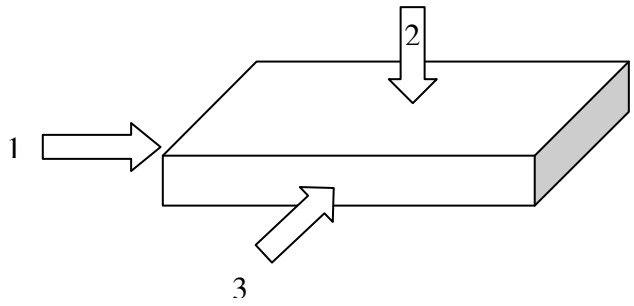

Figure 4.2: Three rolling directions tested for the 1318b aluminium alloy sample, 1 = Longitudinal (roll), 2 = short transverse (minimum dimension) and 3 = long transverse direction.

Table 4-3: Results of BS41 fired into the three different planes of the 1318b aluminium alloy; 1 = Longitudinal (roll), 2 = short transverse and 3 = long transverse. (WB = witness block)

REF	1318b Aluminium alloy WB Split	DoP (mm)	Roll Direction
A4	No	134.26	3
A	Split	113.59	1
B	Split	105.95	1
C	Split	115.34	1
A3	No	110.78	3
F2	No	103.46	2
F1	No	106.21	2
B3	No	104.63	2

Table 4-3 summarises the performance of the BS41 in each witness block roll direction. When the BS41 penetrated the 1318b in the longitudinal direction of roll the 1318b was found to split (*Figure 4.3*).

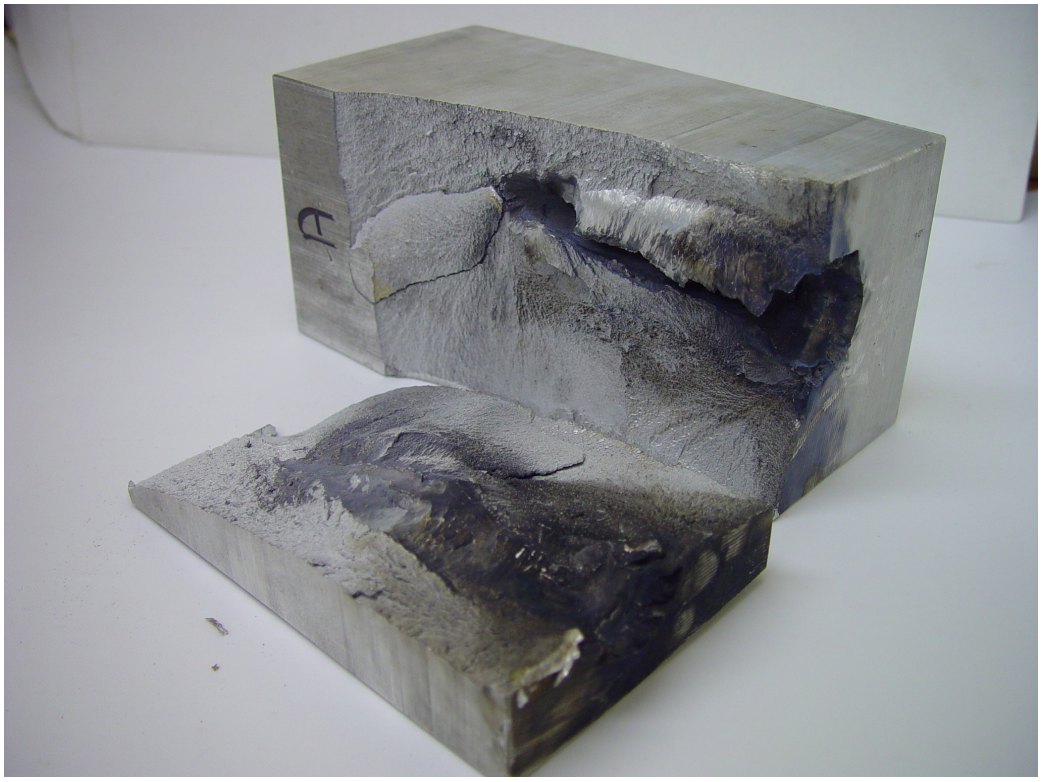

Figure 4.3: 1318b, plane 1 (*Figure 4.2*), after impact from the BS41

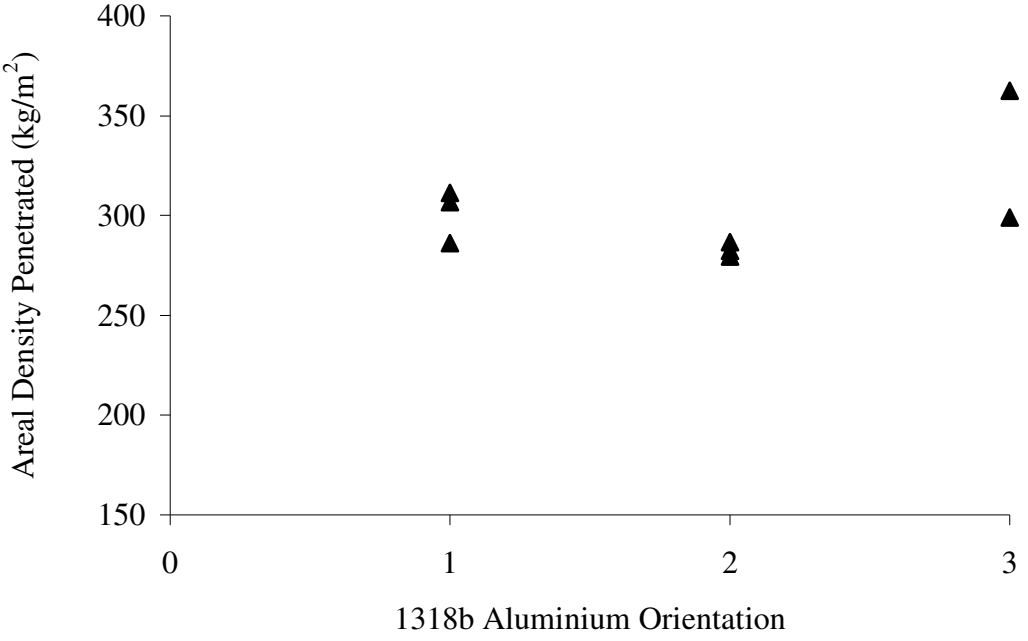

Graph 4-3: Areal density of 1318b penetrated in the three different roll orientations

Graph 4-3 summarises the areal density of 1318b penetrated in the three different roll orientations. It is found that, in the short transverse direction of roll the DoP was the lowest (average of 103.80 mm), whereas in the long transverse direction of roll the DoP was an average of 122.52 mm and in the longitudinal it was found to be 111.63 mm (*Table 4-3*).

The effect of altering the plane of the anisotropic 1318b back-block on DoP was tested and the results were compared. There was no significant difference in DoP but blocks orientated with plane 1, split after being fired at (*Figure 4.3*). This could account for the slight increase in spread of DoP observed in the long transverse and the longitudinal roll direction.

4.1.3 Comparison of Mild Steel and 1318b Aluminium Alloy Witness Block, both with a Sintox-CL Front Plate

A third set of trials was conducted to determine the performance of the BS41 into various thicknesses of confined Morgan Matroc Sintox-CL Al_2O_3 front plate (37 - 97

kg/m^2) using mild steel or 1318b witness blocks. To allow for comparison, 100 x 100 x 100 mm blocks were used of both materials. All the tests as described in *Chapter 3* were carried out at zero obliquity. Once completed the respective areal densities were determined and compared.

In order to judge the merits of Sherman's confinement rig, preliminary trials were carried out firing the 7.62 mm FFV into Sintox-FA Al_2O_3 coupled to a 1318b witness block. During impact of the ceramic target, ejection of comminuted ceramic caused surface damage to the confinement wedges. Therefore, sacrificial 1.0 mm thick brass shims, fully annealed, were always placed around the ceramic front plate to protect the rig wedges. The shim has an acoustic impedance of 27.2 x 10^6 kgs/m^{2}s compared to steel (39.5 x 10^6 kgs/m^{2}s), Al_2O_3 (37.8 x 10^6 kgs/m^{2}s) and SiC (36.3 x 10^6 kgs/m^{2}s). The ductility of the shim enables it to conform to any small irregularities in the mating surfaces, providing an excellent acoustic interface.

Table 4-4 summarises the performance of each witness block against various thicknesses of Sintox-CL front plate.

Table 4-4: Penetration results obtained by altering witness block and Sintox-CL front plate areal density

Target Front Plate	**Plate Thickness (mm)**	**Ceramic Areal Density (kg/m^2)**	**Aluminium Alloy Witness Block Penetrated**		**Mild Steel Witness Block Penetrated**	
			DoP (mm)	**Total Areal Density (kg/m^2)**	**DoP (mm)**	**Total Areal Density (kg/m^2)**
Al_2O_3 Sintox-CL	18	70	59.26	230	40.79	389
			56.21	222	42.10	400
	15	58	60.13	221	43.60	400
			62.32	227	47.00	426
	12	46.5	62.08	211	51.54	450
			61.60	209	53.00	461

Graph 4-4 summarises the results from the performance of the two different witness blocks. The areal densities of the witness block penetrated versus the corresponding ceramic front plate are plotted. To evaluate the critical thickness required to stop the BS41, linear lines of regression were fitted to the data from the various thicknesses of ceramic. Straight lines were plotted in a similar approach as Rozenberg *et al.* where experimental results have been demonstrated to fall on straight lines [93]. Extrapolating the lines of regression to the point where no witness block was penetrated derived the critical thickness. Results are reported in *Table 4-5*. The experimental points for the two different witness blocks with Sintox-CL only showed relatively small scatter.

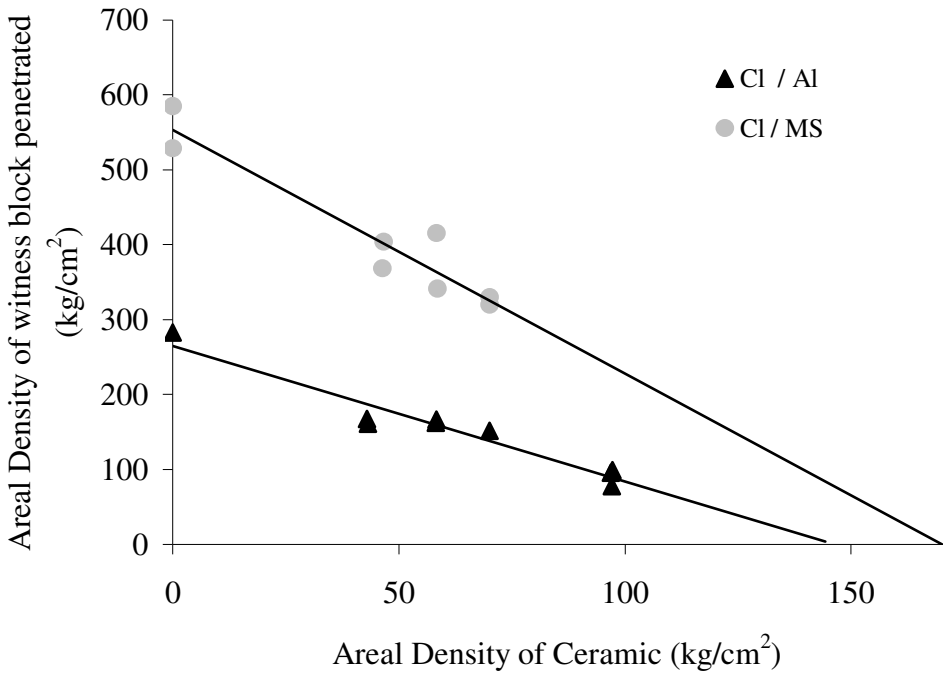

Graph 4-4: Ceramic areal density of three different thicknesses plotted against areal density of witness block penetrated.

Table 4-5: Critical Thicknesses of Ceramic (*Graph 4-4*)

Ceramic Target System	Critical Thickness (mm)
Sintox-CL / Aluminium	37.8
Sintox-CL / Mild Steel	43.2

It can be observed in *Graph 4-4* and *Table 4-5* that the critical thickness of Sintox-CL depends on witness block material. It is found that the critical thickness is reduced when 1318b is used compared to mild steel. When an 18 mm Sintox-CL front plate (70 kg/m^2) with a mild steel witness block is used, there is a 29% reduction in DoP and 74% increase in areal density penetrated, compared to the 1318b. When a mild steel semi-infinite block *without* a ceramic front plate is penetrated there is 107% increase in areal density penetrated compared to 1318b (*Table 4-2, pp. 100)*.

During penetration into the 1318b with a Sintox-CL front plate the penetrator was found to fracture into a larger number of large fragments at the rear of the core compared to penetration into mild steel. It was also found to split into two characteristic spall fragments, front tip and mid section. This is presented in *Chapter 5* in more detail. The most probable explanation of this is the lower acoustic impedance of the 1318b than that of mild steel and Al_2O_3. In the case of an incident wave reflected at the Al_2O_3 and 1318b interface, we would expect a tensile wave whereas for mild steel we would expect a compressive wave (*Section 2.3.3*).

4.2 Part 2: Effects of Altering Confined Ceramic Armour Configuration

The advantage of using a ceramic front plate is that it is good at both eroding and fragmenting the oncoming AP threat, spatially spreading the impact energy into a backing layer. Problems arise because the WC-Co cored ammunition's hardness is higher than that of Sintox-CL and Sintox-FA Al_2O_3 and therefore the latter offers little resistance to penetration. Thus, the characterisation of WC-Co fragment formation and DoP during and after the penetration of different ceramic targets enhances our understanding of a ceramic's ability to stop the projectile.

The mechanisms by which the confined ceramic-faced armour configurations defeat the BS41 were sought by performing impact experiments and examining the fracture morphology and deformation in the recovered targets and fractured cores. Effects were compared at a range of different impact velocities. The DoP technique was implemented and the ballistic performance of each system was compared with the performance of a monolithic armour using the Differential Efficiency equation (*Section 4.1.1*). Both elemental (EDX) and microstructural (SEM) analysis are presented.

4.2.1 Change in Ceramic Strike Face

The objective of the tests was to measure the performance of different ceramics available (ranging from 37 to 98 kg/m^2) with a 1318b witness block. After initial trials (*Section 4.1.2*) the 1318b was used in the short transverse direction of roll as it proved to be more efficient than mild steel. Each target was mounted in the experimental test jig (*Section 3.4.3, pp. 82*).

A general rule used by armour designers is to employ a ceramic front plate 2/3 of the mass, whilst the backing should be 1/3 of the total mass [182]. Whilst this relationship gives a good initial estimate for the optimum configuration, the Florence equation described in *Section 2.3.1* provides a good guide to the start of the experimental research.

Two grades of Al_2O_3 were used: Sintox-FA (95% purity) and Sintox-CL (98.6% purity) and two grades of SiC; AM & T PS 5000 SiC and Cercom SiC B were analysed (*Section 3.3.3*).

4.2.2 Ceramic Front-Plate Ballistic Performance

The Florence theoretical model was used to determine the likely ceramic thickness required to defeat the BS41 in order to set the range of tile thicknesses used in the DoP tests. Data were collated from experimental results for the BS41 (*Appendix 1*). These were used for the prediction of tile thickness using the Florence theoretical model (*Section 2.3.1, pp. 38*) [61,62].

A number of constants were substituted into the Florence equation (*pp. 38, Eq. 2-4 & Eq. 2-5*): the projectile core (WC-Co) had a mass of 38.72 g, diameter 10.8 mm, impact velocity of 976 m/s, and the target was ceramic with an aluminium alloy witness block. P_1 (density of front plate) (Al_2O_3) taken as 3694 kg/m^3, P_2 (density of backing plate) taken as 2700 kg/m^3, UTS of backing plate of 4.74 x 10^8 Nm^{-2} and a ε_c breaking strain = 16% (0.16). The focus of the investigation was to test the ballistic performance of dual-layer composite armour at constant areal density. The BS41 projectile, for which little work has been carried out into the effects of the failure of the WC-Co core, was fired at the targets. At a total areal density of 91.5 kg/m^2 a ratio of Al_2O_3 ceramic to aluminium alloy backing of 2.5:1 is suggested at V_{50} ballistic limit of 1000 m/s. Next, the ballistic performance of each of the ceramics was evaluated. *Table 4-6* summarises the penetration results for each ceramic.

Table 4-6: DoP results for different ceramic front-plates and either 1318b or mild steel witness blocks

Ceramic / Witness Block	Tile Thick-ness (mm)	Areal Density Ceramic (kg/m^2)	Velocity (m/s)	Areal Density of Witness Block Penetrated (kg/m^2)	DoP (mm)
Sintox-CL / 1318b	25.32	97.22	1016	99.14	36.72
	25.27	97.03	1016	77.59	28.74
	25.21	96.81	1016	95.47	35.36
	18.23	70.00	1016	160.00	59.26
	18.26	70.11	1016	151.77	56.21
	15.17	58.25	1016	162.35	60.13
	15.16	58.21	1016	160.81	59.56
	11.23	43.12	1016	167.62	62.08
	11.19	42.97	1016	166.32	61.6
SiC B / 1318 b	18.2	57.86	1031	62.67	23.21
	18.09	57.53	1018	35.69	13.22
	20.07	63.82	1006	51.52	19.08
	20.32	64.61	1016	44.28	16.04
	30.07	95.62	1016	0	0
PS 5000 / 1318 b	18.22	56.48	1016	105.44	39.05
	15.09	46.78	1014	122.63	45.42
	15.26	47.30	1117	180.93	67.01
	12.18	37.75	1018	135.40	50.15
	12.24	37.94	1013	146.85	54.39
	12.03	37.29	1023	134.24	49.72
Sintox-FA / Mild Steel	39.88	147.32	1016	215.33	27.5
	39.69	146.61	1016	200.13	25.56
	34.85	128.74	1016	240.30	30.69
	34.85	128.74	1016	226.91	28.98

Graph 4-5 compares the performance of three of the different ceramic front plates; SiC B, SiC PS 5000 and Sintox-CL with a 1318b witness block. The areal densities of the 1318b witness block penetrated and the corresponding ceramic front plate are plotted. To evaluate the critical thickness required to stop the projectile, linear lines of regression were fitted to the data from the three ceramics. Extrapolating the lines of regression to the point where no witness block was penetrated derived the critical

thickness (*Table 4-7*). Straight lines were plotted in a similar approach as Rozenberg *et al.* [93].

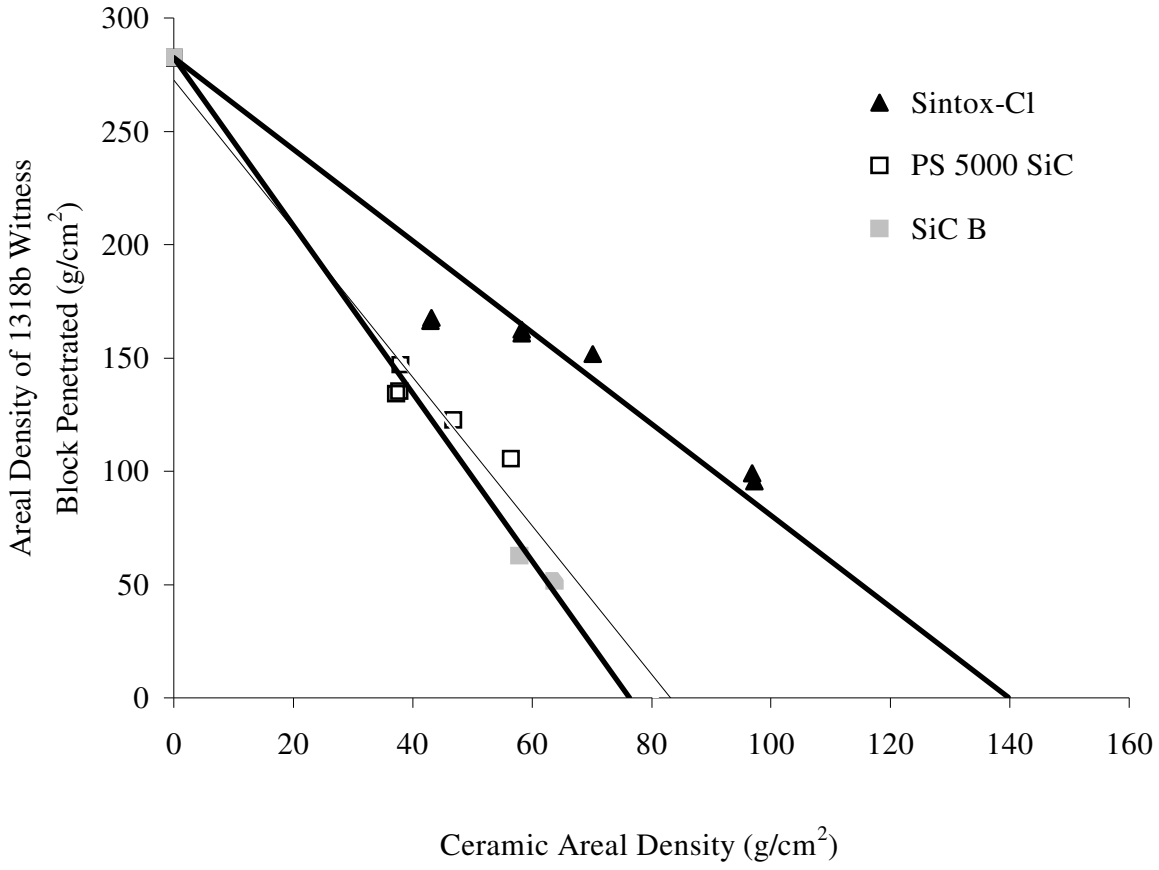

Graph 4-5: Ceramic areal density of three different ceramics plotted against DoP, velocity of impact is kept constant 1016 m/s (± 10 m/s). Refer to *Table 4-2, pp. 100* for 1318b semi-infinite data (short transverse).

Table 4-7: Critical Thicknesses of Ceramic (*Graph 4-5*)

Ceramic	Critical Thickness (mm)
Sintox-CL	37.8
SiC B	24.2
SiC PS 5000	26.5

In comparing the areal density for complete penetration of both SiC B and PS 5000, they consistently out-performed the Sintox-CL. The SiC B and PS 5000 were found to perform similarly despite the PS 5000's higher hardness.

Comparisons were next made between the two Al_2O_3 ceramics with a mild steel witness block. *Graph 4-6* compares the DoP results for Sintox-CL and Sintox-FA into the semi-infinite mild steel. Both hardness and the shear strength of the ceramic are important material properties for the disruption of a projectile. In comparing the areal density for complete penetration of Sintox-CL, it was found to significantly outperform Sintox-FA against the BS41. Therefore, Sintox-CL with a hardness of 1705 Hv was focused on in preference to Sintox-FA (1357 Hv).

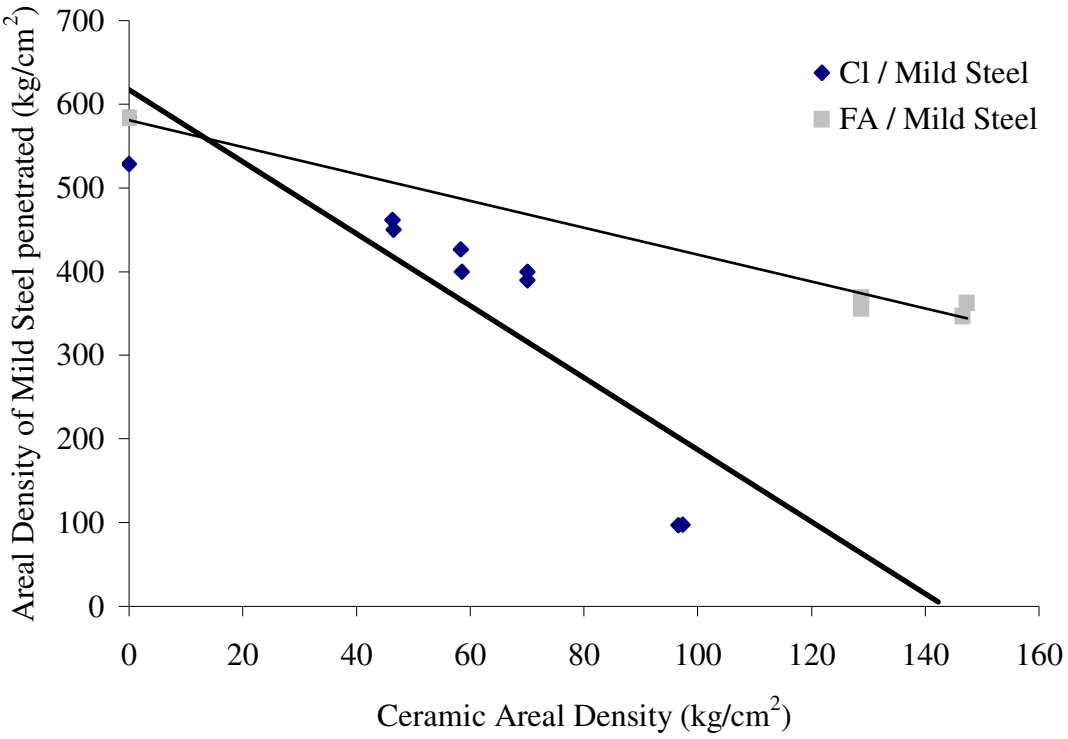

Graph 4-6: Comparing the areal density of mild steel penetrated versus the ceramic areal density of either Sintox-FA or Sintox-CL front plate.

4.2.2.1 WC-Co Fragmentation after Penetrating a Ceramic Applique System

Ceramics are prime candidates at eroding or fragmenting AP projectiles, spatially spreading the impact energy thus decreasing the local pressure on the absorber (*Section 2.3*). When the witness block is protected with a ceramic front plate, the WC-Co failure was dramatically altered compared to firing into monolithic armour (*Figure 4.1, pp. 100*). This was evident from analysis of the WC-Co core fragments retrieved, displayed in *Figure 4.4*.

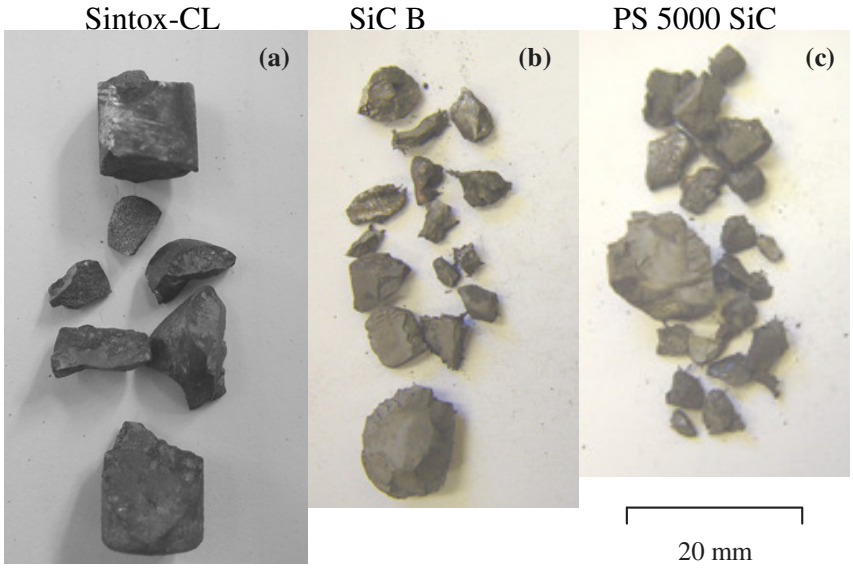

Figure 4.4: WC-Co fragmentation pictures: (a) 58 kg/m^2 Sintox-CL (88%) (b) 58 kg/m^2 SiC B (29%) (c) 58 kg/m^2 SiC PS 5000 (34%). (% Total mass recovered)

Figure 4.4 compares the WC-Co core fragmentation after penetrating 58 kg/m^2 of Sintox-CL (1705 Hv), PS 5000 SiC (2644 Hv) or SiC B (1969 Hv), and a 1318b witness block. Both Sintox-CL Al_2O_3 and the two SiC targets caused fracture across the diameter of the BS41 core. Evaluating the WC-Co recovered from firing into SiC saw a distinct increase in number and greater fragmentation of the core compared to Al_2O_3. The higher level of fragmentation with SiC is because its greater strength and hardness induce a greater shock in the WC-Co core penetrator. Pickup *et al,* presented similar observations after analysis of steel cored projectiles into target materials of different deviatoric strengths [183].

Another interesting aspect that can be noted was the reduced WC-Co core fracture after impact into Sintox-CL with a mild steel witness block compared to that of the 1318b witness block. Similar reduced WC-Co fragmentation was observed after the BS41 penetrated a Sintox-FA front plate compared to that of Sintox-CL, SiC B and PS 5000. Notably, as the hardness of the ceramic front plate was increased from 1357 Hv (Sintox-FA) to 1705 Hv (Sintox-CL), there was a marked increase in fragmentation of the WC-Co core**.**

4.2.3 Effects of Impact Velocity on Ballistic Performance

To evaluate the performance of the BS41 for impacts in the region of 750 to 1100 m/s a series of single shot ballistic firings was conducted. Two different armour systems are reported: SiC B (57 kg/m^2) and Sintox-CL (70 kg/m^2) front plate with a 1318b witness block. *Table 4-8* below summarises the performance of each ceramic front plate at different impact velocities.

Table 4-8: DoP results for two ceramic front plates Sintox-CL and SiC B with 1318b witness block for impacts in the region of 750 to 1100 m/s.

Ceramic Front Plate	Impact Velocity (m/s)	1318b Aluminium Alloy Witness Block Penetrated DoP (mm)	Total Areal Density Penetrated (kg/m^2)
18 mm Sintox-CL	1094	54.81	217.80
	1089	58.59	227.81
	1016	59.26	230.00
	1016	56.21	221.89
	862	40.31	178.65
	842	40.42	178.91
	744	23.00	131.72
	729	23.47	133.14
18 mm SiC B	1094	26.34	128.55
	1096	28.84	135.39
	1031	23.21	120.54
	1018	13.32	93.22
	1015	11.46	88.98
	860	13.13	93.01
	856	0	57.43
	744	0	57.02
	744	0	57.46

Graph 4-7 summarises the performance of Sintox-CL and SiC B. The e_c of the ceramic system comprising of a ceramic front plate and a 1318b aluminium alloy witness block are plotted to allow comparison against impact velocity.

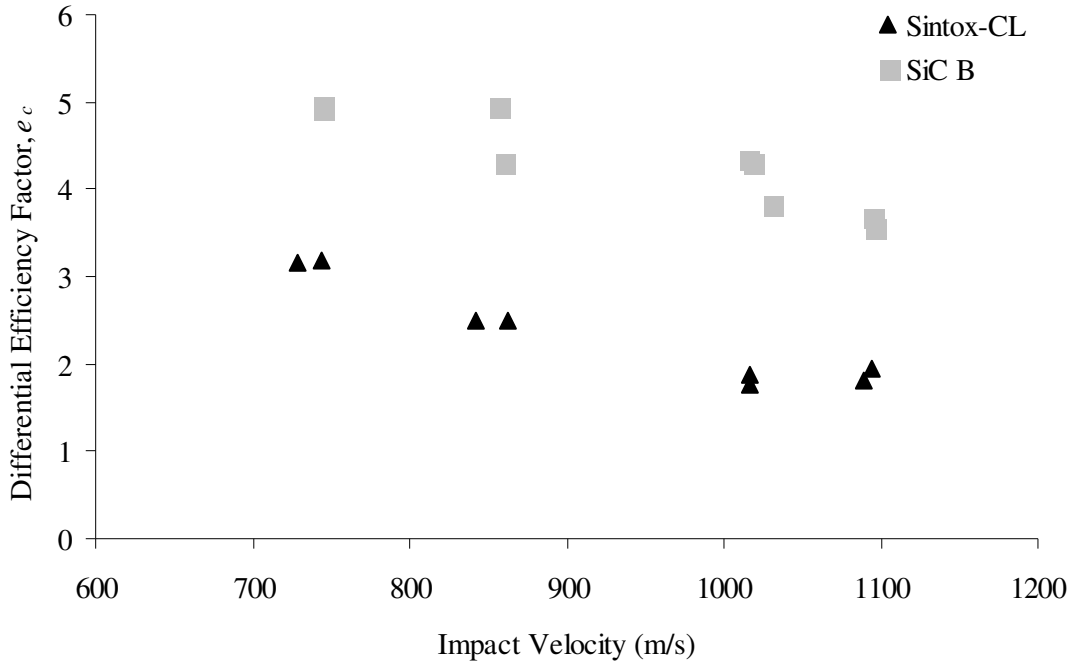

Graph 4-7: Reduction in e_c of the ceramic armour system. Two different ceramic armour systems (SiC B and Sintox-CL) are plotted against impact velocity.

It is interesting to note that SiC B and Sintox-CL both behaved similarly with a decrease in e_c of the ceramic armour system as the impact velocity increases. At both 750 m/s and 1100 m/s there was a 1.6 times increase in e_c of the SiC B ceramic system compared with the Sintox-CL. As the DoP increases, the proportional thickness of ceramic drops, reducing the e_c of the system. As the velocity becomes high and approaches the point where hydrodynamic behaviour may become a factor in the process, the ceramics are less effective.

4.2.4 Velocity Effects on Ceramic Fragmentation

After each firing, fragments from the target were recovered and sieved into different sizes. The ceramic fragment distribution between 9 mm and 600 μm as a function of impact velocity was analysed.

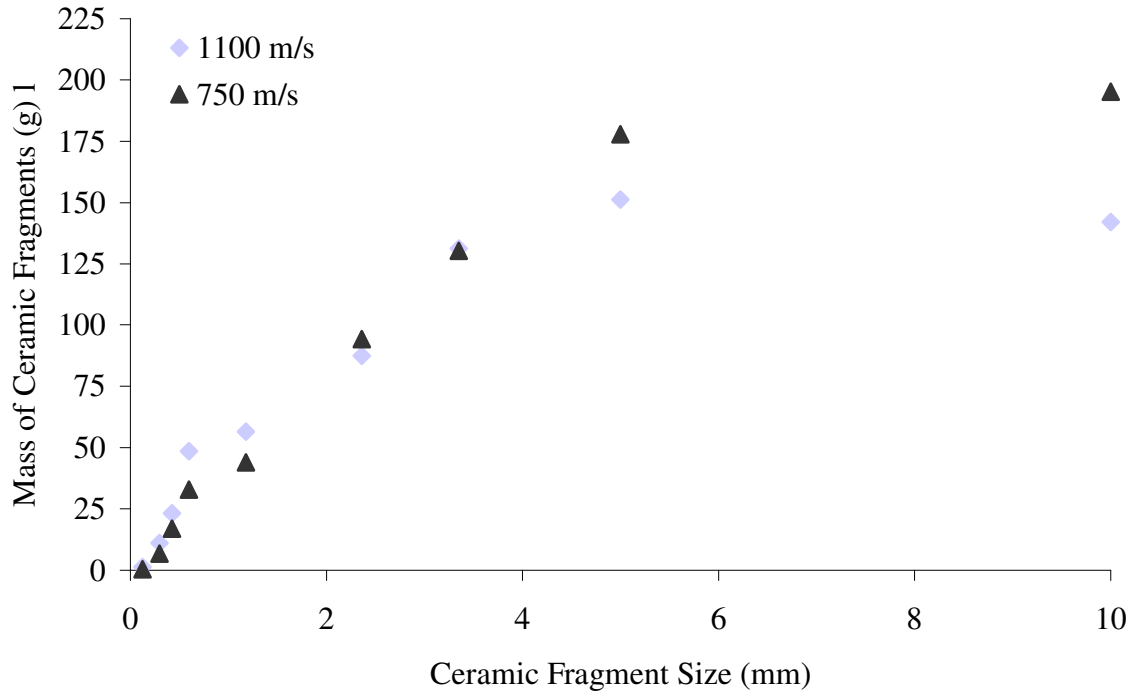

Graph 4-8; Sintox-CL ceramic target fragmentation retrieved after impact from the BS41

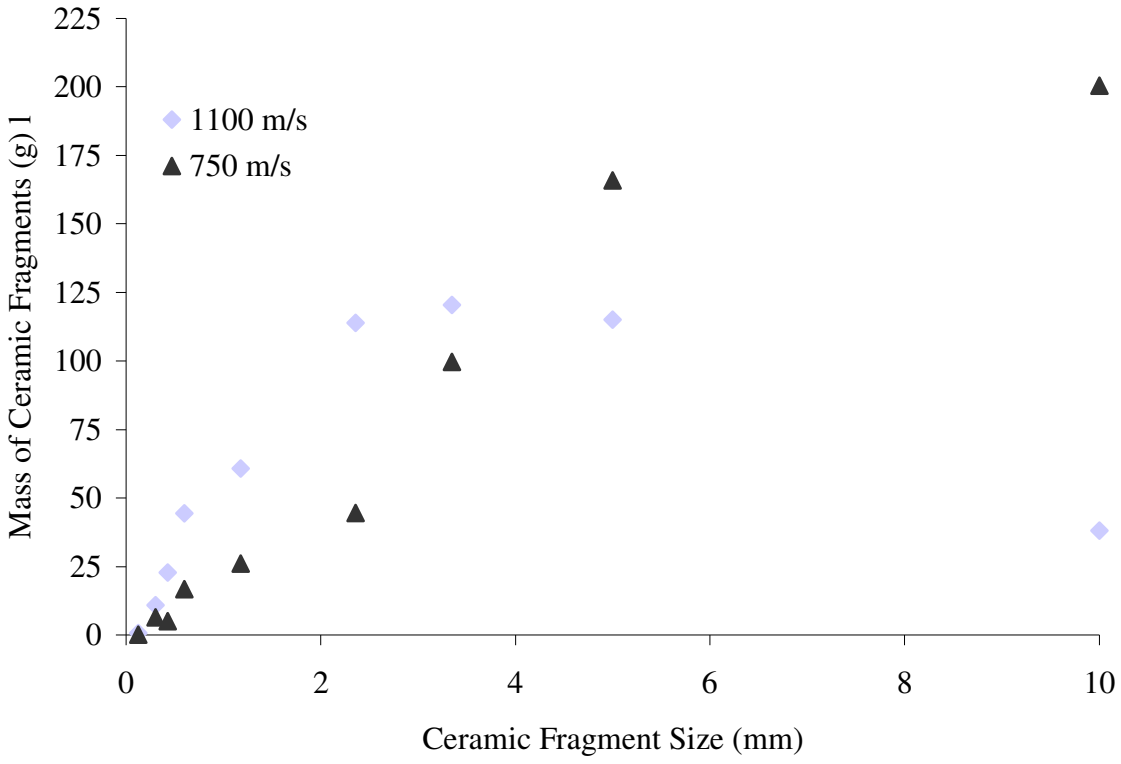

Graph 4-9; SiC B ceramic target (18 mm) fragmentation retrieved after impact from the BS41

Graph 4-8 and *Graph 4-9* summarise the mass of Sintox-CL and SiC B fragments respectively recovered after impact from the BS41 at different velocities. It was observed that greater proportions of smaller SiC B and Sintox-CL fragments were recovered at the higher impact velocity.

4.2.4.1 WC-Co Fragmentation after Impacting Ceramic at a Range of Impact Velocities

Examination of recovered WC-CO core and fragmentation behaviour of ceramic revealed a change in fracture morphology with increased impact velocity. *Figure 4.5* displays the WC-Co core retrieved after firing into two different ceramic front plates at different velocities.

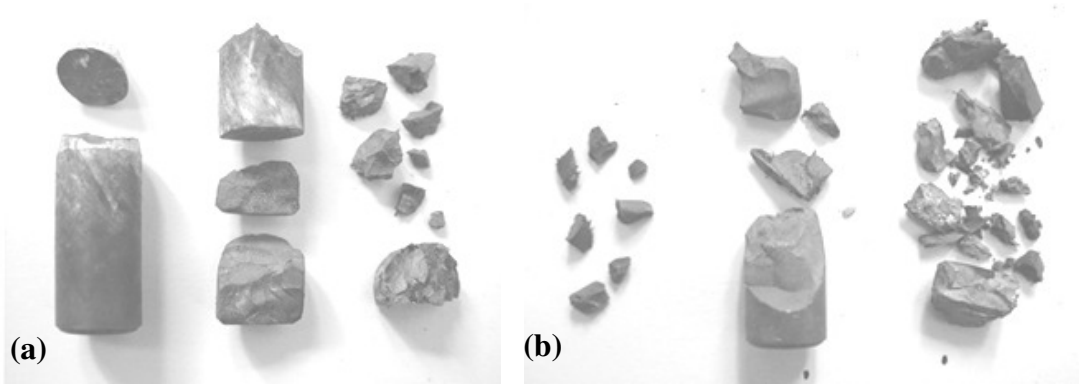

Figure 4.5: WC-Co core fragmentation for two different types of ceramics front plate and 1318b witness block (a) Sintox-CL (b) SiC B. From left to right 750 m/s, 850 m/s and 1100 m/s.

Evaluating the WC-Co recovered from firing into Sintox-CL saw a distinct increase in number and greater fragmentation of the core with increased impact velocity. SiC B displayed unusual behaviour; at 750 m/s, there was relatively large amount of core comminution when compared to the impact at 850 m/s. The core was shattered at all velocities. Further experimental testing is required.

4.2.5 Ceramic Comminution

During penetration compression of a small volume of ceramic adjacent to the leading surface of the advancing penetrator occurs. A subsequent flow of the fine fragments normal to and then opposite the penetrator path forms [184]. Ahead of the penetrator, the pressurised region inhibits the flow of the confined comminuted ceramic material, thus increasing ballistic performance.

The degree of fragmentation and the types of failure in the different captured ceramics were analysed. The work was performed with the aim of relating the types of failure to the effects on ballistic performance of the WC-Co projectile. Depth of Penetration results suggested that different ceramic material properties govern the penetration resistance of these confined ceramics. A microstructural analysis of the ceramic fragmentation is presented. Two types of failure mechanism, transgranular and intergranular are revealed in *Figure 4.6* below.

After comminution, the SiC B consisted of particles of closely interlocked grains. This could provide considerable resistance to deviatoric stresses. It was postulated that if the grains cleave under the applied stress (as was observed by the PS 5000 SiC) and co-operative movement is enabled, the shear strength is reduced. Transgranular cleavage failure in the PS 5000 SiC is evident in *Figure 4.6*. This could suggest why the SiC B matches the PS 5000 SiC in confinement despite the PS 5000's higher hardness value (*Graph 4-5, pp. 110*).

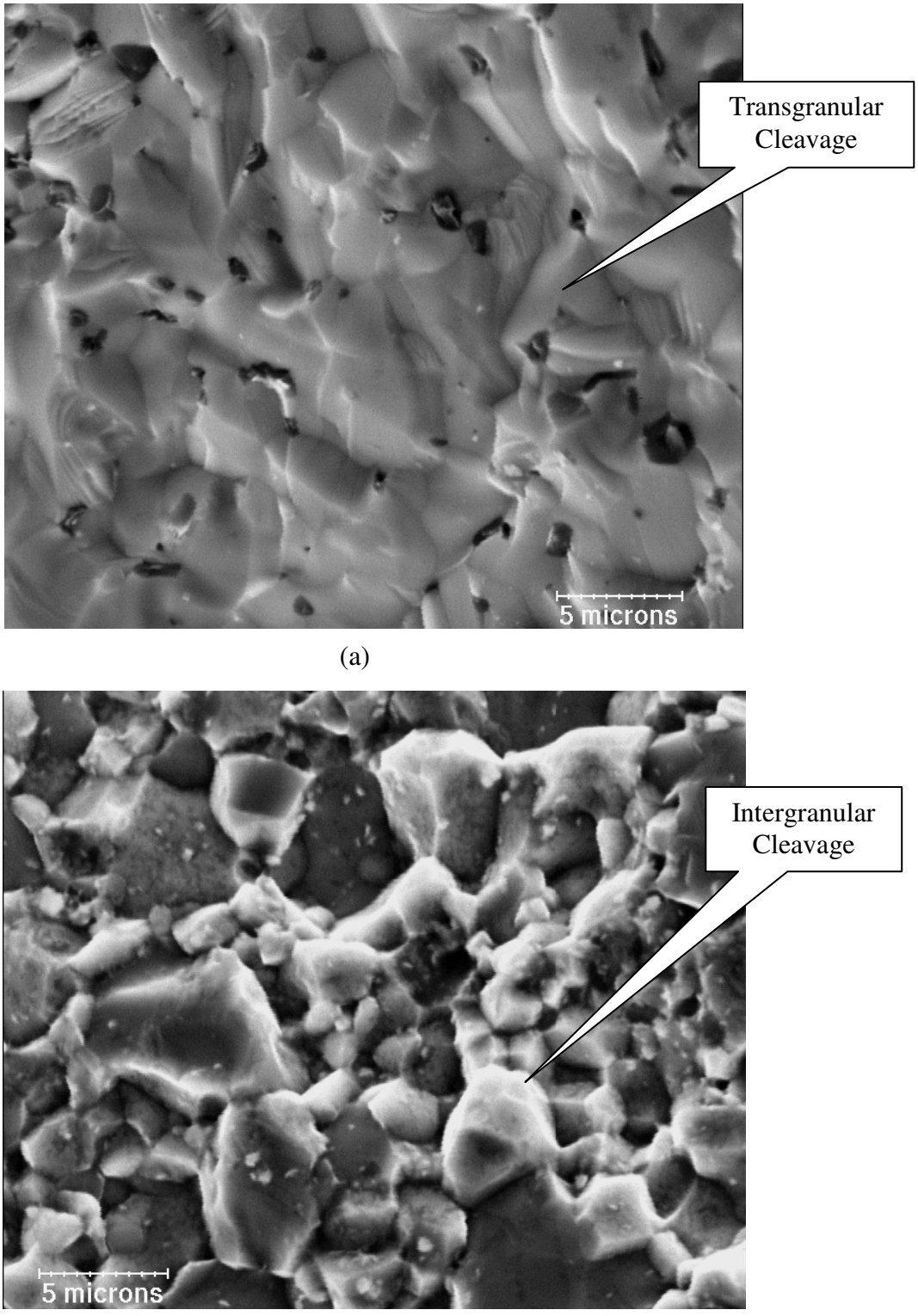

Figure 4.6: Fractographic images of the comminutia resulting from the ballistic impact tests (a) SiC PS 5000 failed in primarily transgranular cleavage mode (b) SiC B failed in primarily intergranular mode.

4.2.6 Effects of Ceramic Armour Appliqué System

To evaluate the performance of the BS41 into a spaced appliqué target the mechanisms by which a ceramic target backed by an 1318b back plate, air gap and 1318b witness block, defeat the projectile were investigated. *Figure 4.7* displays a schematic drawing of the experimental set-up.

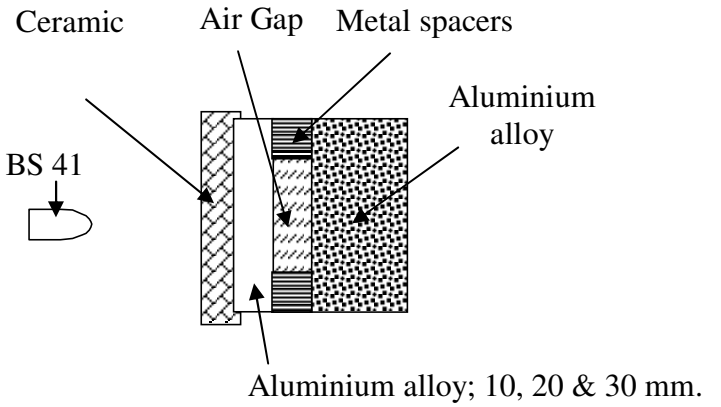

Figure 4.7: Schematic representation of the target configuration for the ballistic test.

Assessment was conducted with a confined ceramic target coupled to a finite 1318b plate (10, 20 and 30 mm). Two types of ceramic front plates were compared: 18 mm Sintox-CL and 18 mm SiC B. A 1318b witness block was used to capture the projectile for DoP analysis. In order to evaluate the influence of an air gap, a 10 mm air gap between the witness block and the front appliqué system was introduced. The goal was to evaluate the performance of a spaced 1318b appliqué armour system, a measure of the influence of the release waves from the target's free edges. *Table 4-9* summarises the DoP results from firing the BS41 into different appliqué systems.

Table 4-9: DoP results from firing the BS41 into different appliqué systems.

Ceramic Front Plate	Aluminium Alloy Thickness (mm)	Air Gap (mm)	Velocity (m/s)	DoP (mm)	Total Areal Density (kg/m^2)	Differential Efficiency e_c
18 mm SiC B	10.00	10	1015	13.82	121.97	2.90
	20.06	10	1006	4.03	122.41	2.44
	30.01	10	1024	0.00	138.68	2.04
18 mm Sintox CL	10.03	10	1021	47.69	226.08	1.58
	10.14	10	1015	48.51	228.52	1.55
	20.21	10	1021	46.10	249.23	1.27
	20.05	10	1013	1.53	128.35	2.24
	30.01	10	1017	37.24	251.62	1.20
	30.08	10	1026	37.52	252.64	1.20

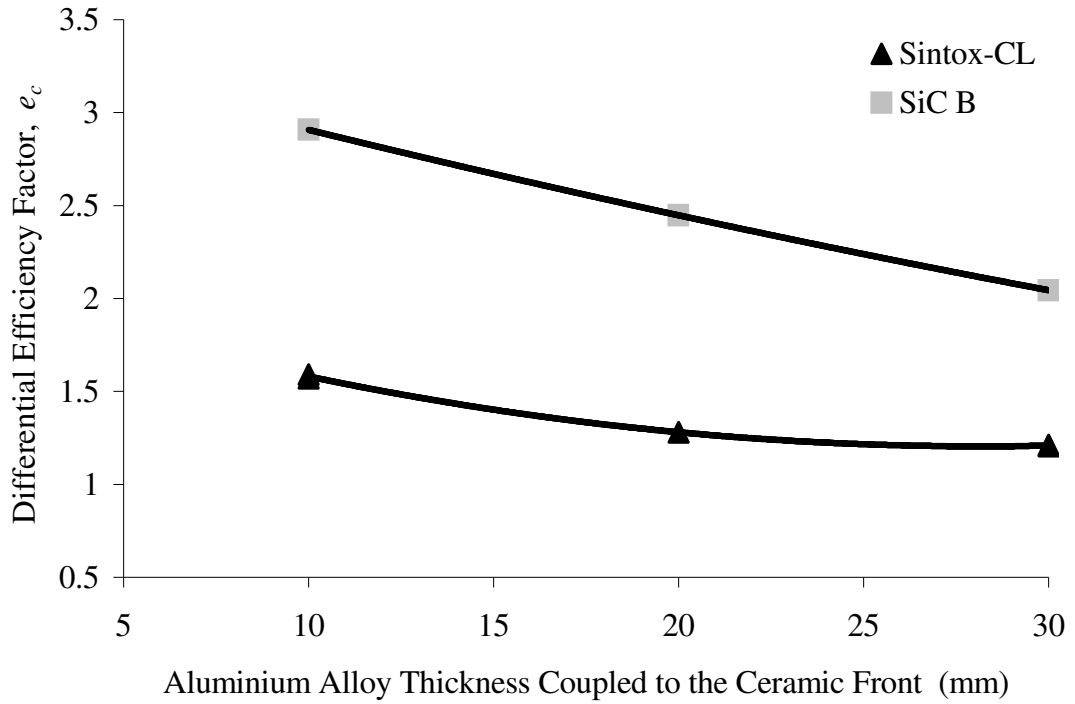

Graph 4-10: The effect of different 1318b thicknesses coupled to two different ceramic (SiC B and Sintox-CL) front plates with a 10 mm air gap on e_c. Velocity of impact is kept constant, 1016 ± 10 m/s

Graph 4-10 displays the $e_{c,}$ for the two appliqué armour systems with different ceramic front plates. Having generated the polynomial curves for the two ceramic tiles a reduction in e_c with increased 1318b thickness coupled to the ceramic face is observed. *Figure 4.8* displays the 1318b plates retrieved after impact.

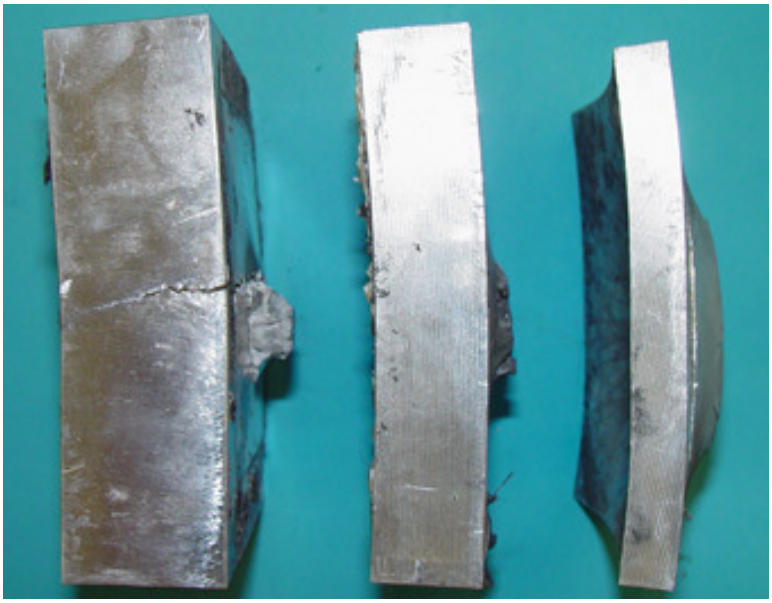

Figure 4.8: Three 1318b aluminium alloy plates, thicknesses 30, 20 and 10 mm, deformed after impact.

In comparing the e_c after complete penetration of the SiC B with 1318b coupled back plates, it consistently out-performed the Sintox-CL. The rate of decrease stayed fairly linear for SiC B backed with an increasing thickness of 1318b, but it levelled off for the similar system with Sintox-CL. The total areal density penetrated from firing into Sintox-CL spaced appliqué system, was found to perform similarly compared to firing into a semi-infinite 1318b witness block. The author refers the reader to *Table 4-8, pp. 113*. Whereas SiC B was found to perform 40% better with a semi-infinite witness block than spaced appliqué system. The data indicate that the e_c of SiC B increases with a high level of rear axial support to the tile. This was evident as the targets with 10 to 30 mm-coupled 1318b left the core largely intact while the semi-infinite 1318b backing caused pulverisation of the round.

Interestingly at 30 mm of 1318b coupled to the SiC B there was no penetration of the witness block. The WC-Co core was completely dispersed on leaving the front appliqué system not providing enough energy to penetrate the witness block.

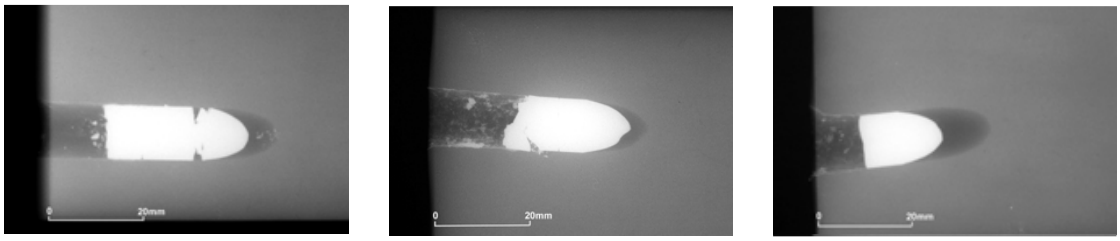

(a) **(b)** **(c)**

Figure 4.9: X-rays of the residual penetration and the remnants of the WC-Co in the 1318b. (a) 10 mm, (b) 20 mm and (c) 30 mm, 1318b coupled to 18 mm Sintox-CL.

Figure 4.9 compares the WC-Co tips captured in the 1318b witness block after firing into the three different ceramic appliqué systems. The residual DoP X-rays showed a relatively intact core at lower thicknesses of 1318b backing, whereas as the thickness was increased, more of the rear portion of the core was dispersed. Greater core loss was due to the formation of the spall crack at different points down the length of the WC-Co core.

4.2.7 Discussion

A technique for conducting DoP tests and evaluation of the data has been demonstrated. Confined ballistic tests of the BS41 impacting a variety of ceramic targets have been performed. In each test, DoP, velocity and fragmentation of both target and penetrator were compared. From these data, average values for DoP and thus e_c were measured and found to vary depending on target and experimental set-up. Measured ballistic performance results showed variation affected by the geometry of the target system. With the limited number of firings and available resources it was deemed impractical to calculate the velocity corrected DoP results.

The performance of the round fired from the 14.5 mm KPV BS41 has been compared with that of the softer cored 14.5 mm B32 projectile into mild steel. An evaluation of the ability of the Soviet projectile to defeat armour has been made. Based on the results against mild steel, the WC-Co cored BS41 projectile appears to outperform the steel cored B32 counterpart. The BS41 achieves a penetration of 10% more than the

B32 steel cored projectile. The high-density WC-Co sub-calibre core raises the KE of the unit cross sectional area in the core. Previous work performed by Hetherington indicates that the WC-Co FFV is stopped by 44 mm of mild steel, unlike the BS41 that requires 75 mm, nearly twice the DoP [128]. It is recommended for future extensive research programmes that the 7.62 FFV round is studied due to lower logistical impact *i.e.,* availability of ammunition and without the requirement of comparably large targets this would also facilitate the use of flash X-ray imagery during penetration.

The backing material is known to have an effect on ceramic tile performance, generally related to the rigidity of support that it provides (*Section 2.3 & 2.4.1*). Two witness block materials were compared, 1318b aluminium alloy (yield strength of 426 MPa and a Vickers hardness of 159 Hv) and mild steel (yield strength of 264 MPa and a hardness of 195 Hv). Several observations can be drawn from the results presented in *Table 4-2* (*pp. 100*) to *Table 4-4* (*pp. 104*) and *Graph 4-4* (*pp. 105*). In comparing the areal density of witness block penetrated, the 1318b consistently outperformed the mild steel witness block. It was observed that the critical thickness of ceramic front plate required for defeat was dependent on witness block material. When 1318b aluminium alloy was incorporated into the target system the critical thickness of Sintox-CL required for defeat was reduced.

Tensile tests revealed that the 1318b had different elongations to failure when tested in different orientations to roll direction (*Table 4-1, pp. 97*). The effect of altering the plane of the anisotropic 1318b witness block was tested and the results were compared. There was no significant difference in DoP but blocks orientated with plane 1, split after penetration (*Figure 4.3, pp. 102*). The plates used in these trials were rolled. During the rolling process the grains are distorted becoming lengthened in the rolling direction. This structural anisotropy leads to anisotropic mechanical properties. Ductility is mainly affected, being lowest in the short transverse direction, intermediate in the long transverse and highest in the longitudinal [185]. Upon impact, significant stresses are generated perpendicular to the impact direction sufficient to cause fracture when they acted in the short transverse direction but not in the other two directions.

Further observations of each of the witness blocks failure revealed penetration by lateral dispersion and ductile hole growth (*Section 2.3.2, pp. 41*). On the entry side, substantial lip formation around the periphery of the impact crater was observed. *Figure 4.10* and *Figure 4.11* below compare examples from firing into 1318b (short transverse roll) and mild steel, respectively. A summary of crater diameters can be found in *Section 7.4.1*.

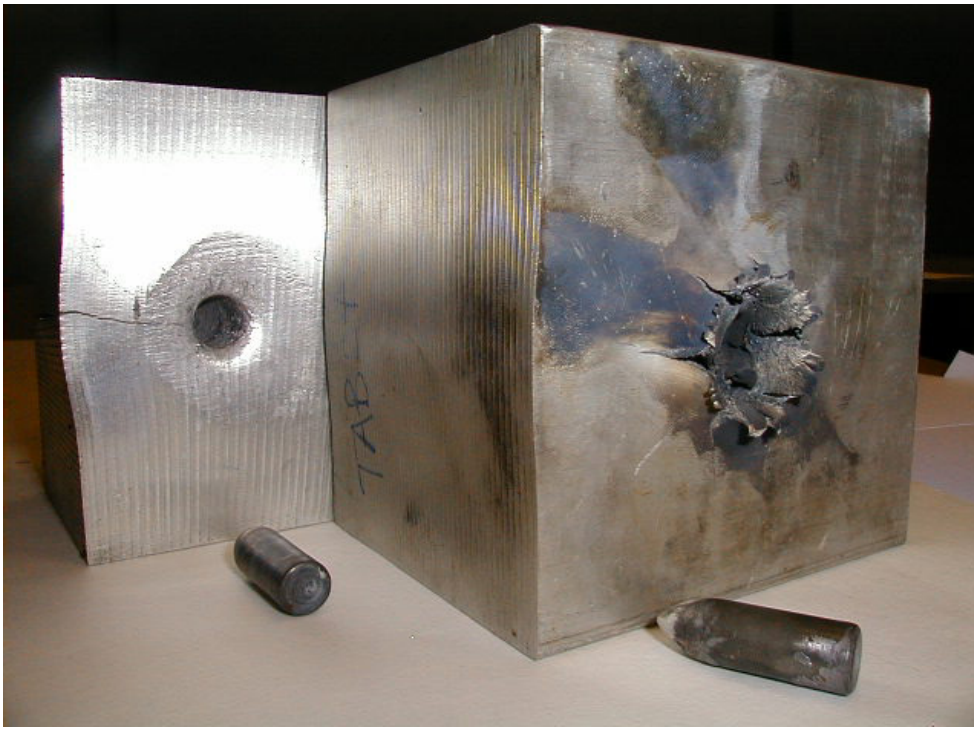

Figure 4.10: Aluminium alloy 1318b block after penetration (short transverse direction – *note* no splitting (*Section 4.1.2*)) from the BS41. Lip formation around the periphery of the impact crater can be observed with ductile hole growth.

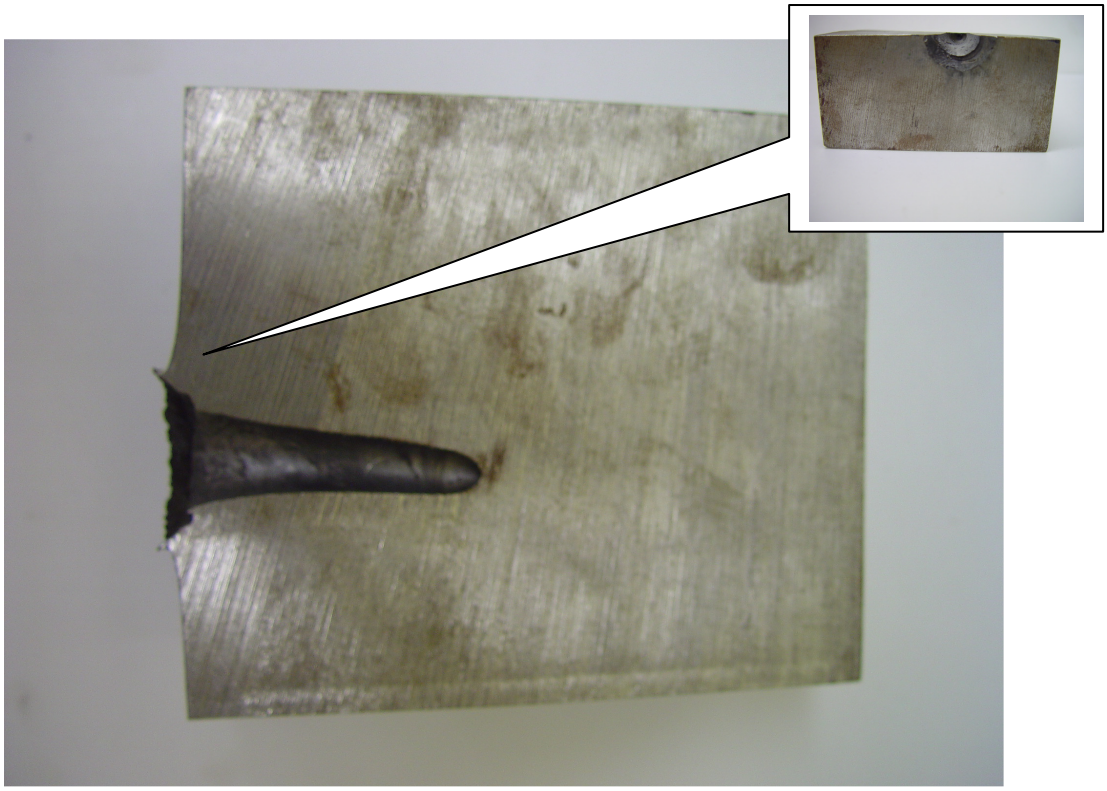

Figure 4.11: Mild Steel witness block after penetration from the BS41. Typical crater formed around the periphery of the impact crater.

With the WC-Co core tip being ogival and the ductile nature of the witness block type, it is less likely to penetrate the armour *via* the plugging mechanism. Therefore, we would expect the BS41 to laterally displace the material ahead of the projectile. The resistance to penetration increases with hardness. This is demonstrated by initial firings into each of the witness blocks. Dikshit *et al*. postulated that increasing the hardness of thick semi-infinite backing blocks increases the resistance to penetration [40]. As the hardness is increased, there is increased resistance, due to the larger energy dissipated in the plastic zone formed in the plate around the projectile.

It was observed that the total areal density and thus Differential Efficiency (e_c) of both witness blocks is dramatically altered when the witness block is protected with a ceramic front plate:

The mechanisms by which different confined ceramic-faced armour configurations defeat the BS41 were sought by examining the fracture morphology and deformation in the recovered targets and fractured cores. Results were compared from the failure

behaviour and DoP of the WC-Co core into different ceramic targets. Effects were compared at a range of different impact velocities.

The constraints placed upon ceramic armour systems, for which WC-Co defeat is required, are detailed. The ceramic front-plate plays a significant part in the failure of WC-Co. When the ceramic plates are used as overlays or incorporated as a layer within conventional monolithic steel or 1318b armour, the ballistic protection is significantly enhanced. Comparisons are made between the ballistic performance of the 1318b and mild steel with the same areal density Sintox-CL front plate. As can be observed in *Graph 4-4, pp. 105*, the 1318b consistently outperformed the mild steel when comparing areal density of witness block penetrated. It is found that, when an 18 mm Sintox-CL front plate (70 kg/m^2) with a mild steel witness block is used, there is a 29% reduction in DoP compared to 1318b yet there is a 74% increase in areal density. The difference was found to increase dramatically to 107% when comparing just the semi-infinite DoP witness block trials, *Section 4.1.1* (*pp. 96*).

Section 4.2 compares the performance of three of the different ceramic front plates; SiC B, SiC PS 5000 and Sintox-CL with a 1318b witness block. In comparing the e_c of the different ceramic tiles the SiC consistently outperformed the Al_2O_3 tiles offering more efficient resistance against the WC-Co core. The results suggest that it is not only the type and hardness of SiC that is important, but also the type of grain failure on impact. The data indicated that the performance of SiC B increased with a higher level of rear axial support to the tile (*Section 4.2.6, pp. 119*). Intergranular failure allowed a well-supported SiC B, despite its lower hardness to PS 5000, to hold together for a greater period of time leading to higher peak stresses in the WC-Co. This could suggest why the SiC B matches the PS 5000 SiC in confinement despite the PS 5000's higher hardness value. After comminution of SiC B, closely interlocked grains of SiC appeared to provide considerable resistance to the deviatoric stresses. If transgranular cleavage is dominant, the grains cleave and co-operative movement is enabled and the shear strength of the ceramic is reduced, leading to a reduction in tile efficiency. The shear strength of the ceramic is a very important material property for ensuring a good level of resistance to WC-Co penetration.

In evaluating armour systems against projectiles with hard cores at different impact velocities, it is possible to encounter a change in both projectile and target defeat mechanisms. The performance of the BS41 for impacts in the region of 750 to 1100 m/s into two different armour systems (SiC B (57 kg/m^2) and Sintox-CL (70 kg/m^2) front plate) with a 1318b witness block, are reported. From these data average values of the DoP and e_c were measured and found to vary linearly with impact velocity. Although this is strictly an empirical relationship, it may be used to interpolate between the impact velocities tested. The DoP increased significantly and the e_c was reduced over the range of impact velocities tested. At long ranges where the projectile's velocity is reduced, differences in the protection level of the armour system against the BS41 will change; this must be taken into consideration if an acceptable armour system is to be produced.

Like Moynihan *et al*. [153] an increase in both Sintox-CL and SiC B target fragmentation was observed with increased velocity. This is probably due to the increase in shock stress that results when a target is struck at higher impact velocities. Furthermore, there is some evidence to suggest that the strength of SiC is reduced with increased shock stress. Though inconclusive, Feng *et al.* extrapolated available data suggesting a gradual softening of SiC with increase in mean stress [186].

Variation of WC-Co failure and fragmentation was apparent between different ceramic and witness block systems:

Despite the WC-Co relatively higher hardness compared to each of the metallic witness blocks, there was a small degree of WC-Co core surface erosion. With the addition of a Sintox-CL front plate, the core was found to fragment into three typical sections. Some form of multi-layer system, harder or simply thicker ceramic, would be proposed to improve the armours effectiveness against the WC-Co penetrator.

A comparison of the cores retrieved after firing into Sintox-CL and either mild steel or 1318b witness block, revealed greater fragmentation of the WC-Co core with 1318b. This may have been due to a greater impedance mismatch with the ceramic – aluminium combination than the ceramic – steel combination leading to higher tensile stresses in the ceramic target. The WC-Co tips were found to penetrate into the

witness block whilst the rear of the core was fragmented and dispersed. The approximate size of WC-Co fragments recovered from the rear of the core increased as the areal density of ceramic decreased.

As the WC-Co penetrated the ceramic target, comminution of the ceramic occurs. The formation of these fragments can account for loss of the penetrators effectiveness and thus, plays an important part in the ceramics ability to defeat the projectile. Examination of recovered WC-Co core and fragmentation behaviour of ceramic revealed a change in fracture morphology with increased impact velocity. Evaluating the WC-Co fragments and Sintox-CL and SiC B comminution recovered at different impact velocities, saw a distinct increase in number and greater fragmentation of both target (*Graph 4-8 and Graph 4-9, pp. 115*) and projectile (*Figure 4.5, pp. 116*) with increased velocity.

The main defeat mechanism involved with the addition of a ceramic plate is fracture of the projectile and distribution of the energy over a larger area of the witness block. It was found that the SiC, with its greater hardness induced a greater shock, imparting greater fragmentation in the WC-Co core than the softer Sintox-CL Al_2O_3. The target interactions caused fracture across the diameter of the core suggesting spall or bending stresses. Initial resistance to penetration is provided by the compressive strength or hardness of the ceramic. Such properties are desirable to fracture and deflect the impacting body. The analysis has shown that it is not only increased ceramic hardness that is important but also the nature of the fracture of the ceramic ahead of the penetrator that may improve the armour's ballistic performance at defeating WC-Co penetrators.

Chapter 5

Microscopic Analysis and Discussion

Scanning Electron Microscopy (SEM) and Energy Dispersive X-radiography (EDX) were employed to investigate the failure of the WC-Co core after impact. Fragments recovered from a series of firings of the BS41 round into various thicknesses and types of Al_2O_3 and SiC, backed by aluminium alloy or mild steel semi-infinite witness blocks, were examined metallographically. This was in order to gain an understanding of the microstructural changes and deformation processes that had occurred during penetration. Macroscopic analysis examined; grain structure, porosity, micro-cracks and fracture, some of which were associated with microstructural discontinuities.

5.1 Scanning Electron Microscopy Analysis from an Unfired Sample of WC-Co Core

Direct knowledge of the fabrication or processing history of the WC-Co core of the 14.5 mm Russian BS41 is unavailable. Without any detailed *a priori* knowledge of its fabrication, both unfired WC-Co sections, and fired fragments having impacted different ceramic armours, of the BS41 core, have been examined. The PUNDIT longitudinal wave velocity analysis and the Vickers hardness indentation testing of the WC-Co are introduced.

Samples of the WC-Co in final manufactured condition, as a Russian KE penetrator, were sectioned using a spark eroder. Sample specimens were taken from the core for chemical analysis. The material examined was a commercially produced WC-Co cermet and was found to have a nominal concentration of W-88.00%–C-5.58% by weight. Chemical analysis revealed the composition of the major metallic constituents to be Co-5.45%-Fe-0.34%. The Vickers hardness was 1289 Hv (2 kgf load) (*Section 3.3.4, pp. 78*). Hardness in WC-Co is largely controlled by the WC content, degree of working and heat treatment temperature (*Section 2.5.3, pp. 59*).

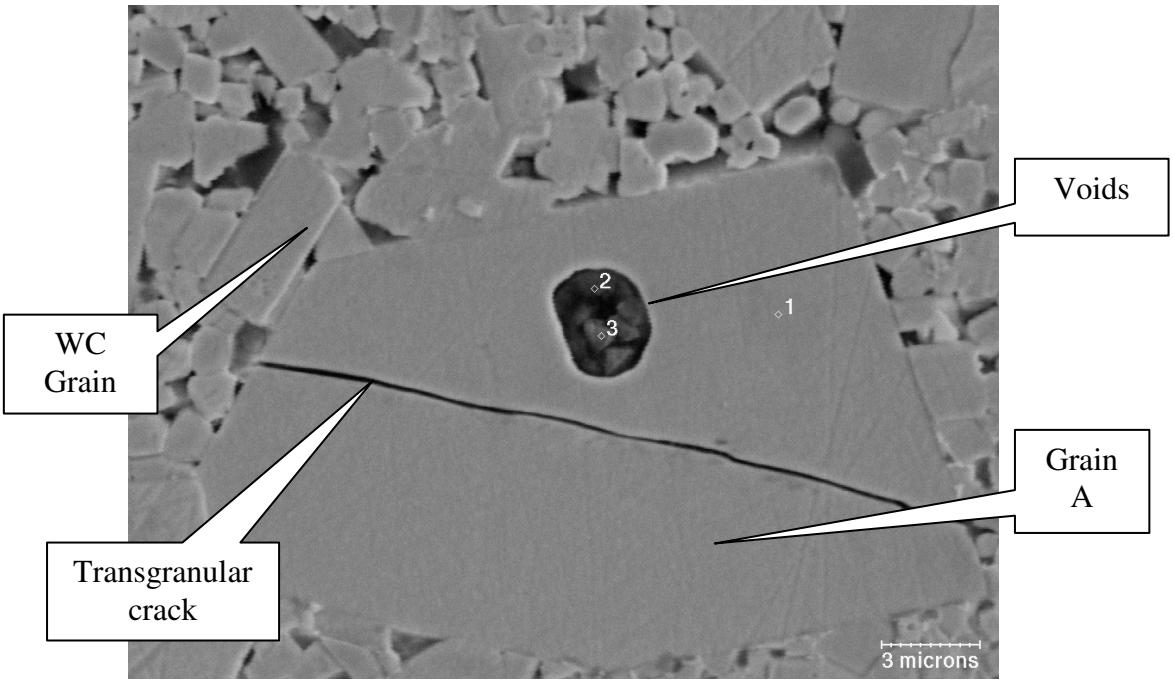

Figure 5.1: Scanning Electron Micrograph of the transverse cross section of the unfired WC-Co core. 1, 2 and 3 represent the locations of EDX analysis displayed in *Figure 5.8.*

Etched transverse (*Figure 5.1*) and longitudinal (*Figure 5.2*) samples of WC-Co, removed from the section of the unfired core, were placed under the SEM to analyse the WC-Co grain structure. Specimen preparation in this case included a final polishing step and etching (*Section 3.6.1, pp. 92*).

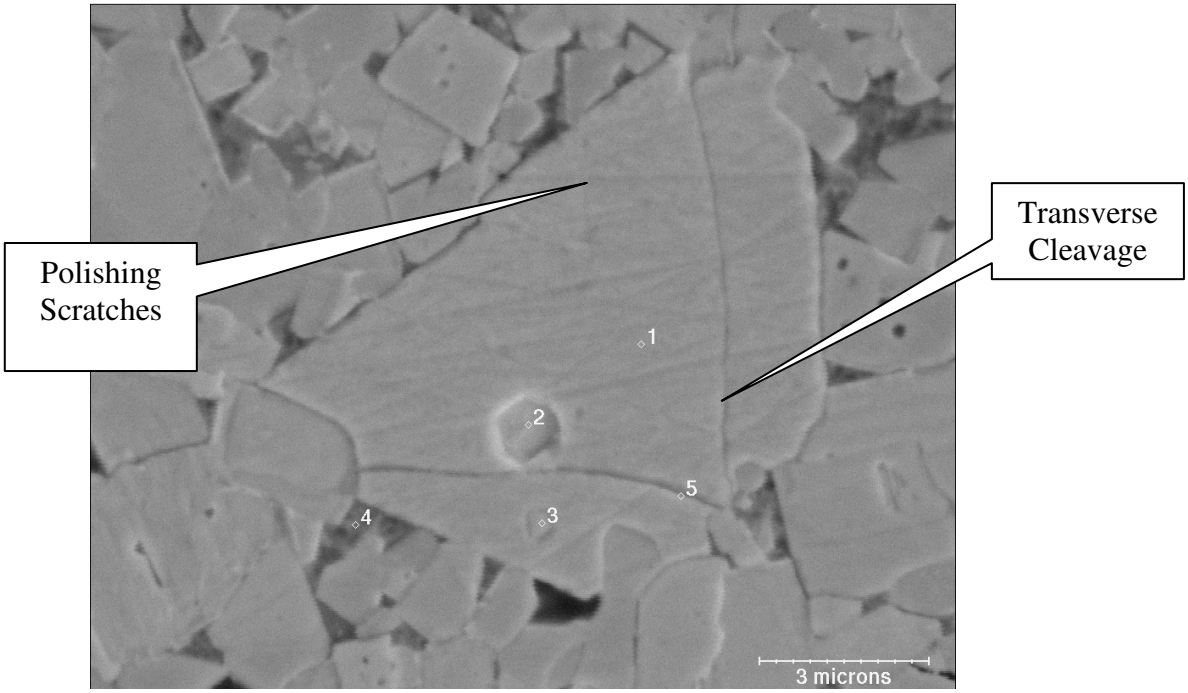

Figure 5.2: Scanning Electron Micrograph of the longitudinal cross section of the unfired WC-Co core. 1, 2, 3, 4 and 5 represent the locations of EDX analysis.

The transverse and longitudinal samples illustrate the microstructure clearly. The WC grains surrounded in the Co matrix and the voids are well defined. *Figure 5.1* shows the WC-Co had great grain size variability. This may be attributed to the impurities like Fe and the variability in the manufacturing process conditions [134,136]. The WC-Co particles varied in grain size mostly between 3 and 7 μm, but Grain A for example is over 20 μm in length. These larger grains were prominent in a number of samples.

The porosity or void content, which is nearly always significant as a result of the incomplete densification of the material during the firing process, is an important factor with ceramics. Notably, the WC-Co sample displayed a high volume of open porosity accessible to the exterior. This is generally an undesirable feature affecting

both crack initiation and propagation, and the mechanical properties, decreasing the Young's modulus.

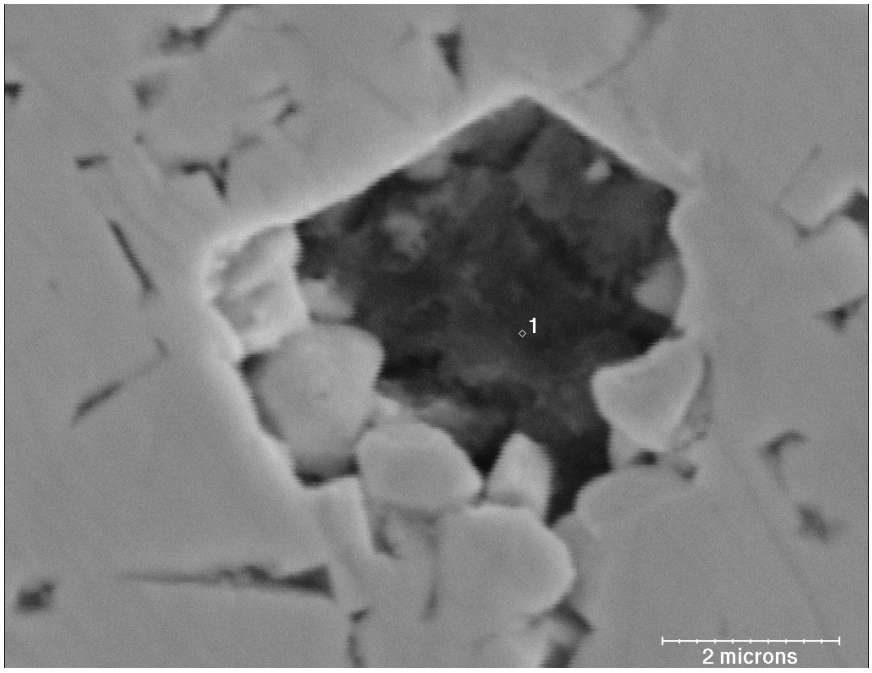

Figure 5.3: Scanning electron micrograph of a void region in an unfired, polished, WC-Co core sample.

Figure 5.3 shows a SEM micrograph of a pore taken from the unfired section of the WC-Co. The pore is clearly much larger than the surrounding grains. Around the surface of the pore sharp cusps which partly penetrate between neighboring grains are revealed. The average pore size was between 5 and 10 μm.

Apart from pores, ceramics are likely to contain other forms of defects. During analysis it was clear that a high concentration of voids, indentations and internal cracks was visible in unfired samples, before dynamic loading. Grain A, *Figure 5.1* (*pp. 130*), for example, displays a clear transgranular crack through the WC grain.

5.2 Energy Dispersive X-radiography Analysis from an Unfired Sample of WC-Co Core

The identity of small particles on substrates is very difficult to determine using SEM imaging. Due to the small particle size and uneven surfaces of any particles present, the electron beam interacts with the substrate as well as the particle. A useful

technique for the identification of particulate material is EDX. This is important in identifying the main modes of fracture in a fired sample (interfacial WC / Co matrix or transgranular). Generally we would expect WC-Co to fail in a complex manner in predominantly 5 possible fracture modes. *Figure 5.4* below shows a schematic diagram of these modes:

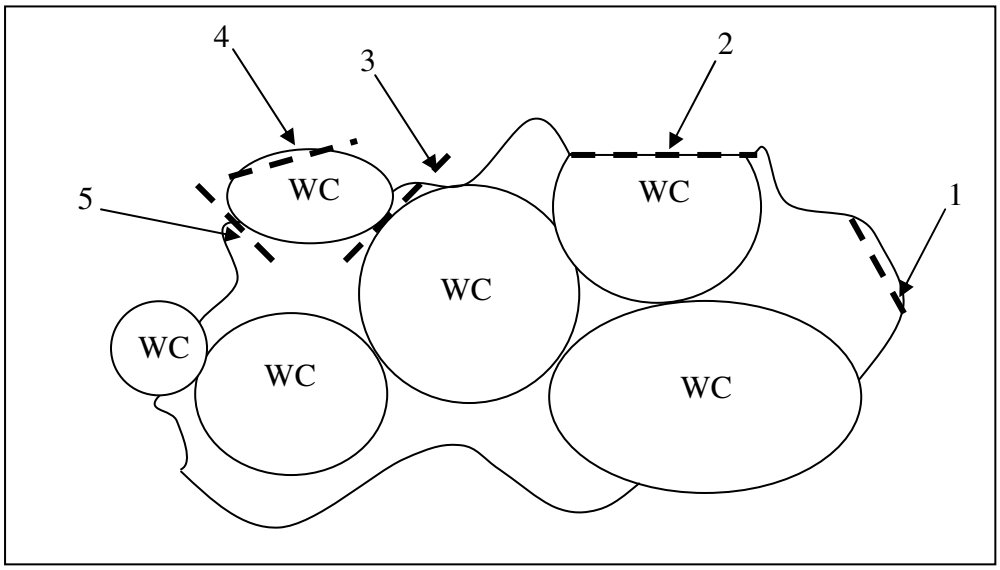

Figure 5.4: Schematic diagram of five possible fracture modes in WC-Co (WC grains surrounded by a Co matrix). 1: Ductile matrix failure, fracture through the Co matrix surrounding the WC grains *or* at cryogenic temperatures cleavage of the matrix, 2: Cleavage of WC grains (transgranular cleavage), 3: WC – WC grain boundary decohesion (intergranular cleavage), 4: WC side of the WC – Co interface decohesion and finally 5: Matrix side of WC – Co interface decohesion.

A scan map using the EDX over the surface of the sample was used to identify the high concentration regions of a number of elements, including Ni, Co, Fe, W and C. *Figure 5.5* displays five transverse elemental maps of a polished sample of WC-Co from a 25 μm wide sample. The microstructure map illustrates clearly the definition of the microstructure. The target element (clockwise from top left map; Ni, Co, Fe, W and C) is identified in the lower left corner of each scan. The bright / white dots represent either noise or possible traces of the element. High Co regions were identified between each of the W grains.

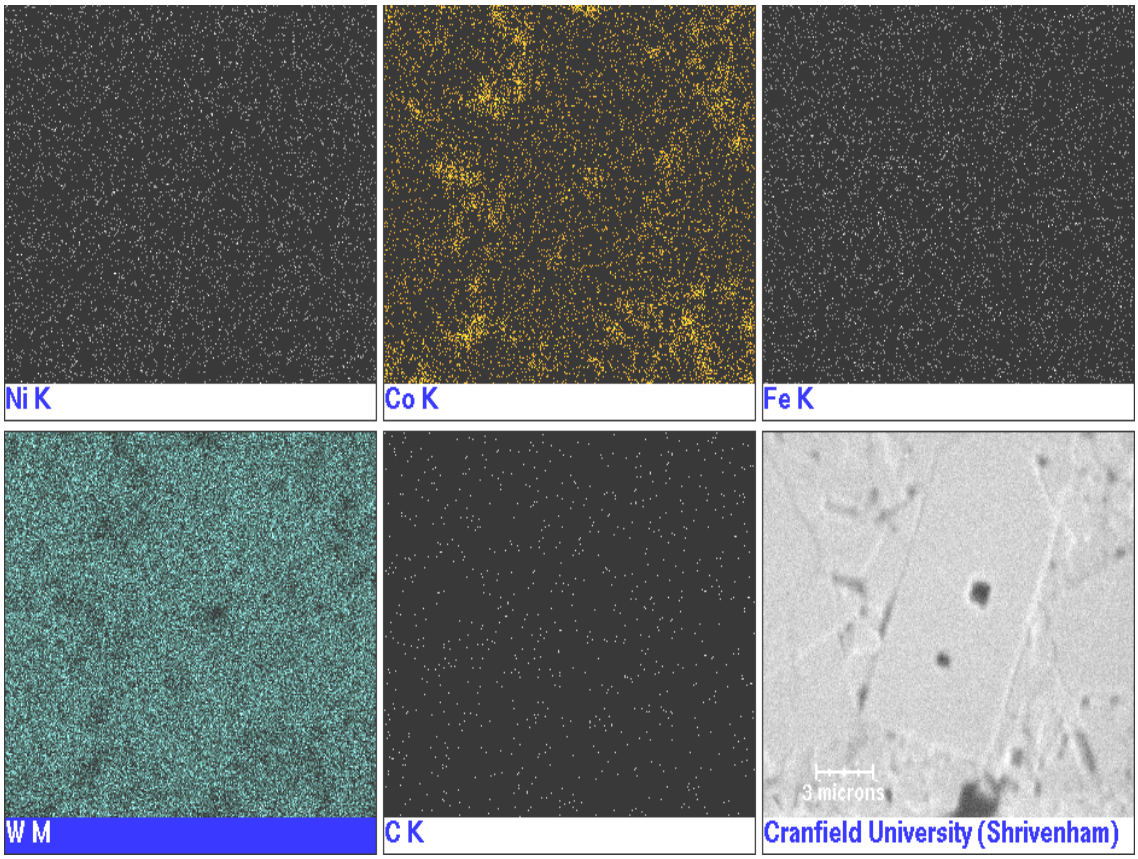

Figure 5.5: Scan map over the surface of the polished WC-Co sample. High Co regions are found between the grains as expected.

Analytical electron microscopy allows the determination of the chemical composition in regions close to the interface. A point EDX was taken at point 4 on the sample displayed in *Figure 5.2* (*pp. 131*) to confirm the presence of Co. The corresponding X-ray spectrum is presented. *Figure 5.6* identifies the presence of the Co matrix between the WC grains.

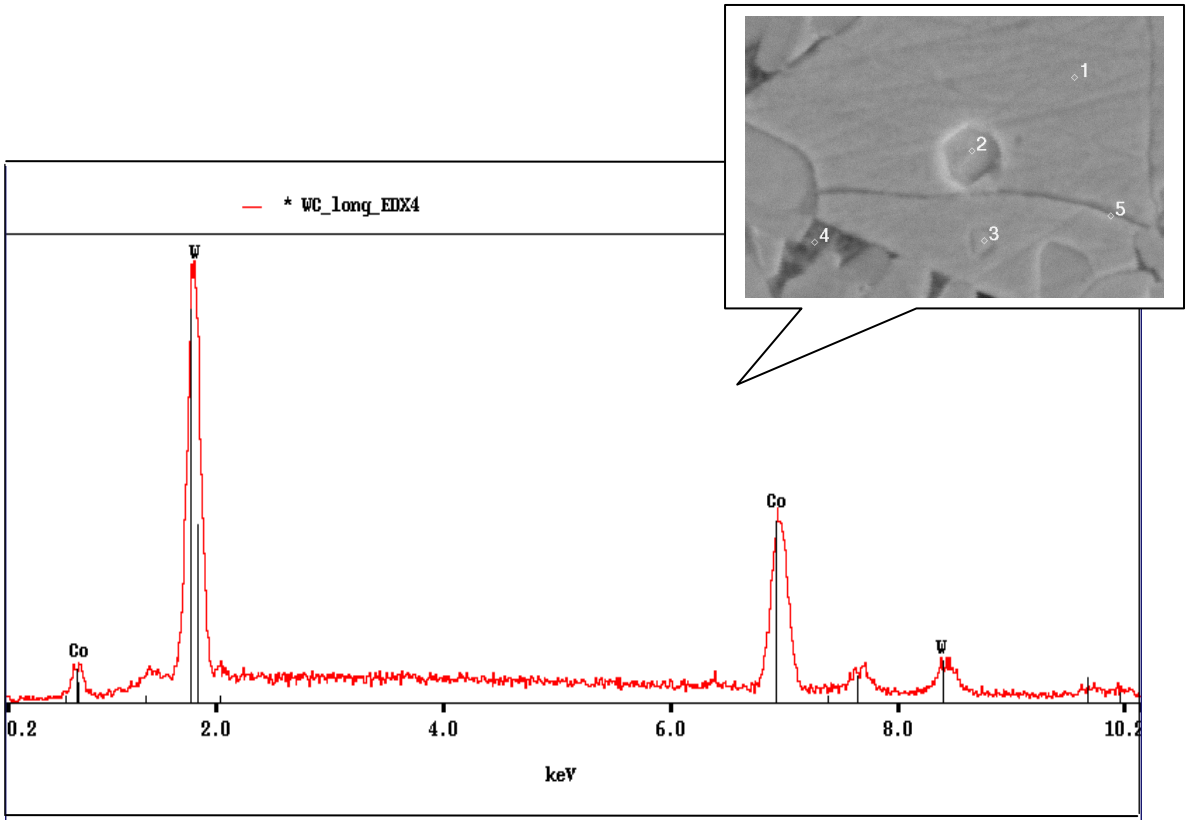

Figure 5.6; Energy Dispersive X-ray; Identification of Co and W from a longitudinal unfired sample of WC-Co core.

A second sample taken from the large void region in *Figure 5.3* (*pp. 132*) was analysed. This was to try and closely identify the Co regions and account for the presence of the pores. *Figure 5.7* displays the results from the mapping. Notably no traces were found of Fe, Co, Ni or other elements.

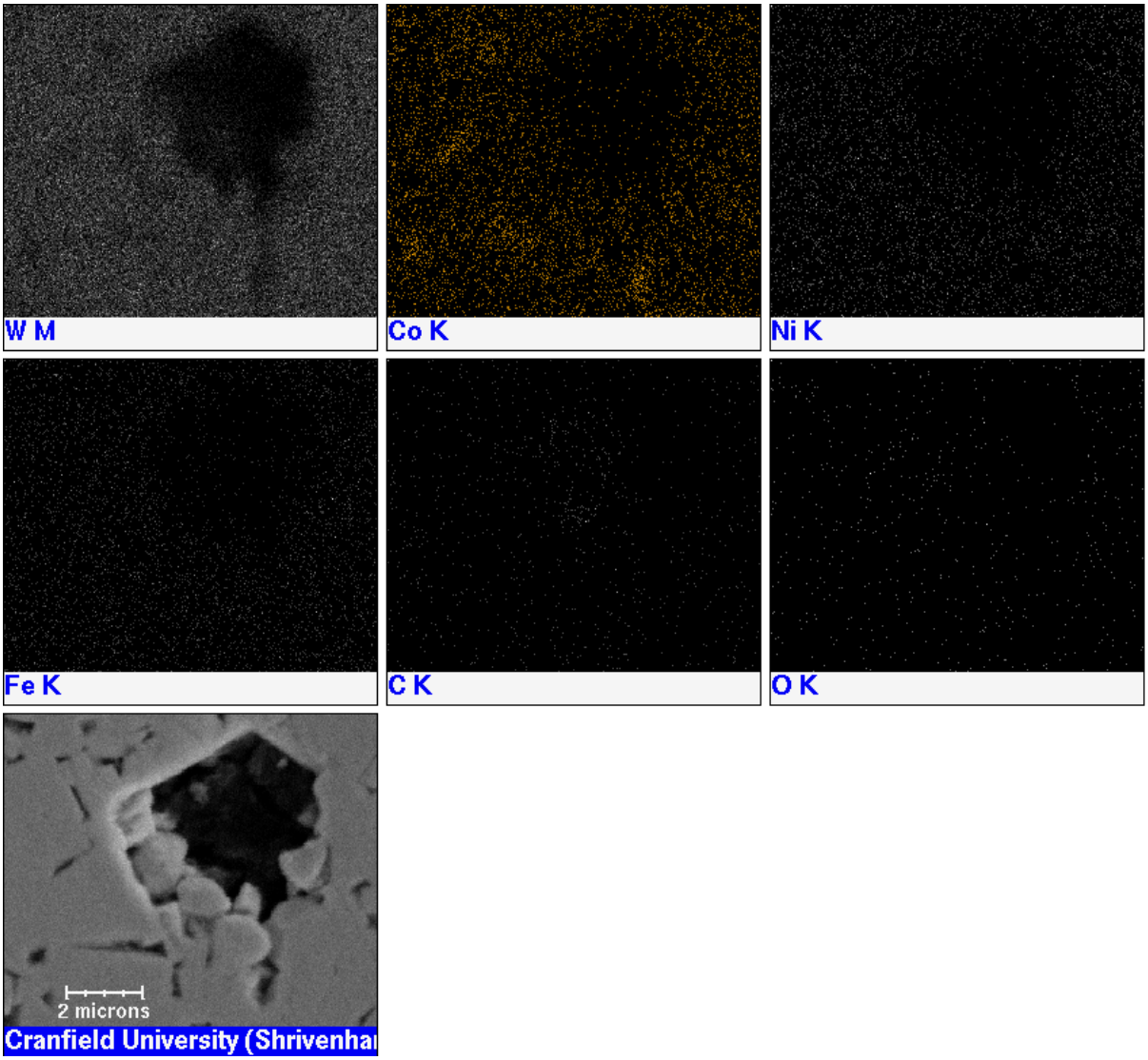

Figure 5.7; Energy Dispersive X-ray map scan of void, point 1 (*Figure 5.3).* The target element is identified in the lower left corner of each scan.

Final EDX samples was taken to account for the impurities within the Russian WC-Co sample. *Figure 5.1* (*pp. 130*) displayed the SEM micrograph image taken at high magnification of the WC-Co polished surface. Points 1, 2 and 3 on the image are the three positions where the EDX readings were taken. The corresponding EDX spectra are shown in *Figure 5.8*. This analysis identified W and impurities such as Pb (lead) and Fe within the sample. This is further substantiated by the presence of these impurities as determined by the Inductively Coupled Plasma, Atomic Emission Spectroscopy analysis (*Results in Chapter 6, Table 6-3, pp. 160*).

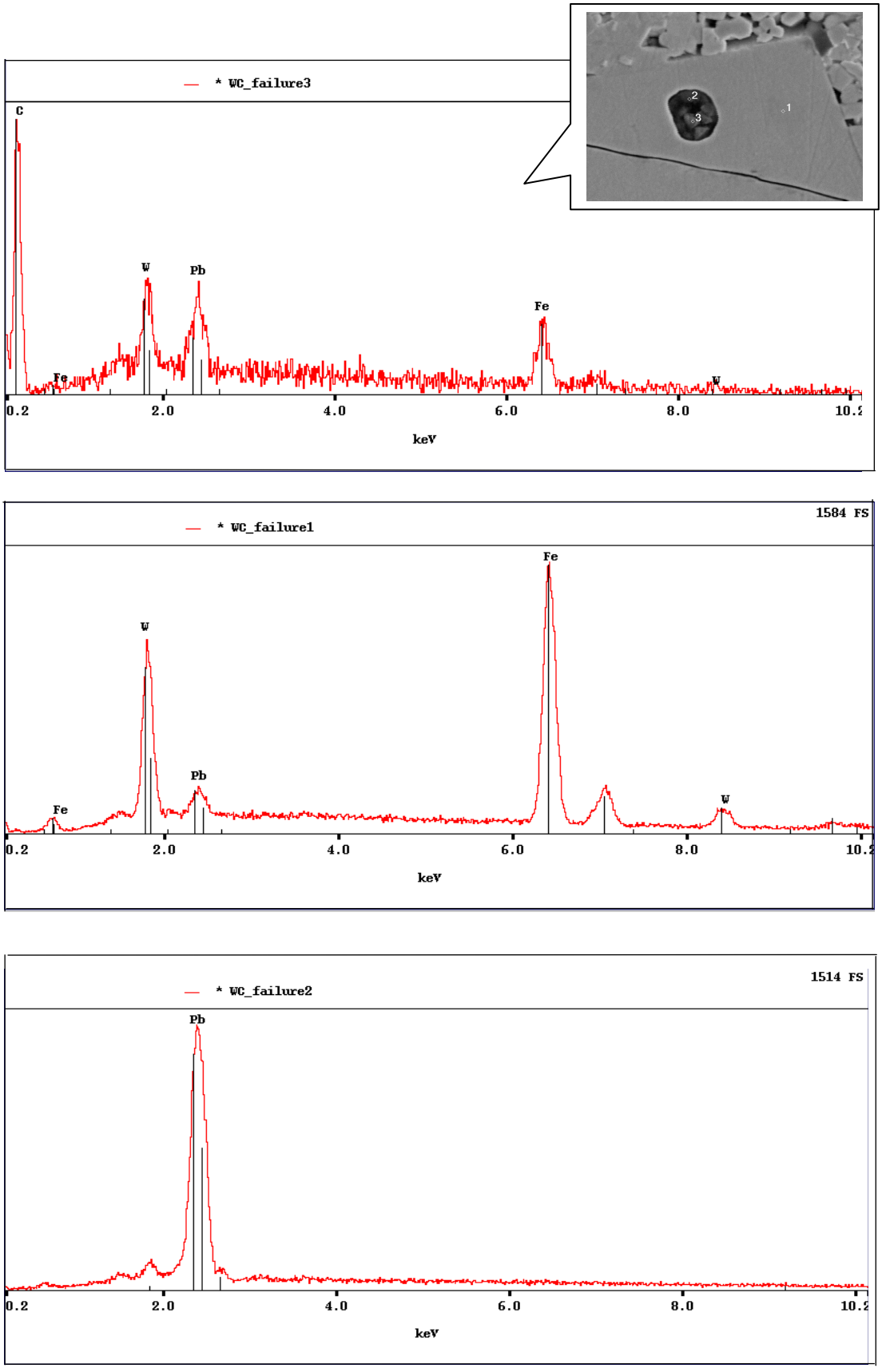

Figure 5.8: Three Energy Dispersive X-rays of three points on the surface of the polished unfired WC-Co core sample shown in *Figure 5.1,* (a) (Point 1), W, C, traces of Fe and Pb (b) (Point 3), high C regions, with W, Pb and Fe (c) (Point 2), Pb.

At point 1, EDX, taken on the W grain, traces of W, Fe and Pb were found. Point EDX 2 and 3 were taken in what appeared to be a void region. A higher concentration of both impurities, Fe and Pb were identified. Traces of W, as expected were also present.

5.3 Fracture Analysis from a Fired Section of WC-Co

Fired WC-Co fragments of the BS41 core, having impacted different ceramic armours, have been examined. *Figure 5.9* compares three recovered fragmented BS41 core specimens retrieved after impact on three different types of ceramic target front-plates. The front end of the penetrator tended to fracture at the transition between the cylindrical body and ogival nose tip. The rear cylindrical body of the core tended to fracture into multiple pieces depending on the target system. Radial displacement and axial splitting was observed in samples, thus reducing the energy of the advancing projectile core.

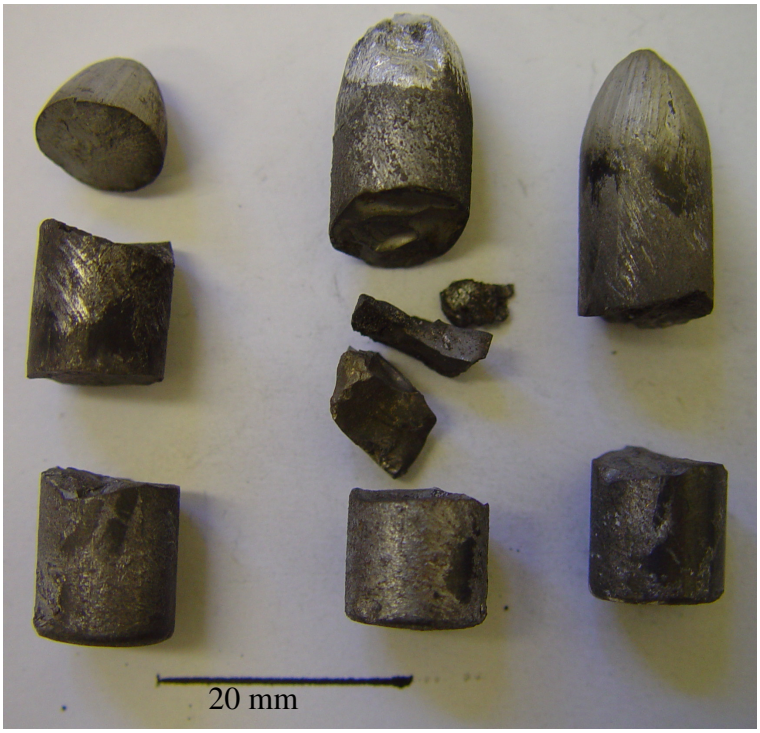

Figure 5.9: BS41 WC-Co fractured core retrieved after firing into, from left to right, 18 mm Sintox-CL / mild steel semi-infinite WP, 18 mm Sintox-CL / aluminium alloy semi-infinite WP and 30 mm FA/ mild steel.

Although the appearance of the fractured cores differed after impacting each target system, the overall failure of the WC-Co was very similar. The core tended to fracture at two dominant positions. The author refers the reader to *Figure 4.5, pp. 116* and *Figure 4.9, pp. 122*, for comparison.

The distribution and failure nature of each penetrator was studied *via* metallographic examinations at different locations on the penetrator fracture surfaces.

Figure 5.10: A SEM micrograph from a recovered WC-Co spall specimen after penetration into a SiC B front plate and a 1318b aluminium alloy witness block.

In *Figure 5.10* a WC-Co spall fragment recovered after penetrating a SiC B front plate and an aluminium alloy witness block was sectioned and mounted for SEM examination. In *Figure 5.11, Figure 5.12* and *Figure 5.13* below, microstructures observed in three regions of the mid section of the residual penetrator, parallel to the plane of the shock wave, are shown. The exposed fracture surface was examined.

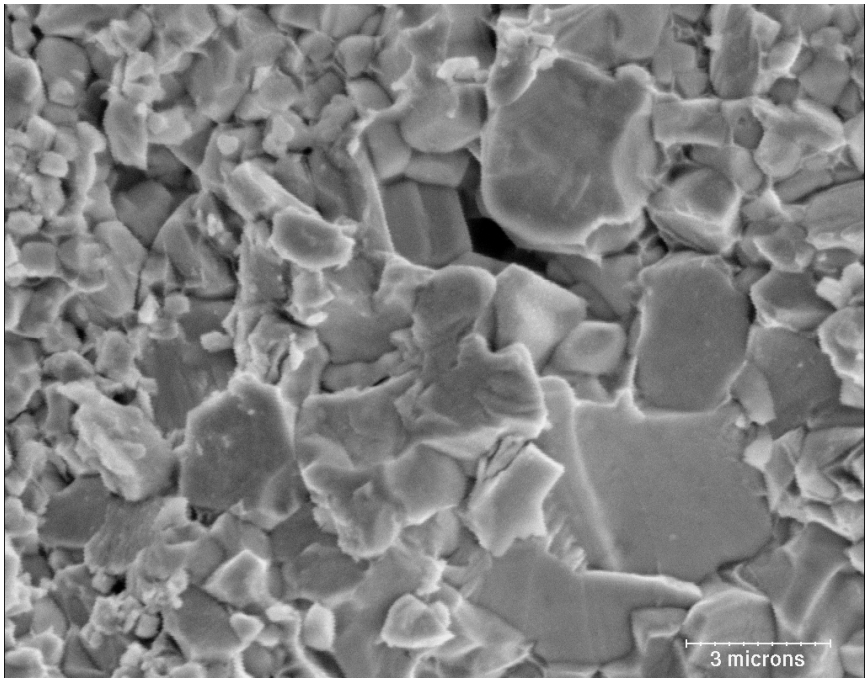

Figure 5.11: Scanning electron micrograph from a sample of WC-Co after penetration through a SiC B front plate and an aluminium witness block. Primary failure mode was transgranular cleavage of large WC grains.

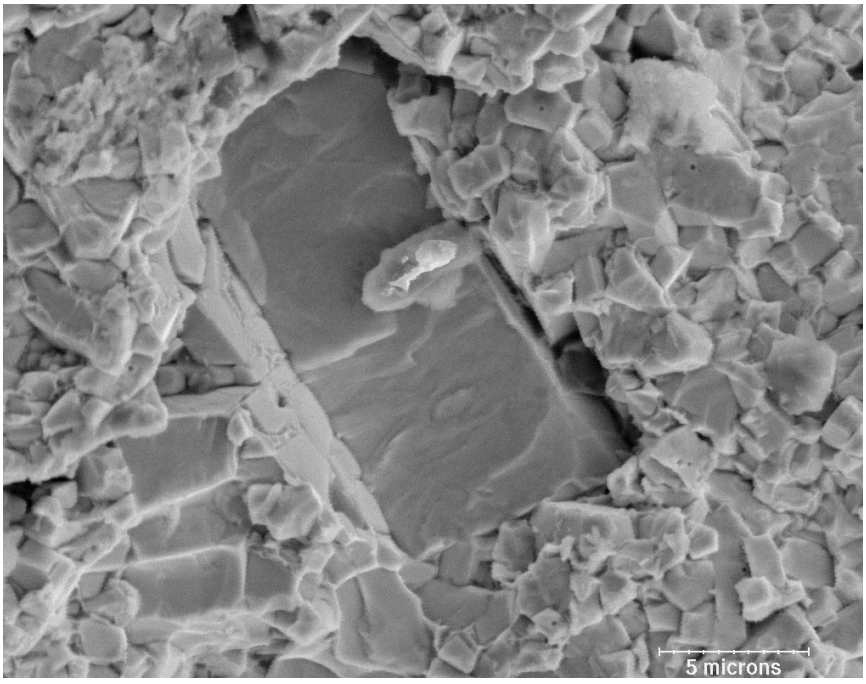

Figure 5.12: A large grain of WC-Co failed by transgranular cleavage. Mixed transgranular and intergranular failure can be observed in the surrounding grains.

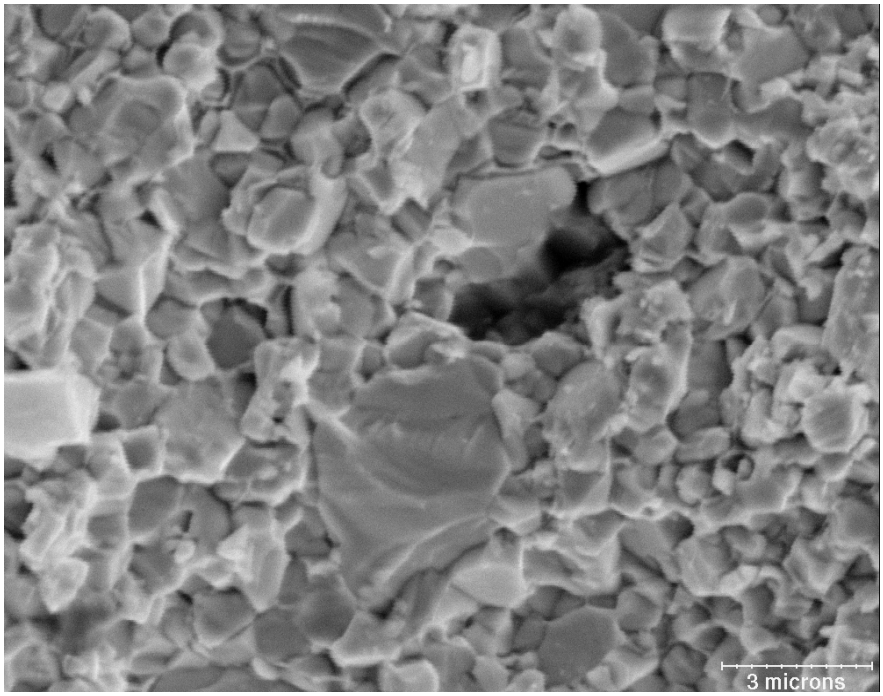

Figure 5.13: Scanning electron micrograph from a sample of WC-Co after penetration through a SiC B front plate and an aluminium witness block. Primary failure mode was intergranular cleavage of the small WC grains.

The region of the spall contained two distinct macroscopic features. High magnification of the fracture surface as shown in *Figure 5.11* and *Figure 5.12*, revealed that a high proportion of WC transgranular cleavage fracture occurred in the large grains of WC. However in the case of small grain size the fracture mode changed to predominantly intergranular cleavage (*Figure 5.13*). Information regarding the proportion of transgranular and intergranular fracture surface can be obtained using prepared mounted samples. For the WC-Co sample generally 68% of the WC grains had failed by intergranular cleavage (grain counting over a specific region). The fracture samples retrieved from the rear cylindrical body of the residual penetrator were found to display the same fracture surface cleavage as the fracture surfaces at the front ogival nose.

Figure 5.14 displays a second WC-Co core spall fragment recovered after penetrating a SiC B front plate and an aluminium witness block, also sectioned and mounted for SEM analysis. This spall fragment was taken from a sample inclined to the plane of shock wave. *Figure 5.15* displays the typical microstructure observed in this region of the residual penetrator.

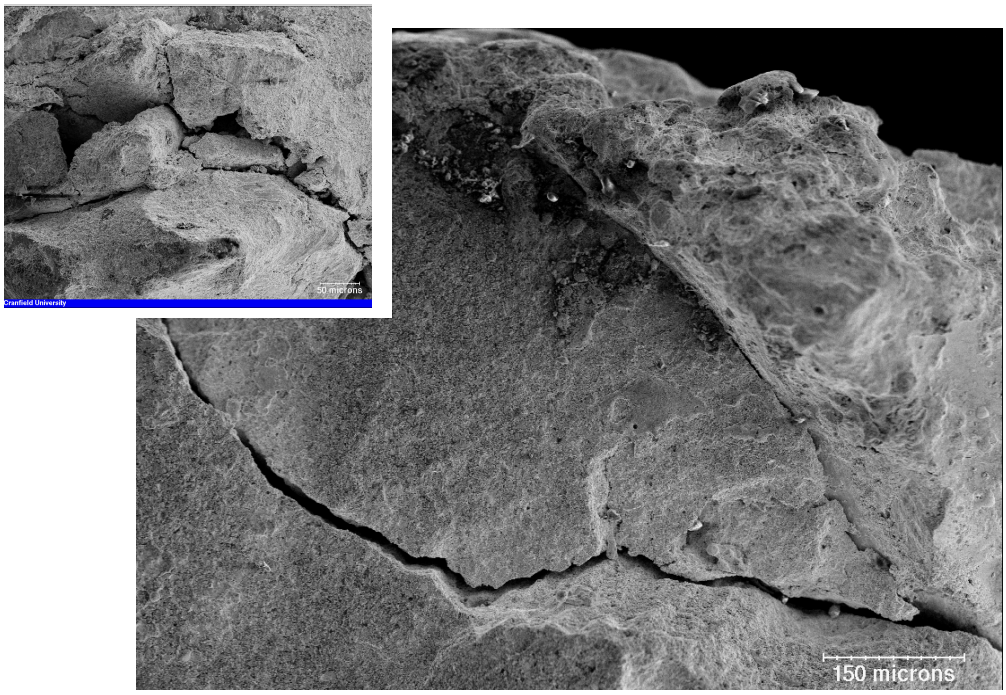

Figure 5.14: Fracture surface of WC-Co taken from a rear sample, revealing a large crack propagated across the diameter of the core. Top left, sample from the same core mid section.

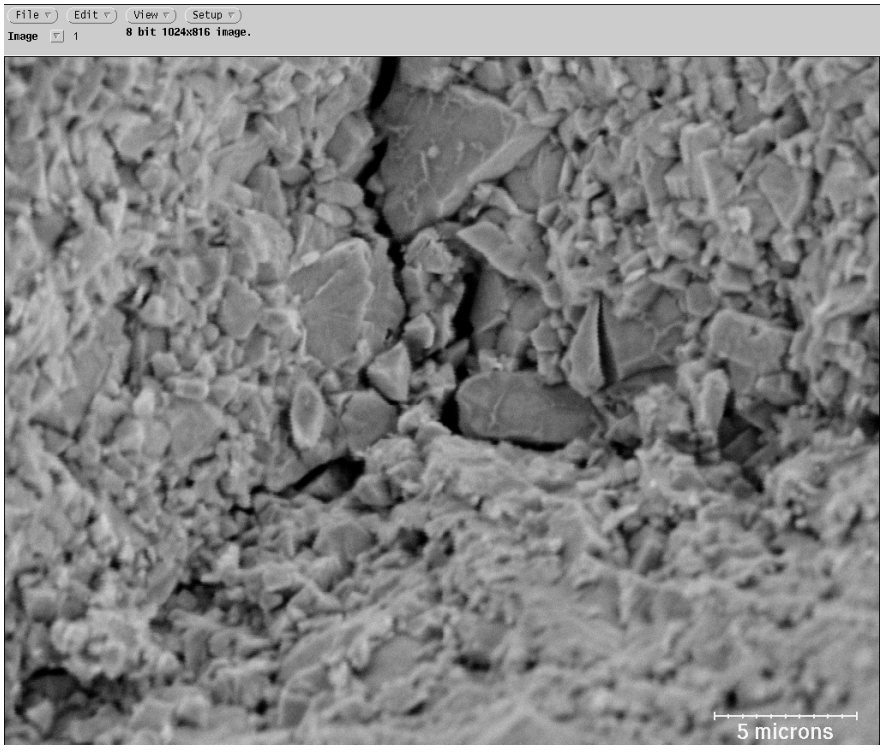

Figure 5.15: Micrograph from a sample of WC-Co after penetration through a SiC B front plate and an aluminium witness block, inclined to the plane of shock-wave (*Figure 5.14*).

Exposed facets such as fracture surfaces can be viewed directly in the SEM. It was noted that the central region of the BS41 WC-Co core contained two distinct macroscopic features. Some regions of fracture were evident on the core surface parallel to the plane of the shock wave and larger areas of rougher surface consisting of facets inclined to the plane of the shock wave. These facets were typically of the order of 10 microns across whereas those in regions parallel to the shock wave plane were of the order of 50 to 100 microns.

A final analysis of the crack propagation was performed. A full description of this fracture phenomenon can be found in Lawn and Wilshaw [187]. *Figure 5.16* displays a crack that was tracked along the fractured core sample retrieved after firing into the SiC B front plate and 1318b witness block. Crack propagation is a complex process involving a large number of microscopic events [188]. For example, *Figure 5.17* shows a secondary crack initiated at particularly weak WC grain adjacent to the main crack. The competition between intergranular and transgranular failure fracture displayed in *Figure 5-11* to *Figure 5-13*, depending on local conditions shows why prognosis of WC-Co failure is generally difficult. As previously described, the simplest inherent flaw to appreciate is the pore, where the largest flaw tends to produce the greatest stress concentration. *Figure 5.3* (*pp. 132*) shows a pore in the WC-Co sample revealed by the SEM. In summary, it was found that the cleavage of WC grains (transgranular failure) at predominately large grains and WC – WC grain boundary decohesion at the Co matrix (intergranular failure) had a tendency to follow paths of undesirable features (such as pores and microcracks).

Microstructural examinations of the residual penetrators retrieved after firing at different velocities (750 – 1100 m/s) into two different ceramic targets (SiC B and Sintox-CL) revealed similar progressions of deformation and failure.

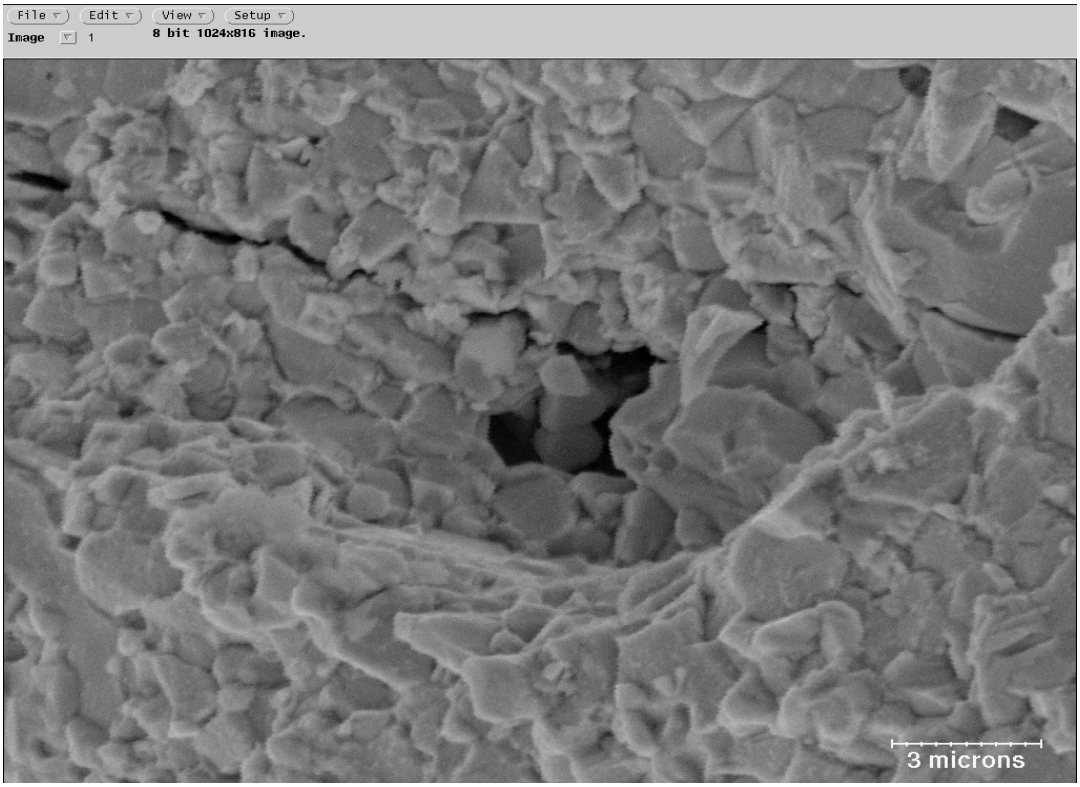

Figure 5.16: Crack propagation arrests at a major void

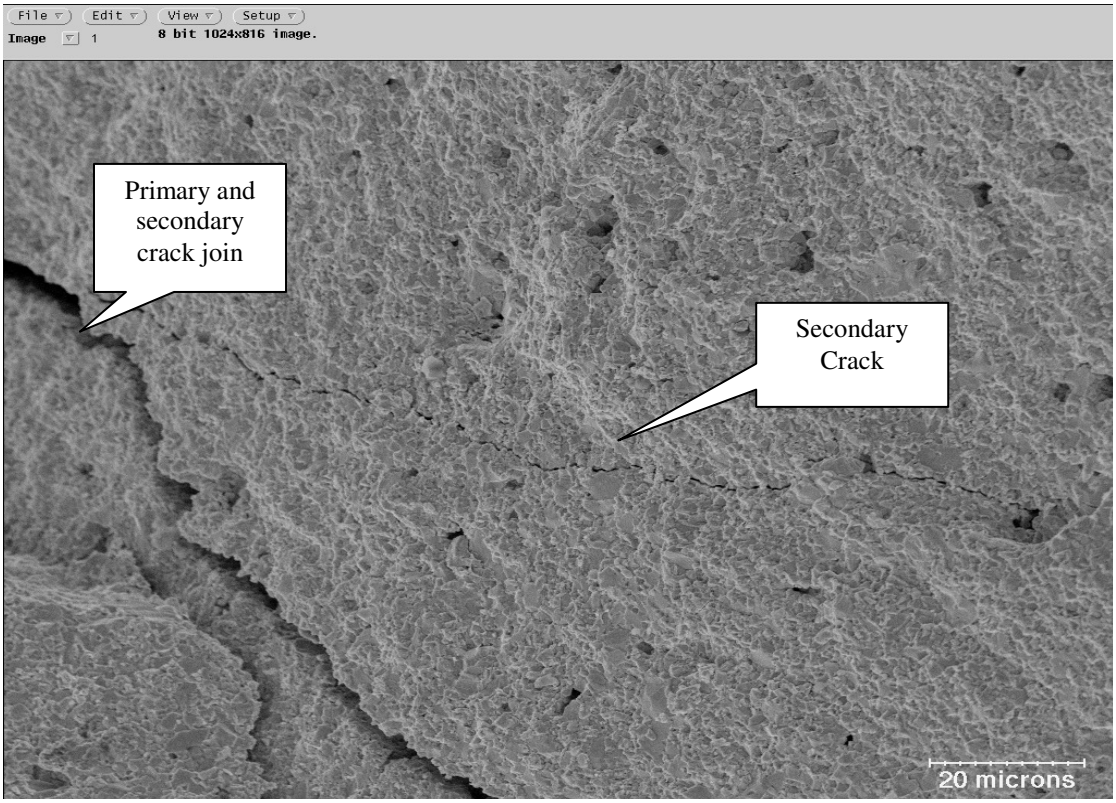

Figure 5.17: Large primary crack with a small secondary crack that propagated through major void regions.

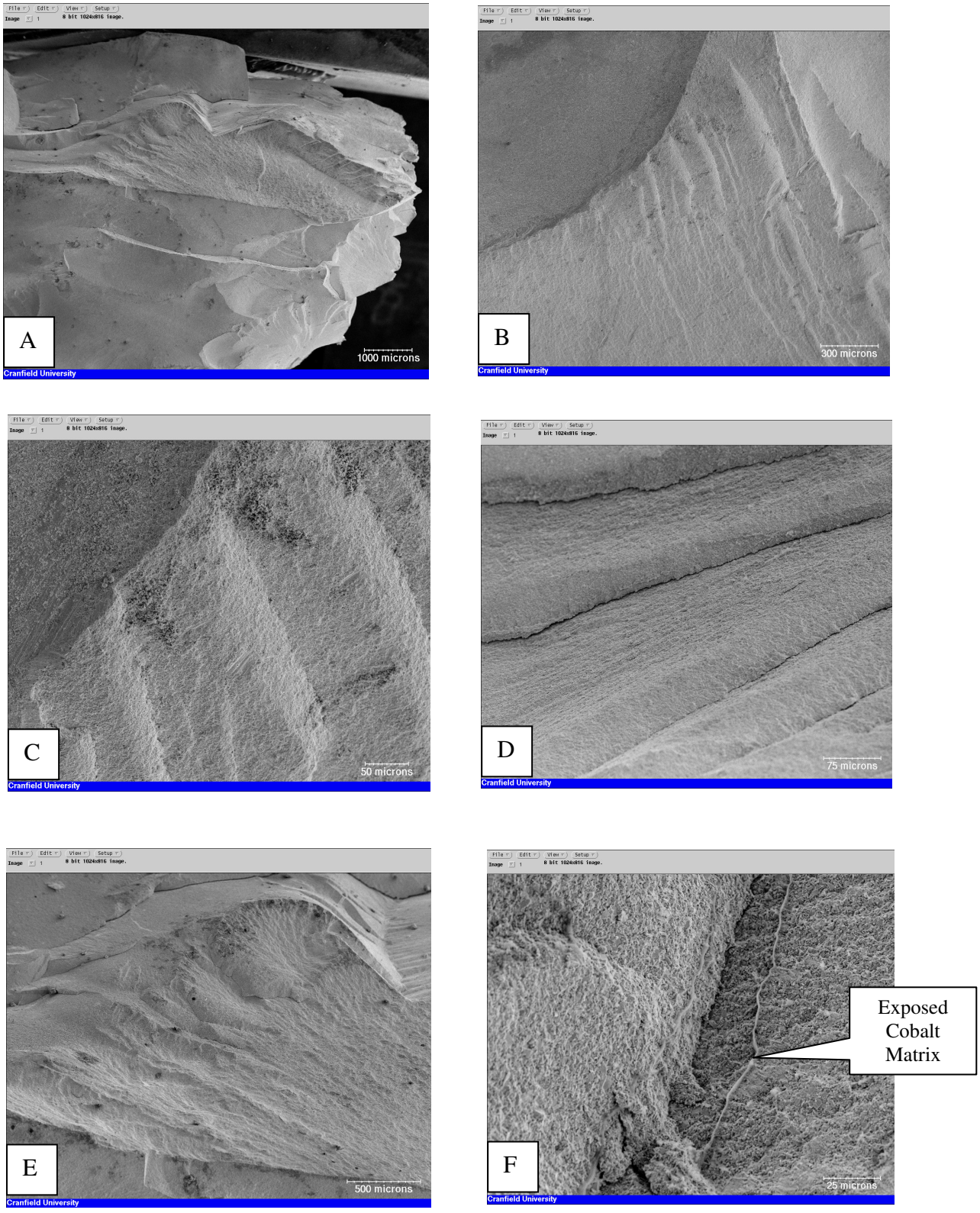

Figure 5.18: Six fracture surfaces removed from different residual penetrators after penetrating SiC B. (A) WC-Co spall section (B – E) Different regions from spall section A - Typically a "River" cleavage failure pattern formed during prominent regions of transgranular cleavage and (F) Exposed Co matrix prominent down a primary crack.

Figure 5.18 (A – F) presents six micrographs taken from a WC-Co spall fragment retrieved after penetrating SiC B at muzzle velocity of 1016 m/s. For all fractured samples subject to microstructural examination, the fracture failure was continuous and distributed between both WC and matrix phases. The brittle fracture propagated over the interface between the second-phase component and the Co matrix. Exposed Co can be observed in *Figure 5.18, F*.

5.4 Discussion

In the initial stages of penetration, the projectile shattering phase is the most critical if the ceramic armour is to be efficient (*Section 2.3.2, pp, 41*). During sub-hydrodynamic impact of the projectile this fracture mechanism occurs early in the process [76]. During penetration, the ceramic fracture conoid initiates at the interface between the projectile and the target. The geometry of the cone will depend on the contact area between the projectile and target, the thickness of the ceramic tile and the velocity of the projectile. As the fracture conoid is formed it effectively reduces the KED of the projectile.

Figure 5.10 (*pp. 139*) displays a typical failed WC-Co core sample in which extensive spallation is clearly visible. As the elastic-plastic stress wave propagates into the projectile upon tip impact, crushing and therefore radial displacement and axial splitting can occur. Material failure near to a free surface away from the area of application of the impulse load has been studied extensively but the phenomenon of the failure of brittle materials is still not well understood. The problem of spallation is discussed by Andrews *et al*. [189], Grady [20,26,190], Pickup *et al*. [183], and in some detail in Zucas [76].

Unlike static fracture where one fracture or crack forms and propagates through the material, dynamic fracture consists of four basic stages [76]:

- Rapid nucleation of micro-fractures at a large number of locations in the material
- Growth of the fracture nuclei in a rather symmetric manner
- Coalescence of adjacent micro-fractures

- Spallation or fragmentation by formation of one or more continuous fracture surfaces through the material.

The rapid nucleation of micro-fractures at a large number of locations can occur due to a number of flaws. Ceramics generally do not come close to their theoretical strength due to a number of inhomogeneities such as pores, voids and micro-cracks providing sources for crack propagation (*Section 2.2.4 & 2.2.6*). The WC-Co samples taken from the BS41 were marked with a high number of these undesirable features. The fracture in brittle materials can occur at usually unpredictable levels of stress, by the sudden propagation of a crack initiated at these features.

The relatively open porous morphology of the WC-Co is revealed. There are two types of pore in sintered materials: open, which are open to the surfaces of the sintered bodies and closed, which are isolated and not open to the surface [34]. The BS41 samples displayed significant open porosity. This is a generally an undesirable feature for many technical applications as it offers large internal surface area for absorption of dirt and more importantly crack propagation. Furthermore, the presence of pores tends to decrease the mechanical strength of the material and the Young's modulus decreases with increased porosity (*Section 2.2.6, pp. 36*) [191]. From its relatively high porosity we can hypothesise that the WC-Co in the BS41 was processed in the traditional low cost liquid phase sintering process. The disadvantage of low temperature processing is that, in the absence of chemical reactions, wetting of the ceramic by the metal phase is not always achieved. In such cases porosity is not completely eliminated. Further understanding of the processing of the Russian WC-Co core could provide answers.

During analysis it was clear that a high concentration of indentations and internal cracks were also visible in unfired samples. It is commonly observed that machining cracks penetrate approximately a grain dimension [35], and the production of the core requires machining operations which could lead to surface damage. A significant number of cracks propagating along grain boundaries on the machined surface and cleavage planes 2 - 5 μm in diameter (approximately one-grain size) suggests cracks formed during machining operations.

Figure 5.19 below shows two prominent exposed grains. A layer of molten aluminium and other impurities had coated each grain. This demonstrates the high temperatures generated during the penetration process. Surface flaws present in the WC-Co material assist these thermal stresses to cause failure.

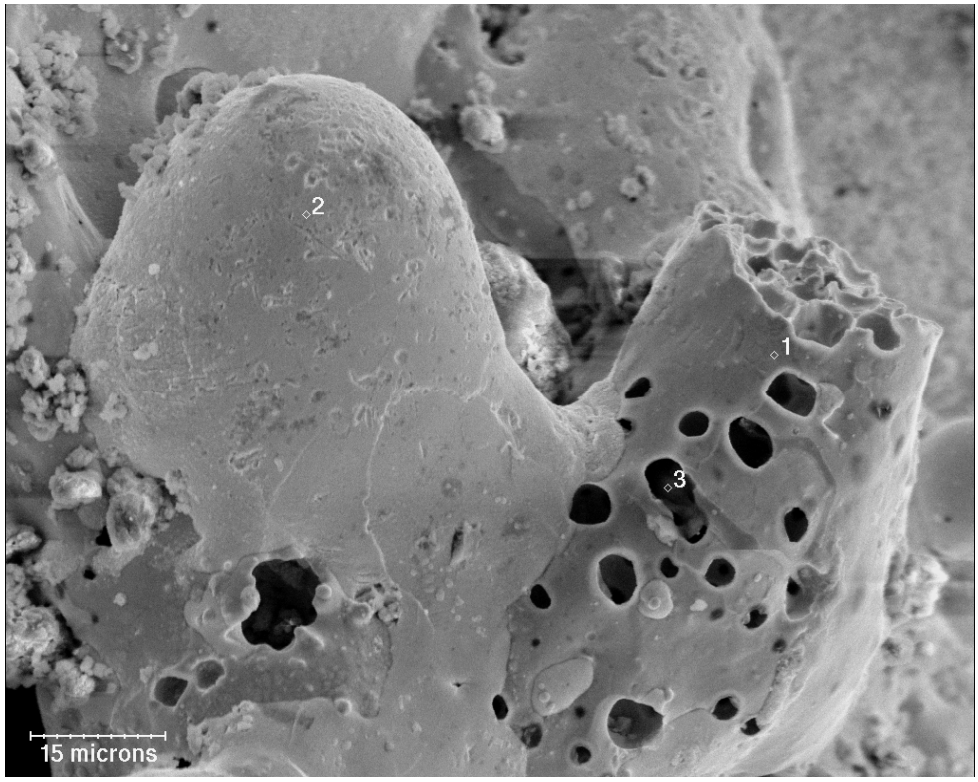

Figure 5.19: Cleavage surface of fractured WC-Co coated in aluminium and other impurities after impact into a SiC B front plate and aluminium witness block

Another important microstructural feature is grain size. The varied WC grain size within the BS41 14.5 mm sample may be attributed to the impurities in the raw materials like Fe and Pb (*Figure 5.8, pp. 137*) and variability in the manufacturing process conditions. During manufacture, to form WC powder requires a number of heating and milling stages. A mass of WC is produced by a solid state reaction is then crushed and milled to form a fine powder. Therefore, such variation in size particles of WC could be the result of incomplete milling (*Section 2.5.3, pp. 59).*

Itia *et al,* analysed three WC-6%-Co samples and found that as grain size was increased (sub-micron to coarse), both hardness (1800 to 1400 Hv) and compressive strength (5400 to 3100 MPa) were reduced whilst fracture toughness increased (10.8

to 12.8 MPa) [192]. The manufacturing process is important because with variations in grain size, porosity and void fraction, the relevant characteristics, namely toughness, strength and hardness may all be affected. These difficulties have mostly been overcome as a result of the careful selection of powders and cleanliness in processing as well as consistency in the processing conditions [36]. The BS41 core had a Vickers hardness of 1289 Hv (2 kgf load). With such a low hardness, comparing *Itia et al,* ceramic samples, we can predict a low compressive strength whilst fracture toughness may be high in the order of 12.8 MPa for the BS41 WC-Co [192].

The present work has clearly suggested that both void fraction and the manufacture of the material both assist and influence the WC-Co failure. The high concentration of flaws observed in the Russian WC-Co sample make it difficult to predict failure *via* numerical analysis.

5.5 Summary

To gain a better understanding of the WC-Co, and the failure after impact, the Scanning Electron Microscope and Energy Dispersive X-Radiography have been used to provide a detailed account of morphology and chemical composition. The aim of this study was to provide useful information to validate a numerical WC-Co material model in the non-linear dynamic code AUTODYN 2D.

The microstructural changes and deformation processes that had occurred in the WC-Co projectile core after planar impact were examined. The work was performed with the aim of analysing the relationship between the observed microstructural damage and the terminal ballistic performance of the WC-Co projectile. This would assist in the development of the numerical model.

During manufacture of WC-Co the processing conditions control such things as porosity, relative proportions and strengths of the phases present and the integrity of the interfaces between these phases. It is these factors which are dominant in determining the material's mechanical properties.

The microstructural evidence presented suggests that spall failure of the WC-Co core was likely to be dominated by a number of microstructural features including grain size, high porosity and microcracking within the manufactured material. Results also strongly suggest that fragmentation is increased as the hardness of the front plate is increased and the acoustic impedance of the witness block is reduced. Therefore careful management of ceramic hardness and, stress and shock wave propagation by altering acoustic impedance properties of the armour system are of paramount importance in providing enhanced resistance to WC-Co penetration.

The core sample failed by two different types of mechanisms, transgranular and intergranular cleavage. The dominant failure mechanism in small grains (3 – 7 μm) was intergranular fracture and transgranular fracture was observed in the larger grains (20 μm). The competition between intergranular and transgranular failure could make it very complex to predict the failure of WC-Co using a numerical model.

The marked variation in DoP observed in *Chapter 4* might be due in part to the uneven distribution of deformation between both WC and the Co matrix phases. The present results strongly suggest that at the cost of high hardness and high porosity, the Russian BS41 sample has a reduced tensile strength and thus low toughness. These are important factors that must be considered for numerical modelling of its failure.

Chapter 6

Development of a Numerical Material Model to Predict Tungsten Carbide – Cobalt Failure

Use of a commercial numerical material model to verify the failure phenomena of WC-Co

A numerical model of the failure of tungsten carbide-cobalt (WC-Co) subject to dynamic loading has been successfully developed. Experimental data from the literature were used to determine constants for the WC-Co material model in AUTODYN 2D. Plate impact test data provided the strength and pressure responses of intact WC-Co.

6.1 Numerical Modelling for Ballistic Application

Numerical models are powerful tools that predict the sequence of events that occur during the penetration process. Development of an appropriate physically-based WC-Co constitutive material model is a practical method of providing insight into the penetration phenomenon observed during the impact of the BS41. It is valuable in both design and planning of an effective armour solution to defeat the projectile. These models represent a significant advantage as they are highly controllable and flexible, whereas practical experimentation is often compromised by physical limitations of the equipment used (*Chapter 3*). A disadvantage, however, is that they require considerable computer processing and are subject to uncertainties and limitations due to inherent assumptions.

Many computer hydrocodes have been developed over the past decade. The impact phenomenon has been accurately simulated by using physically-based constitutive failure models [77]. The WC-Co material model was developed using the non-linear transient dynamic numerical code AUTODYN-2D. Other computer codes have been used to simulate ballistic events. These include; HEMP (Hydrodynamic Elastic Magneto and Plastic Computer Program) [77]; LS DYNA [149,193,194] and CTH (shock wave physics computer code) [20]. Due to unavailability of these codes AUTODYN Hydrodynamics code was used for the numerical analysis.

6.1.1 AUTODYN 2D

AUTODYN was first released by Century Dynamics in 1985 for non-linear dynamic solutions. It is a general-purpose engineering software package that uses finite difference, finite volume and finite elemental techniques to solve a variety of non-linear problems. The earlier codes neglected material strength and only considered hydrodynamic flow, thus became termed Hydrocodes. Today, numerous researchers use AUTODYN to model highly non-linear phenomena with complex material behaviour for a number of different applications, from explosive blast structure behaviour to hypervelocity impact of shaped charge warheads [195]. AUTODYN has provided good agreement with experimental research and insights into different

impact phenomena [116, 196, 197, 198, 199]. It is good for: high strains, large deformations, impact and penetration, material failure and fragmentation. The hydrocode can be characterised as highly time dependent with both geometric non-linearities (*e.g.,* large strains and deformations) and material non-linearities (*e.g.,* plasticity, failure, strain hardening and softening). Although numerical modelling of impact and penetration has been carried out for some time, few attempts to apply it to the response of WC-Co have been made.

A full description of the AUTODYN software may be found elsewhere [203,195,200]. In brief, AUTODYN is based on a set of continuum mechanics equations describing the dynamics of continuous media. These are a set of differential equations established from the principles of conservation of mass, momentum and energy based on initial boundary conditions (*Table 6-1*). These equations are solved numerically in AUTODYN using explicit time integration and various solution techniques.

Table 6-1: Continuum Mechanics Equations [Eq. 6-1 – 6-3] The author refers the reader to the list of abbreviations.

Conservation of Mass	$\frac{D\rho}{Dt} + \rho\nabla \cdot u = 0$
Conservation of Energy	$\frac{\rho Du}{Dt} = -\nabla P$
Conservation of Momentum	$\frac{de}{dt} + P\frac{dV}{dt} = 0$

[Eq. 6-1 – 6-3]

The effective use of AUTODYN numerical software to predict WC-Co failure impacting ceramic armour requires three basic components: *material data input* (*Section 6.2*) from experimental analysis to the constitutive laws, an appropriate *numerical technique* (*Section 7.2*) (termed the processor) and *verification* inferred from a comparison of the computational results to experimental data (*Chapter 7*).

6.2 Material Model Data Input

The BS41 penetrates in the sub-hydrodynamic regime where the material strength and mechanical properties are significant (*Section 2.3.2, pp. 41*). A number of material models in AUTODYN enable the non-linear material properties and empirical constants derived from experimental analysis to be introduced.

The material models of interest in AUTODYN require the user to define four components: *Equation of State* (EOS) (*Sections 6.2.3 - 6.2.5*), *strength model* (*Section 6.2.6*), *failure model* and an *erosion algorithm* (*Section 6.2.7*). Plate impact data (*Section 6.2.2*) were used to derive the data input and constants for part of these four components in AUTODYN 2D [20,147]. Care was taken not to break the simplifying assumptions and exceed the experimental results from which the empirical constants are derived.

6.2.1 Grady's Numerical Model

Numerical simulations were initially performed on the dynamic impact of a 14.5 mm WC-Co core into a 25 mm B_4C front plate with a 25 mm aluminium alloy backing plate. WC-Co material properties for the material model were taken from literature [20]. *Table 6-2* summarises the WC-Co data that was input into AUTODYN 2D from the Grady WC-Co based material model. This was to assess and validate the model data from literature at predicting the experimental failure of WC-Co.

The B_4C was modelled using a Polynomial EOS the Johnson-Holmquist strength model and failure model (*Appendix 5*). The aluminium was modelled using 7039 aluminium, shock EOS and a Johnson Cook strength model (*Appendix 5*). Both the B_4C and aluminium material data can be found in the AUTODYN material libraries [195]. A full description of the AUTODYN EOS, strength and failure models may be found elsewhere [195].

Table 6-2: Inputs to the AUTODYN model. WC-Co Constants from Grady [195]

Equation of State	Shock
Strength Model	Von Mises
Failure Model	Hydro or Principle Strain Failure Model
Erosion	Instant Geometric Strain
Reference Density (g cm^{-2})	14.91 [20]
Gruneisen Coefficient	1.32
Parameter C1 (ms^{-1})	5190
Parameter S1	1.16
Parameter Quad. S2 (sm^{-1})	0.00
Relative Volume, VE	0.00
Relative Volume, VB	0.00
Parameter C2 (ms^{-1})	0.00
Parameter S2	0.00
Reference Temperature (K)	300.00 (Room Temperature)
Specific Heat (C.V.) ($Jkg^{-1}K^{-1}$)	0.00
Shear Modulus (kPa)	2.557×10^8 (calculated assuming v = 0.22 and K = 371.4 GPa) [201]
Yield Stress (kPa)	4.00×10^6 [20]
Tensile Failure Stress (kPa)	0.02
Maximum Shear Strain	1.00×10^{20} *
Hydro Tensile Limit (Pmin) (kPa)	-3.5×10^6
Crack Softening, G_f (Jm^{-2})	0.0
(Kc ($mMm^{-3/2}$)	0.0
Erosion: Inst. Geo. Strain	3.0

* This is the maximum value allowed by AUTODYN 2D and it is input to the simulation to avoid generating unwanted shear failures.
[] Papers used to extract experimental results to implant into the model

Ceramics are generally strong in compression and weak in tension (*Section 2.2*). Such material properties make it difficult to directly predict the response of the material to experimental tests. Numerical simulations enable a wide range of design / analysis studies to be performed in an efficient manner. *Figure 6.1*, *Figure 6.2* and *Figure 6.3* present computational results using the WC-Co material model properties described in *Table 6-2*. *Figure 6.1* shows the WC-Co core impacting the B_4C at 1016 m/s. It can be seen that there is significant dwell and mass erosion of the projectile. The tensile failure strain was increased and the results are shown in *Figure 6.2* and *Figure 6.3*. A summary is presented in *Graph 6-1*.

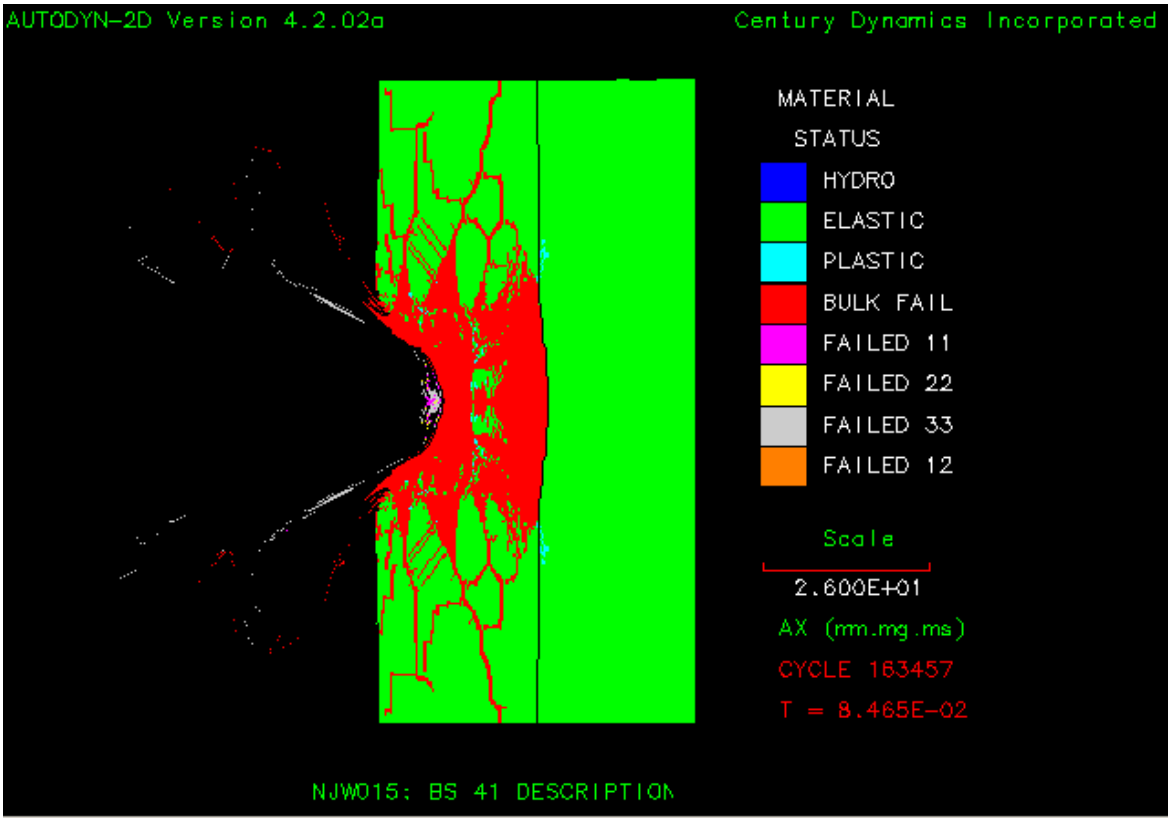

Figure 6.1: 14.5 mm WC-Co core impacting 25 mm B_4C front plate with a 25 mm aluminium alloy back plate, WC-Co tensile failure strain 0.5%.

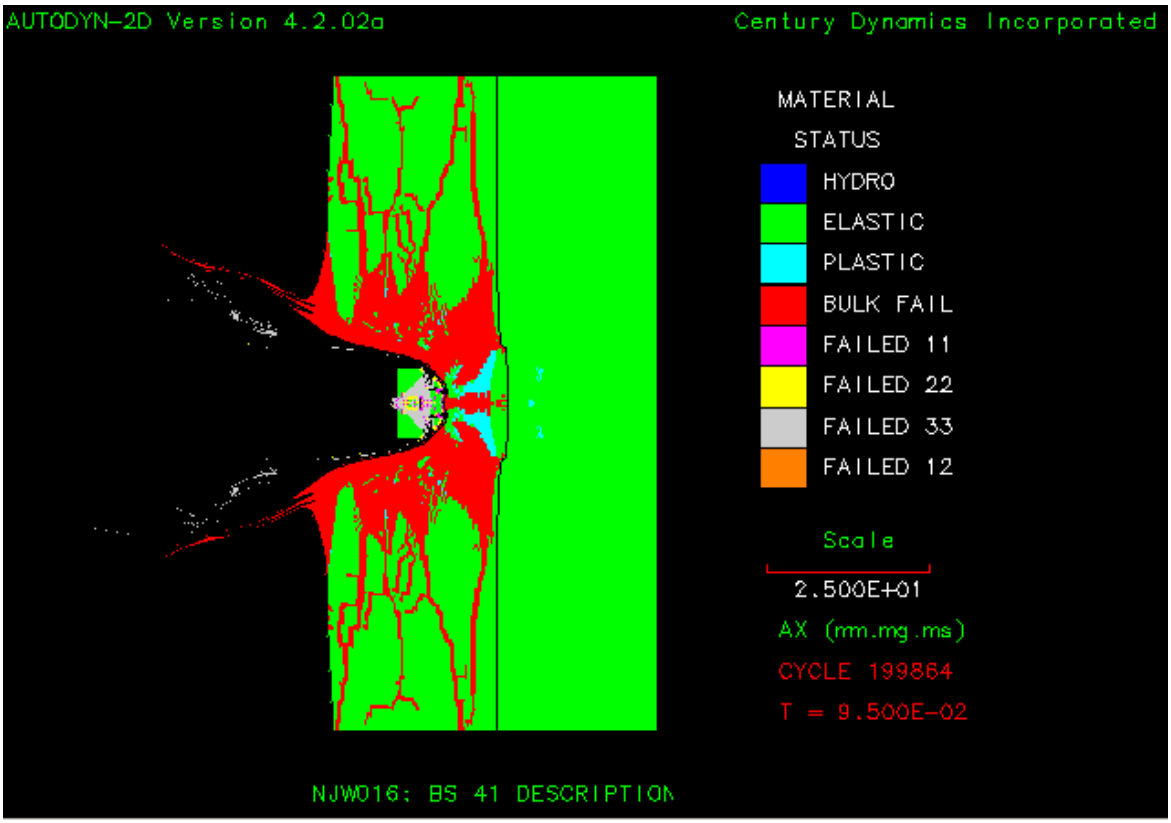

Figure 6.2: 14.5 mm WC-Co core impacting 25 mm B_4C front plate with a 25 mm aluminium alloy back plate, WC-Co tensile failure strain 0.75%.

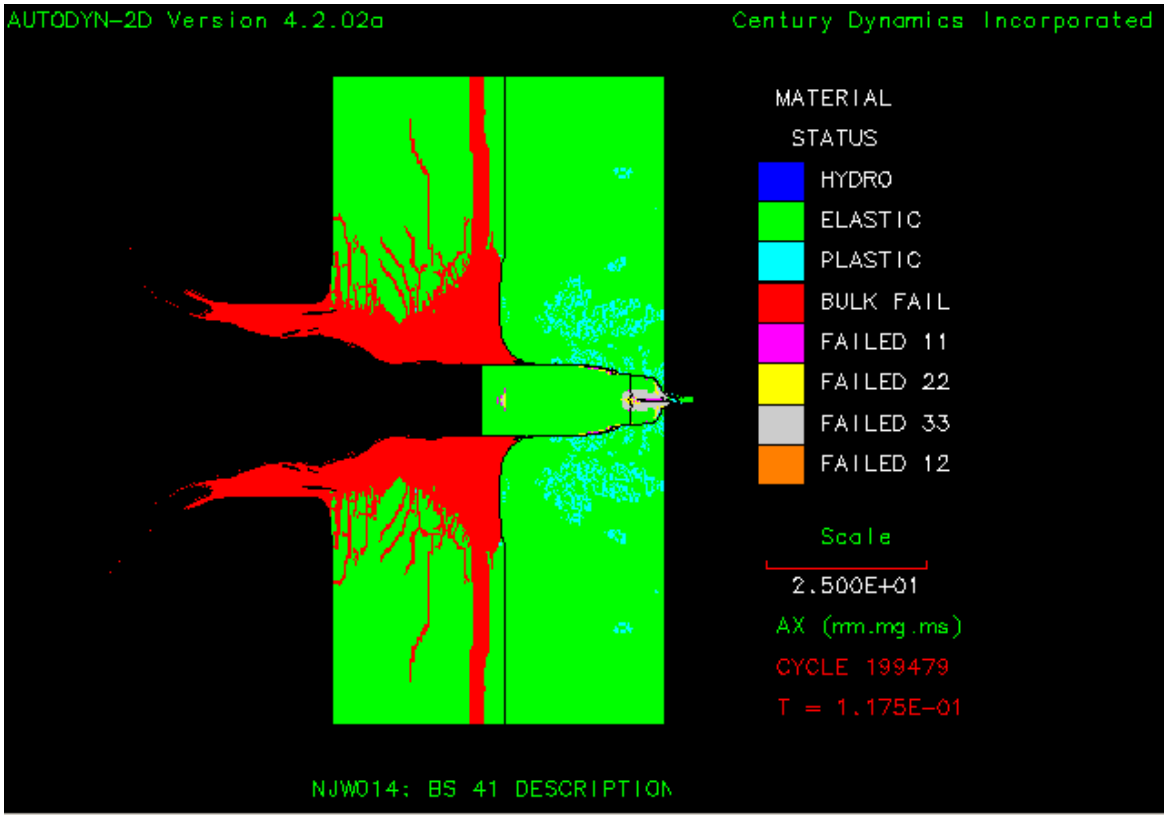

Figure 6.3: 14.5 mm WC-Co core impacting 25 mm B_4C front plate with a 25 mm aluminium alloy back plate, WC-Co tensile failure strain 1.00%.

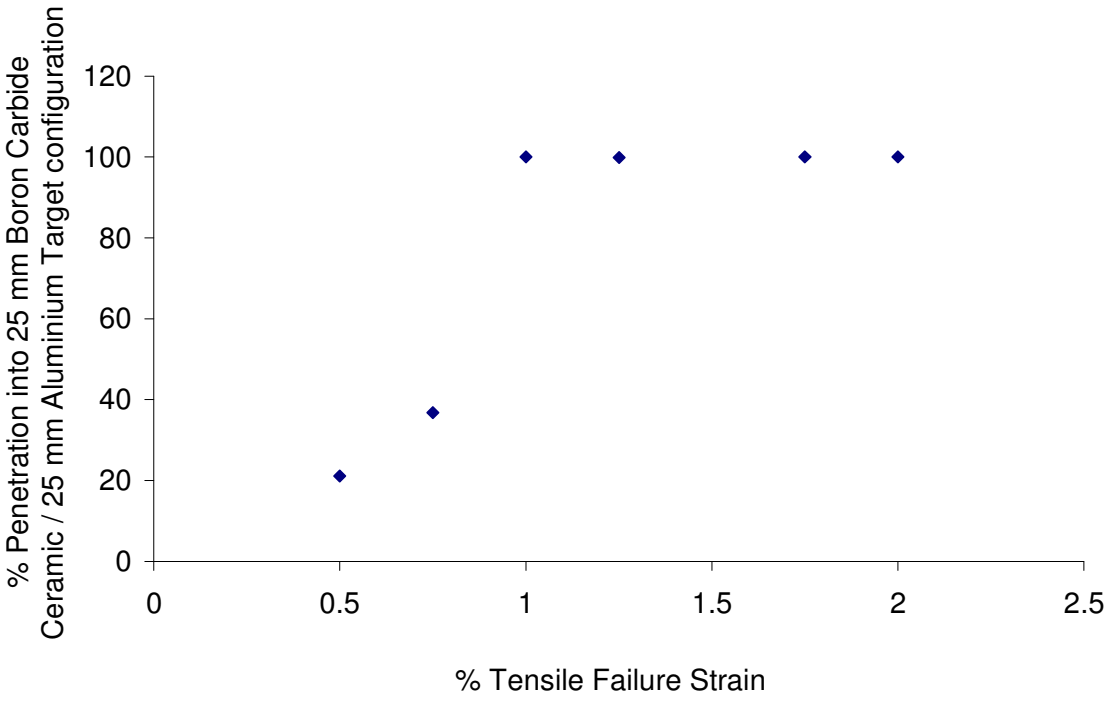

Graph 6-1: Graph displaying WC-Co projectile tensile failure strain against, penetration of a B_4C ceramic front plate and an aluminium back plate.

The factors limiting the strength of ceramics are fracture and plastic deformation. Because WC-Co is a brittle material the typical failure mechanism under dynamic compressive loading is fracture. The fracture evolves at usually unpredictable levels of stress, by the sudden propagation of a crack initiated at a pore, grain boundary or micro-crack (*Section 2.2*). The brittle failure and crack propagation is not exhibited in the computation results using the WC-Co data described by Grady [20]. Experimental results presented by Gooch *et al.* and Roberson *et al.* (*Figure 6.4*) show the brittle nature of a 7.62 mm WC-Co core projectile after impacting a B_4C front plate [22,125]. The effect of tensile failure strain on WC-Co failure, and penetration depth (*Graph 6-1*) can illustrate the importance of the observed failure of WC-Co using the correct inputs in a numerical model.

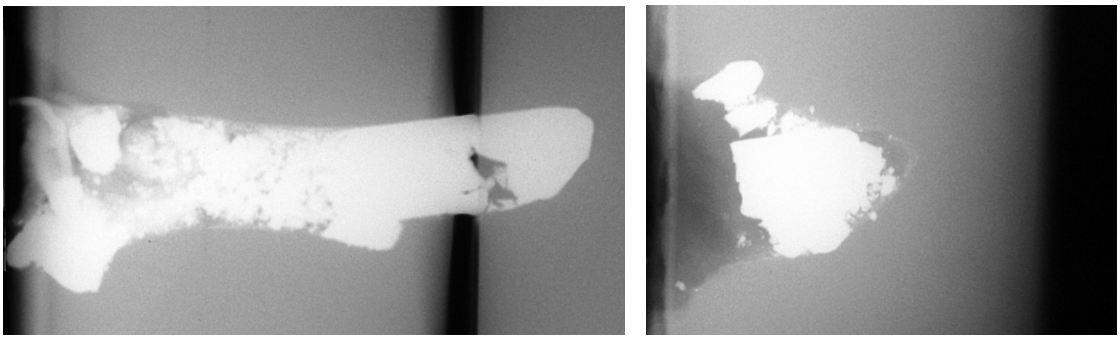

Figure 6.4: Results from Roberson *et al.*: 7.62 mm FFV impacting 6.5 mm and 7.6 mm B_4C from left to right respectively. Increased fragmentation observed with increased thickness of ceramic front plate [125].

An important feature of computational modelling is the assumption that the material fails and has significantly reduced strength after failure. Such an assumption does not relate closely to the crack nucleation and tensile crack growth and strength degradation that one would expect in WC-Co during dynamic loading. Hazell *et al.* provide a comprehensive presentation summarising a physically based crack softening approach to modelling the failure of brittle materials [166,198,202]. A tensile crack softening model is required in the WC-Co material model, improving the post failure response of the WC-Co. The crack softening model allows for the gradual loss of strength as cracks propagate through the material, whereas instantaneous failure models can give rise to mesh sensitive results.

The present AUTODYN numerical software does not contain a WC-Co material model [203]. Experimental data from the literature were used to determine constants

for the WC-Co material model and plate impact test data provided the strength and pressure responses of intact WC-Co. The following presents a discussion of how the pressure, strength of the intact material and the damage of the failed material, are determined. Comparisons are drawn from experimental data in *Chapter 7*.

6.2.2 Plate Impact Data

The well-characterised experiments described were used to derive constants for the AUTODYN numerical material model. Experimental analysis of the uniaxial strain compressive shock and release waves in WC-Co, using a single stage powder gun facility, were performed by Grady [20,26]. When the rate of loading is so fast that the material does not have time to deform radially and instead deformation occurs in only one direction, the loading condition is known as uniaxial strain loading. This is normally used to characterise shock waves experimentally.

The projectile consisted of a mounted disk of aluminium with a poly methyl methacrylate (PMMA) backing. The target consisted of a Kennemetal (K-68) WC-Co target sample bonded with epoxy to a lithium fluoride backing plate. *Figure 6-5* is a schematic diagram of the experimental projectile and target set-up for the plate impact experiment performed by Grady. *Table 6-3* compares the different WC-Co material properties tested (including K-68 material properties), to the Russian BS41 WC-Co core sample.

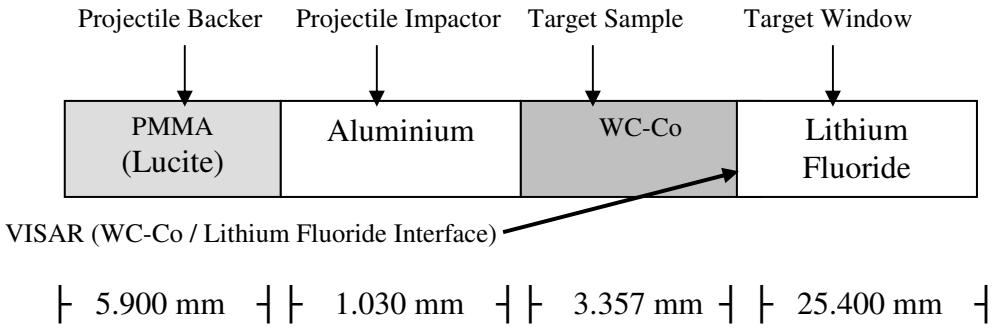

Figure 6.5: Experiment 8403, Tardec Report [27], Grady and Moody [20] Velocity Interferometer System for Any Reflector (VISAR) (*not to scale*).

Table 6-3: Description of different Tungsten Carbide – Cobalt (WC-Co) Materials Tested (Adapted from Tardec and Grady Report [20,27,148].

Reference	**Grady [20,27]**	**Grady [20]**	**Grady [20,27,148]**	**Russian BS41**
Manufacturer	Kennametal-K68	AP	Cercom	Russian
Processing	Pressure-less lq. Phase Sintered	Pressure-less lq. Phase Sintered	Hot Pressed	Un-Known
Average Grain Size (μm)	-	-	0.9	3-20[7]
ρ, Density (kg/m^2)	14930	14910	15530 – 15560	14532[1]
V_L, Longitudinal Velocity (m/s)	6895	6918	7040 – 7050	6800[2]
V_T, Shear Velocity (m/s)	4165	4149	4300 – 4320	4165[6]
Bulk Velocity (m/s)	4941	4991	4960	4959[10]
***E*, Young's Modulus (GPa)**	630	-	692	652[5]
***G*, Shear Modulus (GPa)**	260	257	288	252[4]
Bulk Modulus (GPa)	364.5	371.4	383.0	371.35[9]
***v*, Poisson's Ratio**	0.213	0.219	0.200	0.209[3]
Compressive Strength (GPa)	5.82	4.42	-	4.5[9]
HEL (GPa)	4	4	6.6 ± 0.5	4[9]
Spall Strength (GPa)	2.7	3.5	-	2[10]
Hardness Rockwell (Ra)	93	86 – 92	-	88
Co (% Volume)	5.7	0.05 –0.2	-	5.45[8]
Ta	1.9	-	-	-
Ni	-	3 – 4	-	-
Fe	-	0.4-0.8	-	0.34[8]
Nb	< 0.3	-	-	-
Ti	< 0.3	-	-	-

Explanatory notes to Table 6-3:

[1] The density of the WC-Co Core was determined by immersing the core into de-ionised water at 25 ^{o}C using nylon string with negligible immersed volume.

[2] The PUNDIT Longitudinal Wave Velocity Machine was used to measure the WC-Co longitudinal wave velocity (see *Section 3.6.1*). The Longitudinal Wave Velocity of the BS41 Russian WC-Co sample was 6800 m/s ± 5 m/s.

Relationships were used to derive the elastic parameters of the WC-Co BS41 material including: Poisson's Ratio, Shear Modulus and Young's Modulus.

[3] The Poisons ratio v was determined by using the relationship:

$$\nu = \frac{1 - 2 \cdot (V_T / V_L)^2}{2 - 2 \cdot (V_T / V_L)^2} \qquad \text{[Eq. 6-4]}$$

where, V_T and V_L are the Shear and Longitudinal velocities respectively.

[4] The shear modulus, G was calculated using the relationship:

$$G = V_T^2 \cdot \rho \qquad \text{[Eq. 6-5]}$$

[5] The Young's Modulus, E was calculated using the following relationship:

$$E = \frac{V_L \cdot \rho \cdot (1+\nu)(1-2\nu)}{1-\nu} \qquad \text{[Eq. 6-6]}$$

[6] The Russian BS41 WC-Co sample was taken to have a shear velocity (V_T) of 4165 m/s. This was from the Kennametal, K-68 sample used for the numerical model. K-68 contained a similar percentage concentration of material constituents including Co (*e.g.,* K-68 Co-5.7% / BS41 Co-5.45%) and material properties such as density (*e.g.,* K-68 14930 kg/m^2 / BS41 14532 kg/m^2) to that of the BS41 Russian sample.

[7] The average grain size was measured using the SEM (results presented in *Section 5.1*).

[8] A. Beadsley, Sheffield Testing Laboratory results, 2002.

[9] Reference Grady [20]

[10] Derived from numerical simulations (*Chapter 7*)

When the target is loaded during the plate impact experiment, the impact produces a compressive shear wave of uniaxial strain, which propagates across the WC-Co and through the WC-Co / Lithium Fluoride interface. Plate impact experiments enable various material properties to be measured characterising the WC-Co material response to dynamic loading. A VISAR was used to measure the compressive and release wave behaviour by monitoring the longitudinal motion at the target sample / window interface. This is converted to a time-resolved history of the velocity [20,27]. The results are displayed in *Table 6-4*.

Table 6-4: Test Data from Tardec report, original data from LASL Shock Hugoniot Data [27].

Test No.	**WC-Co Material**	**Initial Density, ρ_0 (g/cm^3)**	**Shock Velocity, U_s (m/s)**	**Particle Velocity, u_p (m/s)**	**Pressure (GPa)**	**Density (g/cm^3) ρ**
1	K-68[1]	15.050	5569	220	18.439	15.669
2		15.010	5706	351	30.062	15.994
3		15.010	5671	369	31.410	16.055
4		15.000	5734	437	37.586	16.237
5		15.060	5720	440	37.903	16.315
6		15.020	5965	679	60.835	16.949
7		14.990	6008	712	64.123	17.005
8		14.990	5971	750	67.129	17.143
9		14.990	6857	1445	148.526	18.992
10		15.030	6927	1484	154.503	19.128
11		15.020	6912	1489	154.585	19.144
12		15.000	7108	1712	182.533	19.759
13		15.010	7175	1751	188.577	19.856
14		15.010	7334	1819	200.242	19.961

[1]K-68 material properties can be found in *Table 6-3*

Table 6-4 provides a description of the shock velocity, U_S against particle velocity, u_p for the K-68 WC-Co material measured during the plate impact experiment. The data also provide the results of the K-68 WC-Co pressure response against compression (volumetric change, initial density (ρ_0) and final density (ρ)).

The peak stress occurs in the σ_x direction and can be measured for both elastic and plastic response (*Figure 6.6*). The lateral stresses σ_y and σ_z, which are equal, occur due to the uniaxial strain configuration of the experiment. *Equation 6-9* relates the pressure P, to σ_x, σ_y and σ_z.

During plate impact experiments a one-dimensional strain shock is formed that can deform the material at a very high rate. Under these impact-loading conditions it is possible to measure, from the shock profile, the point at which the ceramic material ceases to behave elastically, and begins to behave in-elastically. This point, at the peak stress for the elastic regime, is referred to as the Hugoniot Elastic Limit (HEL). The WC-Co samples exhibit a much greater (in the range of 4 - 6.5 GPa) HEL compared to metals (in the range of 0.5 – 2 GPa).

Initial computational runs were performed using two-dimensional AUTODYN analysis concentrating on the σ_x stress, using a Lagrangian mesh.

$$P = \frac{1}{3}\left(\sigma_Z + \sigma_Y + \sigma_X\right) \qquad \text{[Eq. 6-9]}$$

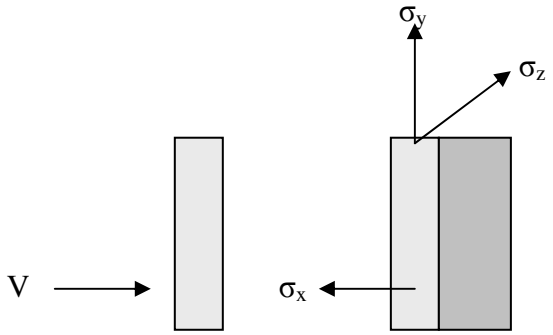

Figure 6.6: Schematic Stress Diagram

The experimental results from plate impact data were used to derive the empirical constants for the numerical model. The following presents a discussion of how the EOS, strength and failure damage model, were determined for the WC-Co material model. A summary of the constants used in the derived material model can be found in *Table 6-10,* page 178.

Initially the WC-Co material model, derived from plate impact data, was compared to the experimental ceramic – window interface velocity profile presented in Grady and Moody (*Table 6-4*) [20,27]. This concentrated on the longitudinal stress analysis from experimental plate impact data. The output of the derived WC-Co model (*Table* 6-10) was then compared to experimental results from the impact of WC-Co spheres into PMMA at various velocities (*Section 7.3*) [20,27]. The computational results were compared with the observed longitudinal and hydrostatic response and the strength (shear and deviator stresses) properties of the WC-Co.

6.2.3 Equation of State

The EOS takes care of the volumetric part (volume change) of the numerical calculation expressing the pressure (volumetric stress) as a function of density and specific internal energy (temperature) within the material. The AUTODYN user manual provides a comprehensive presentation summarising each of the EOS and their derivatives [203].

In the ideal gas equation pressure P is a function of specific density, ρ and entropy e:

$$P = fn(\rho, e) \qquad \text{[Eq.6-10]}$$

If the material is a liquid or gas, the influence of change in entropy e is small or negligible. Therefore, pressure can be considered as a function of density ρ (or specific volume). If the material is a solid, one approach is to consider the initial elastic behaviour expressed by an approximation to Hooke's Law (simplest form of EOS) [203], where strain is nearly proportional to stress, thus we have the linear elastic model:

$$P = K\mu \qquad \text{[Eq. 6.11]}$$

where, K is the material bulk modulus (an elastic constant) and μ is compression expressed by the relationship:

$$\mu = \left(\rho / \rho_o \right) - 1 \qquad \text{[Eq.6-12]}$$

and ρ_0 and ρ are the initial density and final density respectively. This form of EOS is good when considering small compressions. Derived data for the Linear EOS for the WC-Co material model are summarised in *Table 6-5*. The density and the elastic bulk modulus constants are taken from Kennemetal K-68 WC-Co (*Table 6-3*) used in the plate impact experiments performed by Grady [20,27].

Table 6-5: Linear EOS numerical data input for AUTODYN 2D.

	Reference Density (g / cm^3)	**Bulk Modulus (kPa)**	**Reference Temperature (K)**	**Specific Heat (C. V.) (j / kgK)**
Measured Values	14.93	3.64 x 10^8	300.00 (Room Temperature)	Unknown

For higher compressions a more suitable EOS is required for the purpose of comparing the computational failure to the observed behaviour of the BS41. Initial simulation runs were set up comparing the Linear EOS with the two types of EOS most commonly used in simulating ceramic materials, the shock and polynomial EOS. The shock and polynomial EOS are good at simulating ceramic failure at large compressions. These are based on a Mie Gruneisen formulation.

6.2.4 Shock EOS for Material K68

Five shock parameters are considered; P, ρ, e, particle velocity u_p and shock velocity U_S. Once the constants of the EOS are calculated, only one pair of shock parameters is required to derive any of the remaining parameters. These five shock parameters can be separated into ten pairs, provided by twenty different equations described in comprehensive detail in Meyer [204].

During plate impact experiments, by using the VISAR technique, u_p and U_S can be established over a wide range of pressures. A Hugoniot curve can then be constructed describing the relationship. The empirical relationship between shock velocity, U_S and the particle velocity, $u_{p,}$ is described by:

$$U_S = c_O + Su_P \qquad \text{[Eq. 6-13]}$$

where, c_o is the bulk sound speed of the material and S is an empirical constant. This then produces the reference Hugoniot for the Mie Gruneisen EOS.

The plate impact results for u_p and U_S for the plastic regime are reported in *Table 6-4*. *Graph 6.2* below presents the empirical linear relationship between u_p and U_S from the shock velocity data. There is a linear relationship between the shock and particle velocity where S is the gradient and c_o is the intercept.

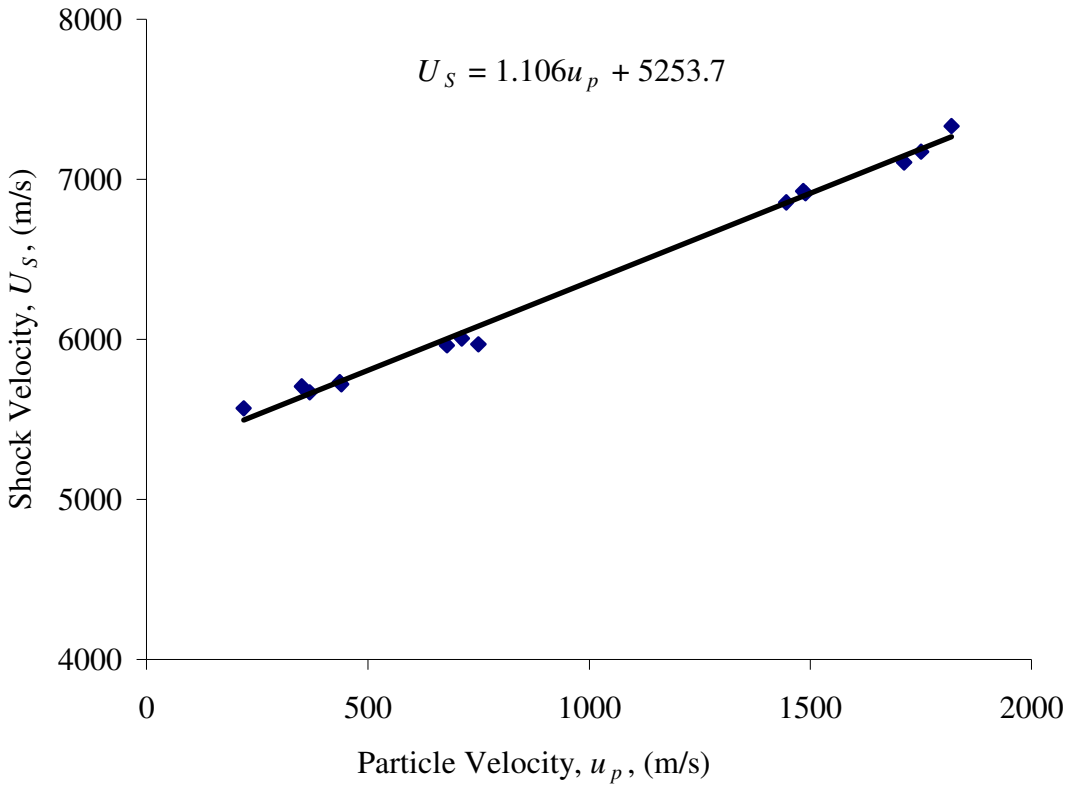

Graph 6-2: Particle – shock, Hugoniot curve, and the derivation of the shock EOS from the shock velocity data, Grady, *Table 6-4* in the plastic regime.

Using the two forms of *Equation 6-14* and 6-*15*, and the linear line fit to *Graph 6-2* derived by Grady impact data, we can determine the bulk velocity, c_o = 5253.7 m/s and the constant S = 1.106 for the EOS model, thus *Equation 6-13* becomes:

$$U_S = 5253.7 + 1.106u_P \qquad \text{[Eq. 6-14]}$$

Based on the shock Hugoniot, the Mie-Gruneisen form of EOS is established from the following equations. The Mie-Gruneisen is of the form where P varies linearly with energy, e at constant volume, V.

$$P = p_H + \Gamma\rho(e - e_H) \qquad \text{[Eq. 6-15]}$$

where Γ is the Gruneisen Gamma and from the conservation of energy, e may be determined. The two functions e_H and P_H are the Hugoniot pressure, and the Hugoniot energy respectively, that may be derived from the following equations:

$$e_H = \frac{1}{2}\frac{p_H}{\rho_O}\left[\frac{\mu}{1+\mu}\right] \qquad \text{[Eq. 6-16]}$$

$$p_H = \frac{\rho_O c_O^2 \mu(1+\mu)}{\left[1-(s-1)\mu\right]^2} \qquad \text{[Eq. 6-17]}$$

where, using the empirical relationship, the Gruneisen Constant is:

$$\Gamma \approx 2S - 1 \approx \frac{\alpha K}{\rho C_R} \qquad \text{[Eq. 6-18]}$$

where, K is the isothermal bulk modulus, α is the coefficient of expansion and C_R is the specific heat at constant volume. Substituting values into *Equation 6-18*, we have:

$$\Gamma = (2 \times 1.106) - 1 \qquad \text{[Eq. 6-19]}$$

where the Gruneisen Gamma Γ is calculated to be equal to 1.212. *Table 6-6* presents the shock and thermodynamic properties of selected materials. *Table 6-7* summarises the shock EOS material data input for AUTODYN 2D, derived from the plate impact data.

Table 6-6: Shock and Thermodynamic Properties of Selected Materials

Material	ρ_0 (g/cm^3)	c_o (m/s)	S	C_p (Jg^{-1}K^{-1})	Γ
LiF	2.64	5150	1.35	1.59	2.0
Al-6061	2.7	5350	1.34	0.89	2.0
PMMA	1.19	2600	1.52	1.2	1.0
WC-Co (BS41)	14.93	5253.7	1.106	-	1.212
W	19.22	4030	1.24	0.13	1.8

Table 6-7: Shock Equation of State Constants for the WC-Co material model

Shock EOS Constants	Data Input	Reference
Reference Density (g/cm^3)	14.91	Material K-68 *Table 6-3*
Gruneisen Coefficient	1.212	*Section 6.2.4*
Parameter C1 (m/s)	5.2537 x 10^3	*Section 6.2.4*
Parameter S1	1.106	*Section 6.2.4*
Parameter Quad S2 (s/m)	0.00	Used for Bi-Linear fits
Relative Volume VE	0.00	Used for Bi-Linear fits
Relative Volume VB	0.00	Used for Bi-Linear fits
Parameter C2 (m/s)	0.00	Used for Bi-Linear fits
Parameter S2	0.00	Used for Bi-Linear fits
Reference Temperature (K)	300.00	Room Temperature
Specific Heat (C. V.)	0.00	Unknown
Shear Modulus (kPa)	2.60 x 10^8	Material K68 *Table 6-3*

It is important to remember that the linear relationship does not always hold true for high compressions and where thermodynamic effects are non-negligible. For cases at high shock strengths, the non-linearity in AUTODYN 2D of the shock and particle relationship can be defined by bi-linear fits. The results from the plate impact data providing a linear fit presented in *Graph 6-2*, so this was not found to be necessary.

6.2.5 Polynomial EOS

Graph 6-3 shows the pressure P as a function of the compression μ derived from *Equation 6-11*. The author refers the reader to *Table 6-4*, for the experimental data. From this we can establish a polynomial EOS. The polynomial EOS is a general form of the Mie-Gruneisen form of EOS. It has different analytic forms for states of

compression and tension. *Equation 6-20* is the form of EOS that defines the pressure. Several parameters are required for the polynomial EOS including the reference density, ρ and constants *A1* (bulk modulus), *A2* and *A3*:

$$P = A_1\mu + A_2\mu^2 + A_3\mu^3 \qquad \text{[Eq. 6-20]}$$

In *Equation 6-20* the constants *A1, A2* and *A3*, for the determination of the pressure are derived: *A1* = 413.26 x 10^6, *A2* = 441.24 x 10^6 and *A3* = 338.28 x 10^6. These constants were determined from the polynomial equation established from *Graph 6-3*.

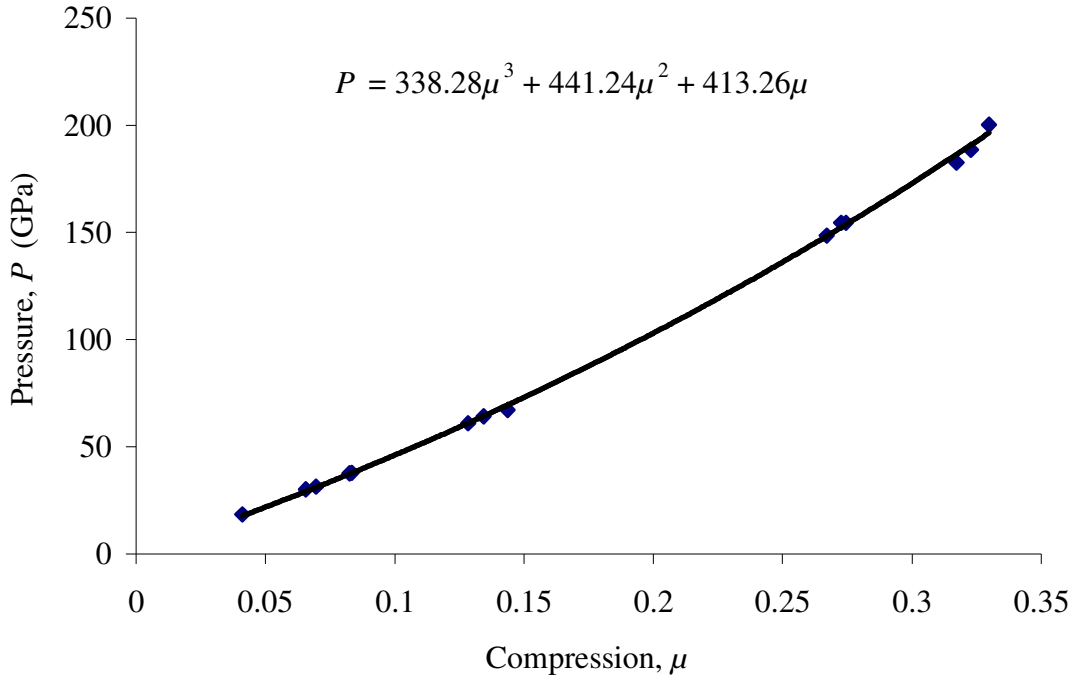

Graph 6-3: Polynomial EOS, data from Grady, *Table 6-4* [20]

Table 6-8 summarises the material property data in AUTODYN 2D for the polynomial EOS.

Table 6-8: Polynomial Equation of State Constants for the WC-Co material model

Polynomial EOS Constants	Data Input	Reference
Reference Density (g/cm^3)	14.91	Material K-68 *Table 6-3*
A1 (GPa)	413.26	*Section 6.2.6*
A2	441.24	*Section 6.2.6*
A3	338.28	*Section 6.2.6*
B0	0.00	-
B1	0.00	-
T1 (kPa)	0.00	(μ <0) Tension
T2 (kPa)	0.00	(μ <0) Tension
Ref. Temperature (K)	300.00	Room Temperature
Specific Heat (C. V.)	0.00	Unknown

As a result of increasing the loading intensity, the pressures generated may exceed the strength of the colliding solids, which then behave hydrodynamically [76]. The linear EOS is good for low compressions in the regions of sub-hydrodynamic behaviour of impacting solids. As the compression is increased significantly with increased dynamic shock, the shock and polynomial EOS are more suitable.

6.2.6 Piecewise Linear Strength Model

The material strength properties are extremely important in AUTODYN. The user is prompted to input a material strength constitutive relationship that calculates the flow stress in terms of a number of material and application-dependent parameters including strain, strain-rate and temperature. During impact of the WC-Co core projectile on a target system, stress waves are created away from the impact area (*Section 2.3.3*). As a result the diverging wave would separate into elastic and plastic deformation waves, with consequent differences in material response. If these local stress levels exceed the strength of the material we can expect failure (see *Figure 5.9, pp. 138* and *Figure 5.10 pp. 139*, for examples of spalling). The numerical methodology in AUTODYN is based on the work by Wilkins (1964) who extended the hydrodynamic codes to include strength effects [203]. The methodology to obtain the stress versus pressure graph was extracted from a Grady paper [20]. Grady indicates that there is little evidence of appreciable strain or strain-rate hardening and

that the dynamic yield stress of the WC-Co is 2.2 GPa. Results from the stress and strain and mean shear stress behaviour were obtained. The pressure was calculated using the equation:

$$\tau = \frac{3}{4}(\sigma_X - P) \qquad \text{[Eq. 6-21]}$$

where τ is the shear stress. Finally the strength (Von Mises equivalent stress) was obtained using equation:

$$\sigma_Y = \tau \cdot 2 \qquad \text{[Eq. 6-22]}$$

Table 6-9: Data extracted from Grady [20]

Strain	**σ_x GPa**	**$\sigma_y = \sigma_z$ GPa**	**Shear, τ**	**P**	**Von Mises**
0.0057417	4.092302	1.001292	1.545505	2.031629	3.091010
0.0075905	5.374931	1.465756	1.954587	2.768814	3.909175
0.0088822	6.125810	1.558058	2.283921	3.080672	4.567842
0.0101988	6.850286	1.922097	2.460945	3.564827	4.928189
0.0117882	8	2.297951	2.851025	4.198634	5.702049
0.0126966	8.589995	2.416836	3.086579	4.474555	6.173159
0.0140453	9.270814	2.690050	3.290382	4.883638	6.580764

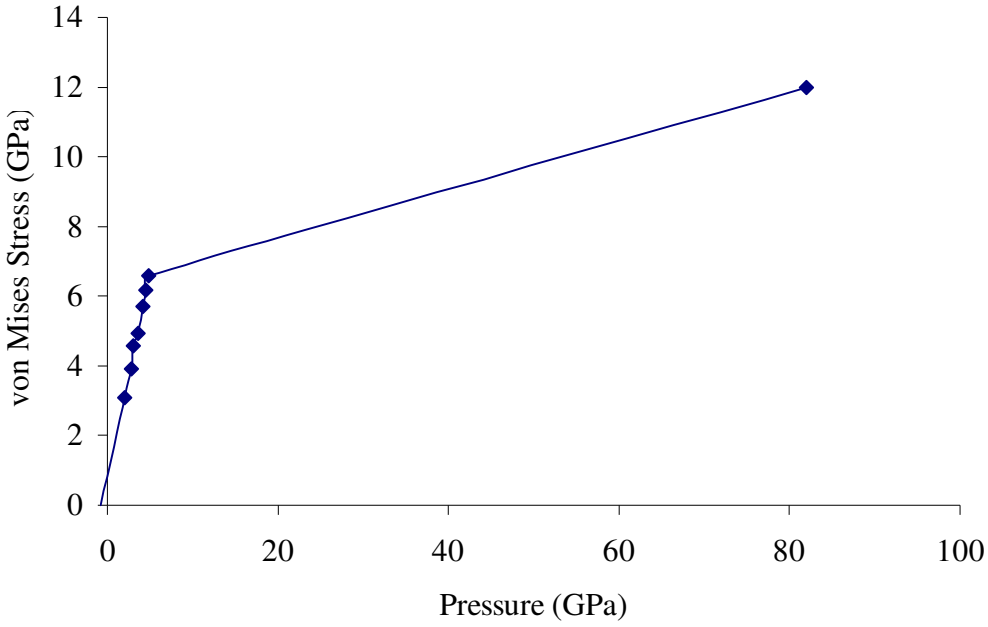

Graph 6-4: Von Mises Stress versus Pressure (GPa)

Graph 6-4 displays the strength (Von Mises equivalent stress) from the data of *Table 6-9* as a function of the pressure. *Table 6-10* summarises the constants used for the strength model. The yield stress at zero strain was taken from Grady [20,147]. The shear modulus used was from K-68, *Table 6-3*.

6.2.7 Failure Model

The fragmentation behaviour of the WC-Co core depends on the local failure of the material, thus the failure criterion plays an important part in the accuracy of the simulation. The failure criterion was derived by a comparison of ceramic–window interface velocity profiles from Grady and Moody plate impact data [20].

Materials are unable to withstand tensile stresses that exceed the local tensile strength. Several different failure models are available for use in AUTODYN. The user manual provides a comprehensive summary of each of the failure models, equations and derivatives [195]. Due to the limited amount of constitutive data available a principle stress model was used to describe the damage of the failed WC-Co material.

The principle stress model is a directional failure model, which is used to model failure initiation appropriate for spalling, plugging, delamination, petalling and disking [203,197]. Failure is initiated if the maximum tensile principle stress, or the maximum shear stress, exceed the materials limits. After failure the material is assumed to be isotropic, have no shear strength and be able to sustain only positive hydrodynamic pressures [203,197].

The dynamic tensile strength of the WC-Co can be tested in a controlled uniaxial strain geometry during plate impact tests. When the projectile (PMMA and aluminium) impacts the WC-Co (*Figure 6.5, pp. 159*), shock waves are created in both samples at the impact plane. The shock waves reflect as waves of decompression (tension) at the respective free surfaces (*Section 2.3.3*). If the tensile stress and duration is sufficient, fractures will nucleate, grow and coalesce at this plane, relaxing the tensile stress to zero.

During the plate impact experiments a low impedance VISAR window material Lithium Fluoride (LiF) is bonded to the back of the WC-Co material. The reflected wave is reduced by the impedance difference between the WC-Co sample and the LiF plates. The results of the spall experiment, in which a plate of WC-Co backed by LiF was subjected to planar impact by a thinner plate of PMMA, is presented. A sensitivity analysis of altering the tensile failure stress was performed. *Figure 6.7* presents the numerical AUTODYN 2D set-up.

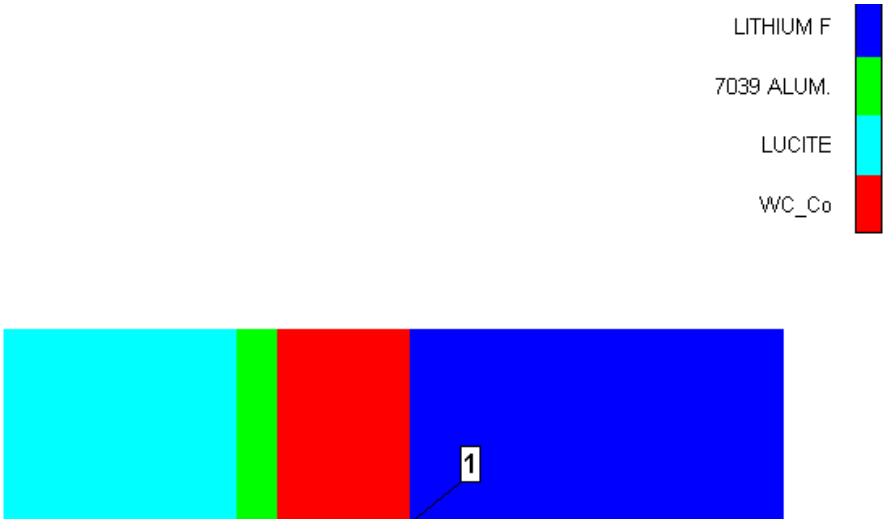

Figure 6.7: AUTODYN 2D numerical set up for plate impact response

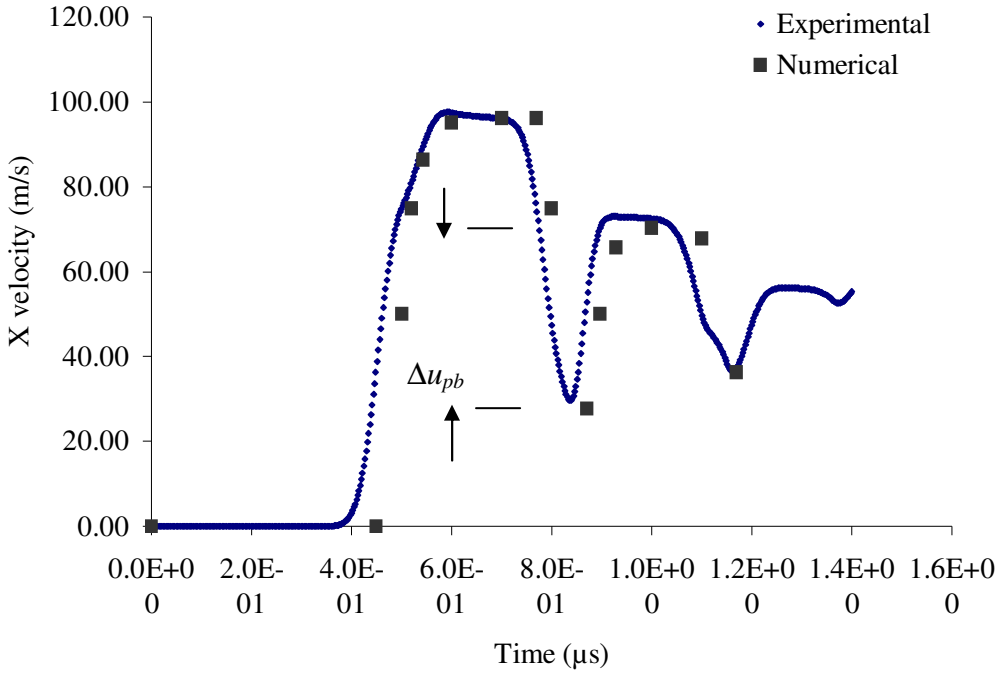

Figure 6.8: Comparison of computed stress history with ceramic-window interface velocity profiles from Test 8403, plate impact experimental data [27].

Figure 6.8 compares the computed stress history with the experimental ceramic-window interface velocity profiles from plate impact experimental data [27]. As previously described, the VISAR was used to monitor the interface velocity history. It

indicates that the computed spall signals from experimental data show good agreement with the numerical profiles.

In *Figure 6.8* the initial jump in velocity amplitude quantifies the magnitude of the precompression shock wave. The release wave is identified by the pullback signal at the recording interface. Spall strengths can be calculated from the tensile magnitude of this pullback through consideration of material impedance differences [190]. The spall strength (σ_{SP}) for the WC-Co can be calculated using the equation described by Grady:

$$\sigma_{SP} = \frac{1}{2}(Z_S + Z_W)\Delta u_{pb} \qquad \text{[Eq. 6-23]}$$

where, Z_S and Z_W are the elastic impedance of the sample and window respectively and Δu_{pb} is the magnitude of the spall-back signal as seen in *Figure 6.8*. Calculated spall strengths for the AP WC-Co are 3.5 GPa, whereas the K-68 WC-Co was 2.7 GPa.

To model the failure of the WC-Co a tensile failure stress of 3.5 GPa was used and the material was not allowed to fail in shear. This allowed the WC-Co to fail only once the maximum tensile failure stress was reached. A tensile crack softening model was used in the material model, improving the post failure response of the WC-Co. The crack softening model, unlike the instantaneous failure models, allows for the gradual loss of strength as cracks propagate through the material [203,58,166,198]. The softening slope is defined as a function of the local cell size and a material parameter, the crack softening (fracture energy) G_f. The fracture energy is related to the fracture toughness of the material by the following relationship (*see Section 2.2.5*):

$$K_c = \sqrt{EG_f} \qquad \text{[Eq. 6-24]}$$

where K_c is the fracture toughness and E is the Young's modulus. Substituting values of E from K-68 *Table 6-3* and K from Grady [20], into *Equation 6-24*, we get:

$$G_f = 160\, J/m^2$$

Finally, to avoid numerical problems with excessive grid distortion, which can cause the analysis to prematurely fail, an Instantaneous Geometrical Erosion Algorithm was used. As the strain in a WC-Co material cell exceeds a specific value the cell is eroded. The cell retains its mass, thus conservation of inertia and continuity of inertia are maintained, yet internal energy and strength are lost.

A comprehensive summary of the WC-Co derived model is described in *Table 6-10.* This model was used as the basis for the validation of the numerical simulation to experimental data.

Table 6-10: WC-Co Constants from the Material Model

Equation of State	Shock
Strength Model	Piecewise Linear
Failure Model	Principle Stress
Erosion	Instant Geometric Strain
Reference Density (g cm^{-2})	14.91 (Slightly below K-68) (*Table 6-3*)
Gruneisen Coefficient	1.212
Parameter C1 (ms^{-1})	5253.7
Parameter S1	1.106
Parameter Quad. S2 (sm^{-1})	0.00
Relative Volume, VE	0.00
Relative Volume, VB	0.00
Parameter C2 (ms^{-1})	0.00
Parameter S2	0.00
Reference Temperature (K)	300.00 (Room Temperature)
Specific Heat (C.V.) ($Jkg^{-1}K^{-1}$)	0.00 (Unknown)
Shear Modulus (kPa)	2.6 x 10^8 (*Table 6-3*, K68)
Yield Stress (kPa)	3.091 x 10^6 (Grady) [20,147]
Eff. Pl. Strain #	1: 0.0075905
Eff. Pl. Strain #	2-10: 1 E 20
Yield Stress #	1: 6.5807642 E 6
Yield Stress #	2-10: 1.2 E 7
Strain rate Constant:	0
Thermal Softening Exponent:	0
Melting Temperature (K):	3100 (WC-Co)
Tensile Failure Stress (kPa)	3.5 x 10^6
Maximum Shear Strain	1.01 x 10^{20} *
Crack Softening, G_f (Jm^{-2})	0.1
(K_c ($mM/m^{3/2}$)	6.4431 x 10^7
Erosion: Inst. Geo. Strain	3.5

* This is the maximum value allowed by AUTODYN 2D and it is input to the simulation to avoid generating unwanted shear failures.

6.3 Summary

The physical processes that occur during penetration are fairly well understood. Some of the important material properties have been identified and presented. As previously discussed, the first step of the proposed research programme was to construct a high level representation of the system. The problem that remained was to incorporate this information into a numerical material development program.

Numerical testing was carried out using the fully integrated, multi-physics, and interactive non-linear dynamic analysis software, AUTODYN 2D. The code has been developed since 1985 and is well suited to the analysis of solving complex engineering and ballistic impact problems analysing the behaviour of materials under transient dynamic loading. The present AUTODYN numerical software does not contain a WC-Co material model.

An initial study has been performed and a simplified methodology was presented to enable the determination of the numerical model strength and failure parameters derived from experimental data. Four components are required to define the WC-CO material model: EOS, strength model, failure model and an erosion algorithm.

The EOS relates the pressure (volumetric) as a function of density and specific internal energy. Experimental results of the uniaxial strain compressive shock and release waves in WC-Co were extracted from literature. A Hugoniot curve formed from experimental plate impact data was used to determine the bulk sound speed and empirical S constant producing the reference Hugoniot for the Mie Gruneisen EOS. Using an empirical relationship as described, the Gruneisen Gamma was derived.

The material strength constitutive relationship calculates the flow stress in terms of number of material and application-dependent parameters including strain, strain-rate and temperature. Using the stress, strain and mean shear stress results from literature, the pressure and von mises equivalent stress were calculated for the Piecewise Linear strength model. The density and shear modulus were taken from the Kennametal sample as it contained similar material constituents to the Russian WC-Co material sample. This aimed to optimise the accuracy of the derived constants for later comparison with the Russian BS41 WC-Co core (*Chapter 7*).

Using a comparison of the ceramic-window interface velocity profile from impact data a sensitivity analysis was performed to derive the tensile stress for the principle stress directional failure model. A tensile crack softening model was required allowing for the gradual loss of cracks propagating through the material. The tensile failure stress of 3.5 GPa was determined and the crack softening was calculated using fracture toughness and Young's modulus providing the remainder criteria for the material model. Extensive grid distortion occurred thus, an Instantaneous Geometrical Erosion Algorithm was incorporated into the material model.

The model was validated comparing the computed stress history with the experimental ceramic-window interface velocity profiles. It was demonstrated that the numerical estimation of WC-Co behaviour using a shock EOS, a piecewise linear strength model and a principle failure stress failure model provides a good method to estimate spall behaviour under dynamic loading in AUTODYN 2D. It indicates that the computed spall signals show good agreement with the numerical profiles. This provides a preliminary tool taking into account the WC-Co core failure observed in experimental analysis.

Chapter 7

Numerical Validation

An initial phase of work has been carried out using the explicit non-linear transient dynamic numerical code AUTODYN 2D. A numerical material model derived from experimental data has been successfully developed to provide a preliminary tool for studying the WC-Co failure (*Chapter 6*). The principle model components included the shock EOS, a piecewise linear strength model and a principle stress failure model. The material model provided a good tool to estimate WC-Co spall behaviour under dynamic loading. Plate impact test data, described in *Section 6.2.2*, provided the strength and pressure responses of intact WC-Co. After the material has failed, there was not enough evidence from classical mechanical test methods on comminuted material to determine the hydrostatic and shear response of the failed material. Thus, the response has been inferred from a comparison of computational results to sphere impact data. To supplement this work, an initial series of numerical simulations has been conducted and compared to experimental data from the impact behaviour of the Russian BS41 14.5 mm projectile. Errors in the results and implementational difficulties are discussed.

7.1 AUTODYN 2D Simulation of WC-Co

7.1.1 Numerical Validation Introduction

The ability to accurately numerically model WC-Co enables a wide range of modelling studies to be designed and used as a tool to predict experimental results. Analysis of the material model requires that the material input properties detailed in *Chapter 6, Table 6-10* are adhered to. Alterations of such data should only be justified by performing appropriate impact experiments to determine the new empirical constants. The reported numerical model was based on data from Kennemetal-K-68, *Table 6-3*. This was used as it had a Co concentration (Co-5.7%) similar to that of the Russian BS41 sample (Co-5.45%). This is important, as it has been shown that the WC-Co properties are affected by altering Co concentration (*Section 2.5.3*).

Derivation and results presented in this work are for two-dimensional analysis with an axially symmetric projectile (*i.e.,* rotations about the axis of symmetry) in normal incidence. Extending the analysis to describe three-dimensional systems would increase the complexity of the numerical run and thus would require a significant increase in computational running time. However, three-dimensional analysis provides a more accurate representation of the circumferential fragmentation [196]. The results of the numerical simulations can be used to offer some insight into the fragmentation process.

7.2 Numerical Processor for Modelling WC-Co Failure

Different physical problems can be modelled using different geometrical mapping techniques. The various processors available use a coupled finite difference / finite volume approach. The numerical processor selected to model the impact of WC-Co on ceramic configured armour was Lagrange. It is used for modelling solid continua and structures and operates on a structured mesh where the vertices of the mesh move with material flow velocity. There is no transport of material from cell to cell unlike, for example, the Eulerian processor where the mesh is fixed and the material moves

through it. The disadvantage with Lagrange is that if excessive material movement occurs, the numerical mesh may become highly distorted leading to an inaccurate and inefficient solution. Rezoning after termination of the problem or altering the erosion strain are possible ways around this. It is also good at tracking free surfaces, interfaces and history-dependent material behaviour. To model WC-Co, localised and material strength characteristics are important: diffusion is not expected within the material, therefore Lagrange is a good processor to use.

The second processor considered is a relatively new technique, Smooth Particle Hydrodynamics (SPH), a Lagrangian gridless technique that uses a set of interpolation points to model a continuum. Lagrange and SPH processors may be combined and interact during a simulation according to the AUTODYN interaction logic. This automatically checks for any interaction between grids and corrects for any penetration that may have occurred. Smooth Particle Hydrodynamics is good at meshing where high deformations are expected. It can be used to overcome problems of mesh tangling and remove the need for erosion algorithms. It can be used in conjunction with erosion and friction, making it an effective processor for ballistic impact. Because of this, SPH and its implementation have been detailed and discussed frequently in literature in recent years [196,205,206,207,208,209].

For full descriptions of the other processors, the author refers the reader to the AUTODYN manuals [195]. Currently other processors include the Euler processor for modelling fluids, gases and large distortions, the Arbitrary Lagrange Euler (ALE) processor for flow models, and the Shell processor for modelling thin structural elements. These processors are generally faster as there is no transport of material through the mesh distortions, yet they are still computationally expensive. During impact of the BS41 into ceramic armour we are only interested in looking at the interaction of solids. Therefore the Lagrangian processor was used with SPH.

Initial modelling predicting the response of WC-Co sphere impact into PMMA was performed using the Lagrangian formulation. Adaptive meshing was used to alleviate the problem of excessive distortion of elements, which occurred during large deformation studies. As a result SPH was used instead to alleviate the problem.

7.3 Sphere Impact Test

Assessment can be made of the accuracy of the numerical simulation and the implanted theoretical prediction models using experimental data. An extensive experimental study on the impact of WC-Co spheres, conducted by Grady *et al*., has been presented [20]. To supplement his experimental work, the WC-Co material model developed in *Chapter 6* was compared to sphere impact data carried out by Grady *et al.* to validate the simulated material response [20,147].

Experimental analysis of the impact of WC-Co spheres into PMMA (density 1186 kg/m^3) at velocities between 2 - 4 km/s ± 1% with a two stage light gas gun has been reported [20,147], (set-up shown in *Figure 7.1*.)

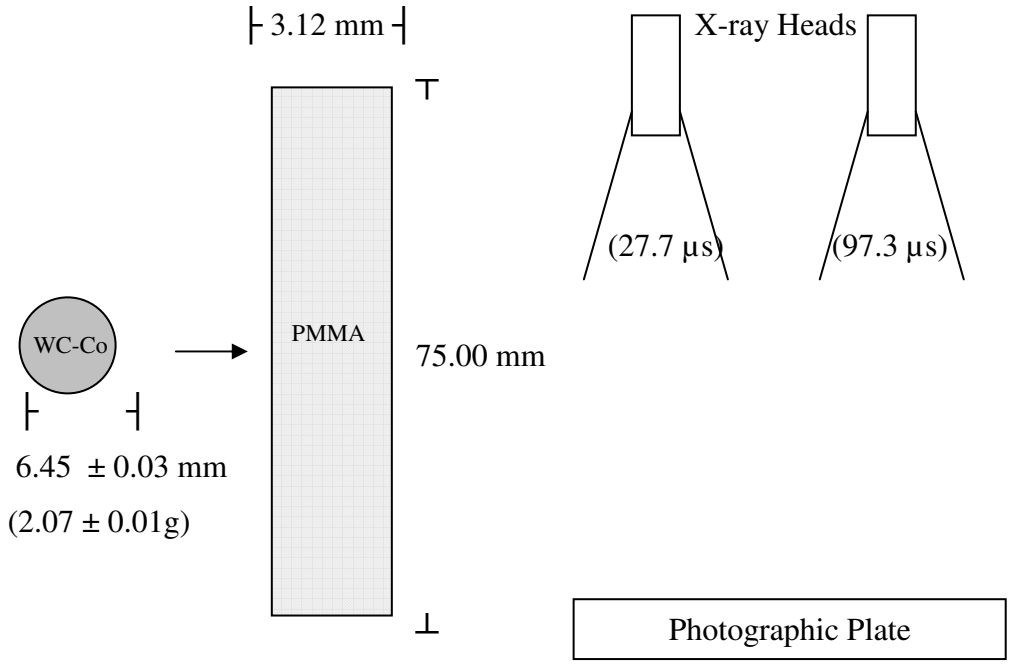

Figure 7.1: Sphere impact set-up, WC-Co Sphere impacting target 75 x 75 x 3.12 mm [20]

Orthogonal shadow-graphs of the WC-Co sphere fragmentation were taken using two 150 keV flash X-ray heads at 27.7 and 97.3 µs time intervals, 400 mm from the line of debris travel. Sphere impact experimental tests performed by Grady and Kipp, taken from the open literature, were compared with the results from numerical modelling to

validate the simulated WC-Co failure response using the WC-Co material model derived in *Chapter 6* [210].

Table 7-1 summarises the experimental tests performed by Grady and Kipp [210]. Three tests are compared to numerical simulations at varying WC-Co sphere impact velocities, from 2350 m/s to 3300 m/s. Flash X-rays were taken at different time intervals as described in *Table 7-1*.

Table 7-1: WC-Co sphere impact experimental and numerical results

	Impact Velocity (m/s)	**Residual Velocity (m/s)**	**Witness Block Hole Size (mm)**	**X-ray 1 (µs)**	**X-ray 2 (µs)**	**Figure Reference**
Test 1	2440	2350	8	27.7	97.3	*Figure 7.4 & Figure 7.5 a*
Test 2	2900	2790	11	26.5	85.6	*Figure 7.6 & Figure 7.7 a*
Test 3	3430	3300	17	21.2	71.4	*Figure 7.8 & Figure 7.9 a*

Figure 7.2 displays the WC-Co sphere and Lucite (PMMA) target mesh description implanted into the AUTODYN 2D numerical suite.

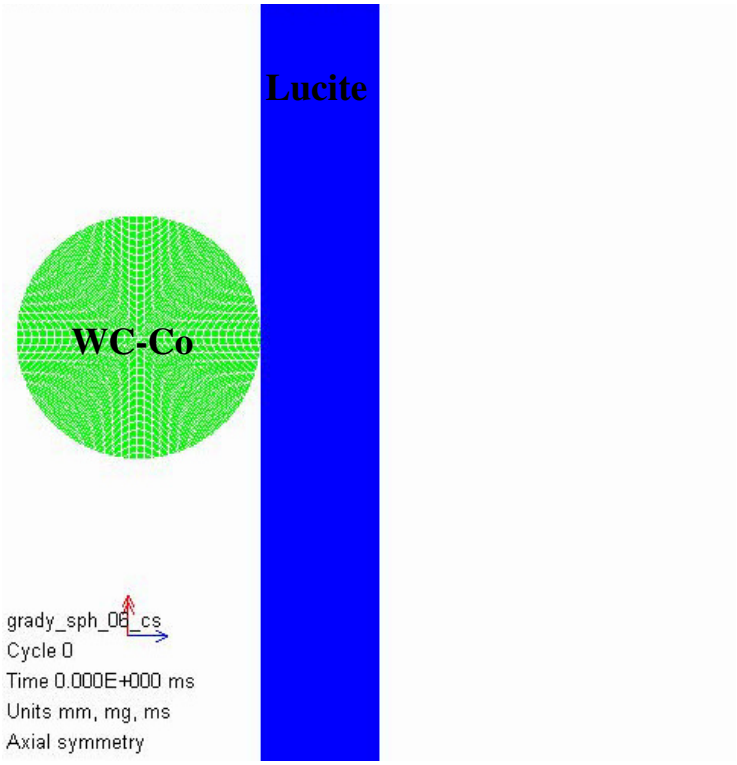

Figure 7.2: WC-Co sphere and Lucite target mesh description implanted into the AUTODYN 2D numerical code

An extensive material database exists in AUTODYN. The Lucite (trade name for PMMA) material model was chosen from the database to reflect the specific nature of the PMMA target material using a shock EOS [211,212,203]. The author refers the reader to *Appendix 5* for the full material description. For each simulation the WC-Co material model developed in *Chapter 6* was used for the sphere projectile. The shock EOS, piecewise linear strength model and the principle stress failure model were used. The numerical and experimental results are presented below in *Figure 7.3* to *Figure 7.9.*

An initial tensile strength and crack softening sensitivity analysis was performed. This was run parallel with the failure criterion derived by a comparison of ceramic – window interface velocity profiles from Grady and Moody plate impact data (see *Section 6.2.7, pp. 174*). This was to validate the principle stress failure model input for predicting the spall failure of the WC-Co sphere.

The principle stress model used for the WC-Co material simulation is a directional failure model. Failure is initiated if the maximum tensile principle stress or the maximum shear stress exceed their limits. After failure the material is assumed to have no shear strength and be able to sustain only positive hydrodynamic pressures [197,203]. A tensile crack softening model was also used in the model, improving the post failure response of the WC-Co. Brittle materials such as WC-Co generally deform inelastically (*Section 2.2*). The inelastic response of these materials is usually attributed to the nucleation, growth and coalescence of microcracks. Cracks cause extensive stiffness loss and strength degradation within the material. Notably, the WC-Co sample was found to possess a marked number of defects that could compromise its ability to withstand load (*Chapter 5*). Therefore, a crack softening model that allows for the gradual loss of strength as cracks propagate through the material was used [58,166,198,203].

Figure 7.3 shows a comparison of selected computational results to illustrate changes in the tensile strength and crack softening failure model. The EOS and strength model constants derived in *Chapter 6, Table 6-10,* remained extant. *Figure 7.3a* and *Figure 7.3b* compare the failure response, with and without a crack softening model (G_f = 102 J/m^2). Using the crack softening model the tensile failure was increased and the results are presented in *Figure 7.3b, Figure 7.3c* and *Figure 7.3d.*

In each simulation the sphere projectile was found to spall. As the tensile strength was decreased there was a pronounced increase in the WC-Co fragmentation. As the crack softening was increased there was also a reduction in the fragmentation. Note the differences in the failure of the spall segments on the front and back of the sphere.

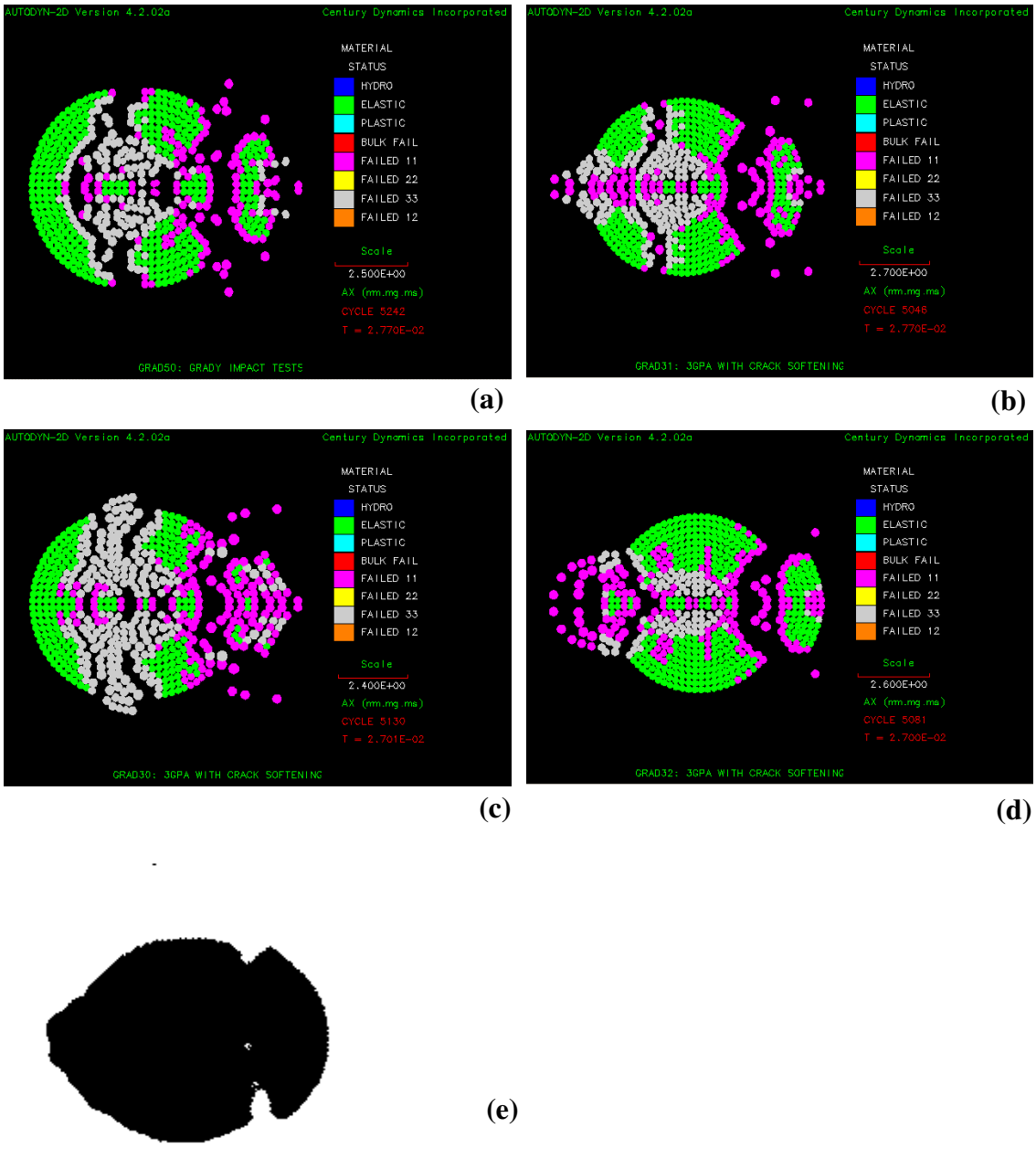

Figure 7.3: Numerical results for WC-Co sphere undergoing high velocity (2.44 km/s) normal impact on plate of PMMA [20,147], AUTODYN 2D SPH 122, 156 SPH (900), 0.224 mm nodes. (a) Tensile Failure Stress (TFS), 3.5 GPa and Crack Softening (G_f) 0 J/m^2: (b) TFS, 3.5 GPa and CS 102 J/m^2 (c) TFS, 3.0 GPa and CS 102 J/m^2: (d) TFS, 4.0 GPa and CS 102 J/m^2: (e) shadowgraph 27.7 µs down-stream from the impact point.

It was found that with both a tensile failure stress of 4 GPa and a tensile crack softening of 160 J/m^2, the numerical results showed good agreement with the spall regions formed in the WC-Co sphere during experimental trials. The results are presented below.

Using the tensile failure stress and crack softening as described, three experimental tests performed by Grady and Kipp were compared to numerical simulations at

varying WC-Co sphere impact velocities, from 2350 m/s to 3300 m/s [210]. The results are presented in *Figure 7.4* to *Figure 7.9*.

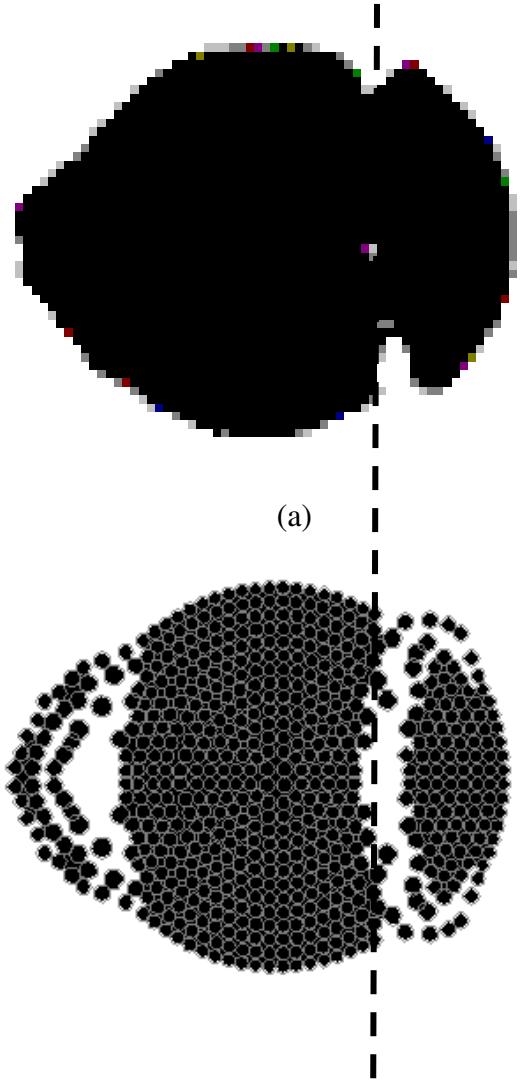

Figure 7.4: (a) WC-Co sphere shadowgraph 27.7 µs down-stream from the impact point, (b) Numerical results for WC-Co sphere undergoing high velocity (2.44 km/s) normal impact on plate of PMMA [20,147], AUTODYN 2D SPH 122, 156 SPH (900), 0.224 mm nodes.

In Test 1 (*see Table 7-1, pp. 185*), at 27.7 µs, the impulse load is sufficient to spall segments off the front and back of the sphere (*Figure 7.4a*). During the penetration process, reflection of the incident-compressive impulses generated can form a tensile wave to reflect back into the projectile sphere. Since WC-Co is strong in compression but weak in tension, when the materials tensile strength has been exceeded, spalling can be expected (*Section 2.3.3*). At 97.3 µs the frontal and back spall dispersal move

further away from the central segment which remains intact (*Figure 7.5a*). This is in good agreement with the numerical results, *Figure 7.4b* and *Figure 7.5b* respectively.

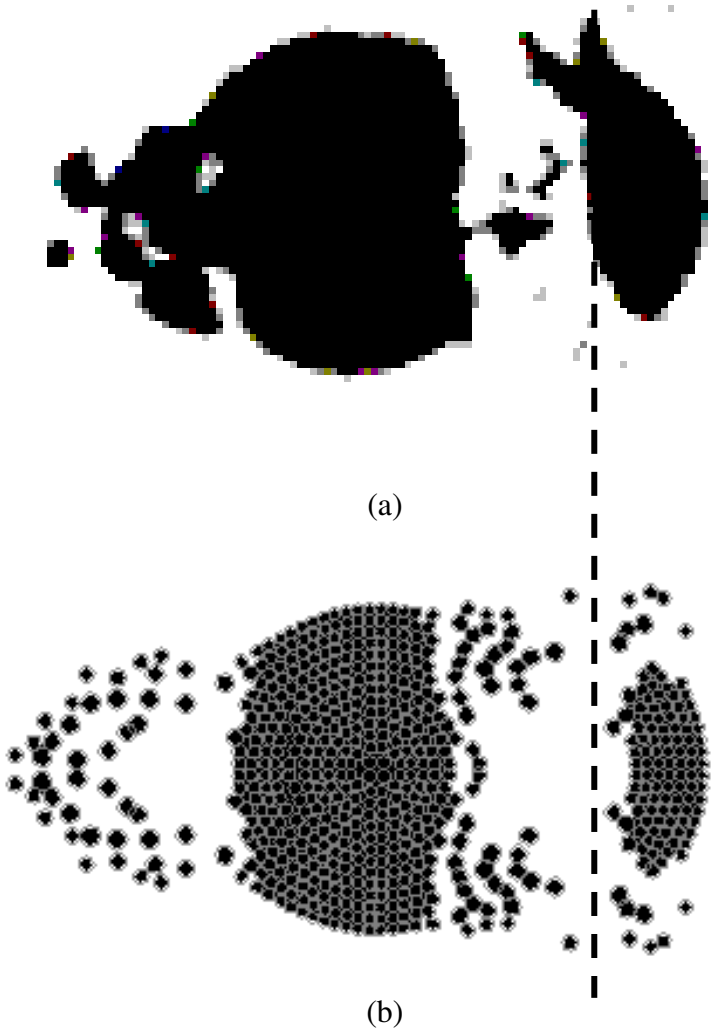

Figure 7.5: (a) Radiograph for WC-Co sphere undergoing high velocity (2.44 km/s) normal impact on plate of PMMA. Shadowgraph 97.3 µs down-stream from the impact point (b) numerical result in AUTODYN 2D.

Small differences in failure observed between the experimental and numerical results could have resulted from differences in the target material used for the numerical simulation. One such difference was the density of the Lucite used in the numerical simulation compared to that of PMMA. The author refers the reader to *Appendix 5* for the full material description. This varied from 1190 kg/m^3 (computational model) to 1186 kg/m^3 (Grady sample). Though this was well within the experimental error, such small changes could induce small changes in the predicted response of the materials.

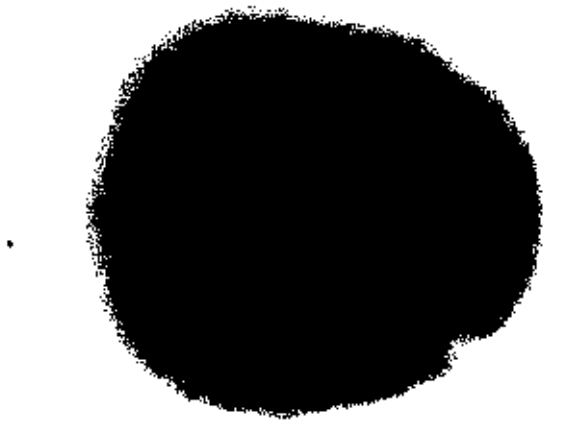

(a)

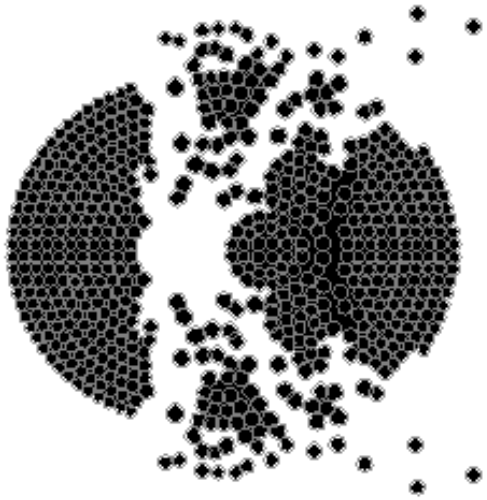

(b)

Figure 7.6: (a) Radiograph for WC-Co sphere undergoing high velocity (2.90 km/s) normal impact on plate of PMMA. Shadowgraph 26.5 µs down-stream from the impact point (b) numerical result in AUTODYN 2D.

Figure 7.6 above and *Figure 7.7* below compare the results of the numerical simulation sphere impact experiments carried out at 2.9 km/s. Experiment and model prediction began to diverge as the velocity was increased but overall, the model still proved to be effective at accounting for the fragmentation behaviour of the sphere. Further work could usefully enhance the capability of the model to predict WC-Co failure at higher impact velocities, enabling it to be applied at the higher velocities achieved by other WC-Co core rounds (*Section 2.5, pp. 55*).

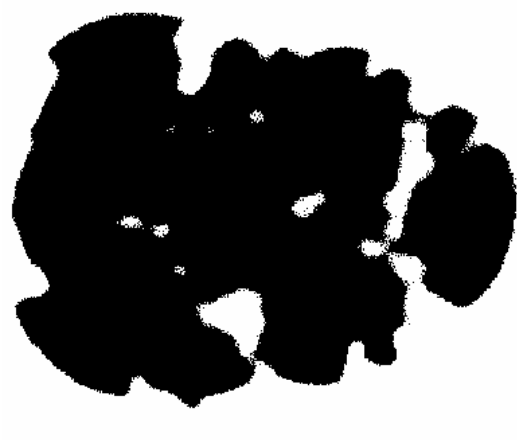

(a)

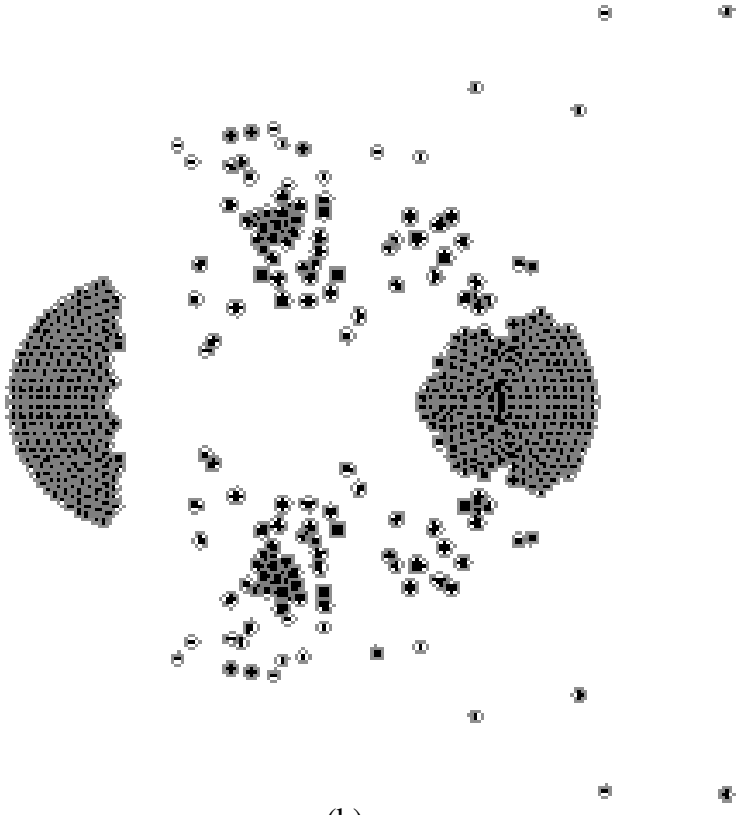

(b)

Figure 7.7: (a) Radiograph for WC-Co sphere undergoing high velocity (2.9 km/s) normal impact on a plate of PMMA. Shadowgraph 85.6 μs down-stream from the impact point. (b) Numerical result in AUTODYN 2D.

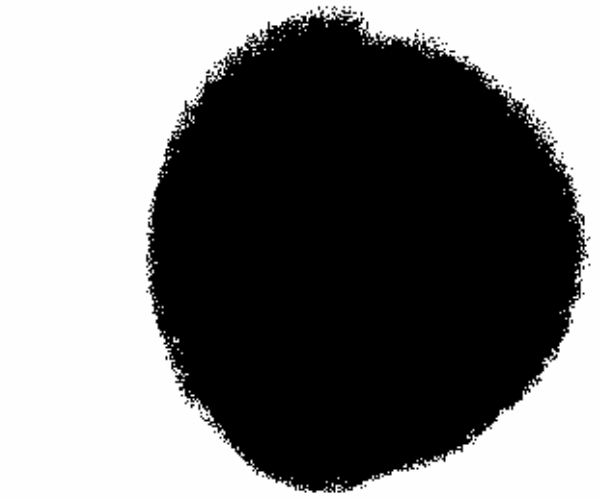

(a)

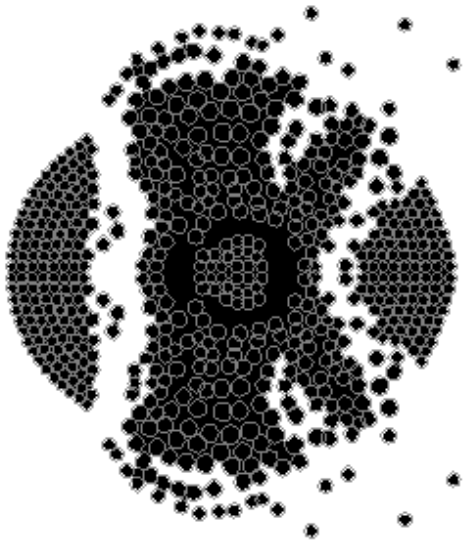

(b)

Figure 7.8: (a) Radiograph for WC-Co sphere undergoing high velocity (3.43 km/s) normal impact on plate of PMMA. Shadowgraph 21.2 μs down-stream from the impact point (b) numerical results in AUTODYN 2D.

Figure 7.8 shows the results for test 3 (impact velocity 3.43 km/s). The experimental X-ray shows a large intact fragment at the centre with some smaller spall behaviour, particularly in the radial direction. The numerical simulation shows small amounts of debris detached radially from the central region of the sphere. Prominent front and rear fragments detached from the central region.

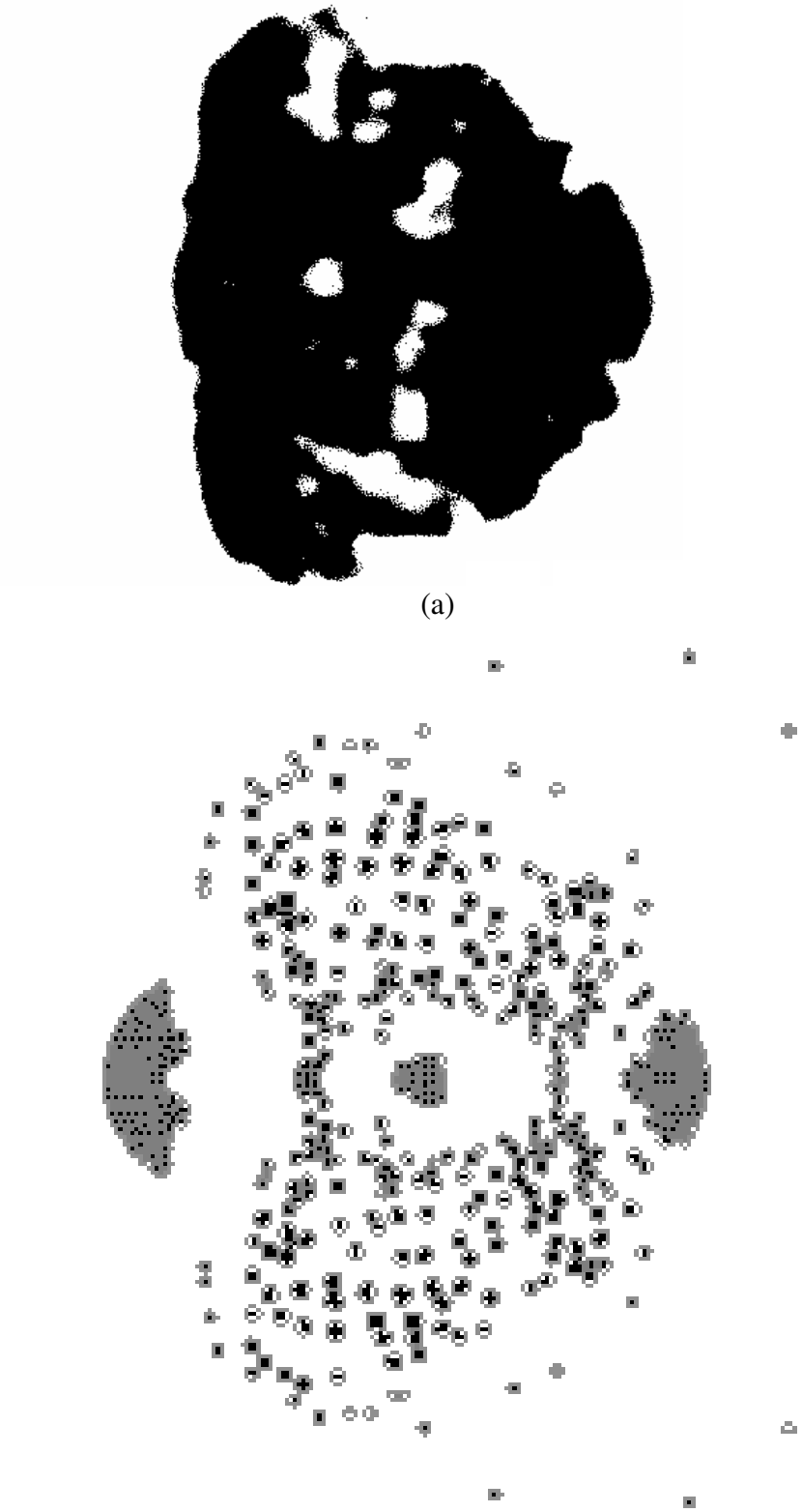

(a)

(b)

Figure 7.9: (a) Radiograph for WC-Co sphere undergoing high velocity (3.43 km/s) normal impact on plate of PMMA. Shadowgraph 71.4 μs down-stream from the impact point (b) numerical results in AUTODYN 2D.

Figure 7.9 shows the results for the final case, Test 3 (3.43 km/s at 71.4 μs). The impact stresses are enough to completely fragment the sphere. The numerical

simulation shows more radial dispersion than the experimental results. The radial and axial velocities were higher than that of the experimental simulations.

The results suggest that the shock energy imparted into the radial expansion of the WC-Co fragmentation debris cloud was dependent upon impact velocity. As the velocity is increased the axial expansion remains fairly constant, whereas the radial expansion increases significantly. Test 1, at an impact velocity of 2.44 km/s, the radial expansion velocity measured is 3 ± 3 m/s, whereas in Test 3, 3.43 km/s the radial expansion velocity measured is 50 ± 4 m/s [20,147]. Numerical simulations show that as the impact velocity was increased, the fragments tended to maintain both their axial and radial residual velocity. The numerical analysis suggests that the material fragmentation behaviour of the WC-Co sphere varies with velocity.

The simulation results show good overall correlation with the WC-Co sphere impact experiments. Note that in each plot the SPH particle represents the intersection of a ring of a material with that slice. To supplement this work, an initial series of numerical simulations presented in *Section 7.4* was then conducted and compared to experimental data from the impact behaviour of the BS41. The experimental investigation compared the BS41 impacting at a range of impact velocities and into different ceramic armour targets (*Chapter 4*). To maintain simplicity and reduce time, only a select number of the experimental results of the target performance from the BS41 impacting SiC B and Sintox-CL were compared to numerical analysis.

7.4 BS41 Computational Study

The BS41 projectile core and jackets were analysed under the shadowgraph to provide an accurate delineation of the projectile exterior and interior. The resulting drawing was undertaken in AutoCAD and then the points were extracted and analysed in Tecplot, a mathematical programme, to analyse the core and jacket tips ready for producing a grid in AUTODYN (*Figure 7.10*).

$$[F(x) = 4.432 \times 10^{-1} - 1.06y - 8.287 \times 10^{-2}\, y^2 - 2.609 \times 10^{-3} y^3]$$

[Eq. 7-1]

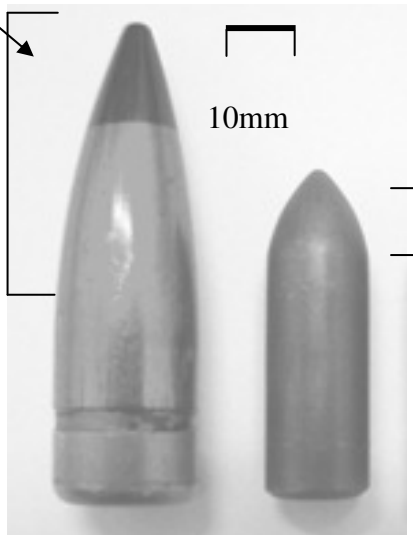

$$[F(x) = 1.255 - 3.632 \times 10^{-1} y - 5.562 \times 10^{-3} y^2 - 7.312 \times 10^{-6} y^3]$$

[Eq. 7-2]

Figure 7.10: 14.5 mm AP-I Type BS41 [9]. Upper Equation [Eq. 7-1] representing the polynomial for the core tip and the lower equation [Eq. 7-2] representing the polynomial for the jacket tip (Tecplot). All measurements performed at the RMCS.

The polynomial equation of the jacket tip (*Equation 7-1*) and the core tip (*Equation 7-2*) were calculated using the analysis in Tecplot. Each point was plotted using a mathematical solution for the curves, mapped into I and J nodes and finally discretised in AUTODYN (*Figure 7.11*).

This mesh was used to represent the BS41 in the numerical analyses in AUTODYN 2D.

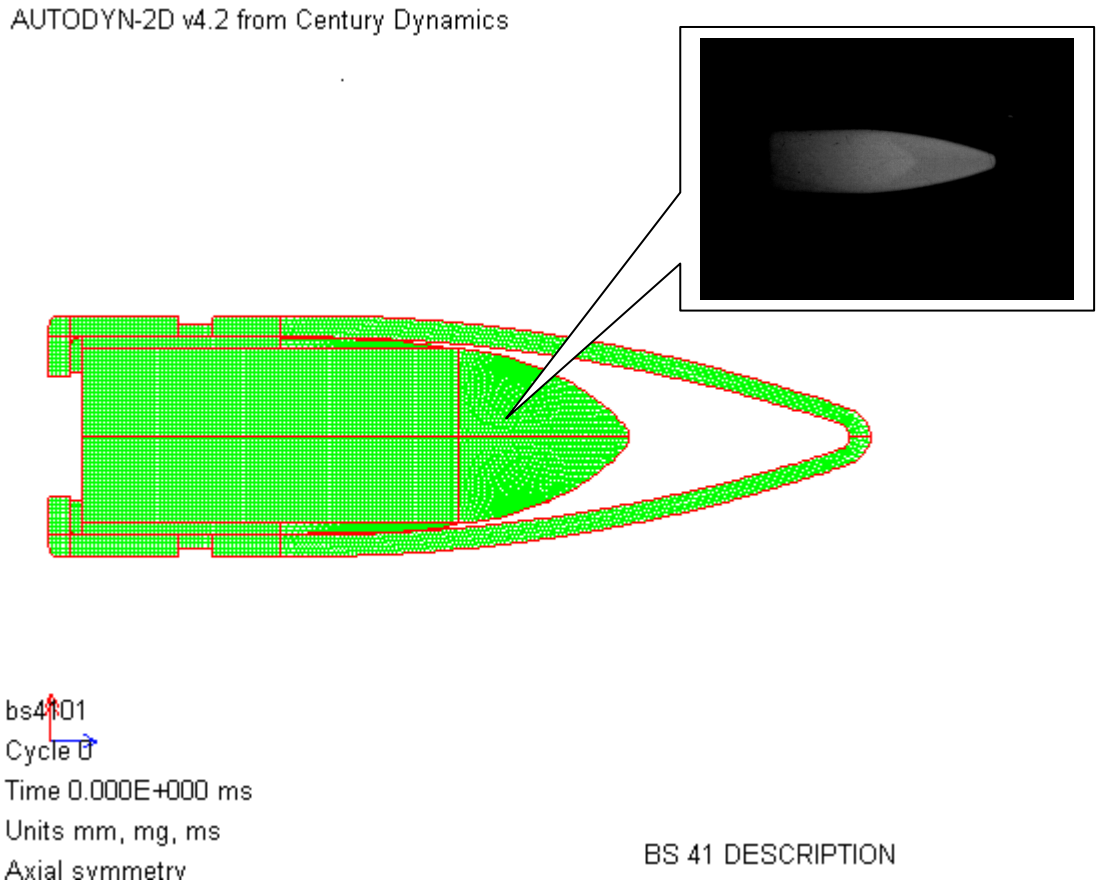

Figure 7.11: Mesh Description of the BS41 projectile implanted into AUTODYN computer numerical programme. Top Right Flash X-ray displaying the BS41 inner core during flight.

Due to the three-part construction of the BS41, its penetration mechanisms are relatively complex and vary depending on the nature of the target. Initial simulation runs compared the penetration of the round with and without the jacket and inner layer jacket. The shock EOS, piecewise linear strength model and the principle stress failure model presented in *Section 7.3* were used to simulate the response of the WC-Co core. The copper gilding metal jacket was modelled using a shock EOS and a Johnson Cook constitutive model. The material model was chosen from the database to reflect the specific nature of the jacket material. The author refers the reader to *Appendix 5* for the full material description.

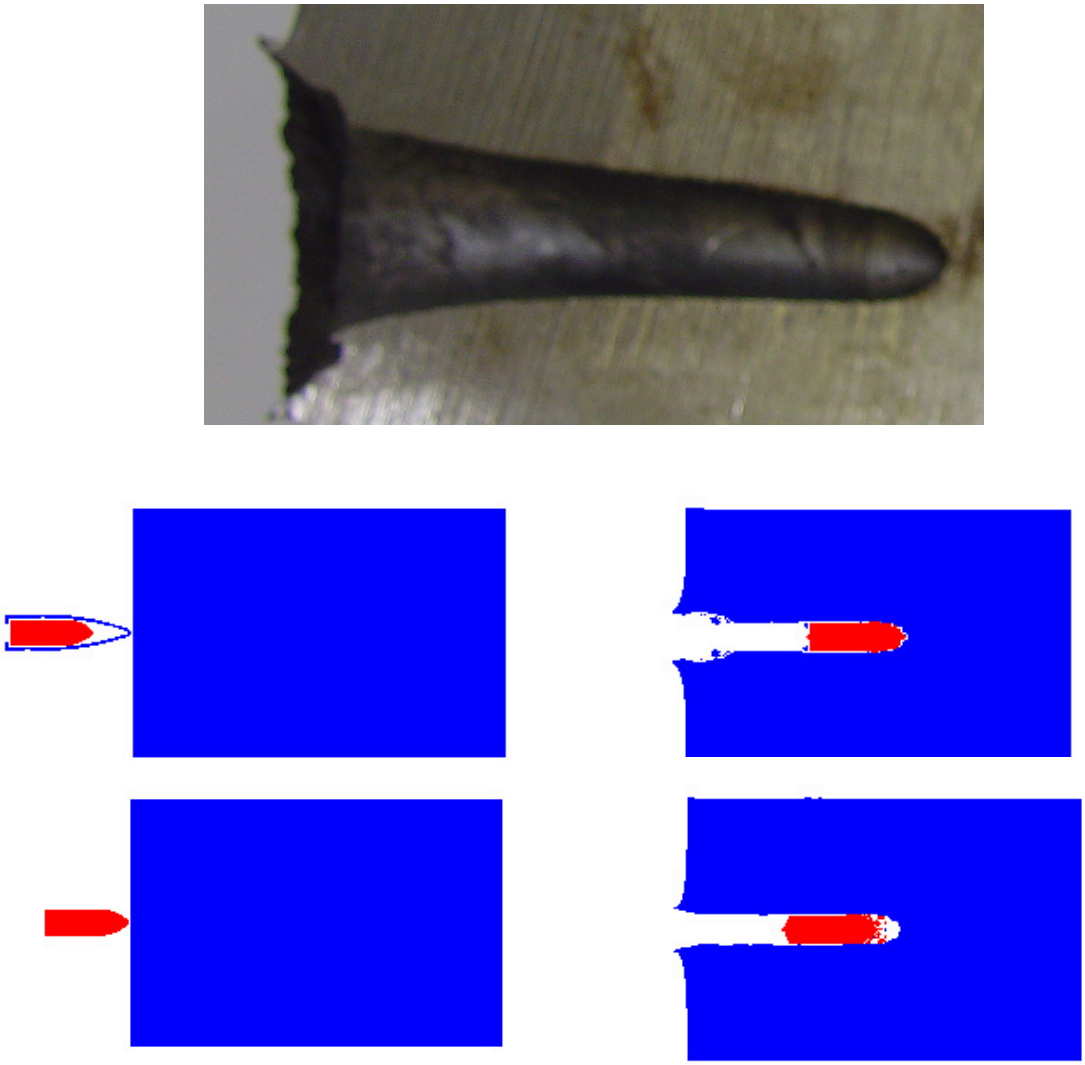

Figure 7.12: Comparison of material plots of the BS41 penetrating mild steel (Top = experimental picture (DoP = 74.69 mm); numerical top *with* (80.49 mm DoP) and bottom picture *without* (80.12 mm) its outer jacket, penetrating a confined 1006 mild steel witness block.

The results of the simulation are shown in *Figure 7.12*. No significant difference in DoP of the WC-Co core between the two numerical tests was observed. There was a 4.00 mm increase in crater diameter when the simulation was performed with the outer jacket of the BS41. After the significant increase in computational time caused by the addition of the jacket, it was decided for future analysis that only the core would be used in the simulations. There was generally good agreement between the computational results and the experimental results.

Within the tip of the BS41, there is an incendiary compound. A numerical model for the incendiary powder has been developed by Moxnes *et al*. [213]. They simulated with good accuracy a common incendiary powder consisting of Al/Mg alloy and

$KClO_4$ with a small amount of calcium resinate as used in military munitions, in AUTODYN 2D [213]. The incendiary plays a key practical role in target marking *i.e.* spotting and target fuel ignition, but has minimum impact on the penetration process. Due to the effect on computational time it has not been analysed for this investigation.

7.4.1 Modelling the DoP into a Witness Block

Before running simulations for the targets used in the tests, it is desirable to model the simulation for a simple witness block. For this purpose computational results were compared to initial experimental reference firings into 1318b aluminium alloy and mild steel semi-infinite witness blocks. The steel back plate was simulated using 1006 steel whilst 7039 aluminium was used to model the 1318b aluminium alloy. These were the closest representative material models in the AUTODYN material library. The 1006 material model was chosen from the database as it had a density of 7896 kg/m^3 and a yield stress of 350 MPa, whereas the mild steel had a density of 7786 kg/m^3 and a yield stress of 264 MPa. For the 1006, a shock EOS and a Johnson Cook strength model were used. The 7039 aluminium was chosen from the database as it had a density of 2700 kg/m^3 and a yield stress of 220 MPa, whereas the 1318b aluminium alloy had a density of 2965 kg/m^3 and a yield stress of 426 MPa. The author refers the reader to *Appendix 5* for the full material description. The numerical Lagrangian formulation was used [203]. *Table 7-2* compares the results from the numerical and experimental tests.

Table 7-2: Empirical and numerical baseline DoP and cratering

Data	Witness block (DoP) (mm)		Crater Diameter (mm)	
	Aluminium Alloy	Steel	Aluminium Alloy	Steel
Experimental	103.8	74.69	26.32	21.00
Numerical	112.00	80.12	12.14	14.03

Reasonable agreement was observed in the penetration depth. In both mild steel and aluminium the DoP was found to be slightly higher than the experimental results but the predicted crater diameter was substantially lower.

The differences in DoP between the simulations and the experiments may be explained as follows. For steels of nominally similar type, higher yield strengths can be accompanied by lower ductilities. Thus, the mild steel used in the experiments may have been more ductile than 1006 and possibly had greater strain hardening. This could account for the lower DoP observed in the mild steel. Regarding the aluminium witness blocks, the yield strength of the 1318b was nearly twice that of the 7039 but the difference in DoP between experiment and simulation was relatively small, suggesting that other factors than simply yield strength were important in determining resistance to penetration. For example, the lower strength alloy may have had a higher strain to failure.

The model was found to underestimate the crater diameter where both 1006 and 7039 were found to be more resistant to lateral displacement. A factor accounting for part of the differences is that the model did not include the inner and outer jacket of the penetrator. However, the current study centres on DoP as a measure of ballistic efficiency. Therefore, although cratering was not modelled well, the numerical DoP results were accurate, giving confidence in the utility of the model for predicting penetration.

From the DoP shown in *Table 7-2* and the rigid core body penetration, it can be inferred that the model reproduces most of the phenomena experimentally observed. It was decided that for future tests to use both the Lagrangian processor and 7039 aluminium material model found in the AUTODYN 2D material database. This aluminium provided the best agreement with test results.

7.4.2 WC-Co Spall Failure Characteristics

The material properties implanted in the numerical model govern the response of a material during an impact. The behaviour of the material under dynamic loading

needs to be described and this requires the specification of its volumetric response (EOS), the deviatoric response, resistance to distortion (the strength model) and the reduction in the ability to carry stress as damage accumulates (a tensile failure criterion). As the fragmentation behaviour of the material depends on the local failure of the material, the failure criterion can be expected to play a large part in the accuracy of the simulation predictions. The model was tested parametrically for sensitivity. The analysis demonstrated that the greatest observed effect on WC-Co failure was due to changing the material tensile strength (*Figure 7.3*).

In order to compare the prediction of the model to the Russian sample, the BS41 impacting a Sintox-CL front plate and 1318b back plate at 1016 m/s was modelled in two dimensions using axial symmetry. The Lagrangian processor was utilised as described earlier with 0.25 x 0.25 mm nodes. The target consisted of a laterally confined 18 mm Sintox-CL front plate with a 10 mm 1318b aluminium alloy backing followed by a 10 mm air gap. Experimental results are presented in *Section 4.2.6*, *pp. 119*. A witness block was used to catch the debris. The numerical model used for the simulation is shown in *Figure 7.13*.

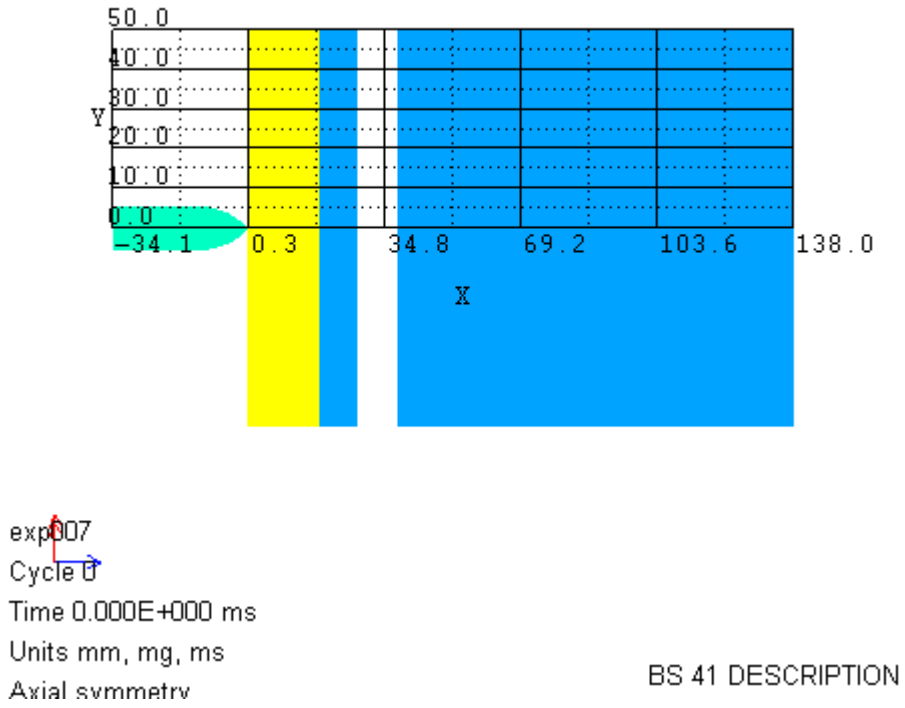

Figure 7.13: AUTODYN 2D material model Set-up: From left to right; BS41-Sintox-CL-Aluminium witness plate-air gap-aluminium witness block

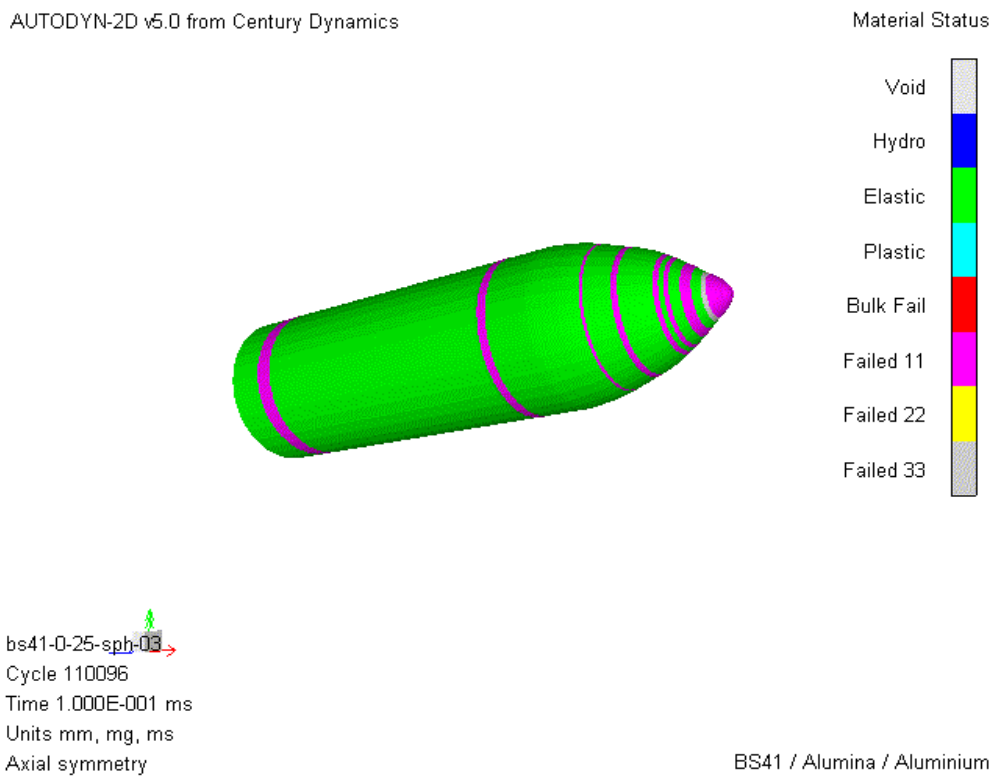

Figure 7.14: 3D model of the WC-Co core captured in an aluminium alloy witness block after penetrating 18.29 mm Al_2O_3 Sintox-CL coupled to a 10 mm aluminium alloy followed by a 10 mm air gap.

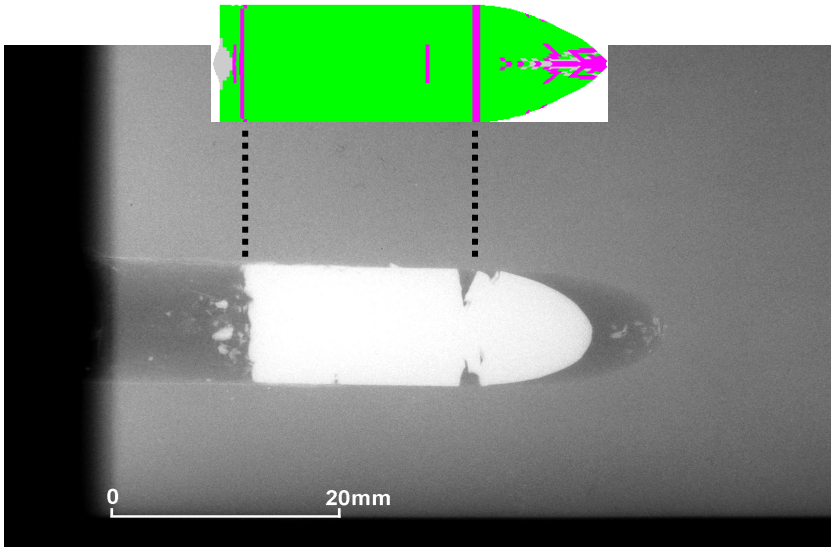

Figure 7.15: From top to bottom a numerical simulation compared to an X-ray of the BS41 WC-Co core captured in a 1318b aluminium alloy witness block after penetrating 18.29 mm Al_2O_3 Sintox-CL coupled to a 10 mm 1318b plate followed by a 10 mm air gap.

The spall behaviour of the WC-Co, observed from the experimental X-ray *Figure 7.15* was compared to the numerical analysis, shown in *Figure 7.14.* Different colours define the computational distribution of damage. Nodes that are coloured green represent material that is currently deforming elastically. Nodes that are coloured cyan represent material that is currently deforming plastically. Good agreement was observed between the experimental and numerical results. The model accurately predicted the spall failure observed in the WC-Co core. However, the numerical core tip was found to be sharper than that of the core after experimental firing. This could be explained by slight turning of the core within the witness block.

It was found that with a spall strength of 2 GPa and a tensile crack softening of 160 J/m^2, the experimental results for targets consisting of 18 mm Sintox-CL tiles and 10 mm aluminium alloy backing followed by an air gap could be reproduced. The tensile crack softening model improved the simulation of the post-failure response of the WC-Co. We can conclude that the WC-Co sample from the Russian BS41 had a lower spall strength (2 GPa) than K-68 WC-Co (2.7 GPa) [20]. Dandekar reported hot pressed WC from Cercom Inc. to have a spall strength of 2.06 ± 0.04 GPa which was reduced to 1.22 ± 0.38 GPa as shock-induced stress increased from 3.4 to 24 GPa [214].

The microstructural evidence presented in *Chapter 5* suggests that spall failure of the WC-Co core was likely to be dominated by a number of microstructural features including grain size, high porosity and microcracking. The relatively open porous morphology observed in the BS41 could explain the low spall strength predicted by the modelling.

Grady reported that at high velocities the shock energy was more uniformly distributed, resulting in a more uniform WC-Co sphere fragmentation distribution [20]. At lower shock velocities localised weak sections of the material are important in influencing the fragmentation behaviour. This may have caused the numerical analysis difficulties in accurately predicting the sizes and distribution of fragments. Further experimental analysis of the impact fragmentation behaviour of the WC-Co spheres at lower impact velocities is required to test this aspect of the model using the Russian sample.

These results demonstrate the first physically based WC-Co material model, parametrically adjusted with other experimental configurations from Grady, capable of reproducing the observed spall failure of the BS41. However, results suggest that it is not only the strength of the WC-Co material that plays the largest role in penetration. In fact it is more than likely to be a combination of the strength of the broken material and the materials defects, pores, grain size and microcracks as observed in *Chapter 5*.

The model overestimated the degree of spall damage in the tip of the projectile. A number of spurious holes formed. Problems may have arisen modelling an inherently three-dimensional phenomenon in two-dimensional cylindrical geometry. In the two dimensional geometry each node is calculated as a ring and so could have significantly different stress and fracture characteristics compared to a three-dimensional analysis [20,203]. Three-dimensional analysis, with its more accurate representation of the circumferential fragmentation, is required for comparison. Another possible problem is the introduction of an erosion algorithm. When an element is eroded it introduces a void which allows surrounding material to expand into the void and to lose pressure as it expands. WC-Co material strength is pressure dependent. Thus, the pressure drop can lead to a lower strength, increased damage, or both.

7.4.3 Flash X-ray Configuration and Material Properties

It is unclear from the experimental data when the BS41 core fragmentation initiated during penetration. Acquiring accurate information on the penetration process is necessary if numerical modelling of such events is to represent reality. Initial trials were performed to see if the high-speed camera could provide detailed visualisation of the WC-Co fragmentation. A ceramic cloud was found to obscure the view of projectile-target penetration and the fragmentation of the WC-Co could not be seen (*Section 3.5.1*).

An alternative to high-speed camera is to use flash X-radiography as described in *Section 3.5.2, pp. 89.* This can be a useful validation tool for the numerical material model. Numerical simulations were compared to two different target system set-ups: the first consisting of the SiC B front plate followed by an air gap, and the second

consisting of a SiC B front plate coupled to a 10 mm 1318b aluminium alloy back plate followed by an air gap (*Figure 7.16*). The Lagrangian processor was used for simulations of WC-Co projectile penetration into two multi-layer target systems. The target, which was the same in all cases, consisted of a laterally unconfined 100 x 100 x 18 mm SiC B tile front plate, whilst the witness block and backing plate were 1318b aluminium alloy. Each target was supported using a bespoke target frame. The WC-Co material model derived in *Chapter 6* was used to model the BS41 core and its behaviour was determined from X-radiographs.

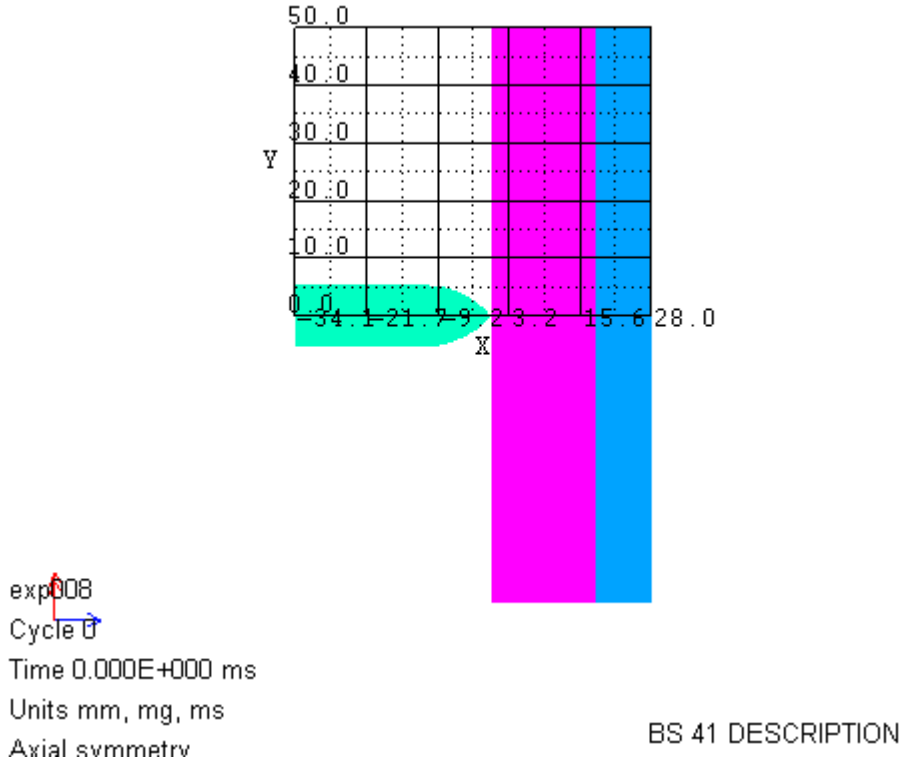

Figure 7.16: Target and Projectile numerical grid

The numerical grid geometry in the impact region is shown in *Figure 7.16*. The 18 mm thick SiC B target, (pink), the 10 mm 1318b backing plate (dark blue) and the projectile (light blue) were each divided into nodes of size 0.25 mm x 0.25 mm.

For the SiC B a polynomial EOS and a Johnson Holmquist strength model provided a good method to estimate material failure behaviour under dynamic loading in AUTODYN 2D [215,216]. Aluminium alloy 7039 from the material libraries, described earlier, was implemented for the back plate. The interaction between the

projectile and target was treated by an internal gap size 3.145 μm. The same logic applied to the interface between the SiC B and the aluminium alloy back plate. The large deformation of the grid in the impact region was managed by an instantaneous geometric strain erosion model. The erosion strains for the WC-Co, aluminium alloy and SiC B were 3.5, 3.0 and 3.0 respectively.

Flash X-ray experimental studies were carried out on firings of nominal velocity 960 m/s. X-radiographs were obtained during the interaction between the projectile and target.

Table 7-3: Flash X-ray trial details used for numerical analysis

Trial No.	Trial Round	Velocity (m/s)	Front Plate (mm)	1318b Back Plate (mm)	Air Gap (mm)	X-ray delay time (μs)
4156	4	958	18.14 SiC B	-	80	80
4157	5	965	18.06 SiC B	-	120	110
4158	6	954	18.21 SiC B	-	120	150
4159	7	962	18.15 SiC B	-	188	200
4160	8	971	18.06 SiC B	10	10	200
4161	9	952	18.14 SiC B	10	10	200
4163	11	945	18.17 SiC B	10	10	150

Table 7-3 describes the details of each test used in the numerical analysis. There was no facility for collecting WC-Co debris after each experiment and this made it difficult to compare the fragmentation prediction from the numerical analysis to experimental data.

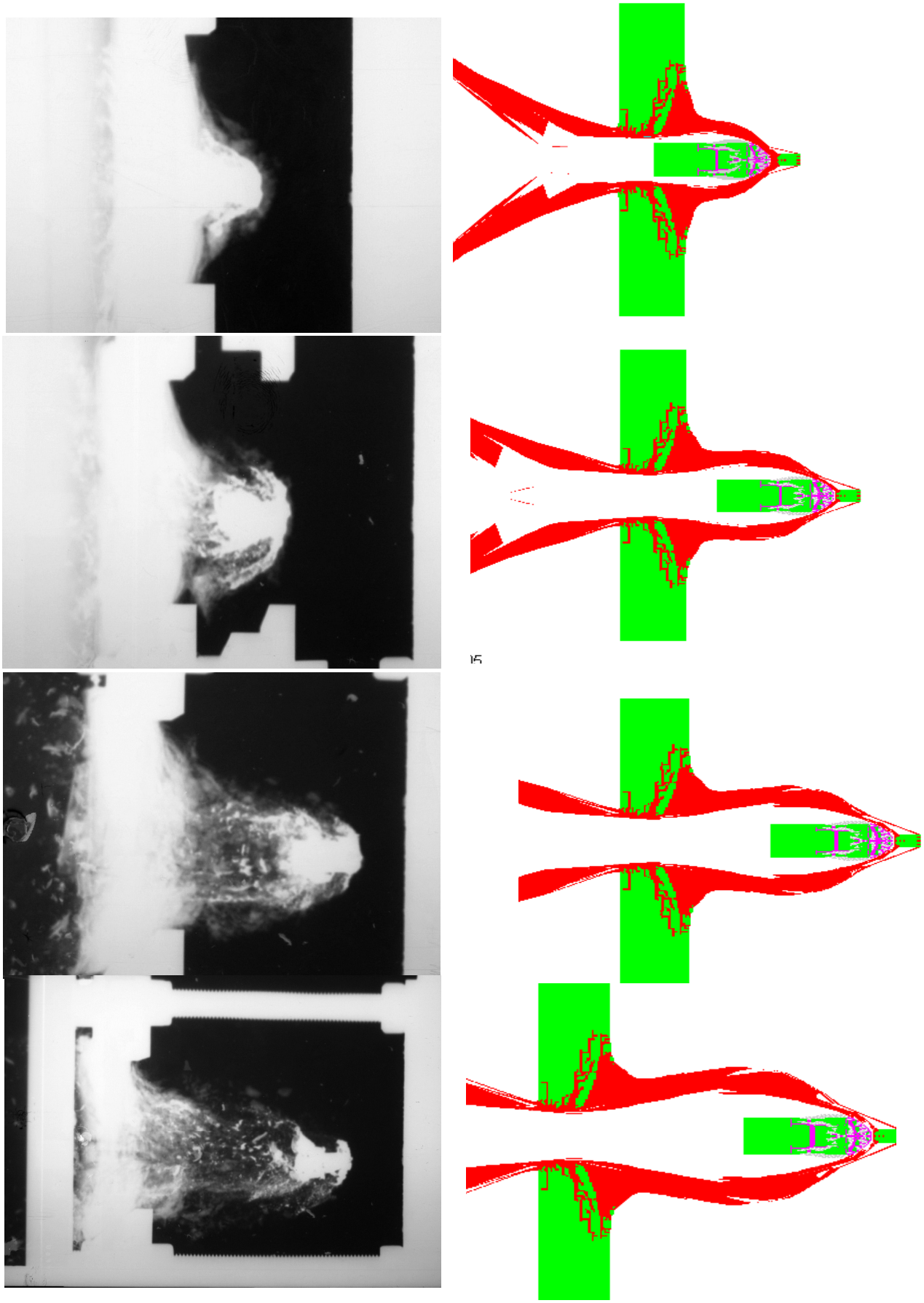

Figure 7.17: Experimental and numerical simulation, SiC B FP. Test Nos., from top to bottom, 4156, 4157, 4158 and 4169.

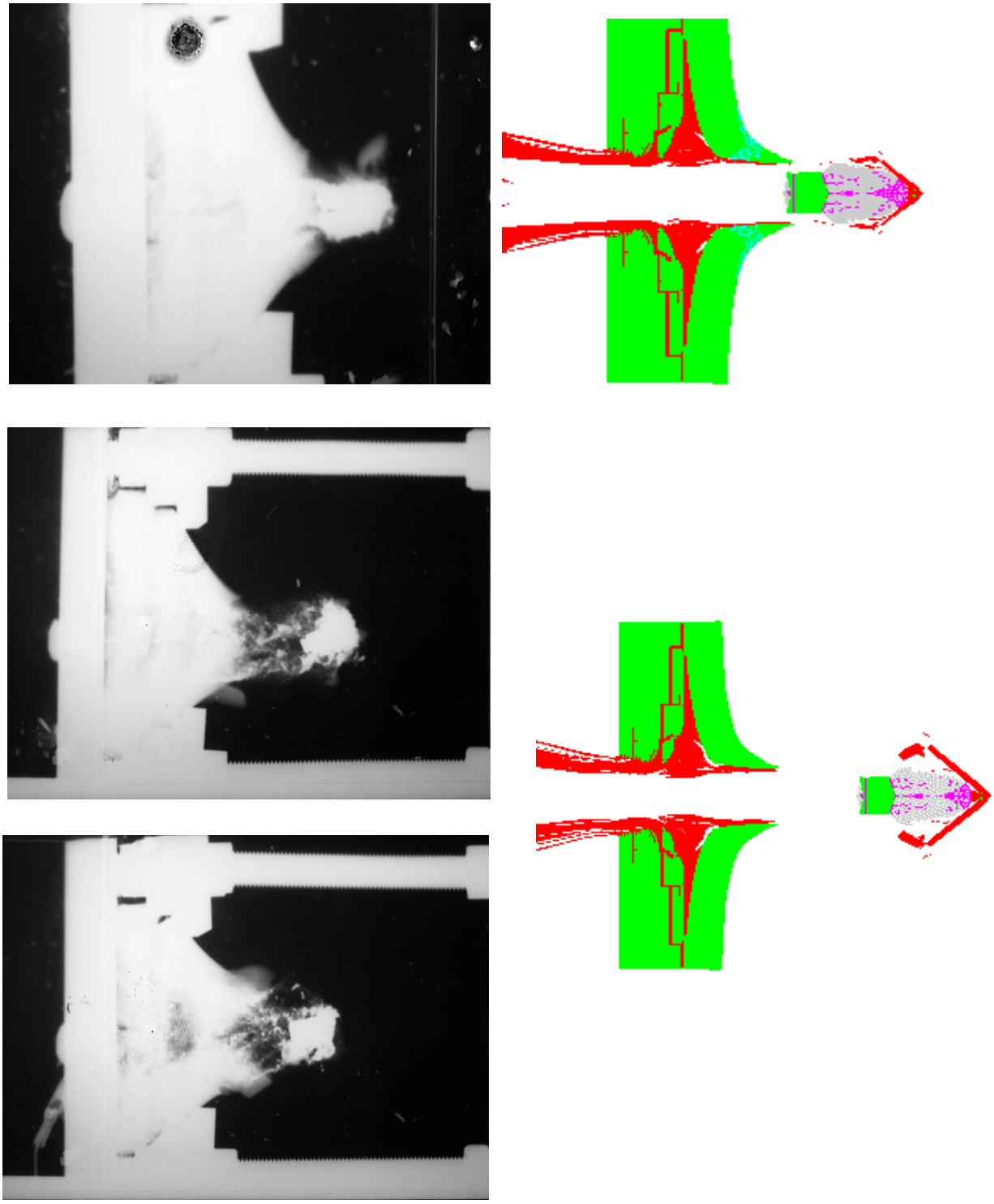

Figure 7.18: Experimental and numerical comparison. BS41 impacting 18 mm SiC B and 10 mm aluminium alloy back plate. Top: 150 µs, Middle & Bottom: 200 µs.

Figure 7.17 and *Figure 7.18* compare several stages in the penetration process between the experimental and numerical results. Different colours define the computational distribution of damage. Nodes that are coloured green represent material that is deforming elastically and nodes that are coloured cyan represent material that is deforming plastically.

Figure 7.17 shows the stages of the WC-Co core penetrator as it leaves the SiC B ceramic tile. The ceramic ejecta can be seen dispersed radially from the back surface. The ejection process clears the pulverised ceramic away, accommodating the passage of the BS41. By 200 μs the ceramic is completely dispersed.

The X-ray measurements were used to calculate the velocity of the penetrator after passing through the target. It was observed that the velocity of the penetrator after passage though the target for samples of just a SiC B front plate was nearly 34% higher than that of the corresponding targets with a 10 mm aluminium back plate. *Figure 7.18* shows that the back face displacement is delayed for the constrained SiC B sample. This implies a reduction in velocity and potentially more damage to the penetrator. Numerical results show increased fracture of the penetrator caused by the addition of a 10 mm aluminium alloy back plate, compared to just a SiC B target shown in *Figure 7.17*. This relates to the experimental data presented in *Section 4.2.6*. The ability of the thinner plates of aluminium alloy to deform and absorb a larger amount of energy per unit thickness of plate due to plastic deformation. Study of the fracture surfaces of SiC B revealed principally intergranular fracture and these closely interlocked grains appeared to improve resistance to deviatoric stresses even after failure (*Section 4.2.5*). With the addition of a 10 mm 1318b back plate on a SiC B front plate it constrained the SiC B further and improved the armours performance.

The numerical model, particularly that presented in *Figure 7.18* captured the ejection of the SiC B. From the results shown in *Figure 7.17* and *Figure 7.18*, it can be inferred that the model reproduced the experimentally observed phenomena.

7.5 Discussion

Practical experimentation is often compromised by physical limitations of the equipment used, thus the work described in this chapter investigates the ability of numerical modelling to predict the fragmentation of WC-Co. Many of the relevant parameters can be determined explicitly (*e.g.*, reference density, shear modulus) but some of the constants for the failed material had to be inferred from ballistic penetration data (*e.g.*, G_f, tensile failure stress).

The difficulties associated with simulating the WC-Co material during impact were discussed and demonstrated. A simplified methodology was presented to enable the determination of the numerical model strength and failure parameters from experimental data (*Chapter 6*). The simulation results in AUTODYN 2D demonstrated the model's ability to reproduce the experimentally measured spall failure and the penetration depth. A significant result is the confirmation of the ability to model the fragmentation behaviour of the WC-Co spheres impacting PMMA by using Smooth Particle Hydrodynamics with a Lagrangian target. To supplement this work, an initial series of numerical simulations was conducted and compared to experimental data from the impact behaviour of the BS41 projectile.

A model of the 14.5 mm BS41 projectile was produced and material data for the targets and projectile jackets were retrieved from the AUTODYN material libraries [195]. Numerical simulations were run and a comparison was made to validate the constitutive model to BS41 experimental data. Differences, including DoP and fragmentation, between experimental and computational analysis have been described.

It was found that with a spall strength of 2 GPa and a tensile crack softening of 160 J/m^2, simulations of the fracture behaviour of the BS41 WC-Co showed good agreement with experiments. The model accurately predicted the high intensity spall regions due to stress wave interaction in the core but overestimated the spall strength when compared to Grady's work on WC-Co. The numerical results also compared favourably with experimental trials with the BS41 where the projectile's residual momentum after target perforation was closely studied.

Results from the numerical simulation show how Sintox-CL (*Section 7.4.2*) and SiC B (*Section 7.4.3*) induce fracture in the BS41 core. The numerical model however, has not been able to determine the size distribution for the WC-Co fragmentation. Due to the inability to collect all the fragmentation from each experiment it was difficult to draw firm conclusions on the accuracy of the numerical simulation of the fragmentation.

The ability to simulate comprehensively the failure of an inhomogeneous ceramic target has proven difficult for decades. In order to do this a powerful model would be required where void distribution and crack propagation could directly be simulated in each particular specimen. Numerical models assume a number of evenly distributed and orientated grains and flaws within the material. Indeed, microstructural analysis of the WC-Co core material revealed a high number of pores and voids. If the fragment size distribution was generated in a random geometric fragmentation process, then a material model closely replicating the event of interest might be expected to better approximate the fragmentation behaviour. To carry out such a daunting solution would require initial impact work to obtain measures of the fragment size, then implant statistical assumptions regarding the distribution of fragment size into the numerical model. Complex mathematical modelling of fragmentation has been proposed by Grady, Kipp and Mott to simulate the fragmentation of bodies subjected to explosive rupture [217].

Numerical techniques can advance our experimental and theoretical outlook of impact. Rapid advances in computer science have aided numerical investigations. Whilst the fragmentation failure is fairly well understood, it is impractical if only the current AUTODYN 2D analysis tool is considered. The numerical modelling may help by representing an approximate effect of the impact phenomena since AUTODYN 2D essentially renders the targets as homogeneous. A numerical solution for such a material model only requires a probabilistic description of the random fragmentation. This provides the essential data required to hypothesise on the effects of impact of WC-Co into different targets. Whilst the regions of extensive spall were well simulated it is vital that, before a good representation of the WC-Co of interest may be made, experimental analysis of the material of interest is required including spall data. One approach is to investigate the statistical random way of partitioning a given

topology. An example is from the Lineau distribution where the problem is modelled as that of one infinite one-dimensional body, or line, in which fractures are introduced with equal probability at any point on that line. Previous work describing the statistical equations derived from the fragmentation behaviour of a one-dimensional body interprets some of these complex processes [217].

No attempt yet has been made to extend these numerical simulations to higher impact shock-induced stress due to limited computational resources and time. Testing of Cercom-tungsten carbide has shown a decrease in spall strength related to increased shock-induced compressive stress [214]. Further work is essential if a full picture of the failure phenomena of WC-Co in the hydrodynamic and sub-hydrodynamic impact regimes is to be gained.

The initial numerical material modelling has been developed allowing the fragmentation onset to be reproduced when compared to plate and sphere impact work in literature. The complexity of the phenomenon may require the conduct of additional tests before a reliable and comprehensive numerical representation of the event can be constructed. It has been shown that such a model can incorporate the major features of the penetration process and permits a good prediction of the failure of WC-Co. While these results are very encouraging, it is important to continue evaluating and improving the model's predictive capability through simulations of more complex ceramic armour impact configurations. The ability to accurately numerically model WC-Co will enable a wide range of modelling studies to be designed and analysed before carrying out potentially expensive experiments. This will prove both time and cost effective, demonstrating the future potential of the technique.

7.6 Summary

A numerical material model in AUTODYN 2D has been produced to account for the nature of failure of WC-Co subjected to dynamic loading during impact into ceramic target systems. The governing equations for the WC-Co material failure model have been described in detail and a set of model constants was proposed for AUTODYN

2D. This set of constants was then employed in a series of finite element simulations of the following benchmark suite of experimental impact configurations:

- plate impact (*Chapter 6*),
- sphere impact, as performed by Grady and Kipp for which X-ray experimental data of WC-Co failure exist [210], and,
- 14.5 mm BS41 projectile penetration into Sintox-CL and SiC B.

It was demonstrated that the numerical estimation of WC-Co behaviour using a shock EOS, a piecewise linear strength model and a principle stress failure model provided a good method to estimate spall behaviour under dynamic loading.

In order to enhance the confidence in the failure model of the WC-Co, comparison with further experimental data would be advantageous. With limited computational resources this has not been possible in the current programme of work.

Chapter 8

Conclusions & Recommendations for Further Work

A detailed account of the research carried out and a summary of objectives of foreseeable future analysis are presented here. The work described investigates the effects of different armour solutions on defeat of the Russian BS41 14.5 mm projectile. The ability of a novel numerical material model to predict the fragmentation of the WC-Co core is presented. Successful numerical simulation of the WC-Co material model demonstrated the future potential of the technique.

8.1 Conclusions

The BS41 is a current threat likely to be encountered in a number of theatres. With its muzzle energy of 33.5 kJ and KED of 359 MJ/m^2 it represents a significant increase in threat level over other small arms, *e.g.,* a muzzle energy of 3.6 kJ and KED of 118 MJ/m^2 for the smaller 7.62 mm FFV (WC-Co core) and the 14.5 mm B32 (steel core) with a muzzle energy of 30.2 kJ and KED of 322 MJ/m^2.

Experimental results are presented from an investigation of the parameters of a ceramic-faced armour system that are required to induce damage in a WC-Co penetrator. Depth of penetration results and ballistic efficiencies of a number of armour systems to defeat the BS41 have been presented. The DoP test has been used as an appropriate and effective experimental validation of armour efficiency. Experimentation was carried using a laterally confined experimental rig. A detailed account of the experimental techniques employed and the rationale behind the approach is discussed in *Chapter 3*.

The Russian BS41 WC-Co 14.5 mm AP round has been fired into various thicknesses and types of Al_2O_3 and SiC, backed by aluminium alloy or mild steel semi-infinite witness blocks. *Chapter 4* presents a summary of the effects of witness block constraint and ceramic armour appliqué systems on BS41 ballistic performance.

By applying a common ballistic performance criterion such as the e_c, the ceramic armours were ranked in order of increasing merit: Sintox-FA Al_2O_3, Sintox-CL Al_2O_3, PS 5000 SiC and SiC B. These rankings mostly followed material hardness and strength, where SiC induced a greater shock in the WC-Co core than conventional Al_2O_3. The exception was the relative performance of the two SiC's. The hardness of PS 5000 was higher (2644 Hv *vs*. 1969 Hv for SiC B) yet it was less effective at defeating the BS41. Fractography revealed that after comminution, the SiC B consisted of particles of closely interlocked grains, failing primarily by intergranular cleavage whereas the failure in PS 5000 was primarily transgranular in nature. It is thought that this type of failure, combined with the degree of confinement common to all materials under test, provided considerable resistance to deviatoric stresses. This result suggests that it is not only the type and hardness of SiC that is important, but also the fracture mechanism. These are important properties for ensuring a good level

of resistance to WC-Co penetration. To effectively fracture a projectile high hardness is required, as observed from cores retrieved after being fired into Al_2O_3 compared to SiC. It was demonstrated that well supported confined ceramic, after failure, provided considerable resistance to penetration and thus was more efficient at defeating and fracturing the BS41 core.

Pickup and Barker [218] studied two similar SiC ceramics that had been subjected to 1D stress experiments at strain rates ranging from 10^{-3}/s to 10^{3}/s. One ceramic was SiC B and the other was SiC 100, a pressureless sintered ceramic. In these experiments they measured the time to failure. They noted that the time to failure of the SiC B was 50% higher than that of the SiC 100 and suggested that this could be explained by the microstructure. The main difference was that there was transgranular cleavage in the SiC 100 and intergranular failure in the SiC B.

Standard metallic blocks impart little damage in WC-Co cored projectiles. The projectile core tends to pass in an un-deformed manner; slight surface erosion was noted despite the relatively higher hardness of the WC-Co core compared to each of the witness materials. The most probable explanation of the surface erosion is grains being pulled from the coarse microstructure of the Russian WC-Co core due to high contact loads between it and the metallic witness block (*Chapter 5*). When comparing the BS41 fired into either 1318b aluminium alloy (yield strength 426 MPa, 159 Hv) or mild steel (yield strength of 264 MPa, 195 Hv) witness blocks with a Sintox-CL front plate, despite its higher hardness less fragmentation was noted with mild steel. For brittle materials strong in compression but weak in tension, when the tensile strength has been exceeded, spalling is to be expected. Numerical analysis comparing the stress and shock wave interactions between the projectile and two witness blocks could provide an explanation to the reduced fragmentation. Further experimental and numerical testing is required.

Ceramic armour failure mechanisms, which give promising results, have been identified.

To understand the failure of WC-Co it is important to appreciate both the threshold conditions that trigger this dynamic fracture and the kinetics by which it proceeds. At

the heart of understanding the factors influencing penetrator performance, and the tests and properties that measure these factors, are microstructural investigations, which can systematically guide analysis. The WC-Co core fragments recovered after impact from the semi-infinite trials were examined metallographically in order to gain an understanding of the microstructural changes and deformation processes that had occurred during penetration. *Chapter 5* provides a detailed account of the morphology and chemical composition, respectively, of the fracture surfaces of failed WC-Co using the Scanning Electron Microscope (SEM) and Energy Dispersive X-ray (EDX). A high proportion of WC transgranular cleavage fracture occurred in the large grains of WC. However, in the case of small grain size the fracture mode changed to predominantly WC-WC grain boundary decohesion, intergranular cleavage. Notably crack propagation had a tendency to follow paths of inhomogeneities within the material.

As described, ceramics and cermets have a maximum theoretical strength that can be achieved for a perfectly uniform, defect free specimen. However, ceramic and cermet materials possess flaws that compromise their ability to withstand load. Thus, the strength of the ceramic depends on the largest critical flaw within the structure. The very low fracture strength of materials compared to their theoretical strength is due to the presence of small cracks, which act to concentrate the stress at their tips. The largest critical flaw cannot be predicted, therefore the strength of a ceramic material is statistical in nature. The Lineau distribution provides a complex statistical analysis of the problem, modelled as that of one infinite one-dimensional body, or line, in which fractures are introduced with equal probability at any point on that line [217]. With only small strains required for fracture to occur, interpretation of results can be difficult. Such sensitivity exhibited during the impact trials could be due to the inhomogeneous nature of the ceramic and WC-Co cermet material samples.

The complexity of WC-Co impact behaviour is demonstrated. This causes large variations in the nature of the resultant fragmentation of the BS41 WC-Co core, depending upon the measurement technique and ceramic test target used. With further analysis and input to the material libraries a meaningful preliminary assessment predicting WC-Co failure may be used for evaluation of target systems under a variety of circumstances.

The present work has clearly suggested that the WC-Co failure is assisted by void fraction, which is determined during manufacture of the material. Micrographs presented of the WC-Co core reveal this inhomogeneity, displaying a number of defects: cracks and relatively open porous morphology. It is these factors which are dominant in determining the materials mechanical properties. Microstructural evidence presented suggests that spall failure of the WC-Co core was likely to be dominated by a number of microstructural features including grain size, high porosity and microcracking within the manufactured material. Results also strongly suggest that fragmentation is increased as the hardness of the ceramic front plate is increased under suitable confinement.

In addition, AUTODYN 2D computational modelling was supported by practical experimentation. Numerical testing was carried out using the fully integrated, multi-physics, and interactive non-linear dynamic analysis software. The numerical simulations aimed to simulate the experimental results and provide a further insight into WC-Co impact phenomena. A WC-Co material model has been successfully developed and implemented within the numerical hydrocode AUTODYN 2D. This numerical approach is detailed in *Chapter 6*. Experimental data from both the literature and analysis was used to determine constants for a novel WC-Co material model in AUTODYN 2D. Plate impact test data provided the strength and pressure responses of intact WC-Co. The failure model was inferred from a comparison of computational results to experimental data.

The understanding of penetration mechanisms gained for numerical simulations was used to guide a parametric investigation, validating the WC-Co material failure model with experimental results. In *Chapter 7*, the computational model was tested against sphere impact experimental results performed by Grady [20]. To supplement this work, numerical simulations have been constructed and compared to experimental data from the impact behaviour of the BS41. A discussion of the parametric investigation is presented in *Chapter 6* and *7*. The work presented is believed to contribute to the further understanding of WC-Co failure.

An initial study has been performed and compared to the computed stress history with the experimental ceramic-window interface velocity profiles from plate impact

experimental data. It was demonstrated that the numerical estimation of WC-Co behaviour using a shock EOS, piecewise linear model and a principle stress failure model, provides a good method to estimate spall behaviour under dynamic loading in AUTODYN 2D. It indicates that the computed spall signals show good agreement with the numerical profiles. A significant result is the demonstrated ability to model the fragmentation behaviour of WC-Co spheres impacting PMMA by using Smooth Particle Hydrodynamics with a Lagrangian target. It was shown *via* a successful computer simulation how the material model could aid in the future analysis of the fragmentation behaviour of WC-Co.

The model was tested parametrically for sensitivity. The analysis demonstrated that the greatest observed effect on WC-Co failure was due to changing the materials tensile strength. After several trials it was found that with a tensile strength of 2 GPa and a tensile crack softening of 160 J/m^2, the numerical results showed good agreement to the spall behaviour observed in the Russian sample. The relatively open porous morphology observed in the BS41 could explain the low predicted tensile failure stress. More work is required in this area.

Brittle materials such as WC-Co generally deform inelastically (*Section 2.2.4*). The inelastic response of these materials is usually attributed to the nucleation, growth and coalescence of microcracks (*Section 2.2.6*). Moreover, these cracks cause extensive stiffness loss and strength degradation within the material [166,198]. Notably, the WC-Co sample was found to possess a marked number of defects that could compromise its ability to withstand load (*Chapter 5*). Therefore the crack softening model that allows for the gradual loss of strength as cracks propagate through the material was used.

This present study has revealed the influence of altering ceramic armour configuration on the fracture morphology of the BS41 WC-Co core. The influence of altered material properties and configuration of ceramic armour on WC-Co failure needs further investigation in order to define the underlying damage mechanisms. Analysis of flash X-rays of the behind armour fragmentation and evolution could provide information on fragmentation behaviour. Careful management of ceramic hardness and stress and shock wave propagation by altering acoustic impedance properties of

the armour system are of paramount importance in providing enhanced resistance to WC-Co penetration.

The information gained could be used to modify existing armour materials in order to create a better balance of physical properties to defeat WC-Co cored rounds. If a superior ballistic response can be attained, controlled and incorporated into practical armour systems, it will provide the basis for an advance in armour protective capability against WC-Co penetrators.

The work presented in this thesis does not represent a complete description of the behaviour of WC-Co material. It is hoped that the work is not presented in a manner which suggests it is. It is desired, however, that it has been shown that some of the difficulties associated with the experimental and numerical measurement methodologies of WC-Co behaviour can be overcome and that the work will act as a catalyst for further research.

8.2 Recommendations for Further Work

Experimentation, theory and modelling have all played vital roles in defining what is known about impact phenomena and their effects on target and projectile material properties and behaviour. Recent technology has become an enabling factor, allowing significant advances to be made on several fronts.

A number of recommendations for continued work in the area have been derived from this investigation. It is essential to repeat experimental trials to gain a more accurate representation of each test and to retrieve more WC-Co core. Preliminary numerical studies have been initiated to assess whether the technique is capable of predicting WC-Co fracture failure by AUTODYN 2D modelling. It would be worthwhile to investigate further the effect of different WC-Co core projectiles and WC-Co materials (*e.g.,* altered Co concentrations) on dynamic loading. It is recommended for future extensive research programmes that the 7.62 FFV round is studied due to lower logistical impact *i.e.,* availability of ammunition and without the requirement of

comparably large targets, this would also facilitate the use of flash X-ray imagery during penetration.

Here is a summary of possible future analysis:

- DoP is often used to calculate a ballistic efficiency for a material. The value calculated depends heavily upon the parameters of the material used as a reference. DoP assessments are made into the back-block material at nominally the same velocity at which the material under test will be tested. This is vital when comparing data to outside sources. It is suggested that experiments are performed to RARDE Standard 816 [17] into a generic UK RHA (yield stress typically 1225 MPa) or HHS (Yield Stress typically 1504 MPa) witness blocks to allow consistent use to be made of the DoP results to industry. It is also recommended that yaw is measured. James *et al.* [18] and provides correction algorithms, normalisation methods and calculations for the determination of the value, for comparing results to open literature.

- Problems arise when the WC-Co cored ammunition's hardness is approximately the same or more than that of most commercial Al_2O_3 and therefore the latter offers little resistance to penetration. The work presented has identified the need to investigate further other ceramic target systems common to armour technology. Examples including: B_4C, which has a greater hardness yet lower compressive strength than that of SiC. Other types of SiC are also possible alternatives including SiC–N, Cercom Ltd, where an increase in fracture toughness (SiC B-4.4 MPa / SiC-N-4.7MPa) has been achieved by improved manufacturing, alternating temperature and pressure regulation during the hot-pressed manufacture route (*Section 2.2.2*). Finally a more detailed account of the effects of TiB_2 with its significant increase in hardness (2700 Hv) compared to other ceramics (*e.g.,* SiC B-1969 Hv) and fracture toughness (6.9 MPa/m). Yet these improvements are achieved at the penalty of increased cost. Titanium Diboride is under consideration for very limited armour design.

- Investigation of the fracture failure of a WC-Co cored projectile as it passes through the ceramic target. This analysis would examine the initiation of fracture in the WC-Co core during the penetration process. Such experimentation would

prove expensive yet flash X-radiography may accurately describe the onset and development of WC-Co core failure.

- Investigation of the application of different layer designs including air gaps and cover plates confining the front of ceramic target systems. This would include additions of different adhesives between mating surfaces.

- Extension of the material model to describe two and three-dimensional imaging of the impact behaviour.

- Investigate the effects of obliquity on target and projectile behaviour.

- Extension of the WC-Co material model to describe the behaviour of other WC-Co material compositions. Obtain a detailed description of the effects of varying;

    - Equation of State
    - Strength Model
    - Failure Model
    - Processor Subgrid Type

- Compare numerical simulations to experimental data obtained using different WC-Co projectiles. Examples are described in *Chapter 2*.

- Extensions of X-ray experimental data to compare with numerical simulations. Results including data on target and WC-Co fragmentation, impact velocity and obliquity. Formation of these fragments should depend on the physical properties and shapes of target and projectile materials.

- Compare experimental data from Gooch and Burkins to numerical simulations using the WC-Co material model derived in *Chapter 6* [22]. Experimental analysis of the impact of 7.62 mm AP WC-Co core projectile into hot pressed Cercom Inc. of Vista, CA, B_4C backed by polyethylene at velocities at 971 m/s ± 2 m/s using the reverse ballistic technique that has been reported.

……..Blank Page…….

CITED REFERENCES

1 Harrison P. G., Everett-Heath E. J., Moss G. M. & Mowat, A. W., *Military Helicopters*, Brassey's Battlefield Weapon Systems & Technology Series, Royal Military College of Science, Volume X1, Brassey's Defence Publishers, 1985

2 Alesi, A. L. & Barron, E. R., "Plastic – Ceramic Composite Armor for Vietnam", *Proc. Of 23rd Annual Tech. Conf. Reinforced Plastics Composite Div*., Soc. Plast. Ind., 1968

3 Bart, R. K. & Lindberg, J. C., "Ceramic Bodyguards", *Advanced Materials & Processes inc., Metal Progress*, 1987, Vol. 9

4 Gooch, W. A., "An Overview of Ceramic Armour Applications", *U. S. ARL, Ceramic Armour Materials by Design, Ceramic Transactions*, 2001, Vol. 134

5 Armour School RAC Centre, *Terminal Ballistics and Armoured Fighting Vehicle Protection*, September, 1980

6 Jane's Defence Weekly, *The Worlds News and Analysis*, 20th October 2004, Vol. 41

7 Shiyong, D., "Development of Armour Piercing Projectiles", *Bingqi Zhishi*, 1984, September, No. 5, pp. 8 – 9

8 P. Labbett & F. A. Brown, *Technical Ammunition Guide*, Series 3, Pamphlet 4, R/95/290 Royal Military College of Science

9 Woolmore, N. J., Hazell P. J. & Stuart, T. P., "An Investigation Into Fragmenting the 14.5 mm BS41 Armour Piercing Round by Varying a Confined Ceramic Target Set-up", *Ceramic Armour and Armour Systems, Ceramic Transactions*, 2003, Vol. 151, The American Ceramic Society, Edited Eugene Medvedovsk. APPENDIX 2

10 Armoured Fighting Vehicles, 2000, URL: http://www.taos-inc.com/afvs.htm

11 Jane's Defence Weekly, *The Worlds News and Analysis*, 2004, Vol. 41, 22nd September

12 Jane's, Armour and Artillery, Date Posted 12th June 2000

13 Ministry of Defence, 2006, URL: http://www.mod.uk

14 Bless, S. J. & Anderson Jr., C. E., "Penetration of Hard Layers by Hypervelocity Rod Projectiles" *International Journal of Impact Engineering*, 1993, Vol. 14, pp. 85 – 93

15 Delgrave, R., "Applying *EM* Computed from DoP Testing Results to the Design of Actual Ceramic Armour Systems", *17th International Symposium on Ballistics*, South Africa, 23 – 27th March 1998

16 Senf, H., Straßburger, E., Rothenhäusier, H. & Lexow, B., "The Dependency of Ballistic Mass Efficiency of Light Armour on Striking Velocity of Small Caliber Projectiles", *17th International Symposium on Ballistics*, South Africa, 23 – 27th March 1998

17 James, B. J., *The DoP Test: Methodology, Measurement and Calculation of Ballistic Efficiency*, DRA/LSF3c/TR95/002/1.0, 1995, June

18 James, B. J., "Depth of Penetration Testing", *Ceramic Armour Materials by Design, Ceramic Transactions*, 2001, Vol. 134

19 Subramaniam, R., Bless, S. J., Cazamias, J. & Berry, D., "Reverse Impact Experiments Against Tungsten Rods and Results for Aluminium Penetration Between 1.5 and 4.2 km/s", *International Journal of Impact Engineering*, 1995, Vol. 17, pp. 817 – 824

20 Grady, D.E.,"Impact Failure and Fragmentation of Tungsten Carbide", *International Journal of Impact Engineering*, 1999, Vol. 23, pp. 307 – 317

21 Baxter, A. G. & James, B. J., *Through Thickness Flash X-Radiography of Ceramic during Impact. Report No. 2*, DRA/LSF3/TR95/021/1.0, May 1996

22 Gooch, W. A., Burkins, M. S., Kingman, P., Hauver, G., Netherwood, P. & Benck, R., "Dynamic X-ray Imaging of 7.62 mm APM2 Projectiles Penetrating Boron Carbide", *18th International Symposium on Ballistics*, San- Antonio, 15 – 19th November 1999

23 "Flash Radiography Sources", 14th November 2001, URL www.mindspring.com/ ,

24 Wilson D. J., & Hetherington, J. G., "Analysis of Ballistic Impact on Ceramic Faced Armour using High Speed Photography", *Lightweight Armour Systems Symposium, Royal Military College of Science*, 28th – 30th June 1995

25 Weber, K., "High Speed Cameras", *Laser Focus World*, June 2000, URL: www.optoelectronics-world.com

26 Grady, D. E., "Shock Compression Properties of Ceramics", in *High Pressure Research*, ed. Singh, A. K., Oxford and IBH Publishing, 1992

27 Tardec Report

28 Callister Jr, W. D., *Materials Science and Engineering, An Introduction*, 3rd Edition, John Wiley and Sons, Inc, New York, 1994

29 Ashby, M. F. & Jones, D. R. H., *Engineering Materials 2", An Introduction to Microstructures, Processing and Design*, Pergamon Press, 1988

30 McColm, I. J., *Ceramic Science for Materials Technologists*, Pub. Leonard Hill, USA Chapman & Hall, 1983

31 Segal, D., *Chemical Synthesis of Advanced Ceramic Materials*, Cambridge University Press, 1989

32 Ryan, W., *Properties of Ceramic Raw Materials*, Pergamon Press, 1978

33 McColm, I. J., & Clark, N. J., *High-Performance Ceramics*, Blackie, USA Chapman and Hall, New York, 1988

34 Yanagida, H., Koumoto, K. & Miyayama, M., *The Chemistry of Ceramics*, Pub. Wiley and Maruzen, 1996

35 Davidge, R. W., *Mechanical Behaviour of Ceramics*, Cambridge Solid State Science Series, 1979

36 *Enhanced Ceramic Armour Materials*, A Review of the open Literature, Royal Military College of Science, Report No. SEAS/MSE/1H/145/97, 1997

37 Anderson, C. E., & Royal-Timmons, S. A., " Ballistic Performance of Confined 99.5%-AL2O3 Ceramic Tiles", *International Journal of Impact Engineering*, 1997, Vol. 19, pp. 703 – 713

38 Pickup, I. M., *Compressive Strength Characterisation of Alumina*, DRA/FVS/AM/CR94013/1.1, 1994

39 James, B., "The Influence of the Material Properties of Alumina on Ballistic Performance", *15th International Symposium on Ballistics*, Israel, 1995

40 Dickshit, S. N., Kutumbarao, V. V., & Sundararajan, G., "The Influence of Plate Hardness on the Ballistic Penetration of Thick Steel Plates." *International Journal of Impact Engineering*., 1995, Vol. 16, No. 2, pp. 293 – 320

41 Arnold, P. J., Barr, A. J. P., Pizii, R. L., Simmons, J. A. & Thompson, R. P. D., *Protection for Combat Vehicles (U)*, RMCS, Defence Technology Course, 1998

42 Bruchey, W. J. & Burkins, M. S., "Suppression of Material Failure Modes in Titanium Armours", *17th International Symposium on Ballistics*, South Africa, 1998

43 Olgilvy, J., "Titanium's Growing Role in Defence Applications", Vol. 23, Armour Special Addition, SE1-Armour, *Outlook*, 2002

44 Ashby, M. F. & Jones, D. R. H., *Engineering Materials 1, An Introduction to their properties and applications*, 2nd Edition, Butterworth Heinemann, 1998

45 Case, J. & Chilver, A. H., *Strength of Materials and Structures, An Introduction to the Mechanics of Solids and Structures*, 2nd Edition, Edward Arnold, 1972

46 Martin, S. R., "Experimental Characterisation of the Effect of Microstructure on Dynamic Behaviour of SiC", MSc Dissertation, Georgia Institute of Technology, June, 2004.

47 Rosenberg, Z., Bless, S. J. & Brar, N. S., "On the Influence of the Loss of Shear Strength on the Ballistic Performance of Brittle Solids", *International Journal of Impact Engineering*, 1990, Vol. 9, No. 1, pp. 45 –49

48 O'Donnell, R. G., "An Investigation of the Fragmentation Behaviour of Impacted Ceramics", *Journal of Material Science Letters*, 1991, 10, pp. 685 – 688

49 Horsfall, I. & Buckley, D., "Multi-Hit Capability and Damage Tolerance of Ceramic Faced Armour Systems", *Lightweight Armour Systems Symposium*, Cranfield University, RMCS, June 1995

50 Wachtman, J. B., "Elastic Deformation of Cermaics and Other Refractory Materials", *Mechanical and Thermal Properties of Ceramics*, 1969, 303, pp.139

51 Orsini, H., "Impact Behaviour of Bilayer Armours." *Lightweight Armour Systems Symposium*, Cranfield University, RMCS, 1995

52 Ben-Dor, G., Dubinsky, A. & Elperin, T., "On the Ballistic Resistance of Multi-Layered Targets with Air Gaps." *International Journal of Impact Engineering*, 1998, Vol. 35, pp.3097 – 3103

53 Espinosa, H. D., Brar, N. S., Yuan, G., Xu, Y. & Arrieta, V., "Enhanced Ballistic Performance of Confined Multi-Layered Ceramic Targets against Long Rod Penetrators through Interface Defeat." *International Journal of Solids and Structures*, 2000, 37

54 Lee, Y. L. & Iremonger, M. J., "Experiments into the Effect of Various Radically Different Interlayer Materials & Interface Conditions on some Alumina Faced Steel Backed Lightweight High Velocity Armours", *Lightweight Armour Systems Symposium*, Cranfield University, RMCS, 1995

55 Mackiewicz, J. F., "Advanced Ceramic / Composite Armor for the Defeat of Small Arms", U.S. Army Laboratory – materials, *Lightweight Armour Systems Symposium*, 1995

56 Sierakowski, R. L., Ross, C. A., Malvern, L. E. & Cristescu, N., *Studies on the Penetration Mechanics of Composite Plates*, DAAG29-76-G-0085, University of Florida, 1976

57 Rolsten, R. F., Bodine, E. G. & Dunleavy, J. G., *Breakthrough in Armour, Space and Aeronautics*, 1968, 50 (1), pp. 55 – 63

58 Hazell, P. J. & Iremonger, M. J., "Ceramic Armour Penetration", Engineering Systems Department, Royal Military College of Science, *Lightweight Armour Systems Symposium*, 10-12th November, 1999

59 Scilame, J. M., "LIBA New Concept for Light Ballistic Protection", Ten Cate Advances Composites, *Lightweight Armour Systems Symposium*, RMCS, 11th November, 1999

60 Lowery, B., *Optimisation of a Composite Armour System to Defeat FFV 7.62mm AP Projectiles*, No 18 Military Vehicles Technology, Royal Military College of Science, MSc Project Report, Cranfield University, November 1990

61 Florence, A. L. & Ahrens, T. J., I*nteraction of Projectiles and Composite Armor*, Final Report, AMRA CR 67 – 05 (F), 1st January, 1967

62 Florence, A. L., *Interaction of Projectiles and Composite Armor Part II*, AMMRC CR 69 – 15, August, 1969

63 Hetherington, J. G., *Terminal Ballistics*, Royal Military College of Science, Cranfield University, 2000

64 Hetherington, J. G., "The Optimization of Two Component Composite Armours", *International Journal of Impact Engineering*, Vol. 12, No. 3, pp. 409 – 414, 1992

65 Wilkins, M. L., *Fourth Progress Report on Light Armour Program*, LLNL, UCLR-50694, 1969

66 Wilkins, M. L., *Second Progress Report on Light Armour Program*, LLNL, UCLR-50349, 1967

67 Wilson, D. J. & Hetherington, J. G., "Analysis of Ballistic Impact on Ceramic Faced Armour using High Speed Photography", *Lightweight Armour Systems Symposium*, Royal Military College of Science, 28th – 30th June, 1995

68 Prior, A. M., *The Ballistic Impact of Small Calibre Ammunition on Ceramic Composite Armour*, Ph.D. Thesis, Defence Academy, Royal Military College of Science, July 1988

69 James, B., "Practical Issues in Ceramic Design", *Ceramic Armour Materials by Design*, 2002, Vol. 134

70 Iremonger, M. J., *A Novel Concept for Spaced Armour*, ESD Royal Military College of Science, Cranfield University, 1996

71 Zaera, R. & Sanchez-Galvez, V., "Analytical Modelling of Normal and Oblique Ballistic Impact on Ceramic/ Metal Lightweight Armours", *International Journal of Impact Engineering*, 1998, Vol. 21, No. 3, pp. 133 – 148

72 Iremonger, M. J., "Normal and Oblique Impact of Steel by Small Arms Bullets: Hydrocode Simulations and Experimental Observations", *Lightweight Armour Systems Symposium*, RMCS, June, 1995

73 Bruce, A. A., *The Effect of Obliquity on the Penetration of Mild Steel Plates from Small Arms Fire*, RMCS, April 1991

74 Gupta, N. K. & Madhu, V., "An Experimental Study of Normal and Oblique Impact of Hard-Core Projectiles on Single and Layered Plates", *International Journal of Impact Engineering*, 1997, Vol. 19, pp. 395 – 414

75 Gooch, W. A., "An Overview of Ceramic Armour Applications." *Ceramic Armour Materials by Design*, 2001, Vol. 134

76 Zucas, J. A., Nicholas, T., Swift, H. F., Greszczuk, L. B. & Curran, D. R., *Impact Dynamics*, Krieger Publishing Company, 1992

77 Laible, R. C., *Methods and Phenomena 5, Ballistic Materials and Penetration Mechanics*, Elsevier Scientific Publishing Company, 1980

78 Ernst, H., Wiesner, V. & Wolf, T., "Armour Ceramics Under High-Velocity Impact of a Medium Calibre Long Rod Penetrator", *Ceramic Armour Materials by Design, Ceramic Transactions*, 2001, Vol. 134

79 Orphol, D. L., "Long Rod Penetration of Ceramics", *Ceramic Armour Materials by Design, Ceramic Transactions*, 2001, Vol. 134

80 Schonberg, W. P. & Williamsen, J. E., "Empirical Hole Size and Crack Length Models for Dual-Wall Systems Under Hypervelocity Projectile Impact", *International Journal of Impact Engineering*, 1997, Vol. 20, pp. 711 – 722

81 Partom, Y., "On the Hydrodynamic Limit of Long Rod Penetration", *International Journal of Impact Engineering*, 1997, Vol. 20, pp. 617 – 625

82 Merzhievsky, L. A., "Crater Formation in a Plastic Target Under Hypervelocity Impact", *International Journal of Impact Engineering*, 1997, Vol. 20, pp. 557 –568

83 Rosenberg, Z. & Dekel, E., "Further Examination of Long Rod Penetration; the Role of Penetrator Strength at Hypervelocity Impact", *International Journal of Impact Engineering*, 2000, Vol. 24, pp. 85 – 102

84 Tate, A., *Extensions of the Hydrodynamic Theory*, Report 16 / 85, 1986

85 Rosenberg, Z. & Tsaliah, J., "Applying Tate's Model for the Interaction of Long Rod Projectiles with Ceramic Targets", *International Journal of Impact Engineering*, 1990, Vol. 9, pp. 247 – 251

86 Schonberg, W. P. & Williamsen, J. K., "Empirical Hole Size and Crack Length Models for Dual-Wall Systems under Hypervelocity Projectile Impact." *International Journal of Impact Engineering*, 1997, Vol. 20, pp. 711 – 722

87 Szendrei, T., "Link between Penetration and Radial Crater Expansion in Hypervelocity Impact.", *17th International Symposium on Ballistics*, 23 – 27th March, 1998

88 Bless, S. J. & Anderson, C. E., "Penetration of Hard Layers by Hypervelocity Rod Projectiles.", *International Journal of Impact Engineering*, 1997, Vol. 14, pp. 85 – 93

89 Winkler, S., Senf, H. & Rothenhausler, H., "Wave and Fracture Phenomena in Impacted Ceramics", *IWM-Bericht V 23/89,* AD-A213454, December 1989

90 Bourne, N. K., Rosenberg, Z. & Millett, J. C. F., "The Plate Impact Response of Three Glasses", *Structures Under Shock and Impact*, 1996, pp. 553-562

91 Najar, J., "Dynamic Tensile Fracture Phenomena at Wave Propagation in Ceramic Bars" *Journal de Physique IV*, September 1994

92 Chung, S. K., "Fracture Characterisation of Armour Ceramics", *Ceramic Bulletin*, 1990, Vol. 69, No.3, pp. 358-366

93 Rozenberg, Z. & Yeshurun, Y., "The Relation Between Ballistic Efficiency and Compressive Strength of Ceramic Tiles", *International Journal of Impact Engineering*, 1988, Vol. 7, No. 3, pp. 357-362

94 Sherman, D. & Brandon, D. G., "The Ballistic Failure Mechanisms and Sequence in Semi-Infinite Supported Alumina Tiles." *Journal of Materials Research*, 1997, Vol. 12, No. 5

95 Milton, A. L., *An Investigation into the Ballistic Performance of Heavily Confined Silicon Carbide Impacted by Tungsten Long Rods,* DRA/LS4/TR96/029/1.0, May, 1996

96 Sherman, D. & Ben-Shushan, T., "Israel Institute of Technology", Poster Report, 1993

97 Hauver, G., & Dehn, J., "Interface Defeat Mechanisms in Delayed Penetration*", 14th DEA-G-1060 Armour / Anti-armour Workshop*, 1987

98 Littlefield, D. L., Anderson, C. E., Partom, Y. & Bless, S. J., "The Penetration of Steel Targets Finite in Radial Extent", *International Journal of Impact Engineering*, 1997, Vol. 19, No 1, pp. 49 - 62

99 Rosenberg, Z., Dekel, E., Hohler, V., Stilp, A. J. & Weber, K., "Hypervelocity Penetration of Tungsten Alloy Rods into Ceramic Tiles: Experiments and 2-D Simulations." *International Journal of Impact Engineering*, 1997, Vol. 20, pp. 675 – 683

100 Westerling, L., Lundberg, P. & Lundberg, B., "Tungsten Long-Rod Penetration into confined cylinders of Boron Carbide at and above Ordnance Velocities". *International Journal of Impact Engineering*, 2001, 25, pp. 703 - 714

101 Lundberg, P., Holmberg, L. & Janzon, Bo., "An Experimental Study of Long Rod Penetration into Boron Carbide at Ordnance and Hyper Velocities", *17th International Symposium on Ballistics*, 23 - 27th March 1998.

102 Brunchey, W. J. & Horwath, E. J., "System Consideration Concerning the Development of High-Efficiency Ceramic Armours", *17th International Symposium on Ballistics*, 23 - 27th March 1998

103 Anderson, C. E. & Royal-Timmons, S. A., "Ballistic Performance of Confined 99.5% Al2O3 Ceramic Tiles." *International Journal of Impact Engineering*, 1997, Vol.19, No. 8

104 Tod, D. A. & Wylie, P., *Assessment of Adhesives for Military Applications*. DRA/DWS/WX4/TR94197/1.0, July 1994

105 Brown, A. F., Lloyd, E. A. & Wadwani, D. S.*, Testing of Adhesive-Bonded Joints by Broad-Band Ultrasound*, RT42090/018STR-FR, 1979

106 Drew, R. C., "The Improvement in Damping Properties of CFRP Materials over a Wide Temperature Range", *Institute of Sound and Vibration Research*, R/95/215, ISVR Contract Report 91/27, August 1991

107 Skeldon, M., Thompson, G. E., Wood, G. C., Johnson, B. & Wilford, P.*, Adhesive Bonding of Aluminium Alloys*, Final Report, 2044/0130 XR/MAT, 1987

108 Marsh, R. J.*, Performance of Adhesive used to Secure Steel Plates to Concrete in Fortified Structures*, Royal Military College of Science, Defence Technology Project, 1992

109 Pink, E. & Campbell, J. D., *The Effect of Strain Rate and Temperature on the Deformation Behaviour of Reinforced and Un-reinforced Epoxy Resin*, Engineering Laboratory, Oxford, Report No. 1040/72, July, 1972

110 Ignjatovic, M., Chalkey, P. & Wang, C.*, The Yield Behaviour of a Structural Adhesive under Complex Loading*, DSTO-TR-0728.

111 Chalkley, P. & van den Berg, J.*, On Obtaining Design Used in the Bonded-Composite Repair of Aircraft*. DSTO-TR-0608, 1998

112 Pollock, E. A., "*Final Report on Agreement No. 2065/55*, 1986

113 Paul, N. C. & Richards, D. H.*, Technical Report, No. 234, A Room Temperature Cured Flexible Epoxy Adhesive*, July 1975

114 Luoma, G. A., Yee, L. K. & Rowland, R. D.*, Room Temperature Curing Adhesives for Bonding Carbon Fibre Reinforced Epoxy Composites*, Technical Memorandum 86 – 3, Department of National Defence, 1986

115 Tickner, R. L., Shaw, S., Digby, R. P., Bowditch, M. R., Gardham, L. M. & Wylie, P., *A Survey of Adhesives for Non-Lethal Warfare*, DRA/SMC/TR963010/1.0, March, 1996

116 Zaera, R., Sanchez-Saez, S., Perez-Castellanos, J. L. & Navarro, C., *Modelling of the Adhesive Layer in Mixed Ceramic / Metal Armours Subjected to Impact*, Mechanical Engineering Department, Madrid, Spain.

117 Aldridge, M. J., *The Effect of Adhesive on the Performance of Composite Armour*, RMCS, April 1996

118 Kent, M. C., *Effects of Varying Adhesive Layer Parameters upon the Ballistic Performance of Lightweight Ceramic Faced Aluminium Armour*, RMCS, ESD, July 2000

119 Shiyong, D., "Development of Armour-Piercing Projectiles", *Bingqi Zhishi*, September 1984, No.5, pp. 8 - 9,

120 URL http://www.primextech.com/lca.html , "Large Caliber Ammunition", 2000

121 Defence Intelligence Services facsimile transmission, "14.5 mm Ammunition", Ref. TIS/00/403, 6th September, 2000

122 Jane's Information Group, *Jane's Ammunition Handbook, Small Arms*, Date Posted December 10th 1999, URL http://is.rmcs.cranfield.ac.uk/janes/jah99/jah_0102.htm

123 Military Equipment of Ukraine, Russia, Belarus and other former Soviet Union Countries, http://www.taos-inc.com/smarms.htm,

124 Dowding, R. J., Hogwood, M. C., Wong, L., & Woodward, R. L., "Tungsten Alloy Properties Relevant to Kinetic Energy Penetrator Performance", *Tungsten & Refractory Metals 2*, 1994

125 Roberson, C. & Hazell, P. J., "Resistance of Four Different Ceramics Materials to Penetration by a Tungsten Carbide Cored Projectile", *Ceramic Armour and Armour Systems, Ceramic Transactions*, 2003, Vol. 151, The American Ceramic Society, Ed. Eugene Medvedovsk

126 Ness, L. & Williams, A., *Jane's Ammunition Handbook 2005 - 2006*, Jane's Information Group Ltd, ISBN 07106 2685 1, 2005

127 Pageau, G. & Bourget, D., "Influence of Target Material Configuration on the Relative Penetration Capability of Small Caliber Bullets", *XI European Small Arms Symposium*, RMCS, 26th – 27th August, 1997

128 Hetherington, J. G., "A Comparative Study of Applique Systems for Up-Armouring APC", *Lightweight Armour Systems Symposium*, RMCS, 1997

129 Woodward, R. L., Baxter, B. J. & O'Donnell, R. G., *Ballistic Evaluation of Applique Armours – Presentation and Interpretation of Ballistic Data*, Defence Science Technology Organisation", Technical Note, 1988

130 Peskes, G. J. J. M. & Barbero, E., "Optimisation of Light Weight Add-On Armour for Infantry Fighting Vehicles", *17th International Symposium on Ballistics*, 23 – 27th March, 1998

131 Hauver, G. E., Netherwood, P. M., Benck, R. F. & Kecskes, L. J., "Enhanced Ballistic Performance of Ceramics", Army Ballistic Research Laboratories, *19th Army Science Conference*, 1994

132 Gagne, M. P., *The Penetration of Small Arms Projectiles in Ceramic Faced Armours*, RMCS, Cranfield University, Report, 1988

133 Pyzik, A. J., Aksay, I. A. & Sarikaya, H., "Microdesigning of Ceramic-Metal Composites", *Ceramic Microstructures, Materials Science Research*, 1986, Vol. 21

134 Bal-Tec, "Tungsten Carbide", 2006, URL http://www.precisionballs.com

135 McColm, I. J. & Clark, N. J., *High-Performance Ceramics*, Publishers Chapman and Hall, 1988

136 Inframat, "Description of Tungsten Carbide Technology – Superfine Tungsten Carbide for Bulk Hardmetal Applications", 2004, URL www. Inframat.com

137 Woolmore, N. J., "House of Commons Young Engineer Presentation", 2002

138 Ramkumar, J., Aravindan, S., Malhotra, S. K. & Krishnamurthy, R., "Enhancing the Metallurgical Properties of WC insert (K-20) Cutting Tool through Microwave Treatment", *Materials Letters*, March 2002, 53, pp. 200 – 204

139. Milman, Yu. V, Chugunova, S. I., Goncharova, I. V., & Lucyckx, S., "Determination of Ductility and Stress Strain Curve of WC Based Hard Metals by Indentation Method", *Science of Sintering*, 1997, 29 (3), pp. 155 – 161

140 Kalpakjian, S., *Manufacturing Processes for Engineering Materials*, Second Edition, World Student Series Edition, Addison – Wesley Publishing Company, (1991).

141 Sherman D. & Ben-Shushan T., "Quasi-Static Impact Damage in Confined Ceramic Tiles", *International Journal of Impact Engineering*, 1998, Vol. 21, No. 4, pp. 245 – 265

142 C. E. Anderson, J. D. Walker & T. R. Sharron, "The Influence of Edge Effects on Penetration", *17th International Symposium on Ballistics*, 23 – 27th March 1998

143 O'Donnell, R. G., Woodward, R. L.*, Fragmentation of Alumina in Ballistic Impact as a Function of Grade and Confinement*, US Army Ballistic Laboratories,

144 Catmur, D., Horsfall, I., Edwards, M. & Hallas, M., *The Effects of Confinement on the Performance of Ceramic Faced Armour against Shaped Charge Attack*, Royal Military College Science, Cranfield University.

145 Williams, T., *Metallurgical aspects of the response of 1 in. thick Armour Plate Steels to Attack by two Types of small Tungsten Carbide Projectiles*. MOD, Royal Armament Research and Development Establishment, R / 71 / 216.

146 Andersson, M., Persson, J. & Rowcliffe, D. J., "Impact on Ceramic Armour Materials with Small Tungsten Carbide Spheres, Experimental and Numerical Studies." *13th International Symposium on Ballistics, Stockholm*, 1 – 3rd June, 1992

147 Hertal, E. S. & Grady, D. E., "Tungsten Carbide Fragmentation; Experimental Characterisation and Numerical Modelling", *15th International Symposium on Ballistics*, Israel, 21 – 24th May 1995

148 Dandekar, D. P. & Grady, D. E., "Shock Equation of State and Dynamic Strength of Tungsten Carbide", *Shock Compression of Condensed Matter*, 2001, pp. 783 – 786

149 Martineau, R. L., Prime, M. B. & Duffey, T., "Penetration of HSLA-100 steel with Tungsten Carbide Spheres at Striking Velocities Between 0.8 and 2.5 km/s." *International Journal of Impact Engineering*, May 2004, Vol. 30

150 Franzen, R. R., Orphal, D. L. & Anderson, C. E. Jr., " The Influence of Experimental Design on Depth of Penetration (DoP) Test Results and Derived Ballistic Efficiencies." *International Journal of Impact Engineering*, 1997, Vol. 19, No. 8, pp. 727 – 737

151 Fortier, C., Bourget, D., Pageau, G. & Beaubien, N., "Comparative Study of Selected Methods for Estimating Ballistic Limit Velocities of Armour Materials", *17th International Symposium on Ballistics*, 23 – 27th March, 1998

152 Hironaka, Y., Tamura, H., Tanabe, Y. & Sawaoka, A., "Fragmentation and Dispersion of Aluminium Nitride Ceramic Plates by Hypervelocity Impact", *International Journal of Impact Engineering*., 1997, Vol. 19, No. 4, pp. 285 – 295

153 Moynihan, T. J., LaSalvia, J. C. & Burkins, M. S., "Analysis of Shatter Gap Phenomenon in a Boron Carbide / Composite Laminate Armor System." *20th International Symposium on Ballistics*, Orlando Florida, 23 – 27th September 2002

154 Bjerke, T., Silsby, G., Scheffler, R. M., "High Yaw Penetration of Long Rods Penetrators", *Proceedings of the 13th International Symposium on Ballistics*, 1992

155 Yaziv, D., Rosenberg, G., Partom, Y., "Differential Ballistic Efficiency of Applique Armour", *9th International Symposium on Ballistics*, UK, 1986

156 Partom, Y., Anderson, C. E. & Yaziv, D., "Penetration of AP Projectiles into Spaced Ceramic Targets", *19th International Symposium on Ballistics*, pp.1175 – 1181, 7 – 11th May, 2001

157 Hazell, P. J., *Terminal Ballistics*, FES Course, Royal Military College of Science, Cranfield University, 1999

158 Hetherington, J. G., *Terminal Ballistics*, Royal Military College of Science, Cranfield University, 2000

159 Propellant Tables, 2002, URL www.astronautix.com/articles/solables.htm

160 Fordham, S., *High Explosives and Propellants*, 2nd Revised Edition, Pergamon International Library, Pergamon Press, 1980

161 Cartwright, M., *Chemistry of Explosives*, Royal Military College of Science, 2001 Edition, Ammunition Technical Officers Course, 2001

162 Department of the Army Technical Manual, *Military Explosives*, TM 9-1300-214-T0 11A-1-34, Department of the Army and the Air Force, November 1967

163 Rosenberg, Z., Dekel, E., Hohler, V., Stilp, A. J. & Weber, K., "Hypervelocity Penetration of Tungsten Alloy Rods into Ceramic Tiles: Experiments and 2-D Simulations." *International Journal of Impact Engineering*, 1997, Vol. 20, pp. 675 – 683

164 Cercom website, URL http://www.thomasregister.com/olc/cercom/scb.htm

165 Manufacturer's Results obtained from Morgan Matroc, 2002

166 Hazell, P. J., *The Failure of Ceramic Armour Subjected to High Velocity Impact*. Ph.D. Thesis, Cranfield University, Royal Military College of Science, October 1998

167 Roberson, C. J., Hazell, P. J., Gotts, P. L., Pickup, I. M. & Morrell, R., *The Effective Hardness of Hot Pressed Boron Carbide with Increasing Shock Stress*, The American Ceramic Society, 2005

168 Tuck, J. R., Korsunsky, A. M., Bull, S. J. & Davidson, R. I., "On the Application of the Work of Indentation Approach to Depth Sensing Indentation Experiments in Coated Systems", *Surface and Coatings Technology*, 2001, 137

169 Zeng, K., Söderland, E., Giannakopoulos, A. E. & Rowcliffe, D. J., "Controlled Indentation: A General Approach to Determine Mechanical Properties of Brittle Materials", *Acta. Mater*., 1996, Vol. 44, pp. 1127 – 1141

170 Atkinson, M., "Calculation of Characteristic Macro Hardness from Low Load Indentation Tests", *Materials Science and Engineering*, 1995, A197

171 Wang, H. L. & Hon, M. H., "Temperature Dependence of Ceramics Hardness", *Ceramics International*, 1999, 25

172 Zeng, K. & Rowcliffe, D., "Analysis of Penetration Curves Produced by Sharp Indentations on Ceramic Materials", *Philosophical Magazine A*, 1996, Vol. 74, pp. 1107 –1116

173 Andrews, E. W., Giannakopoulos, A. E., Plisson, E. & Suresh, S., "Analysis of the Impact of a Sharp Indenter", *International J. of Solids and Structures*, 2002, 39, pp. 281 – 295

174 Bush, M. B., "Simulation of Contact Induced Fracture", *Engineering Analysis with Boundary Elements*, 1999, 23, pp. 59 – 66

175 Milman, Y. U. V., Galanov, B. A. & Chugunova, S. I., "Overview No. 107, *Acta. Metall. Mater*., 1993Vol. 41, No. 9, pp. 2523 – 2532

176 Mendelson, M., *J. Amer. Ceram. Soc*., 1969, 52 (8), pp. 443 – 446

177 Sherman, D. & Ben-Shushan, T*., The Ballistic Failure Mechanisms and Sequence in Confined Ceramic Tiles*, Israel Institute of Technology, TNS Meeting, Pitzbourg, 1993

178 FasTTrax, BBC Learning Zone Documentary, 2003

179 Kennedy, E. W., "Influence of Microstructure on Fracture Characteristics and Tensile Properties of Two Tungsten Heavy Alloys", Tungsten and Refractory Metals 2, Proceedings of the International Conference on Tungsten and Refractory Metals, 1994

180 Chaiat, D., Gutmanas, E. Y. & Gotman, I., "Effect of Processing and Alloying on Microstructure and Properties of Tungsten Heavy Alloys", *Tungsten and Refractory Metals 2, Proceedings of the International Conference on Tungsten and Refractory Metals,* 1994

181 Schwartz, A. J., Kumar, M. & Adams, B. L., *Electron Backscatter Diffraction in Materials Science*, Kluwer Academic, Plenum Publishers.

182 James, B., "Practical Issues in Ceramic Armour Design*", Ceramic Armor Materials by design, Ceramic Transactions*, 2003, Vol. 134

183 Pickup, I. M., Barker, A. K., James, B. J., Cottenot, C. & Orsini, H., "The Effects of Stress Pulse Characteristics on the Defeat of Armour Piercing Projectiles", *19th International Symposium on Ballistics*, 7 – 11th May 2001, pp. 1305 – 1312

184 Shockey, D. A., & Marchand, A. H., " Failure Phenomenology of Confined Ceramic Targets and Impactor Rods", *Ceramic Armour Materials by Design, Ceramic Transactions*, 2002, Vol. 134

185 Dieter, G. E., "Mechanical Metallurgy", SI Metric Edition, McGraw-Hill Book Company, 1988 ISBN 0-07-100406-8

186 Feng, R., Raiser, G. F. & Gupta, Y. M., "Material Strength and Inelastic Deformation of Silicon Carbide under Shock Wave Compression", *Journal of Applied Physics*, 1998, Vol. 83, No. 1

187 Lawn, B. R. & Wilshaw, T. R., *Fracture of Brittle Solids*, Cambridge Solid State Science Series, 1975

188 Hayden, H. W., Moffatt, W. G. & Wulff, J., "The Structures and Properties of Materials", in *Mechanical Behaviour, Volume III*, John Wiley & Sons, 1965

189 Andrews, T. D., Goldthorpe, B. D. & Tickner, R. L., *Brittle Fracture in Penetrator and Target Materials*, DERA/SMC/CR973027/1.0, December 1997

190 Grady, D. E., "Dynamic Failure in Brittle Solids", *Europe-US Workshop on Fracture and Damage of Materials*, Prague, September, 21 – 23, 1994

191 Wachtman, J. B., "Elastic Deformation of Ceramics and Other Refractory Materials", *Mechanical and Thermal Properties of Ceramics*, 1969, 303, pp.139

192 Itia, 2006, "Cemented Carbides", URL http://www.itia.org.uk

193 Mahfuz, H., Zhu, Y., Haque, A., Abutalib, A., Vaidya, U., Jeelani, S., Gama, B., Gillespie, J. & Fink, B., "Investigation of High Velocity Impact on Integral Armor using Finite Element Method." *International Journal of Impact Engineering*, 2000, Vol. 24, pp. 203 – 217

194 Gailly, B. A. & Espinosa, H. D., "Modelling of Failure Mode Transition in Ballistic Penetration with a Continuum Model Describing Microcracking and Flow of Pulverised Media", *International Journal of Numerical Methods in Engineering*, 2002, 54, pp. 365 – 398

195 AUTODYN, The Interactive Software for Non-Linear Dynamic Analysis, Introductory Training Course, Century Dynamics, 2002

196 Verolme, K., *Numerical Prediction of Fragmentation On-set. Part 2; Tungsten Alloy fragments*. TNO Prins Maurits Laboratory. November 2000

197 Robertson, N. J., Hayhurst, C. J. & Fairlie, G. E., "Numerical Simulation of Explosive Phenomena." IJCAT, Twenty years of finite Element Analysis; Review and Future Prospects, *International Journal of Computer Applications in Technology*, 1994, Vol. 7, Nos. 3 - 6, pp 316 - 329

198 Hazell, P. J., "Modelling the Failure of a Ceramic Subjected to High Velocity Impact." *18th International Symposium on Ballistics*, San Antonio, 1999

199 Westerling, L., Lundberg, P., Holmberg, L. & Lundberg, B., "High Velocity Penetration of Homogeneous Segmented and Telescopic Projectiles into Alumina Targets." *International Journal of Impact Engineering*, 1997, Vol. 20, pp. 817 – 827

200 Anderson, C. A., "An Overview of the Theory of Hydrocodes." *International Journal of Impact Engineering*, 1987, Vol. 5, pp. 33 – 59

201 Tungsten Carbide Engineering Ltd. URL www.tungsten -carbide.com/carbide.htm

202 Hazell, P. J. & Iremonger, M. J., "The Numerical Analysis of Dynamically Loaded Ceramic: a Crack Softening Approach", *International Journal of Numerical Methods in Engineering*., 2000, 48, pp. 1037 – 1053

203 AUTODYN^{TM} "Interactive Non-Linear Dynamic Analysis Software Theory Manual", Century Dynamics, 1998

204 Meyers, M. A., *Dynamic Behaviour of Materials*, John Wiley & Sons, Inc., 1994

205 Hayhurst, C. J., Clegg, R. A., Livingstone, I. H. & Francis, N. J., "The Application of SPH Techniques in AUTODYN 2D to Ballistic Impact Problems", *16th International Symposium on Ballistics*, San Francisco, 1996

206 Libersky, L. D., Randles, P. W., Carney, T. C. & Dickenson, D. L., "Recent Improvements in SPH Modelling of Hypervelocity Impact", *International Journal of Impact Engineering*, 1997, Vol. 20, pp. 525 – 532

207 Clegg, R. A., Hayhurst, C. J. & Meuric, O. F. J., "Combined Mesh and Mesh Free Numerical Techniques to Efficiently Predict the Response of Concrete Structures to Impact", *Structures Under Shock and Impact*, 3 – 5th July 2000

208 Meina, D. F. & Chen, J. K., "Three-Dimensional Simulations of Impact Induced Damage in Composite Structures Using the Parallelized SPH Method", *Composites, Part A*, 2000

209 Wittenborn, K. G., *Armour Penetration Simulation Using SPH*, RMCS, Vehicle Technology Course Project, 2000

210 Grady, D. E. & Kipp, M. E.. "Experimental Measurement of Dynamic Failure and Fragmentation Properties of Metals", *International Journal of Solids and Structures*, 1997, 20, pp. 293 – 308

211 IDES, 2006, URL http://www.ides.com/generics/acrylic

212 Plastics Website, Ridoutplastics, 2006, URL http://www.ridoutplastics.com

213 Moxnes, J. F., Odegardstuen, G., Atwood, A. & Curran, P., "Mechanical Properties of a Porous Material Studied in a High Speed Piston Driven Compaction Experiment.", *30th International Annual Conference of ICT*, June 29 – July 2nd 1999

214 Dandekar, D. P., *Spall Strength of Tungsten Carbide*, Army Research Laboratories Aberdeen Proving Ground MD, February 2004

215 Holmquist, T. J. & Johnson, G. R., "Response of Silicon Carbide to High Velocity Impact", *Journal of Applied Physics*, 2002, Vol. 91, No. 9

216 Holmquist, T. J. & Johnson, G. R., "Modelling Ceramic Dwell and Interface Defeat", *Ceramic Armour Materials by Design, Ceramic Transactions*, 2003, Vol. 134

217 Grady, D. E., *Fragmentation of Rings and Shells, The Legacy of N. F. Mott*, Springer Report.

218 Pickup, I. M. & Barker, A. K., "Deviatoric Strength of Silicon Carbide Subject to Shock", *Shock Compression of Condensed Matter*, 1999, pp. 573 – 576

Appendix 1

14.5 mm BS41 Russian Armour Piercing Incendiary Projectile

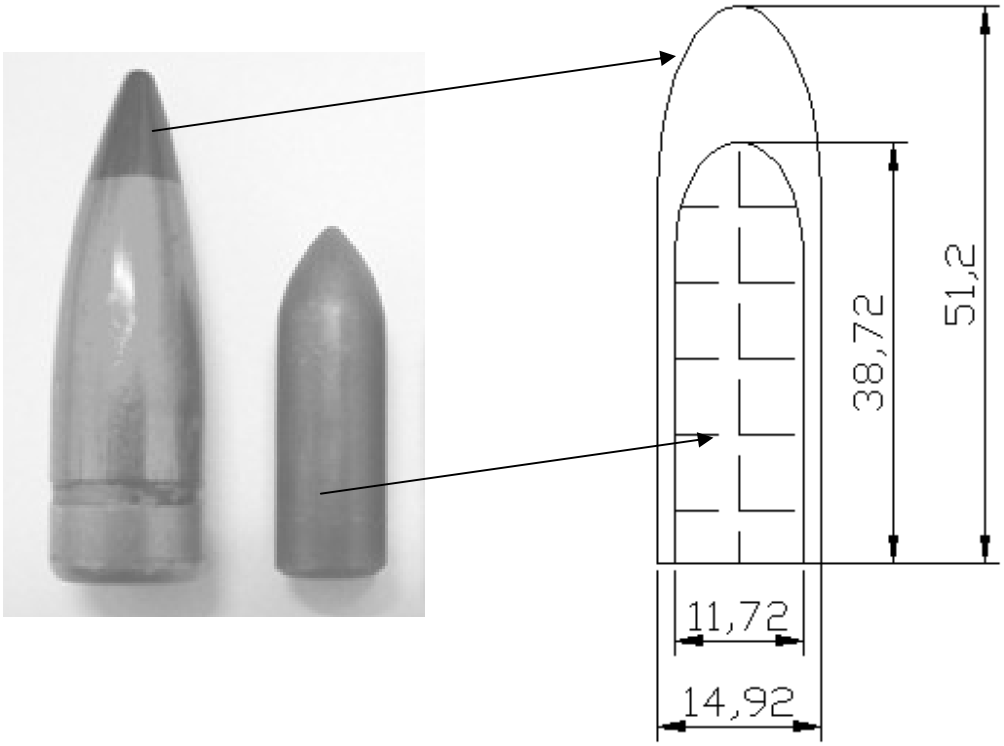

Figure A1.1: Above: 14.5 mm BS41 dimensions. Below, Cartridge and Propellant.

Table A1-1: BS41 Summary Projectile Part, Weight Measurements

Projectile Part	Propellant	Inner Jacket	Core	Incendiary	Outer Jacket	Cartridge Case & Primer
Weight (g)	30.86	9.22	38.72	0.97	14.37	106.36

Table A1-2: Description and codes of the different types of BS41

14.5mm Type	Description	Codes
Type BS 41	**Armour Piercing / Incendiary (Tungsten Carbide Core)**	**Red projectile and black tip (some bullets are half-red, half-black) Black Primer.**
Type B 32	Armour Piercing / Incendiary (Steel Core)	Black Tip over red band
Type BZT	Armour Piercing / Incendiary / Tracer	Purple Tip over red Band
Type ZP	Incendiary / Tracer	Red Tip
Type MDZ	High Explosive / Incendiary	All red bullet
Chinese Ammunition Type 56	Armour Piercing/ Incendiary (design similar to USSR Type B32)	Pre-1967, black tip over red band From 1967, black tip only.
Chinese Ammunition Type 56	Armour Piercing / Incendiary / Tracer (design similar to USSR Type BZT)	Pre-1967, purple tip over red band From 1967, purple tip only
Chinese Ammunition Type 56	Incendiary / Tracer (design similar to USSR Type ZP)	Red Tip

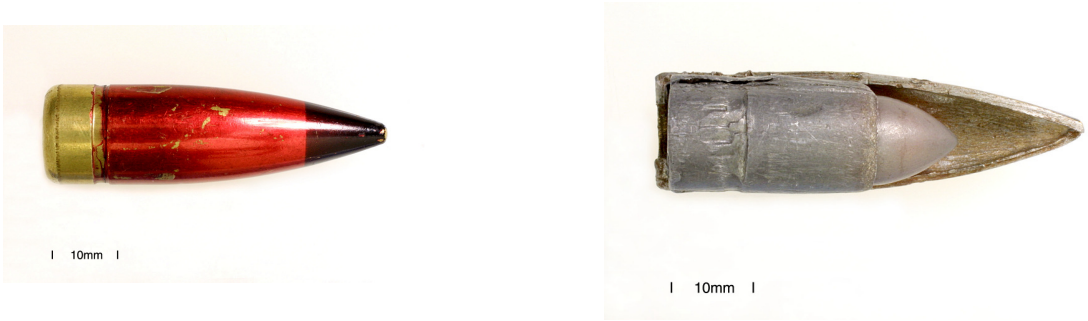

Figure A1.2: Internal View of the Russian BS41. The core is held within a soft steel inner jacket.

Figure A1.3: From left to Right: 14.5 mm B32 core, Bofors 7.62 x 51 mm FFV[1], bullet and core, BS41 Core.

[1] C. Roberson & P. J. Hazell, "Resistance of Four Different Ceramic Materials to Penetration by a Tungsten Carbide Cored Projectile",Paper 23, ACS, (2003).

APPENDIX 2

- Paper A2.1: N. J. Woolmore, P. J. Hazell & T. P. Stuart, "An Investigation into Fragmenting the 14.5 mm BS41 Armour Piercing Round by Varying a Confined Ceramic Target Set-Up", Ceramic Armor and Armor Systems, Ceramic Transactions, Vol. 151, (2003).

APPENDIX 3

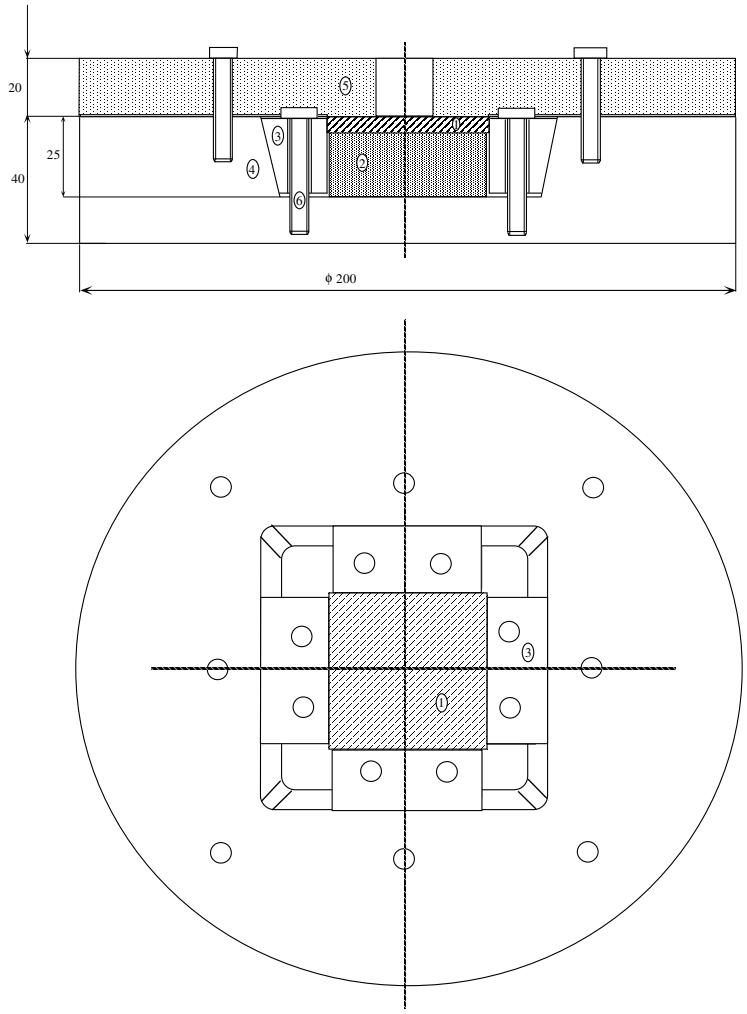

Figure A3-1: Confinement Frame from Sherman *et al.*[2] used for the initial 7.62 x 51 mm FFV Trials (without front face) see Chapter 3, section 3.3.

[2] D. Sherman and T. Ben-Shushan, "The Ballistic Failure Mechanisms and Sequence in Confined Ceramic Tiles," Israel Institute of Technology, TNS Meeting, Pitzbourg, (1993).

APPENDIX 4

- Precision non-contact three dimensional surface profiling: BS41 Surface Analysis WC-Co core fired into Sintox-CL and an Aluminium Alloy Witness Block

- Precision non-contact three dimensional surface profiling: BS41 Surface Analysis from a WC-Co sample from a stripped round.

APPENDIX 5

- AUTODYN 2D Material Models

Material – 1006 Steel

Equation of State	**Shock**
Parameter	Value (units – if any)
Reference density	7.896 (g/cm^3)
Gruneisen coefficient	2.17
Parameter C1	4.569x10^3 (m/s)
Parameter S1	1.49 (s/m)
Parameter Quad. S2	0.00
Relative Volume, VE	0.00
Relative Volume, VB	0.00
Parameter C2	0.00
Parameter S2	0.00
Reference Temperature	3.00x10^2 (K)
Specific Heat	4.52x10^2 (J/kg·K)

Strength	**Johnson Cook**
Parameter	Value (units – if any)
Shear modulus	8.18x10^7 (kPa)
Yield Stress	3.50x10^5 (kPa)
Hardening Constant	2.75x10^5 (kPa)
Hardening Exponent	3.60x10^{-1}
Strain Rate Constant	2.20x10^{-2}
Thermal Softening Exponent	1.00
Melting Temperature	1.811x10^3 (K)
Strain Rate Correction	None

Failure	**None**

Erosion	**Geometric Strain**
Parameter	Value (units – if any)
Erosion Strain	1.50
Type of Geometric Strain	Instantaneous

Material Cutoffs	
Parameter	Value (units – if any)
Maximum Expansion	1.00x10^{-1}
Minimum Density Factor (Euler)	1.00x10^{-5}
Minimum Density Factor (SPH)	1.00x10^{-5}
Maximum Density Factor (SPH)	1.00x10^{20}
Minimum Soundspeed	1.00x10^{-6} (m/s)
Maximum Soundspeed	1.01x10^{20} (m/s)
Maximum Temperature	1.00x10^{20} (m/s)
Reference	-

Material – WC

Equation of State	**Shock**
Parameter	Value (units – if any)
Reference density	1.491x10^1 (g/cm^3)
Gruneisen coefficient	1.32
Parameter C1	5.19x10^3 (m/s)
Parameter S1	1.16 (s/m)
Parameter Quad. S2	0.00
Relative Volume, VE	0.00

Relative Volume, VB	0.00
Parameter C2	0.00
Parameter S2	0.00
Reference Temperature	$3.00x10^{2}$ (K)
Specific Heat	0.00 (J/kg·K)

Strength **von Mises**

Parameter	Value (units – if any)
Shear modulus	$2.557x10^{8}$ (kPa)
Yield Stress	$4.00x10^{6}$ (kPa)

Failure **Hydro (Pmin)**

Parameter	Value (units – if any)
Hydro Tensile Limit	$-3.50x10^{6}$ (kPa)
Reheal	Yes
Crack Softening	No
Stochastic failure	No

Erosion **Geometric Strain**

Parameter	Value (units – if any)
Erosion Strain	3.00
Type of Geometric Strain	Instantaneous

Material Cutoffs

Parameter	Value (units – if any)
Maximum Expansion	$1.00x10^{-1}$
Minimum Density Factor (Euler)	$1.00x10^{-5}$
Minimum Density Factor (SPH)	$1.00x10^{-5}$
Maximum Density Factor (SPH)	$1.00x10^{20}$
Minimum Soundspeed	$1.00x10^{-6}$ (m/s)
Maximum Soundspeed	$1.01x10^{20}$ (m/s)
Maximum Temperature	$1.00x10^{20}$ (m/s)
Reference	-

Material – 7039 BRAD

Equation of State **Shock**

Parameter	Value (units – if any)
Reference density	2.77 (g/cm^{3})
Gruneisen coefficient	2.00
Parameter C1	$5.328x10^{3}$ (m/s)
Parameter S1	1.338
Parameter Quad. S2	0.00 (s/m)
Relative Volume, VE	0.00
Relative Volume, VB	0.00
Parameter C2	0.00 (m/s)
Parameter S2	0.00
Reference Temperature	$3.00x10^{2}$ (K)
Specific Heat	$8.75x10^{2}$ (J/kg·K)

Strength **Johnson Cook**

Parameter	Value (units – if any)
Shear modulus	$2.76x10^{7}$ (kPa)
Yield Stress	$2.20x10^{5}$ (kPa)
Hardening Constant	$5.00x10^{5}$ (kPa)

Hardening Exponent	$2.20x10^{-1}$
Strain Rate Constant	$1.60x10^{-2}$
Thermal Softening Exponent	$9.05x10^{-1}$
Melting Temperature	$9.33x10^{2}$ (K)
Strain Rate Correction	None

Failure **Principal Stress**

Parameter	Value (units – if any)
Principal Tensile Failure Stress	$7.00x10^{5}$ (kPa)
Max. Princ. Stress Difference / 2	$1.01x10^{20}$ (kPa)
Crack Softening	No
Stochastic failure	No

Erosion **Geometric Strain**

Parameter	Value (units – if any)
Erosion Strain	3.00
Type of Geometric Strain	Instantaneous

Material Cutoffs

Parameter	Value (units – if any)
Maximum Expansion	$1.00x10^{-1}$
Minimum Density Factor (Euler)	$1.00x10^{-5}$
Minimum Density Factor (SPH)	$1.00x10^{-5}$
Maximum Density Factor (SPH)	$1.00x10^{20}$
Minimum Soundspeed	$1.00x10^{-6}$ (m/s)
Maximum Soundspeed	$1.01x10^{20}$ (m/s)
Maximum Temperature	$1.00x10^{20}$ (m/s)
Reference	-

Material – WCGRADY

Equation of State **Shock**

Parameter	Value (units – if any)
Reference density	$1.49x10^{1}$ (g/cm^3)
Gruneisen coefficient	1.212
Parameter C1	$5.2537x10^{3}$ (m/s)
Parameter S1	1.106
Parameter Quad. S2	0.00 (s/m)
Relative Volume, VE	0.00
Relative Volume, VB	0.00
Parameter C2	0.00 (m/s)
Parameter S2	0.00
Reference Temperature	$3.00x10^{2}$ (K)
Specific Heat	0.00 (J/kg·K)

Strength **Piecewise JC**

Parameter	Value (units – if any)
Shear modulus	$2.76x10^{7}$ (kPa)
Yield Stress (zero plastic strain)	$2.20x10^{5}$ (kPa)
Eff. Plastic Strain #1	$1.00x10^{20}$
Eff. Plastic Strain #2	$1.00x10^{20}$
Eff. Plastic Strain #3	$1.00x10^{20}$
Eff. Plastic Strain #4	$1.00x10^{20}$
Eff. Plastic Strain #5	$1.00x10^{20}$
Eff. Plastic Strain #6	$1.00x10^{20}$
Eff. Plastic Strain #7	$1.00x10^{20}$
Eff. Plastic Strain #8	$1.00x10^{20}$

Eff. Plastic Strain #9	$1.00x10^{20}$
Eff. Plastic Strain #10	$1.00x10^{20}$
Yield Stress #1	$6.58076x10^{6}$ (kPa)
Yield Stress #2	$1.20x10^{7}$ (kPa)
Yield Stress #3	$1.20x10^{7}$ (kPa)
Yield Stress #4	$1.20x10^{7}$ (kPa)
Yield Stress #5	$1.20x10^{7}$ (kPa)
Yield Stress #6	$1.20x10^{7}$ (kPa)
Yield Stress #7	$1.20x10^{7}$ (kPa)
Yield Stress #8	$1.20x10^{7}$ (kPa)
Yield Stress #9	$1.20x10^{7}$ (kPa)
Yield Stress #10	$1.20x10^{7}$ (kPa)
Strain Rate Constant	0.00
Thermal Softening Exponent	0.00
Melting Temperature	$3.10x10^{3}$ (K)

Failure **Principal Stress**

Parameter	Value (units – if any)
Principal Tensile Failure Stress	$3.50x10^{6}$ (kPa)
Max. Princ. Stress Difference / 2	$1.01x10^{20}$ (kPa)
Crack Softening	Yes
Fracture Energy, Gf (=$[K^2]$/E)	$1.00x10^{-1}$ (J/m^2)
Flow Rule	No Bulking
Stochastic failure	No

Erosion **Geometric Strain**

Parameter	Value (units – if any)
Erosion Strain	3.50
Type of Geometric Strain	Instantaneous

Material Cutoffs

Parameter	Value (units – if any)
Maximum Expansion	$1.00x10^{-1}$
Minimum Density Factor (Euler)	$1.00x10^{-5}$
Minimum Density Factor (SPH)	$1.00x10^{-5}$
Maximum Density Factor (SPH)	$1.00x10^{20}$
Minimum Soundspeed	$1.00x10^{-6}$ (m/s)
Maximum Soundspeed	$1.01x10^{20}$ (m/s)
Maximum Temperature	$1.00x10^{20}$ (m/s)
Reference	-

Material – SIC

Equation of State **Polynomial**

Parameter	Value (units – if any)
Reference density	3.215 (g/cm^3)
Bulk Modulus A1	$2.20x10^{8}$ (kPa)
Parameter A2	$3.61x10^{8}$ (kPa)
Parameter A3	0.00 (kPa)
Parameter B0	0.00
Parameter B1	0.00
Parameter T1	$2.20x10^{8}$ (kPa)
Parameter T2	0.00 (kPa)
Reference Temperature	0.00 (K)
Specific Heat	0.00 (J/kg·K)

Strength	**Johnson-Holmquist**
Parameter	Value (units – if any)
Shear modulus	1.93×10^{8} (kPa)
Hugoniot Elastic Limit	1.17×10^{7} (kPa)
Intact Strength Constant A	8.60×10^{-1}
Intact Strength Exponent N	5.00×10^{-1}
Strain Rate Constant C	9.00×10^{-3}
Fracture Strength Constant B	4.00×10^{-1}
Fracture Strength Exponent M	1.00
Max. Fracture Strength Ratio	1.32×10^{-1}

Failure	**Johnson-Holmquist 2**
Parameter	Value (units – if any)
Damage Constant, D1	6.12×10^{-2}
Damage Constant, D2	1.00
Bulking Constant, Beta	1.00
Hydro Tensile Limit	-7.50×10^{5} (kPa)
Damage Type	Instantaneous (JH1)
Tensile Failure	Hydro (Pmin)

Erosion	**Geometric Strain**
Parameter	Value (units – if any)
Erosion Strain	3.00
Type of Geometric Strain	Instantaneous

Material Cutoffs

Parameter	Value (units – if any)
Maximum Expansion	1.00×10^{-1}
Minimum Density Factor (Euler)	1.00×10^{-5}
Minimum Density Factor (SPH)	1.00×10^{-5}
Maximum Density Factor (SPH)	1.00×10^{20}
Minimum Soundspeed	1.00×10^{-6} (m/s)
Maximum Soundspeed	1.01×10^{20} (m/s)
Maximum Temperature	1.00×10^{20} (m/s)
Reference	-

Material – AL203-99.5

Equation of State	**Polynomial**
Parameter	Value (units – if any)
Reference density	3.89 (g/cm^3)
Bulk Modulus A1	2.31×10^{8} (kPa)
Parameter A2	-1.60×10^{8} (kPa)
Parameter A3	2.774×10^{9} (kPa)
Parameter B0	0.00
Parameter B1	0.00
Parameter T1	2.31×10^{8} (kPa)
Parameter T2	0.00 (kPa)
Reference Temperature	0.00 (K)
Specific Heat	0.00 (J/kg·K)

Strength	**Johnson-Holmquist**
Parameter	Value (units – if any)
Shear modulus	1.52×10^{8} (kPa)
Hugoniot Elastic Limit	6.57×10^{7} (kPa)
Intact Strength Constant A	8.80×10^{-1}
Intact Strength Exponent N	6.40×10^{-1}

Strain Rate Constant C	$7.00x10^{-3}$
Fracture Strength Constant B	$2.80x10^{-1}$
Fracture Strength Exponent M	$6.00x10^{-1}$
Max. Fracture Strength Ratio	1.00

Failure **Johnson-Holmquist 2**

Parameter	Value (units – if any)
Damage Constant, D1	$1.00x10^{-2}$
Damage Constant, D2	$7.00x10^{-1}$
Bulking Constant, Beta	1.00
Hydro Tensile Limit	$-2.60x10^{5}$ (kPa)
Damage Type	Gradual (JH2)
Tensile Failure	Hydro (Pmin)

Erosion **Geometric Strain**

Parameter	Value (units – if any)
Erosion Strain	3.00
Type of Geometric Strain	Instantaneous

Material Cutoffs

Parameter	Value (units – if any)
Maximum Expansion	$1.00x10^{-1}$
Minimum Density Factor (Euler)	$1.00x10^{-5}$
Minimum Density Factor (SPH)	$1.00x10^{-5}$
Maximum Density Factor (SPH)	$1.00x10^{20}$
Minimum Soundspeed	$1.00x10^{-6}$ (m/s)
Maximum Soundspeed	$1.01x10^{20}$ (m/s)
Maximum Temperature	$1.00x10^{20}$ (m/s)
Reference	-

Material – AL203-99.7

Equation of State **Polynomial**

Parameter	Value (units – if any)
Reference density	3.80 (g/cm^3)
Bulk Modulus A1	$2.00x10^{8}$ (kPa)
Parameter A2	0.00 (kPa)
Parameter A3	0.00 (kPa)
Parameter B0	0.00
Parameter B1	0.00
Parameter T1	$2.00x10^{8}$ (kPa)
Parameter T2	0.00 (kPa)
Reference Temperature	0.00 (K)
Specific Heat	0.00 (J/kg·K)

Strength **Johnson-Holmquist**

Parameter	Value (units – if any)
Shear modulus	$1.35x10^{8}$ (kPa)
Hugoniot Elastic Limit	$5.90x10^{6}$ (kPa)
Intact Strength Constant A	$9.89\ x10^{-1}$
Intact Strength Exponent N	$3.755\ x10^{-1}$
Strain Rate Constant C	0.00
Fracture Strength Constant B	$7.70x10^{-1}$
Fracture Strength Exponent M	$1.00x10^{-1}$
Max. Fracture Strength Ratio	$5.00x10^{-1}$

Failure **Johnson-Holmquist 2**

Parameter	Value (units – if any)
Damage Constant, D1	$1.00x10^{-2}$
Damage Constant, D2	1.00
Bulking Constant, Beta	1.00
Hydro Tensile Limit	$-2.90x10^{4}$ (kPa)
Damage Type	Gradual (JH2)
Tensile Failure	Hydro (Pmin)

Erosion **Geometric Strain**

Parameter	Value (units – if any)
Erosion Strain	3.00
Type of Geometric Strain	Instantaneous

Material Cutoffs

Parameter	Value (units – if any)
Maximum Expansion	$1.00x10^{-1}$
Minimum Density Factor (Euler)	$1.00x10^{-5}$
Minimum Density Factor (SPH)	$1.00x10^{-5}$
Maximum Density Factor (SPH)	$1.00x10^{20}$
Minimum Soundspeed	$1.00x10^{-6}$ (m/s)
Maximum Soundspeed	$1.01x10^{20}$ (m/s)
Maximum Temperature	$1.00x10^{20}$ (m/s)
Reference	-

Material – BORONCARBIDE

Equation of State **Polynomial**

Parameter	Value (units – if any)
Reference density	2.5160 (g/cm^3)
Bulk Modulus A1	$2.33x10^{8}$ (kPa)
Parameter A2	$5.00x10^{7}$ (kPa)
Parameter A3	0.00 (kPa)
Parameter B0	0.00
Parameter B1	0.00
Parameter T1	$2.33x10^{8}$ (kPa)
Parameter T2	0.00 (kPa)
Reference Temperature	0.00 (K)
Specific Heat	0.00 (J/kg·K)

Strength **Johnson-Holmquist**

Parameter	Value (units – if any)
Shear modulus	$1.99x10^{8}$ (kPa)
Hugoniot Elastic Limit	$1.25x10^{7}$ (kPa)
Intact Strength Constant A	$9.87\ x10^{-1}$
Intact Strength Exponent N	$7.70\ x10^{-1}$
Strain Rate Constant C	2.70x10-2
Fracture Strength Constant B	$5.00x10^{-1}$
Fracture Strength Exponent M	1.00
Max. Fracture Strength Ratio	$1.50x10^{-1}$

Failure **Johnson-Holmquist 2**

Parameter	Value (units – if any)
Damage Constant, D1	$1.00x10^{-1}$
Damage Constant, D2	1.00
Bulking Constant, Beta	1.00
Hydro Tensile Limit	$-7.30x10^{6}$ (kPa)

Damage Type	Gradual (JH2)
Tensile Failure	Hydro (Pmin)

Erosion **None**

Material Cutoffs

Parameter	Value (units – if any)
Maximum Expansion	$1.00x10^{-1}$
Minimum Density Factor (Euler)	$1.00x10^{-5}$
Minimum Density Factor (SPH)	$1.00x10^{-5}$
Maximum Density Factor (SPH)	$1.00x10^{20}$
Minimum Soundspeed	$1.00x10^{-6}$ (m/s)
Maximum Soundspeed	$1.01x10^{20}$ (m/s)
Maximum Temperature	$1.00x10^{20}$ (m/s)
Reference	-

Material –7039 ALUM

Equation of State **Shock**

Parameter	Value (units – if any)
Reference density	2.77 (g/cm^3)
Gruneisen coefficient	2.00
Parameter C1	$5.328x10^3$ (m/s)
Parameter S1	1.338 (s/m)
Parameter Quad. S2	0.00
Relative Volume, VE	0.00
Relative Volume, VB	0.00
Parameter C2	0.00
Parameter S2	0.00
Reference Temperature	$3.00x10^2$ (K)
Specific Heat	$8.75x10^2$ (J/kg·K)

Strength **Johnson Cook**

Parameter	Value (units – if any)
Shear modulus	$2.76x10^7$ (kPa)
Yield Stress	$3.37x10^5$ (kPa)
Hardening Constant	$3.43x10^5$ (kPa)
Hardening Exponent	$4.10x10^{-1}$
Strain Rate Constant	$1.00x10^{-2}$
Thermal Softening Exponent	1.00
Melting Temperature	$8.77x10^2$ (K)
Strain Rate Correction	None

Failure **None**

Erosion **Geometric Strain**

Parameter	Value (units – if any)
Erosion Strain	3.00
Type of Geometric Strain	Instantaneous

Material Cutoffs

Parameter	Value (units – if any)
Maximum Expansion	$1.00x10^{-1}$
Minimum Density Factor (Euler)	$1.00x10^{-5}$
Minimum Density Factor (SPH)	$1.00x10^{-5}$

Maximum Density Factor (SPH)	$1.00x10^{20}$
Minimum Soundspeed	$1.00x10^{-6}$ (m/s)
Maximum Soundspeed	$1.01x10^{20}$ (m/s)
Maximum Temperature	$1.00x10^{20}$ (m/s)
Reference	-

Material – WC-Co BS41

Equation of State **Shock**

Parameter	Value (units – if any)
Reference density	$1.491x10^{1}$ (g/cm^3)
Gruneisen coefficient	1.09
Parameter C1	$5.253x10^{3}$ (m/s)
Parameter S1	1.11
Parameter Quad. S2	0.00 (s/m)
Relative Volume, VE	0.00
Relative Volume, VB	0.00
Parameter C2	0.00 (m/s)
Parameter S2	0.00
Reference Temperature	$3.00x10^{2}$ (K)
Specific Heat	0.00 (J/kg·K)

Strength **Piecewise JC**

Parameter	Value (units – if any)
Shear modulus	$2.57x10^{8}$ (kPa)
Yield Stress (zero plastic strain)	$2.85x10^{6}$ (kPa)
Eff. Plastic Strain #1	$7.94x10^{-3}$
Eff. Plastic Strain #2	$1.00x10^{20}$
Eff. Plastic Strain #3	$1.00x10^{20}$
Eff. Plastic Strain #4	$1.00x10^{20}$
Eff. Plastic Strain #5	$1.00x10^{20}$
Eff. Plastic Strain #6	$1.00x10^{20}$
Eff. Plastic Strain #7	$1.00x10^{20}$
Eff. Plastic Strain #8	$1.00x10^{20}$
Eff. Plastic Strain #9	$1.00x10^{20}$
Eff. Plastic Strain #10	$1.00x10^{20}$
Yield Stress #1	$7.43550x10^{6}$ (kPa)
Yield Stress #2	$1.20x10^{7}$ (kPa)
Yield Stress #3	$1.20x10^{7}$ (kPa)
Yield Stress #4	$1.20x10^{7}$ (kPa)
Yield Stress #5	$1.20x10^{7}$ (kPa)
Yield Stress #6	$1.20x10^{7}$ (kPa)
Yield Stress #7	$1.20x10^{7}$ (kPa)
Yield Stress #8	$1.20x10^{7}$ (kPa)
Yield Stress #9	$1.20x10^{7}$ (kPa)
Yield Stress #10	$1.20x10^{7}$ (kPa)
Strain Rate Constant	0.00
Thermal Softening Exponent	0.00
Melting Temperature	$3.10x10^{3}$ (K)

Failure **Principal Stress**

Parameter	Value (units – if any)
Principal Tensile Failure Stress	$2.05x10^{6}$ (kPa)
Max. Princ. Stress Difference / 2	$1.01x10^{20}$ (kPa)
Crack Softening	Yes
Fracture Energy, Gf (=[K^2]/E)	$1.60x10^{2}$ (J/m^2)
Flow Rule	No Bulking

Stochastic failure	No

Erosion **Geometric Strain**

Parameter	Value (units – if any)
Erosion Strain	3.00
Type of Geometric Strain	Instantaneous

Material Cutoffs

Parameter	Value (units – if any)
Maximum Expansion	$1.00x10^{-1}$
Minimum Density Factor (Euler)	$1.00x10^{-5}$
Minimum Density Factor (SPH)	$1.00x10^{-5}$
Maximum Density Factor (SPH)	$1.00x10^{20}$
Minimum Soundspeed	$1.00x10^{-6}$ (m/s)
Maximum Soundspeed	$1.01x10^{20}$ (m/s)
Maximum Temperature	$1.00x10^{20}$ (m/s)
Reference	-

Material – LITHIUM F

Equation of State **Shock**

Parameter	Value (units – if any)
Reference density	2.638 (g/cm^3)
Gruneisen coefficient	1.69
Parameter C1	$5.15x10^3$ (m/s)
Parameter S1	1.35
Parameter Quad. S2	0.00 (s/m)
Relative Volume, VE	0.00
Relative Volume, VB	0.00
Parameter C2	0.00 (m/s)
Parameter S2	0.00
Reference Temperature	$3.00x10^2$ (K)
Specific Heat	$1.56x10^3$ (J/kg·K)

Strength **Steinberg Guinan**

Parameter	Value (units – if any)
Shear modulus	$4.90x10^7$ (kPa)
Yield Stress	$3.60x10^5$ (kPa)
Maximum Yield Stress	$3.60x10^5$ (kPa)
Hardening Constant	0.00
Hardening Exponent	0.00
Derivative dG/dP	2.45
Derivative dG/dT	$-3.02x10^4$ (kPa)
Derivative dG/dY	$1.80x10^{-2}$
Melting Temperature	$3.10x10^3$ (K)

Failure **None**
Erosion **None**
Material Cutoffs

Parameter	Value (units – if any)
Maximum Expansion	$1.00x10^{-1}$
Minimum Density Factor (Euler)	$1.00x10^{-5}$
Minimum Density Factor (SPH)	$1.00x10^{-1}$
Maximum Density Factor (SPH)	3.00
Minimum Soundspeed	$1.00x10^{-6}$ (m/s)
Maximum Soundspeed	$1.01x10^{20}$ (m/s)
Maximum Temperature	$1.00x10^{20}$ (m/s)
Reference	-

Material – LUCITE

Equation of State **Shock**

Parameter	Value (units – if any)
Reference density	1.181 (g/cm^3)
Gruneisen coefficient	7.50x10^{-1}
Parameter C1	2.26x10^3 (m/s)
Parameter S1	1.816
Parameter Quad. S2	0.00 (s/m)
Relative Volume, VE	0.00
Relative Volume, VB	0.00
Parameter C2	0.00 (m/s)
Parameter S2	0.00
Reference Temperature	0.00 (K)
Specific Heat	0.00 (J/kg·K)

Strength **None**

Failure **None**

Erosion **None**

Material Cutoffs

Parameter	Value (units – if any)
Maximum Expansion	1.00x10^{-1}
Minimum Density Factor (Euler)	1.00x10^{-5}
Minimum Density Factor (SPH)	2.00x10^{-1}
Maximum Density Factor (SPH)	3.00
Minimum Soundspeed	1.00x10^{-6} (m/s)
Maximum Soundspeed	1.01x10^{20} (m/s)
Maximum Temperature	1.01x10^{20} (m/s)
Reference	-

Material – WC GRADY Y

Equation of State **Shock**

Parameter	Value (units – if any)
Reference density	1.5013x10^1 (g/cm^3)
Gruneisen coefficient	1.05
Parameter C1	5.253x10^3 (m/s)
Parameter S1	1.11
Parameter Quad. S2	0.00 (s/m)
Relative Volume, VE	0.00
Relative Volume, VB	0.00
Parameter C2	0.00 (m/s)
Parameter S2	0.00
Reference Temperature	3.00x10^2 (K)
Specific Heat	0.00 (J/kg·K)

Strength **Piecewise JC**

Parameter	Value (units – if any)
Shear modulus	2.557x10^8 (kPa)
Yield Stress (zero plastic strain)	2.865x10^6 (kPa)
Eff. Plastic Strain #1	7.94x10^{-3}
Eff. Plastic Strain #2	1.00x10^{20}
Eff. Plastic Strain #3	1.00x10^{20}
Eff. Plastic Strain #4	1.00x10^{20}
Eff. Plastic Strain #5	1.00x10^{20}
Eff. Plastic Strain #6	1.00x10^{20}
Eff. Plastic Strain #7	1.00x10^{20}
Eff. Plastic Strain #8	1.00x10^{20}

Eff. Plastic Strain #9	$1.00x10^{20}$
Eff. Plastic Strain #10	$1.00x10^{20}$
Yield Stress #1	$7.43550x10^{6}$ (kPa)
Yield Stress #2	$1.20x10^{7}$ (kPa)
Yield Stress #3	$1.20x10^{7}$ (kPa)
Yield Stress #4	$1.20x10^{7}$ (kPa)
Yield Stress #5	$1.20x10^{7}$ (kPa)
Yield Stress #6	$1.20x10^{7}$ (kPa)
Yield Stress #7	$1.20x10^{7}$ (kPa)
Yield Stress #8	$1.20x10^{7}$ (kPa)
Yield Stress #9	$1.20x10^{7}$ (kPa)
Yield Stress #10	$1.20x10^{7}$ (kPa)
Strain Rate Constant	0.00
Thermal Softening Exponent	0.00
Melting Temperature	$3.10x10^{3}$ (K)

Failure **Principal Stress**

Parameter	Value (units – if any)
Principal Tensile Failure Stress	$3.905x10^{6}$ (kPa)
Max. Princ. Stress Difference / 2	$1.01x10^{20}$ (kPa)
Crack Softening	No
Stochastic failure	No

Erosion **Geometric Strain**

Parameter	Value (units – if any)
Erosion Strain	3.50
Type of Geometric Strain	Instantaneous

Material Cutoffs

Parameter	Value (units – if any)
Maximum Expansion	$1.00x10^{-1}$
Minimum Density Factor (Euler)	$1.00x10^{-5}$
Minimum Density Factor (SPH)	$2.00x10^{-1}$
Maximum Density Factor (SPH)	3.00
Minimum Soundspeed	$1.00x10^{-6}$ (m/s)
Maximum Soundspeed	$1.01x10^{20}$ (m/s)
Maximum Temperature	$1.00x10^{20}$ (m/s)
Reference	-